

Ultrasound Stimulation of a Piezoelectric Composite with Compliant Layers on Power Output for Bone Healing in Spinal Fusion Applications

By
Kyle Coates

Submitted to the graduate degree program in Mechanical Engineering and the Graduate Faculty of the University of Kansas in partial fulfillment of the requirements for the degree of Master of Science

Chairperson Dr. Elizabeth Friis

Dr. Xinmai Yang

Dr. Sara Wilson

Date Defended: January 17th, 2018

The Thesis Committee for Kyle Coates
certifies that this is the approved version of the following thesis:

Ultrasound Stimulation of a Piezoelectric Composite with Compliant Layers on Power Output for Bone
Healing in Spinal Fusion Applications

Chairperson Dr. Elizabeth Friis

Date Approved: 1/24/2018

Abstract

Spinal fusion devices have up to 50% failure rates for patients who smoke or are diabetic ¹. Bone healing has been accomplished through direct current (DC) electrical stimulation to improve bone healing rates ². Current DC electrical stimulation can accomplish bone healing, but batteries are used as a source of power. Replacing a battery after fusion would require a second surgery. Many microgenerators use piezoelectric material to convert mechanical energy into electrical potential ³. In a pilot ovine study, composite spinal interbody implants made with stacked layers of piezoelectric fibers provided DC electrical stimulation at the fusion site and substantially enhanced fusion under normal loading after six weeks as compared to a control ^{2,4,5}. To improve manufacturability while maintaining material toughness of the interbody implants, alternative manufacturing methods were explored in which compliant layers of epoxy (EPO-TEK[®] 301, Billerica, MA) were inserted between stacked discs of piezoelectric material, PZT-SM111 (STEMiNC-0.4mm thickness, 10mm diameter, Part No. SMD10T04F5000S111, Doral, FL). For patients with limited weight bearing abilities that cannot provide enough mechanical energy from human body movement, another method of mechanically stimulating the PZT discs would be beneficial. Many methods of wirelessly powering medical devices have been investigated including electromagnetic waves, thermoelectric devices, and ultrasound ³. Transmitted ultrasound waves can be used to mechanically activate a medical device implanted into human tissue with PZT elements ³. Using ultrasound as the loading source, the effect of varying compliant layer thicknesses on generated electrical potential and power output of the PZT compliant layer adaptive composite stacks (CLACS) in different media (water, tissue, and tissue plus bone), media thicknesses (20mm and 40mm), and loading orientations of the PZT composites with respect to the ultrasound wave front (perpendicular and parallel) were investigated.

An Acuson 128xp ultrasound medical imaging machine (Mountain View, CA) was used to mechanically stimulate the PZT elements in the compliant layer thickness composites and voltage measurements were made with a Tektronix (Beaverton, OR) DPO 3034 Digital Phosphor Oscilloscope (300 MHz). The PZT composite was manufactured with six through thickness pre-poled PZT-SM511 discs (STEMiNC-0.4mm thickness, 10mm diameter, Part No. SMD10T04F5000S111, Doral, FL) that were connected electrically in parallel (EPO-TEK® H20E, Billerica, MA) with copper strips, varying compliant layer thickness (0, 0.2, 0.4, and 0.8 mm \pm 0.02 mm) of medical grade epoxy slices (EPO-TEK® 301, Billerica, MA) interposed between the PZT discs, and encapsulated in medical grade epoxy (EPO-TEK® 301, Billerica, MA).

After assembly, the CLACS were tested at each combination of media type, media thickness, and loading orientations. The CLACS were subject to 4MHz ultrasound waves (1 W) in a Gaussian shape pattern with a V4 vector 128 PZT element array probe (Mountain View, CA). Voltage measurements before rectification (alternating current - AC) and after rectification (direct current - DC) were recorded. Power was computed after rectification by applying an average voltage measured across the lumped internal Oscilloscope channel impedance (1 M Ω) with the influence of a variable load resistance (Ω) and capacitor (c) connected in parallel and then using $P=V^2/R$ by combining Joule's and Ohm's law.

By adding a compliant layer thickness in between the PZT discs of the CLACS, generated electrical potential and power output increased. As the compliant layer thickness increased there were significant increases in power output due to more deformation that occurred along the entire face and edges of the PZT discs. As media thickness increased, DC power output decreased. The CLACS produced the most power with water as the media. Significantly less power was produced in tissue media, and even less in the tissue plus bone medium ($p < 0.05$ BoxCox Transformation). When the stacked PZT layers were being loaded perpendicular to the wave front of the ultrasound waves, there was significantly

more power output than when the stacked PZT layers were being loaded parallel to the ultrasound wave front ($p < 0.05$ BoxCox Transformation).

Future work could build off this foundational study to further characterize the CLACS power output behavior. These future studies would include focused vs. unfocused ultrasound loading sources to increase the amount of mechanical energy that influences the CLACS, differing operating frequencies to match and mismatch the resonant frequency of the PZT discs and to determine optimum frequencies for certain media depths, testing more varied loading orientations, differing ultrasound intensity levels, using a combination of radially and through-thickness poled PZT discs, designing circuit components to improve electrical energy transfer (impedance matching) efficiency and implementing pulsed DC circuit logic after rectification to approach a more realistic application of DC electrical stimulation in bone healing for spinal fusion.

Acknowledgements

- **Dr. Elizabeth Friis** for all her support and guidance during my graduate career. The passion and drive she has for this project and to help others is inspiring and contagious. This project would not be where it is today without Dr. Friis and her wisdom. Under her wing I feel I have become a better researcher and graduate student.
- **Eileen Cadel, Ember Krech, Kelly Tong, and Colton Lowe** for all their support, guidance, and friendship. I couldn't have accomplished much without you guys. I have been blessed with great lab mates that challenge me to be better every day. You all have made the Spine Biomechanics Lab a special, comforting, and fun place to be a graduate student.
 - **Eileen Cadel** for imparting her wisdom and experience in the lab to help me better understand spine biomechanics, spine anatomy, designing studies, setting up tests, manufacturing methods, troubleshooting, reading papers, statistics, and what it means to be a graduate student.
 - **Ember Krech** for imparting her wisdom and experience in the lab to help me better understand spine biomechanics, spine anatomy, designing studies, setting up tests, manufacturing methods, reading papers, statistics, and what it means to be a graduate student. In addition, I would like to thank Ember for manufacturing all the compliant layer adaptive composite stack samples that I used in my study.
 - **Kelly Tong** for imparting her knowledge of spine biomechanics, spine anatomy, and statistics. Her drive and passion to get things done is contagious. You helped me understand more about data transformations, ANOVA, and Tukey-Kramer tests. You always pushed me with your productivity to do more each day and have been a great lab mate.

- **Colton Lowe** for imparting his knowledge of spine biomechanics, spine anatomy, and statistics. You helped me understand more about data transformations, ANOVA, and Tukey-Kramer tests.
- **Dr. Xinmai Yang** for his support during the design of my study and frequent contributions throughout my graduate career to help me better understand designing studies, setting up tests, sound, piezoelectric material, data sampling, circuits, and for providing the Spine Biomechanics lab with an ultrasound imaging machine.
- **Dr. Sara Wilson** for agreeing to be a part of my thesis committee, giving her time, and help and encouragement both with my thesis project and in class.
- **The Mechanical Engineering Department** for providing a great environment to work at and learn in for the last year and a half during my graduate career.
- **Kate Maisch** and **Ansel Armstrong** for always being supportive and answering my questions promptly no matter how many times I have bothered them and for brightening my day every time I see them.
- **Dr. Geng Ku** for his support with data collection ideas, help with fixing the ultrasound machine used in this study, and answering any questions I had about designing studies.
- **Damon Mar** for imparting his wisdom with ultrasound, designing studies, setting up tests and what it means to be a graduate student.
- **All my lab mates, Nolan Norton, Nick Riggert, Alyssa Rollando, Robbie Hable, Hal Peebles, Mathew Dickenson, Fallon Fitzwater, Kait Howard, Lance Frazer, Camillo Giraldo Grisales, Logan Sidner, John Liu, John Stark, Charu Srivasta, Sarath Challa, Nathan Klein, Carsten Holtorf,** and friends from other labs for the great memories throughout my graduate school career. Whether we were just hanging out, getting ice cream, eating sushi, going to Mass Street, playing soccer, volleyball, basketball, flag football, ultimate frisbee, swimming, watching

sports, watching a Solar Eclipse, going to trivia, dressing up for Halloween, gathering for Friendsgiving, or gathering for a winter holiday party, you all have made my graduate experience one to remember. The last year and a half would not have been nearly as enjoyable without you all.

- **My parents Mike and Kathleen Coates** and **siblings Logan and Eryn Coates** for always pushing me to be the best that I can be. Thank you all for your support throughout my graduate career.
- **Amy Hein** for being my biggest fan and for all her support this past year.

This work was supported by the NIH grant R44AR070088.

Table of Contents

Abstract.....	iii
Acknowledgements.....	vi
Table of Contents.....	ix
Image List - Thesis.....	xi
Image List – Journal of Orthopaedic Research Manuscript.....	xv
Equation List.....	xvii
Table List.....	xx
Chapter 1. Background and Literature Review.....	1
1.1 Problem Statement.....	1
1.2 Spinal Fusion.....	5
1.2.1 Spinal Interbody Fusion Devices.....	5
1.2.2 Electrical Stimulation.....	7
1.2.3 Electromechanical Properties of Bone.....	9
1.3 Piezoelectric Materials.....	10
1.3.1 Basic Piezoelectric Theory.....	10
1.3.2 Stacked PZT Layers vs. Monolithic PZT.....	13
1.4 Acoustics.....	14
1.4.1 Acoustics – Physics of Wave Motion.....	14
1.4.2 Acoustics - Rayleigh Distance.....	17
1.4.3 Acoustics - Sound Reflection and Transmission at an Interface.....	19
1.4.4 Acoustics - Attenuation.....	29
1.4.5 Acoustics - Medical Imaging Ultrasound.....	32
1.4.6 Acoustics - Powering Medical Devices with Ultrasound in Literature.....	45
Chapter 2. Journal of Orthopaedic Research Paper (In Progress).....	56
2.1 Manuscript for Journal of Orthopaedic Research.....	56
2.1.1 Abstract.....	57
2.1.2 Keywords.....	57
2.1.3 Introduction.....	58
2.1.4 Methods.....	59
2.1.5 Results and Discussion.....	64
2.1.6 Conclusion.....	80
2.1.7 Acknowledgements.....	81

2.1.8 References.....	81
2.2 Additional Figures and Information	83
2.2.1 After Rectification Total Power Figures	83
2.2.2 After Rectification Load Power Figures.....	85
2.2.3 Capacitor and Oscilloscope Power Curves.....	89
Chapter 3. Detailed Methods.....	90
3.1 Manufacturing of Spinal Fusion Devices with varying Compliant Layers	90
3.2 Experimental Setup.....	97
3.3 Parameters Tested	101
3.4 Medical Imaging Ultrasound Machine and Probe – Acuson 128xp, V4.....	105
3.5 Measuring Device – Tektronix DPO 3034 Digital Phosphor Oscilloscope.....	109
3.6 Rectifying Circuit	111
3.6.1 Isolation Transformer – CyanKen EI14 (1:1)	115
3.6.2 Equivalent Impedance of the Rectifying circuit	121
3.7 Generic Testing Procedure.....	130
3.7.1 Measurements Before Rectification (V_{BR}).....	136
3.7.2 Measurements After Rectification (V_{AR})	140
3.7.3 Recording Data.....	142
3.8 Data Analysis Methods	143
3.8.1 Data Analysis Methods - MATLAB.....	143
3.8.2 Data Analysis Methods – Organization in Excel.....	152
3.8.3 Statistical Analysis Methods – MATLAB.....	152
Chapter 4. Conclusions and Future Work	159
References	161
Appendix A: MATLAB Code used for Analysis.....	165
Appendix A.1: MATLAB Code used to analyze Oscilloscope Waveform Data	165
Appendix A.2: MATLAB Code used for Statistical Analysis	180
Appendix A.3: MATLAB Code for after rectification filtering.....	191
Appendix B: Ultrasound Machine Startup Procedure.....	194

Image List - Thesis

Figure 1 - PZT Fiber Stacked Composite isometric (a) and front (b) view	3
Figure 2 - Compliant Layer Adaptive Composite Stack (CLACS) isometric (a) and side (b) view	3
Figure 3 - Vertebral disc anatomy example showing compression on spinal nerve by herniated disc (Public Domain, commons.wikipedia.org, labeled for reuse) ¹³	5
Figure 4 – Sagittal image showing compression on spinal nerve by bulging disc in lumbar spine (Public Domain, commons.wikipedia.org, labeled for reuse) ¹⁴	6
Figure 5 - Schematic example of tension on bone yielding positive electrical potential and compression yielding negative electrical potential (Adapted from Basset and Becker) ²¹	9
Figure 6 - Schematic example of tension and compression on PZT material with metal plates as electrodes (Public Domain, commons.wikipedia.org, labeled for reuse with modification) ²⁴	11
Figure 7 - Schematic example of piezoelectric material dipole moments before and after poling (large voltage applied across the material)	12
Figure 8 – Scematic illustration of -31 and -33 modes of operation for piezoelectric material (Adapted from Anton and Sodano ²³)	13
Figure 9 - Longitudinal and Transverse Waves described by particle movement relative to the direction of the propagating wave.....	16
Figure 10 – Transition from plane wave to spherical wave for a point source at approximately half of the Rayleigh Distance	18
Figure 11 - Reflection and Transmission Sound Pressure at an Impedance Mismatching Interface with the same Cross-Sectional Area	20
Figure 12 - Reflection and Transmission Sound Pressure at an Impedance matching Interface with different Cross-Sectional Areas	23
Figure 13 - The behavior of an incident wave striking the boundary between two impedance mismatching mediums	26
Figure 14 - Compression and Rarefactional Pressure on Particle Virbration Position and Movement (Adapted from ²⁸)	29
Figure 15 - Gating of Ultrasound Frequency generator and effect on voltage pulse commands to PZT elements and pressure waves generated in low and high transducer damping (Adapted from ²⁸).....	35
Figure 16 - Weakly focused single element transducer (left) and strongly focused (right) (Adapted from ²⁸)	36
Figure 17 - Ultrasound linear array probe with rectangular PZT elements design (Adapted from ²⁸).....	38
Figure 18 - Operation of linear array. Sequential excitation of small PZT element groups used to produce a two-dimensional image (Adapted from ²⁸)	39
Figure 19 - Phased array probe (Adapted from ²⁸)	40
Figure 20 - Beam forming for phased array ultrasound probe. Elements are excited symmetrically in sequence about the center of the array creating a focus point for the ultrasound wave to occur at the center of the array in a medium (Adapted from ²⁸).....	41
Figure 21 - Beam Steering of phased array ultrasound probe to create different focal points for ultrasound wave by exciting elements at different times (Adapted from ²⁸)	42
Figure 22 - Dynamic focusing of phased array ultrasound probe used to improve lateral resoultion at multiple depths in a medium being imaged. The distance between the elements and the focal point is small in "a" and more elements are excited in "b" and "c" to achieve a similar focus at greater depths in the medium (Adapted from ²⁸)..	42
Figure 23 - Acuson 128xp V4 Phased Array Ultrasound Probe Vector Array Ultrasound Scan Format (Adapted from ³⁰)	43
Figure 24 - Testing the poling direction of a PZT disc (Ember Krech Compliant Layer Thickness Study Protocol – used with permission)	91
Figure 25 - Placing a copper strip in between two silicone sheets on a piece of Delrin (Ember Krech Compliant Layer Thickness Study Protocol – used with permission).....	92
Figure 26 - Placing conductive epoxy (EPO-TEK® H20E, Billerica, MA) on the copper strip within the hole cutouts (Ember Krech Compliant Layer Thickness Study Protocol – used with permission)	92

Figure 27 - Placing PZT discs in hole cutouts (Ember Krech Compliant Layer Thickness Study Protocol – used with permission)	93
Figure 28 - Placing conductive epoxy on top of PZT discs and placing copper strip on top of conductive epoxy (Ember Krech Compliant Layer Thickness Study Protocol – used with permission).....	93
Figure 29 - Electrical connection testing across PZT disc thickness after assembly curing (Ember Krech Compliant Layer Thickness Study Protocol – used with permission).....	94
Figure 30 - Electrical connection on one side of each PZT disc after assembly curing (Ember Krech Compliant Layer Thickness Study Protocol – used with permission).....	94
Figure 31 - Stacking electrically connected PZT discs in an accordion style (Ember Krech Compliant Layer Thickness Study Protocol – used with permission).....	95
Figure 32 – Stacked assembly of electrically connected PZT discs with varying compliant layer thicknesses (cured epoxy slices) and goopy epoxy interposed for oven curing. Pieces of silicone placed on the top and bottom of the assembly and weights (metal nuts) placed on top of the assembly (Ember Krech Compliant Layer Thickness Study Protocol – used with permission).....	96
Figure 33 - Encapsulating the stacked in series PZT disc assembly in a dragon skin mold (Ember Krech Compliant Layer Thickness Study Protocol – used with permission).....	96
Figure 34 - Excess epoxy was carefully removed using a Dremel so that the epoxy encapsulating the assembly had faces that are as flat as possible (Ember Krech Compliant Layer Thickness Study Protocol – used with permission).....	97
Figure 35 – Schematic Ultrasound Testing System Setup	98
Figure 36 - Ultrasound Testing System Setup	99
Figure 37 - Thin PVC gel film placed on top of the V4 cardiac phased vector array ultrasound probe face	100
Figure 38 - Water media used in testing.....	101
Figure 39 - Tissue media used in testing.....	102
Figure 40 - Tissue plus bone media used in testing.....	102
Figure 41 - Tissue thicknesses at two different spots on the exterior of a person's back to the center of the intervertebral body in the lower back (Lumbar spine L3)	103
Figure 42 - Perpendicular and Parallel Loading Orientations	105
Figure 43 - Acuson 128XP/10 Ultrasound Medical Imaging Machine (Mountain View, CA)	106
Figure 44 - Acuson V4 Ultrasound cardiac phased vector array probe (Mountain View, CA)	107
Figure 45 - Ultrasound machine screen showing set parameter values for medical imaging.....	108
Figure 46 – Tektronix DPO 3034 Digital Phosphor Oscilloscope (Beaverton, OR) used to take measurements in this study	109
Figure 47 - Looped wire wrapped around the Ultrasound probe wire to capture the magnetic field generated by moving electrons in the probe wire	110
Figure 48 - Rectifying Circuit Diagram. Before rectification measurements are represented by VBR, after rectification measurements are represented by VAR, DB1 represents a full wave rectifier (4 diodes), C1 represents a polarized tantalum capacitor, R1 represents a variable load resistance and T1 represents a 1:1 turns isolation transformer. All values for these electrical components can be seen in Table 1	112
Figure 49 - CyanKen Audio Isolation Transformer	115
Figure 50 - Rectifying circuit without an isolation transformer where the current travels in one particular direction (green arrows) out of the symbolized Compliant Layer Adaptive Composite Stack (CLACS).....	116
Figure 51 - Rectifying circuit without an isolation transformer where the current alternates and travels in the opposite direction (red arrows) out of the symbolized Compliant Layer Adaptive Composite Stack (CLACS) compared to the current path in Figure 50.....	117
Figure 52 - Rectifying circuit with an isolation transformer where the current travels in one particular direction (green arrows) out of the symbolized Compliant Layer Adaptive Composite Stack (CLACS).....	118
Figure 53 - Rectifying circuit with an isolation transformer where the current alternates and travels in the opposite direction (red arrows) out of the symbolized Compliant Layer Adaptive Composite Stack (CLACS) compared to the current path in Figure 52.	119
Figure 54 – CH1 vs. CH2 peak-to-peak voltage (AC)	121

Figure 55 - Rectification Circuit used in Testing. The green circled area represents the lumped impedance (Z_{eq}) of a capacitor ($C1$) in parallel with a variable load resistance ($R1$) in parallel with the lumped Oscilloscope Channel 3 resistance ($1M\Omega$) in which after rectification measurements were taken (V_{AR})	122
Figure 56 - RCS box used as a variable load resistance	131
Figure 57 - Physical layout of rectification circuit	132
Figure 58 - CLACS placed on top of 20mm tissue thickness media for testing.....	134
Figure 59 - Tissue plus bone media with a little slab of tissue placed above the small part of the "T" bone to achieve 20mm media thickness.	135
Figure 60 - Global perspective identifying peak of Gaussian responses (a) and then zooming in on one Gaussian shape to find its peak and take measurements (b).....	137
Figure 61 – Example of before rectification electrical responses from the magnetic field of the Ultrasound probe wire, acoustic response of the incident ultrasonic waves, and the acoustic reflection	138
Figure 62 – Example of before rectification acoustic response measurement	138
Figure 63 – Example of before rectification reflection response measurement	139
Figure 64 – Example of before rectification magnetic field response measurement.....	140
Figure 65 – Example of after rectification DC voltage measurement.....	141
Figure 66 - Before rectification waveform (AC) for the TS85 sample in water medium, at 20mm media thickness, and perpendicular loading orientation	145
Figure 67 - After rectification waveform (DC) for the TS85 sample in water medium, at 20mm media thickness, perpendicular loading orientation, and $10M\Omega$ load resistance.....	147
Figure 68 - Braided wire used throughout rectification circuit for testing in an attempt to reduce the effect of unwanted magnetic fields	148
Figure 69 - Fast Fourier Transform (FFT) Response of after rectification waveform (DC) in Figure 67.....	149
Figure 70 - Fast Fourier Transform (FFT) Response of after rectification waveform (DC) in Figure 67 and of filtered after rectification waveform.....	150
Figure 71 – Unfiltered and filtered after rectification waveform (DC) for the TS85 sample in water medium, at 20mm media thickness, perpendicular loading orientation, and $10M\Omega$ load resistance	151
Figure 72 - Example organized data set for statistical analysis. This data set is organized for comparing different CLACS types within each media parameter and for comparing each media parameter within each CLACS.....	153
Figure 73 - Normality plots for a non-normal data set and the transformed (BoxCox) data set for the CLACSs within the water testing parameter.	155
Figure 74 - Residual plot for non-normal data set and transformed (BoxCox) data set for media testing parameters within the 0.8mm CLACS.....	156
Figure 75 - Multiple Comparison Plot (Tukey-Kramer) comparing CLACS group means within the water testing parameter. The 0.2mm group mean is significantly different from the 0.8mm group mean ($p<0.05$).	157
Figure 76 – An example of a select portion of the before rectification data set used in the statistical analysis. Vectors of information were used in one-way ANOVA and Tukey-Kramer pair wise multicomparison tests to determine significance within that vector of information. The highlighted red column represents a vector of information in which statistical significance tests were run between CLACSs (0mm, 0.2mm, 0.4mm, and 0.8mm) and a testing parameter (water). The highlighted blue column represents a vector of information in which statistical significance tests were run between testing parameters (water, tissue, tissue plus bone) within a CLACS (0mm). .	158
Figure 77 - Plugging in V4 Ultrasound Probe.....	195
Figure 78 - Location of power switch on Acuson 128XP/10 ultrasound medical imaging machine	195
Figure 79 - Contents of Ultrasound Imaging Screen after waiting a few minutes for the machine to startup.....	196
Figure 80 - Location of the "Reset" button	197
Figure 81 - Contents of Ultrasound Imaging Screen after waiting a few minutes again for the machine to startup	197
Figure 82 - Contents of ultrasound imaging screen after pressing any key to continue.....	198
Figure 83 – Unlocking the V4 probe from the ultrasound imaging machine.....	198
Figure 84 - Buttons pushed all at the same time to open General settings screen.....	199
Figure 85 - General settings screen and roller ball on ultrasound imaging machine used to navigate through items on the screen	199
Figure 86 – Ultrasound Probe encryption string screen.....	200

<i>Figure 87 - Provided encryption strings for ultrasound probes.....</i>	<i>200</i>
<i>Figure 88 - Filled out encryption strings.....</i>	<i>201</i>
<i>Figure 89 - Saving the encryption strings.....</i>	<i>201</i>
<i>Figure 90 - Reset the ultrasound medical imaging machine after entering and saving the encryption strings</i>	<i>202</i>
<i>Figure 91 - Ultrasound imaging screen after resetting the machine after entering encryption strings.....</i>	<i>202</i>
<i>Figure 92 - Locking the V4 probe into the ultrasound imaging machine</i>	<i>203</i>
<i>Figure 93 - Ultrasound imaging screen if the probe is not fully connected to the machine</i>	<i>203</i>
<i>Figure 94 - Ultrasound imaging screen initializing if probe is connected to machine</i>	<i>204</i>
<i>Figure 95 - Ultrasound imaging screen if probe is connected to machine after initializing is done</i>	<i>204</i>
<i>Figure 96 - Power off the ultrasound imaging machine</i>	<i>205</i>

Image List – Journal of Orthopaedic Research Manuscript

Figure 1 - Schematic of Ultrasound Testing System.....	60
Figure 2 - Rectifying Circuit Diagram. Before rectification measurements are represented by VBR, after rectification measurements are represented by VAR, DB1 represents a full wave rectifier (4 diodes), C1 represents a polarized tantalum capacitor, R1 represents a variable load resistance and T1 represents a 1:1 turns isolation transformer. All values for these electrical components can be seen in Table 1.....	60
Figure 3 - Voltage signal before rectification (a) and after rectification (b).....	63
Figure 4 - Average peak voltage (n=5) as a function of media and compliant layer thickness at 20 mm media thickness for loading perpendicular to the PZT disc face. Within compliant layer groups all media comparisons are significantly different. In water: * represents significant difference from 0.8mm. In tissue plus bone: + represents significant difference from 0.2mm. ($p < .05$ Box-Cox Transformation).....	65
Figure 5 - Average peak voltage output (n=5) as a function of media thickness and compliant layer thickness in water media for loading perpendicular to the PZT disc face. At 20mm media thickness: * represents significant difference from 0.8mm. In 0.4mm: + represents significant difference from 20mm. ($p < .05$ Box-Cox Transformation).....	67
Figure 6 - Average peak voltage output (n=5) as a function of loading orientation and compliant layer thickness in water media at 20mm media thickness. Within compliant layer groups all loading orientation comparisons are significantly different. Perpendicular: * represents significant difference from 0.8mm. ($p < .05$ Box-Cox Transformation).....	68
Figure 7 - Average Total Power (W) as a function of Load Resistance (Ω) and compliant layer thickness at 20mm media thickness and loading perpendicular to the PZT disc face in water media after rectification (n=5). For the last four resistances of the load resistance sweep (500K Ω – 10M Ω), the 0.8mm and 0.4mm compliant layer groups are significantly larger than the 0 and 0.2mm groups and the 0.8mm and 0.4mm compliant layer groups are not significantly different compared to each other as well as the 0mm and 0.2mm groups ($p < .05$ Box-Cox Transformation). Error bars excluded for visual clarity.....	71
Figure 8 - Average total power (W) as a function of load resistance (Ω) and media thickness in water media and loading perpendicular to the PZT face (n=5). (a) represents 0mm, (b) represents 0.2mm, (c) represents 0.4mm and (d) represents 0.8mm compliant layer media thickness comparisons. Note that (a,b) is on a scale that is 1/10th of (c,d). Error bars excluded for visual clarity	75
Figure 9 - Average Load Resistance Power (W) as a function of Load Resistance (Ω) and compliant layer thickness at 20mm media thickness and loading perpendicular to the PZT disc face in water media after rectification (n=5). (a) represents the average load resistance power across the whole resistance sweep. (b) represents the average load resistance power across the higher end of the resistance sweep (10K Ω – 10M Ω). For the last four resistances of the load resistance sweep (500K Ω – 10M Ω), the 0.8mm and 0.4mm compliant layer groups are significantly larger than the 0 and 0.2mm groups and the 0.8mm and 0.4mm compliant layer groups are not significantly different compared to each other as well as the 0mm and 0.2mm groups ($p < .05$ Box-Cox Transformation). Error bars excluded for visual clarity	79
Figure 10 - Average total power (W) as a function of load resistance (Ω) and media at 20mm media thickness and loading perpendicular to the PZT disc face (n=5). (a) represents 0mm, (b) represents 0.2mm, (c) represents 0.4mm and (d) represents 0.8mm compliant layer media comparisons. Note that (a,b) is on a scale that is 1/10th of (c,d). Error bars excluded for visual clarity.....	83

Figure 11 - Average total power (W) as a function of load resistance (Ω) and loading orientation in water media at 20mm media thickness (n=5). (a) represents 0mm, (b) represents 0.2mm, (c) represents 0.4mm and (d) represents 0.8mm compliant layer loading orientation comparisons. Note that (a,b) is on a scale that is 1/10th of (c,d). Error bars excluded for visual clarity85

Figure 12 - Average load resistance power (W) as a function of load resistance (Ω) and media at 20mm media thickness and loading perpendicular to the PZT disc face (n=5). (a) represents 0mm, (b) represents 0.2mm, (c) represents 0.4mm and (d) represents 0.8mm compliant layer media comparisons. Note that (b,c,d) are on a scale that is a magnitude less than (a). Error bars excluded for visual clarity86

Figure 13 - Average load resistance power (W) as a function of load resistance (Ω) and media thickness in water media and loading perpendicular to the PZT face (n=5). (a) represents 0mm, (b) represents 0.2mm, (c) represents 0.4mm and (d) represents 0.8mm compliant layer distance comparisons. Note that (b,c,d) are on a scale that is a magnitude less than (a). Error bars excluded for visual clarity.....87

Figure 14 - Average load resistance power (W) as a function of load resistance (Ω) and loading orientation in water media at 20mm media thickness (n=5). (a) represents 0mm, (b) represents 0.2mm, (c) represents 0.4mm and (d) represents 0.8mm compliant layer loading orientation comparisons. Note that (b,c,d) are on a scale that is a magnitude less than (a). Error bars excluded for visual clarity88

Equation List

Equation 1 – Sound pressure as a function of particle velocity (u) and specific acoustic impedance (Z).....	19
Equation 2 – Specific acoustic impedance as a function of medium density (ρ) and speed of sound (c).....	19
Equation 3 – Reflection coefficient (R) equation as a function of reflected (p^-) and incident (p^+) pressure	20
Equation 4 - Transmission coefficient (T) equation as a function of transmitted (p_{tr}) and incident (p^+) pressure...	20
Equation 5 - Pressure balance equation on boundary of two mediums as a function of incident (p^+), reflection (p^-), and transmission (p_{tr}) pressure	21
Equation 6 - Coefficient balance equation on boundary of two mediums as a function of the reflection (R) and transmission (T) coefficients	21
Equation 7 - Particle velocity balance equation as a function of incident (u^+), reflection (u^-), and transmission (u_{tr}) particle velocity.....	21
Equation 8 – Acoustic impedance boundary balance condition expressed as a function of incident (p^+), reflection (p^-), and transmission (p_{tr}) pressure and specific acoustic impedance of the incident (Z_1) and transmitted (Z_2) mediums	21
Equation 9 – Acoustic impedance boundary balance condition expressed as a function of the reflection (R) and transmission (T) coefficients and the specific acoustic impedance of the incident (Z_1) and transmitted (Z_2) mediums	22
Equation 10 - Reflection coefficient (R) as a function of the incident (Z_1) and transmitted (Z_2) specific acoustic impedances.....	22
Equation 11 - Transmission coefficient (T) as a function of the incident (Z_1) and transmitted (Z_2) specific acoustic impedances.....	22
Equation 12 - Surface area boundary condition as a function of incident (u^+), reflection (u^-), and transmission (u_{tr}) particle velocities and the surface area of the incident (S_1) and transmitted (S_2) mediums.....	24
Equation 13 – Surface area boundary balance condition expressed as a function of the reflection (R) and transmission (T) coefficients and the surface area of the incident (S_1) and transmitted (S_2) mediums.....	24
Equation 14 - Reflection coefficient (R) as a function of the incident (S_1) and transmitted (S_2) surface areas.....	24
Equation 15 - Transmission coefficient (T) as a function of the incident (S_1) and transmitted (S_2) surface areas.....	24
Equation 16 – Combined effects of specific acoustic impedance and surface area for the incident and transmitted mediums boundary balance expressed as a function of the incident (Z_{ac1}) and transmitted (Z_{ac2}) acoustic impedances and the reflection (R) and transmission (T) coefficients	25
Equation 17 - Reflection coefficient (R) as a function of the incident (Z_{ac1}) and transmitted (Z_{ac2}) acoustic impedances.....	25
Equation 18 - Transmission coefficient (T) as a function of the incident (Z_{ac1}) and transmitted (Z_{ac2}) acoustic impedances.....	26
Equation 19 - Relationship between the incident (θ_i) and reflection (θ_r) angles of sound waves at an impedance mismatch boundary condition	27
Equation 20 - Snell's law as a function of the speed of sound in the incident (c_1) and transmitted (c_2) mediums and the incident (θ_i) and transmitted (θ_t) angles	27
Equation 21 – Normal component of particle velocities boundary condition as a function of incident (u^+), reflection (u^-), and transmission (u_{tr}) particle velocities, and the incident (θ_i) and transmitted (θ_t) angles	27
Equation 22 - Combined effects of specific acoustic impedance and incident and transmitted angles boundary condition expressed as a function of the incident (Z_1) and transmitted (Z_2) specific acoustic impedances and the reflection (R) and transmission (T) coefficients and the incident (θ_i) and transmitted (θ_t) angles.....	27
Equation 23 - Reflection coefficient (R) as a function of the incident (Z_1) and transmitted (Z_2) specific acoustic impedances and the incident (θ_i) and transmitted (θ_t) angles	28
Equation 24 - Transmission coefficient (R) as a function of the incident (Z_1) and transmitted (Z_2) specific acoustic impedances and the incident (θ_i) and transmitted (θ_t) angles	28
Equation 25 - The critical angle ($\theta_{critical}$) as a function of the speed of sound in the incident (c_1) and transmitted (c_2) mediums	28

Equation 26 - The relaxation absorption coefficient (β_r) as a function of operating frequency (f), relaxation frequency (f_r) and a constant (B_0)	30
Equation 27 - Overall relaxation absorption coefficient (β_r , tissue) as a summation function of "n" iterations, operating frequency (f), "nth" relaxation frequency (f_r, n) and a constant (B_0).....	30
Equation 28 - Sound intensity (I) as a function of the intensity attenuation coefficient (μ) and depth (z).....	31
Equation 29 - Sound Pressure (p) as a function of the sound pressure attenuation coefficient (α) and depth (z)	31
Equation 30 - Unit conversion relationship for the intensity attenuation coefficient.....	31
Equation 31 - Pressure amplitude of a spherical wave as a function of radius (r) from the source, pressure amplitude of pulsating sphere (P_0), and pulsating sphere radius (R_0)	32
Equation 32 - Relationship between the thickness of PZT crystals (t), operating frequency (f_0), wavelength (λ_{crystal}), and speed of sound in the crystal (c_{crystal}).....	34
Equation 33 - Specific acoustic impedance of a matching layer as a function of PZT (Z_{PZT}) and tissue/skin ($Z_{\text{tissue/skin}}$) specific acoustic impedance	34
Equation 34 - "F" number (curvature of ultrasound lens with PZT elements) as a function of focal distance and aperture dimension	36
Equation 35 - Lateral resolution of an circular ultrasound probe as a function of wavelength (λ), frequency (f), and diameter (D) of probe face	37
Equation 36 - Mechanical index as a function of operating frequency (f_0), rarefactional pressure (p_r), and depth (z)	44
Equation 37 – Equivalent impedance (Z_{eq}) as a function of the oscilloscope lumped channel impedance (Z_{osc}), load resistance impedance (Z_{R1}), and capacitor impedance (Z_{c1}) which has a -j because it is purely imaginary impedance (reactance).....	122
Equation 38 - Impedance of a capacitor as a function of operating frequency (f) and capacitance (C).....	123
Equation 39 - Capacitor impedance at 4MHz operating frequency (f) and 2.2 μf capacitance (C)	123
Equation 40 – Common denominator for load resistance component impedance (Z_{R1}) as a function of the oscilloscope channel lumped impedance (Z_{osc}), load resistance impedance (Z_{R1}), and capacitor impedance (Z_{C1})	123
Equation 41 - Common denominator for oscilloscope channel lumped impedance component (Z_{osc}) as a function of the oscilloscope channel lumped impedance (Z_{osc}), load resistance impedance (Z_{R1}), and capacitor impedance (Z_{C1}).....	123
Equation 42 - Common denominator for capacitor component impedance (Z_{C1}) as a function of the oscilloscope channel lumped impedance (Z_{osc}), load resistance impedance (Z_{R1}), and capacitor impedance (Z_{C1}).....	124
Equation 43 - Equivalent impedance (Z_{eq}) as a function of the oscilloscope lumped channel impedance (Z_{osc}), load resistance impedance (Z_{R1}), and capacitor impedance (Z_{c1}) which has a -j because it is purely imaginary impedance (reactance).....	124
Equation 44 - Equivalent impedance (Z_{eq}) as a function of the oscilloscope lumped channel impedance (Z_{osc}), load resistance impedance (Z_{R1}), and capacitor impedance (Z_{c1}) which has a -j because it is purely imaginary impedance (reactance) after performing the complex conjugate	124
Equation 45 - Equivalent impedance (Z_{eq}) as a function of three variables, a, b, and c which represent parts of equation 44.....	124
Equation 46 - "b" variable part of equation 45 as a function of the oscilloscope lumped channel impedance (Z_{osc}), load resistance impedance (Z_{R1}), and capacitor impedance (Z_{c1})	125
Equation 47 - "c" variable part of equation 45 as a function of the oscilloscope lumped channel impedance (Z_{osc}), load resistance impedance (Z_{R1}), and capacitor impedance (Z_{c1})	125
Equation 48 - "a" variable part of equation 45 as a function of the oscilloscope lumped channel impedance (Z_{osc}), load resistance impedance (Z_{R1}), and capacitor impedance (Z_{c1})	125
Equation 49 - Equivalent impedance magnitude (Z_{eq}) as a function of, b, c, and a from equations 46, 47, and 48 respectively.....	125
Equation 50 - Example calculation of equation 46 using the result from equation 39, a 100 Ω load resistance and the oscilloscope channel lumped impedance of 1,000,000 Ω	125
Equation 51 - Example calculation of equation 47 using the result from equation 39, a 100 Ω load resistance and the oscilloscope channel lumped impedance of 1,000,000 Ω	125

Equation 52 - Example calculation of equation 48 using the result from equation 39, a 100Ω load resistance and the oscilloscope channel lumped impedance of $1,000,000\Omega$	126
Equation 53 - Example calculation of equation 45 using the results from equations 50, 51, and 52.....	126
Equation 54 - Equivalent resistance as a function of the oscilloscope channel lumped impedance (Z_{osc}) and the load resistance impedance (Z_{R1}).....	126
Equation 55 - Equivalent impedance (Z_{eq}) as a function of the equivalent resistance (R_{eq}) and the capacitor impedance (Z_{c1}) which has a $-j$ because it is purely imaginary impedance (reactance).....	126
Equation 56 - Equivalent impedance (Z_{eq}) as a function of the equivalent resistance (R_{eq}) and the capacitor impedance (Z_{c1}) which has a $-j$ because it is purely imaginary impedance (reactance).....	127
Equation 57 - Equivalent impedance (Z_{eq}) as a function of the equivalent resistance (R_{eq}) and the capacitor impedance (Z_{c1}) which has a $-j$ because it is purely imaginary impedance (reactance) after performing the complex conjugate.....	127
Equation 58 - Equivalent impedance (Z_{eq}) as a function of three variables, a , b , and c which represent parts of equation 57.....	127
Equation 59 - "b" variable part of equation 45 as a function of the equivalent resistance (R_{eq}) and capacitor impedance (Z_{c1}).....	127
Equation 60 - "c" variable part of equation 45 as a function of the equivalent resistance (R_{eq}) and capacitor impedance (Z_{c1}).....	127
Equation 61 - "a" variable part of equation 45 as a function of the equivalent resistance (R_{eq}) and capacitor impedance (Z_{c1}).....	128
Equation 62 - Example calculation of equation 54 at 100Ω load resistance and oscilloscope channel lumped impedance of $1,000,000\Omega$	128
Equation 63 - Example calculation of equation 59 using the result from equation 39, a 100Ω load resistance and the oscilloscope channel lumped impedance of $1,000,000\Omega$	128
Equation 64 - Example calculation of equation 60 using the result from equation 39, a 100Ω load resistance and the oscilloscope channel lumped impedance of $1,000,000\Omega$	128
Equation 65 - Example calculation of equation 61 using the result from equation 39, a 100Ω load resistance and the oscilloscope channel lumped impedance of $1,000,000\Omega$	128
Equation 66 - Example calculation of equation 45 using the results from equations 63, 64, and 65.....	128
Equation 67 - Electrical power as a function of voltage and impedance.....	129
Equation 68 - Peak value as a function of the max and min values of before rectification waveforms.....	144
Equation 69 - Average value of a waveform as a function of the upper and lower bounds of the waveform.....	145
Equation 70 - Trapezoidal Rule approximating the area under a curve.....	146
Equation 71 - Average value of a curve as a function of the approximated sum using the trapezoidal rule (equation 70) and the upper and lower bounds of the curve.....	146
Equation 72 - Transforming data using the BoxCox method as a function of λ , which is determined by the MATLAB program.....	154
Equation 73 - If λ is equal to 0 then the log transformation is performed.....	154

Table List

<i>Table 1 - Tabulated Values of Rectifying Circuit Components</i>	<i>112</i>
<i>Table 2 - Equivalent Impedance Values calculated using Load Resistance Sweep values and the Oscilloscope lumped internal impedance value</i>	<i>129</i>

Please note that the Table 1 is also listed on page 61 for the Manuscript for the Journal of Orthopaedic Research (JOR).

Chapter 1. Background and Literature Review

This chapter discusses the need for this work followed by background and literature review information to better understand this work. A foundational knowledge of spinal fusion, the electromechanical properties of bone, electrical stimulation in spinal fusion applications, PZT, and sound is necessary to better understand this work. The need for spinal fusion will be introduced followed by current spinal fusion techniques. Electromechanical properties of bone and the use of electrical stimulation in spinal fusion applications will be explored. Fundamental knowledge about piezoelectric materials and, lastly, the basic physics of sound and medical imaging ultrasound will also be covered.

1.1 Problem Statement

Back pain in the lumbar spine is one of the major reasons for physician office visits in the United States ⁴. Typically, surgery with a spinal fusion interbody device is used to alleviate this back-pain and over 600,000 fusion operations are conducted each year ². These spinal fusion interbody devices have an opening in their center which is filled with a structured bone graft material typically taken from the hip, loose bone chips, or artificial material ^{6,7}. The device is then placed in the intervertebral space and posterior instrumentation (rods and pedicle screws) is used to stabilize the site to encourage a bony fusion over time. Lumbar spinal fusion success rates are reported as high as 90% ^{8,9}. For hard-to-heal patients who smoke, are obese, or are diabetic, spinal fusion failure rates range from 40-47% ^{1,10}. For over 30 years, spinal fusion success rates have been improved with the addition of electrical stimulation ¹⁰. With the addition of direct current (DC) electrical stimulation, bone healing has been improved in spinal fusion ². Electrical stimulation techniques accomplish bone healing, but suffer some drawbacks. A battery is used to provide electrical stimulation in the spinal fusion and requires a longer surgery time to be carefully implanted near the spinal fusion device. Implanted batteries are invasive and will require replacement once they can no longer sustain electrical charge and removing a battery after fusion has

been accomplished would require a second surgery^{2,4}. To eliminate a second surgery that would detract from the overall patient experience, spinal fusion interbody devices that use DC electrical stimulation to help improve bony fusion need a self-powering method to generate electrical energy for the stimulation. Many microgenerators use piezoelectric material to convert mechanical energy into electrical potential³. Due to the piezoelectric effect, applied mechanical stresses on piezoelectric material generate electrical potential in direct proportion¹¹. With piezoelectric material, spinal fusion interbody devices can generate electrical energy from cyclic mechanical loading patterns in the spine that are present during walking to provide DC electrical stimulation without an external battery source and invasive wires. Unfortunately, since piezoelectric material has high electrical impedance, it is difficult to develop practical piezoelectric generators because a high source electrical impedance would require a high load impedance to harness the generated power¹¹. To improve power harvesting of spinal fusion interbody devices with piezoelectric material, the electrical source impedance can be reduced by using stacked layers of Lead Zirconate Titanate (PZT) material fibers connected electrically in parallel and mechanically in series^{2,4}. It was found in recent studies that by increasing the number of stacked PZT layers, the electrical impedance of the spinal fusion interbody device decreased with a slight increase in power generation^{2,4,5,11}. In a pilot ovine study, composite spinal interbody implants made with stacked layers of piezoelectric (PZT) fibers provided DC electrical stimulation at the fusion site and substantially enhanced fusion under normal loading after six weeks as compared to a control (Figure 1)^{2,4,5}.

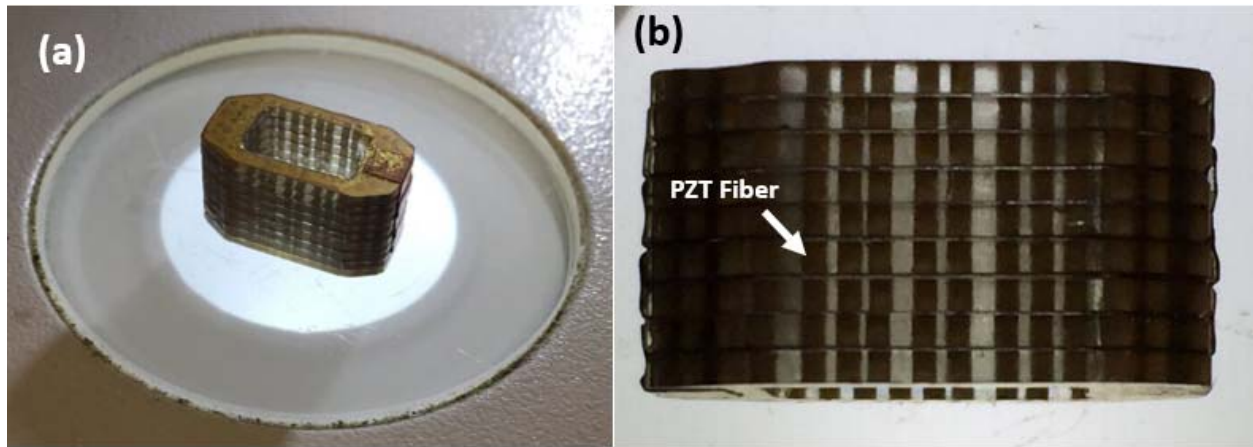


Figure 1 - PZT Fiber Stacked Composite isometric (a) and front (b) view

To improve manufacturability while maintaining material toughness of the composite material, alternative manufacturing methods were explored in which compliant layers of epoxy were inserted between stacked discs of PZT to become a compliant layer adaptive composite stack (CLACS) (Figure 2).

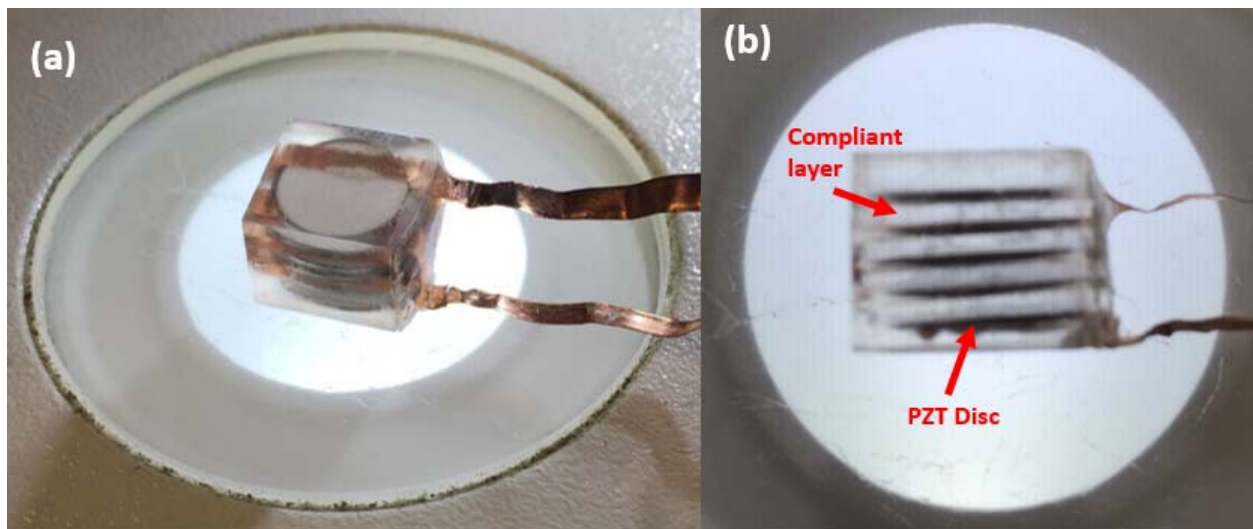


Figure 2 - Compliant Layer Adaptive Composite Stack (CLACS) isometric (a) and side (b) view

Spinal fusion interbody devices that are self-powering can generate electrical potential from cyclic mechanical loading (walking) in the lumbar spine. However, electrical stimulation cannot be provided to the fusion site if the patient is unable to sufficiently move and produce mechanical stresses. For patients with limited weight-bearing abilities that cannot provide enough mechanical energy from

natural human body movement, another method of mechanically loading the PZT discs contained within the spinal fusion devices would be beneficial. Many methods of wirelessly powering medical devices have been investigated including inductive coupling, capacitive coupling, thermoelectric devices and ultrasound. It was reviewed that electromagnetic power supply systems may have negative influence on the human body and its surroundings while being used to power implanted medical devices³. Transmitted ultrasound waves can be used to mechanically activate a medical device implanted into human tissue with PZT elements³. In a simulated study, ultrasound power delivery outperformed inductive coupling for small implantable devices at large distances between the sound source and PZT receiver with a tissue medium in between¹². Acoustic power delivery has therefore become more attractive for energizing medical devices as they get smaller in size and are more deeply implanted in the human body. Ultrasound is a non-invasive medical imaging technique used mostly for fetal imaging of women during pregnancy and has benefits such as sufficient power transfer efficiency in deeply implanted biomedical devices, avoidance of tissue damage by ionizing radiation, high availability in hospitals, and low operation and training cost^{3,12}.

This study investigates the energy generation potential of compliant layer adaptive composite stacks of PZT discs using medical imaging ultrasound as the loading source. Using medical imaging ultrasound to mechanically load PZT discs within the CLACS, the effect of varying compliant layer thicknesses in the CLACS on generated electrical potential and power output at varying load resistances (10) were studied in various mediums for the ultrasound waves to propagate through (3 – water, tissue, and tissue plus bone), media thicknesses or distance between the ultrasound probe face and the CLACS (2 – 20mm, 40mm), and loading orientations of the PZT disc faces within the CLACS relative to the direction of the propagating ultrasonic waves (2 – perpendicular, parallel).

1.2 Spinal Fusion

This section provides background for spinal interbody fusion techniques, electromechanical properties of bone, and electrical stimulation adjunct therapy techniques in spinal fusion.

1.2.1 Spinal Interbody Fusion Devices

The purpose of spinal fusion is to eliminate back pain from compressed spinal nerve roots. When an intervertebral disc becomes herniated, bulges, or fails, nerve roots that flow between the bony processes of the vertebrae can be pinched or compressed by the failed intervertebral disc or bony processes causing back pain (Figures 3,4) ^{13,14}.

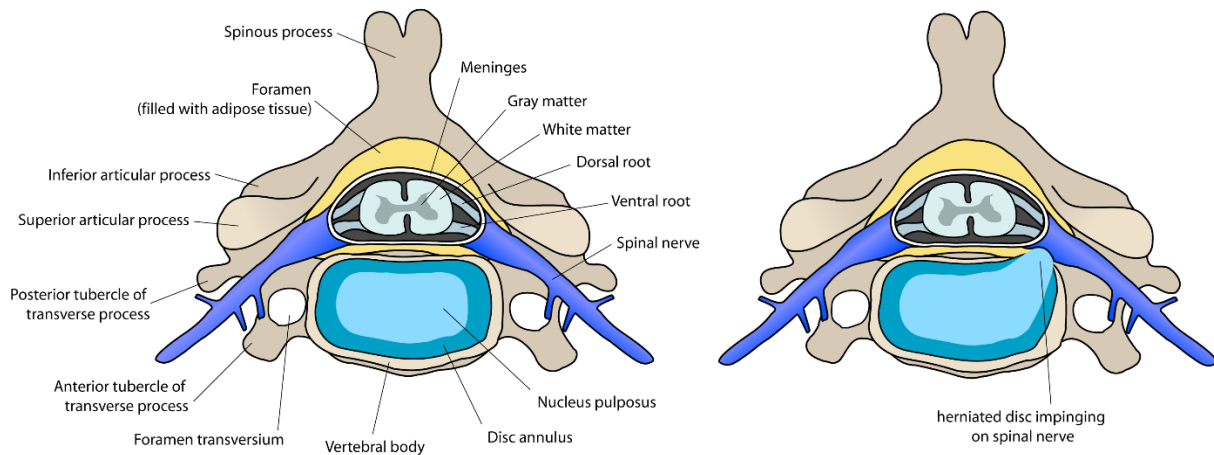


Figure 3 - Vertebral disc anatomy example showing compression on spinal nerve by herniated disc (Public Domain, commons.wikipedia.org, labeled for reuse) ¹³



Figure 4 – Sagittal image showing compression on spinal nerve by bulging disc in lumbar spine (Public Domain, commons.wikipedia.org, labeled for reuse)¹⁴

Intervertebral discs in the lumbar spine experience the highest loads from everyday movement (walking) and have a higher tendency to fail. Upon failure, the intervertebral disc no longer serves as a spacer and shock absorber between two adjacent vertebral bodies and thus these spinal nerve roots are compressed. Spinal fusion is a surgical technique used to alleviate back pain from compressed spinal nerve roots by restoring intervertebral disc height and stabilizing the spinal segment. Originally, spinal fusion consisted of replacing the failed intervertebral disc with bone graft material and over time the patient's body would fuse the two vertebrae together. To improve the success rates of spinal fusion surgery, interbody cages are used. These cages were used as stand-alone devices for anterior/posterior lumbar interbody fusion (ALIF/PLIF), but now posterior instrumentation (rods and pedicle screws) is used in addition to interbody fusion devices to help stabilize the fusion site, increasing bony fusion^{6,7}. The failed intervertebral disc and cartilaginous endplates of the adjacent vertebrae located above and below the desired fusion site are removed. An interbody cage is then placed in the intervertebral space in which a pre-load is applied on the cage by tension in back muscles. This tension helps keep the interbody cage in the desired fusion site and helps provide stability¹⁵. The interbody cage has a

hollowed-out region in its center that is packed with structured bone graft material typically taken from the hip, loose bone chips, or artificial material^{6,7}. In addition to retaining the height and providing stability and support of the interbody space, bone fusion occurs within and around the cage to help increase spinal fusion surgery success rates. Interbody devices come in various shapes and sizes depending on patient size and location of fusion in the spine. Patients that smoke, are obese, or are diabetic are considered “hard-to-heal” and have experienced spinal fusion failure rates range from 40-47%^{1,10}. To further improve spinal fusion success rates for these types of patients, adjunct therapies including electrical stimulation have been explored and employed.

1.2.2 Electrical Stimulation

Electrical stimulation has been used for over 30 years to enhance spinal fusion and has been approved by the FDA¹⁰. Glazer and Gan summarized and compared studies involving different methods of adjunctive electrical stimulation with spinal fusion on bone growth which include direct current (DC), inductive coupling (IC), and capacitive coupling (CC)¹⁰. In this review article, it was found that there is a clinical benefit of electrical stimulation as an adjunct therapy to spinal fusions and that DC stimulation is particularly successful in treating difficult-to-fuse cases and is cost effective compared to the IC and CC methods.

A constant localized direct current (DC) at the fusion site generates a biologically effective field of influence that promotes bone growth¹⁰. Generated electric fields from DC electrical stimulation may exhibit similar behavior to the basis of why bone remodels in response to mechanical loading¹⁰. When bone is mechanically strained, electronegative potentials are found in areas of compression while electropositive potentials are found in areas of tension. Bone forms in electronegative regions and resorbs in electropositive regions. The mechanism of action for DC electrical stimulation involves an upregulation of osteoinductive factors present in bone formation¹⁰. Studies summarized in the review

article showed results that supported the newly elucidated mechanism of action behind DC stimulation and multiple studies comparing electrically stimulated and non-stimulated groups and their bony fusion success rates were listed.

Fredricks et. al conducted a rabbit model study where DC stimulation was applied to an L4-L5 fusion with autograft and it was found that specific temporal and spatial gene expression of osteoinductive growth factors bone morphogenetic protein were upregulated enabling bone growth ¹⁶. In the bilateral fusions, the DC-stimulated group had 100% bony fusion success rate where the autograft alone (non-stimulated) group had 33%. In another study, it was found that the faradic reactions that occur at the cathode site during DC stimulation lowered oxygen concentration, increased pH, and produced hydrogen peroxide which reduced media calcium release levels and increased pH resulting in accelerated remodeling and an improved clinical outcome ¹⁷. A decrease in oxygen concentration was found to enhance bone growth (osteoblastic activity), an increase in pH was found to also increase bone growth while decreasing bone resorption (osteoclastic activity), and hydrogen peroxide helps release an angiogenic factor which is crucial for bone healing ^{18,19}. In a study using a sheep interbody fusion model with electrified titanium cage, there was a fusion success rate of 100% for the stimulated group and 27% for the non-stimulated group ⁸. An in vivo study using DC stimulation with a titanium interbody in adult pig-tailed macaques found that the electrically stimulated devices were 4.5 times more likely to have fusion and 5.25 times more likely to have greater than 50 % AP healing compared to non-stimulated devices ⁹.

Using adjunctive DC stimulation with spinal fusion improves the rate of bony fusion compared to a non-stimulated technique. A basic understanding of the electromechanical properties of bone is explored in section 1.2.3.

1.2.3 Electromechanical Properties of Bone

Bone is optimized to provide maximum strength for a minimum mass and when it is mechanically strained, it remodels itself (Wolff's Law)²⁰. The generation of electric potentials in bone in response to mechanical stress was observed by Basset and Becker and they found that bone in compression forms negative electrical potentials and in tension forms positive electrical potentials (Figure 5)²¹.

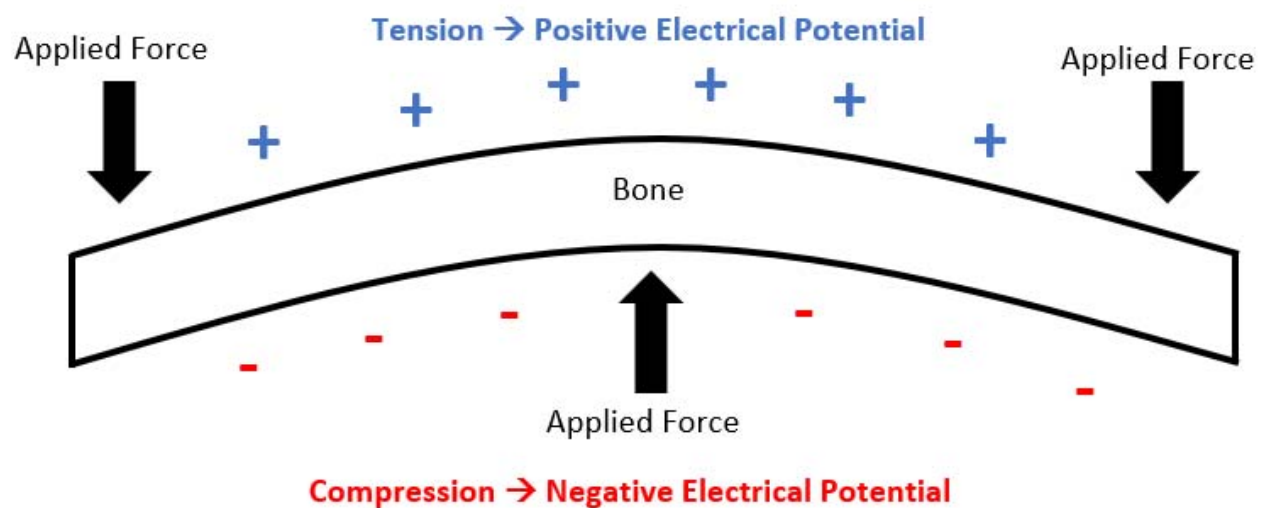


Figure 5 - Schematic example of tension on bone yielding positive electrical potential and compression yielding negative electrical potential (Adapted from Basset and Becker)²¹

It was hypothesized that the piezoelectric properties of bone may be responsible for the conversion of mechanical stress to electrical potential and that the type of loading applied (tension or compression) determines the polarity of the electrical potential. In a follow-up in vivo study conducted by Basset, three levels of direct current (1 μ A, 10 μ A, and 100 μ A) were applied in adult dogs at the cortex and 3-4mm into the medullary canal with a battery in series with a resistor over a period of 21 days²². It was found that the larger applied current levels grew more bone and that bone formation mechanisms depended on the polarity of the applied current. The collagen matrix within bone generates electrical

potentials when strained in tension or compression. Bone formation occurs when electronegative potential is generated, and bone resorption occurs when electropositive potential is generated ¹⁰.

1.3 Piezoelectric Materials

Current portable and wireless electronic devices require a source of power to operate and are designed to either house or be incorporated with a battery ²³. In some applications like implantable spinal fusion devices that use electrical stimulation to help improve bony fusion rates, using a battery as the power source is undesirable. Implanted batteries used to power medical devices are invasive, have a limited lifespan, and will need to be replaced ^{2,4,23}. For medical devices implanted in a patient that use electrical stimulation, a second surgery would be required to replace the battery or remove it and this could detract from the patient experience. Some methods of energy harvesting that have been explored include waste heat, mechanical vibration, electromagnetic waves, wind, solar energy, and flowing water. While these energy harvesting methods can provide power, piezoelectric materials are the most commonly used energy harvester in small electronic device applications (medical devices) ²³. This section provides basic piezoelectric knowledge which includes the piezoelectric effect, poling, and coupling orientation and differences between two PZT material designs.

1.3.1 Basic Piezoelectric Theory

Piezoelectric material exhibits a local charge separation known as an electric dipole. This allows for an energy conversion to occur between applied strain and electrical potential ²³. When mechanical energy (strain) is applied to a piezoelectric material, an electrical potential is generated and conversely when an electrical potential is applied to a piezoelectric material, a mechanical deformation occurs (Figure 6).

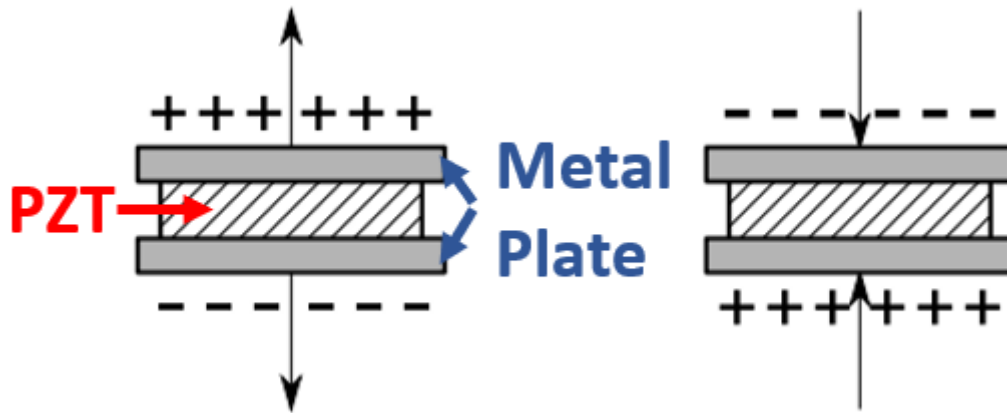


Figure 6 - Schematic example of tension and compression on PZT material with metal plates as electrodes (Public Domain, commons.wikipedia.org, labeled for reuse with modification) ²⁴

This relationship is called the direct and indirect piezoelectric effect respectively ²⁵. The most common type of piezoelectric material that is used in power harvesting applications is Lead Zirconate Titanate (PZT), a piezoelectric ceramic ²³. This ceramic is unfortunately brittle and is subject to crack failure at high frequency loading applications ²³. Also, this means less strain can be applied before mechanical failure occurs, which limits the energy harvesting ability of the material. To reduce the chance of mechanical fatigue failure and improve the energy harvesting ability of the PZT in high loading and frequency application, combining the PZT with another material like epoxy to make a composite design would be beneficial.

Before the direct and indirect piezoelectric effects can occur, the piezoelectric material must be poled. This process requires the material to be subject to a large voltage across it so the dipoles within the matrix realign in the direction of the electric field and create a net dipole moment (Figure 7).

PZT Material – Prior to Poling

PZT Material – After Poling

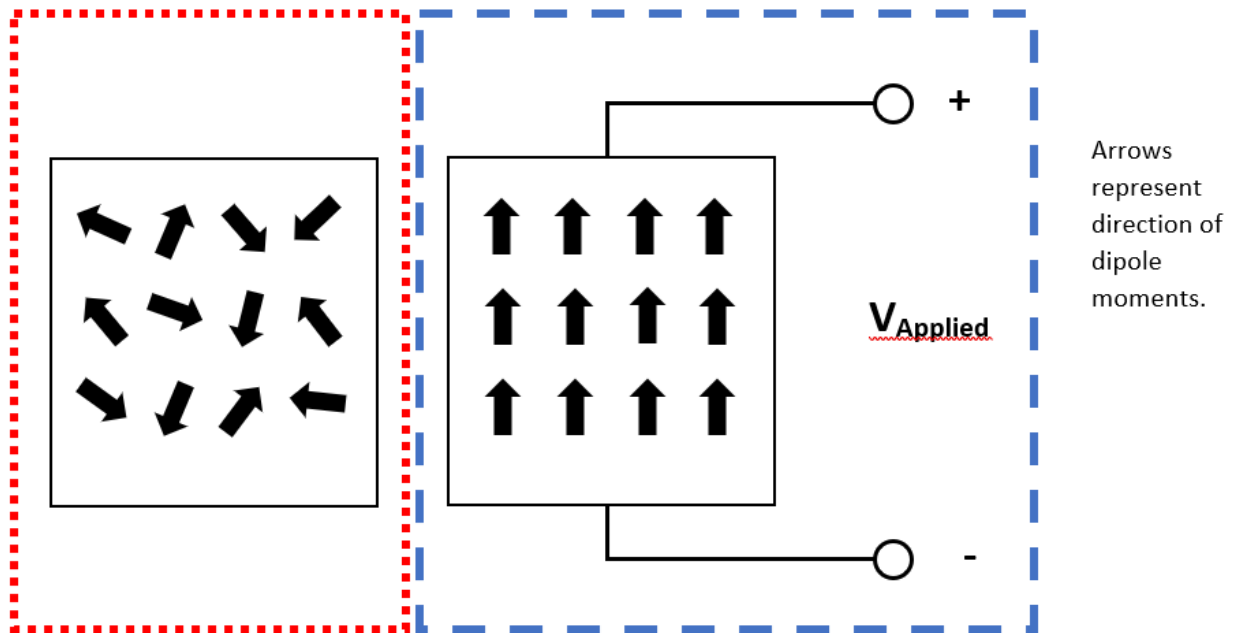


Figure 7 - Schematic example of piezoelectric material dipole moments before and after poling (large voltage applied across the material)

The poling direction also affects the energy harvesting ability of the piezoelectric material. Two practical coupling modes used in piezoelectric materials are the 31 and 33 modes. In the 31 mode, an external force (mechanical strain) is applied to the piezoelectric material in the direction perpendicular to the poling direction and in the 33 mode, an external force is applied in the same direction as the poling direction (Figure 8)²³.

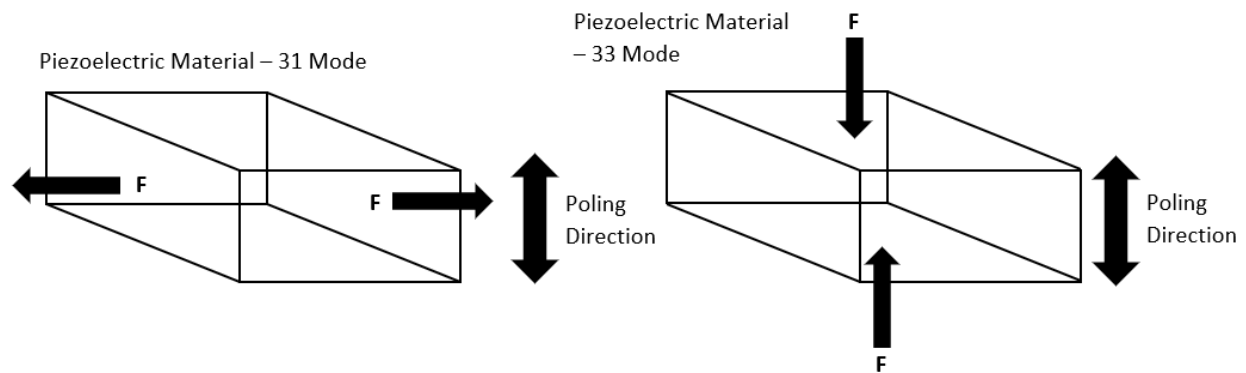


Figure 8 – Schematic illustration of -31 and -33 modes of operation for piezoelectric material (Adapted from Anton and Sodano ²³)

Even though the -31 mode is the most widely used, it has a lower coupling coefficient than the -33 mode of operation. Higher coupling coefficients lead to greater conversion efficiencies in piezoelectric material ²³. Baker et al. also showed that the -33 mode exhibits a higher coupling coefficient than the -31 mode, but when comparing a piezoelectric stack operating at -33 mode to a cantilever piezoelectric beam operating at -31 mode, the beam produced two orders of magnitude higher power when subjected to the same force ²⁶. The high mechanical stiffness of the piezoelectric stack did not allow for sufficient strain to be applied to the piezoelectric material which lowered the power output in that configuration. By understanding the poling direction modes of operation in a PZT material and how to efficiently strain it, more energy can be harvested and converted into electrical power. The power harvesting capabilities of a PZT material can also be improved by changing its design.

1.3.2 Stacked PZT Layers vs. Monolithic PZT

For through-thickness poling directions, monolithic and stacked energy harvesters have been explored. Platt et al. investigated power harvesting between a monolithic PZT cylinder and 145 thin PZT wafers that were stacked mechanically in series but connected electrically in parallel ¹¹. Each had the same dimensions, volume of PZT, and cross-sectional area for loading. Piezoceramics have high

impedance, high voltage, and low current characteristics that are not useful in low frequency power harvesting applications such as spinal fusion with electrical stimulation ¹¹. The monolithic cylinder had high impedance and a lower capacitance. The stack had higher capacitance which is useful in energy harvesting and a lower impedance. By creating a stack of PZT wafers, it was shown that the impedance of the stacked PZT assembly decreased while maintaining the same power as the monolithic PZT cylinder which occurred at a higher impedance ¹¹. This helps with electrical impedance matching to get optimal power outputs, because less impedance and the same amount of electrical potential yields more current that can be used in electrical stimulation for bone healing applications. It is hypothesized that the stack design also adds toughness to the composite material making it desirable for spinal fusion applications in the lumbar spine where high forces are experienced.

1.4 Acoustics

A fundamental understanding of sound is necessary for this work. This section describes the basic physics of wave motion, defines Rayleigh distance, explains sound reflection, transmission, and attenuation coefficients, provides background information on medical imaging ultrasound, and discusses how ultrasound is used in literature to power implantable devices.

1.4.1 Acoustics – Physics of Wave Motion

A wave is a small disturbance or deviation from a pre-existing condition similar to ripples generated by an object being thrown onto the surface of a still pond ²⁷. The motion of this disturbance constitutes a transfer of information from one point in space to another. There are two basic types of waves called mechanical and electromagnetic waves. Mechanical waves are defined as wave motion through a material medium ²⁷. Electromagnetic waves are capable of transmitting energy through a vacuum and are produced by the vibration of charged particles. Since sound is a pressure wave that

propagates in a material medium and is the loading source focus of this study on power generation in a spinal fusion interbody composite, more information about mechanical waves is provided.

Particles in a medium vibrate about their mean positions when impacted by a pressure source or a small deviation in pressure. A small deviation in pressure or disturbance that generates wave motion does not need to be oscillating like a time-dependent sinusoid, but can also be an impulse. As a particle vibrates, energy is transferred from one particle to another and causes that adjacent particle to vibrate back and forth as well. Particle velocity is based on how fast a particle moves back and forth about its mean position and the wave speed is determined by the speed at which energy is transferred from particle to particle. The distances that the particles move back and forth about their mean positions are small compared to the gross movement of energy transfer speed between particles (pressure wave velocity) in the medium. For mechanical waves, there are two basic types of wave motion called longitudinal and transverse waves (Figure 9).

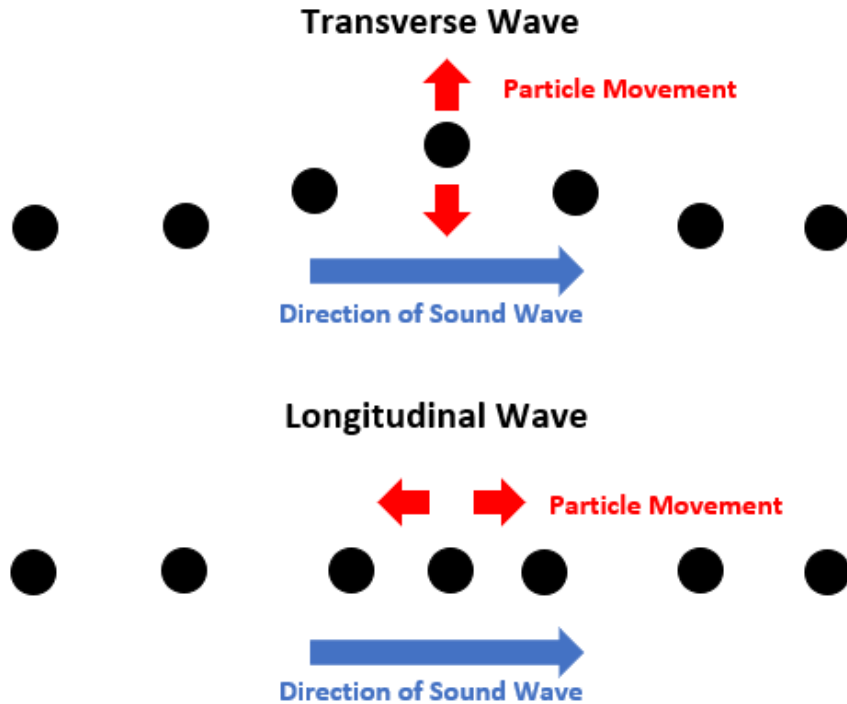


Figure 9 - Longitudinal and Transverse Waves described by particle movement relative to the direction of the propagating wave

A longitudinal wave is described by the direction of particle vibration moving parallel to the direction of the propagating wave velocity. A transverse wave is described by the direction of particle vibration moving perpendicular to the direction of the propagating wave velocity. Transverse waves are also called shear waves because the bond between the two interacting particles is broken when the incident particle vibrates orthogonal to the longitudinal direction next to an adjacent particle. Longitudinal waves travel faster than transverse waves. For example, in the event of an earthquake, the ground moves up and down for a small duration of time at first which is the effect of a longitudinal wave. Following this initial movement, everything begins to shake rapidly which is the effect of a transverse wave.

Sound waves are considered longitudinal waves because the directions of the particle vibration and wave propagation are the same²⁸. They are also referred to as compression or pressure waves.

Sound is time dependent, travels at finite speeds and is described as mechanical waves of pressure traveling through a material medium such as air, water, or tissue. Unlike electromagnetic waves, sound waves are mechanical waves and cannot propagate through a vacuum. Sound is also categorized along the frequency spectrum. Infrasound is a sound wave that propagates in a medium with a frequency of 20 Hz or less. Sound at a frequency of about 20 kHz or higher is referred to as ultrasound. In between these two categories are sound waves that the human ear can hear. Since the spinal fusion composite needs cyclic mechanical deformation to generate electrical potential, ultrasound is a pressure source that represents cyclic mechanical loading and can be used as the loading source in this study.

1.4.2 Acoustics - Rayleigh Distance

Acoustic attenuation is the measure of energy loss of a propagating sound wave in a material medium. It is analyzed differently based on what type of wave it is. To determine the type of sound wave used in this study, the Rayleigh Distance must be calculated. The Rayleigh distance helps describe the distance from a radiating source to a point where the generated plane wave from that sound source transitions into a spherical wave (Figure 10).

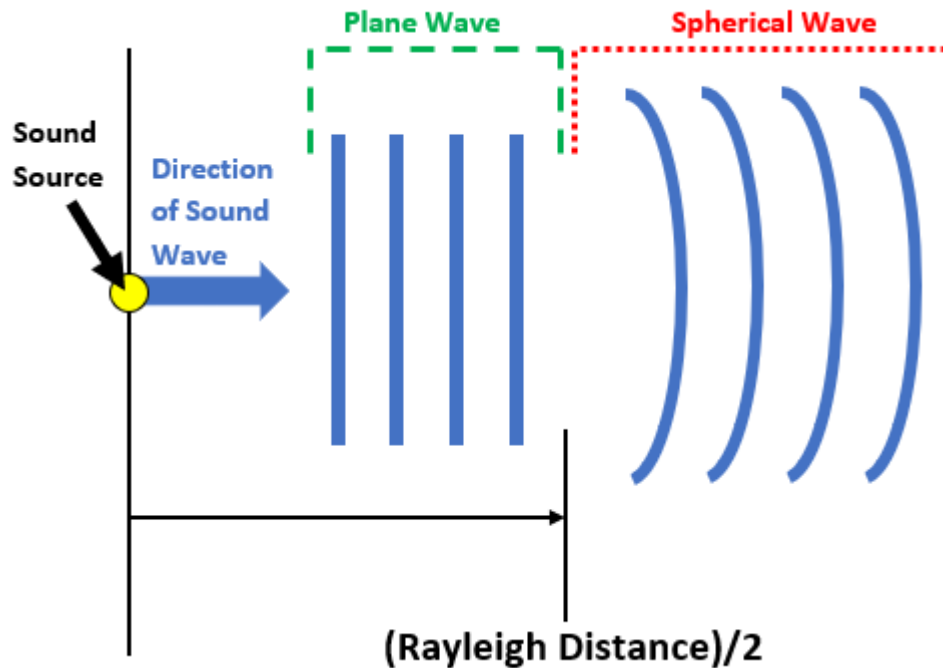


Figure 10 – Transition from plane wave to spherical wave for a point source at approximately half of the Rayleigh Distance

From the source face up until about half of the Rayleigh distance is considered the near-field region. In this region, the sound wave is considered a plane wave. The region beyond half of the Rayleigh distance is considered the far-field region. In this region, the sound wave is considered a spherical wave. The number of null points in the near-field region where the pressure amplitude of the sound wave is zero is described by a/λ , where a is the radius of the piston source and λ is the wavelength of the sound wave. The Rayleigh distance is the point at which spherical spreading takes over attenuation. For this study, since the Rayleigh distance is approximately 1.6m in water, 1.5m in tissue, and 0.6m in bone, and the thicknesses of the media tested was only up to 40mm, the sound waves impacting the spinal fusion interbody composite were plane waves. Basic plane wave theory is used to help predict pressure amplitude decreases at the interface between two impedance mismatching mediums with varying cross-sectional areas and from attenuation of the sound wave traveling through a medium.

1.4.3 Acoustics - Sound Reflection and Transmission at an Interface

This section provides background knowledge of sound reflection and transmission at an impedance mismatching interface between two different mediums of different cross-sectional areas. All sound waves are considered normally incident plane waves of arbitrary waveform. The pressure of a sound wave is described by the particle velocity, and specific acoustic impedance of the medium (equation 1) ²⁷.

$$p = u * Z$$

Equation 1 – Sound pressure as a function of particle velocity (u) and specific acoustic impedance (Z)

The specific acoustic impedance is characterized by the speed of sound in the medium multiplied by the density of the medium (equation 2) ²⁷.

$$Z = \rho * c$$

Equation 2 – Specific acoustic impedance as a function of medium density (ρ) and speed of sound (c)

A sound wave that is traveling towards an impedance mismatching interface between two different media that have the same cross-sectional areas has positive pressure (Figure 11).

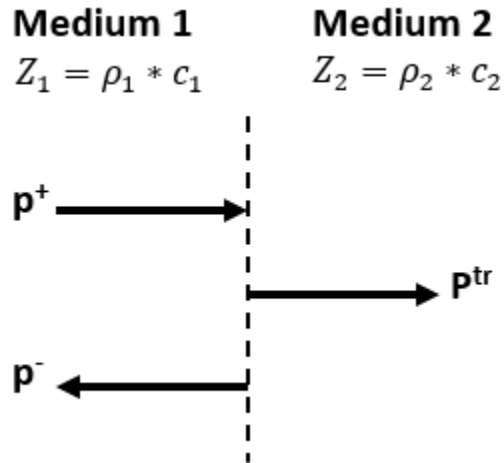


Figure 11 - Reflection and Transmission Sound Pressure at an Impedance Mismatching Interface with the same Cross-Sectional Area

Some of the incident wave will transmit through the interface into the next media and the rest of it will be reflected off the interface back into the incident media. The incident wave pressure is represented by p^+ , p^- is the pressure from the reflected wave, and p^{tr} is the pressure from the transmitted wave. The specific acoustic impedances of the incident medium and transmitted medium are Z_1 and Z_2 respectively. These are each described as the medium material density multiplied by the speed of sound in that medium. The reflection coefficient and transmission coefficient are defined in equations 3 and 4 respectively ²⁷.

$$R = \frac{p^-}{p^+}$$

Equation 3 – Reflection coefficient (R) equation as a function of reflected (p^-) and incident (p^+) pressure

$$T = \frac{p^{tr}}{p^+}$$

Equation 4 - Transmission coefficient (T) equation as a function of transmitted (p^{tr}) and incident (p^+) pressure

The pressure must be the same on both sides of the interface because otherwise if it was massless, it would experience infinite acceleration (equation 5) ²⁷.

$$p^+ + p^- = p^{tr}$$

Equation 5 - Pressure balance equation on boundary of two mediums as a function of incident (p^+), reflection (p^-), and transmission (p^{tr}) pressure

Equation 5 is an expression that describes the amount of pressure on each side of the interface. By dividing equation 5 by p^+ and applying equations 3 and 4, a relationship between the reflection coefficient (R) and transmission coefficient (T) is achieved (equation 6) ²⁷.

$$1 + R = T$$

Equation 6 - Coefficient balance equation on boundary of two mediums as a function of the reflection (R) and transmission (T) coefficients

The particle velocity on both sides of the interface must also be equal where u^+ is the particle velocity of the incident wave, u^- is the particle velocity of the reflected wave, and u^{tr} is the particle velocity of the transmitted wave (equation 7) ²⁷.

$$u^+ + u^- = u^{tr}$$

Equation 7 - Particle velocity balance equation as a function of incident (u^+), reflection (u^-), and transmission (u^{tr}) particle velocity

This boundary condition can be expressed in terms of the reflection and transmission coefficients by substituting equation 1 into equation 7 and including a minus sign for the backward traveling wave (equation 8) ²⁷.

$$\frac{p^+}{Z_1} - \frac{p^-}{Z_1} = \frac{p^{tr}}{Z_2}$$

Equation 8 – Acoustic impedance boundary balance condition expressed as a function of incident (p^+), reflection (p^-), and transmission (p^{tr}) pressure and specific acoustic impedance of the incident (Z_1) and transmitted (Z_2) mediums

By multiplying equation 8 by Z_1 , dividing by p^+ , and using equations 3 and 4, an expression relating specific acoustic impedance and the reflection and transmission coefficients is achieved (equation 9) ²⁷.

$$1 - R = \frac{Z_1}{Z_2} * T$$

Equation 9 – Acoustic impedance boundary balance condition expressed as a function of the reflection (R) and transmission (T) coefficients and the specific acoustic impedance of the incident (Z₁) and transmitted (Z₂) mediums

Now using equations 6 and 9, the reflection and transmission coefficients are solved in terms of specific acoustic impedance (equations 10 and 11) ²⁷.

$$R = \frac{Z_2 - Z_1}{Z_2 + Z_1}$$

Equation 10 - Reflection coefficient (R) as a function of the incident (Z₁) and transmitted (Z₂) specific acoustic impedances

$$T = \frac{2 * Z_2}{Z_2 + Z_1}$$

Equation 11 - Transmission coefficient (T) as a function of the incident (Z₁) and transmitted (Z₂) specific acoustic impedances

There are three special cases to consider when determining reflection and transmission coefficients of a normally incident sound wave at an interface between two media. If the specific acoustic impedance of the incident media (Z₁) is much greater than the specific acoustic impedance of the transmitted media (Z₂), then from equations 10 and 11 the reflection coefficient becomes -1 and the transmission coefficient becomes zero respectively. This scenario is called a pressure release boundary in which the incoming incident pressure wave gets reflected off the interface between the mediums and the direction of its waveform is reversed or it undergoes a 180° phase shift. An example of a pressure release boundary is the boundary between water and air. For a water to air boundary, if sound is produced in water, a person above water is unable to hear any transmitted sound. Another scenario is a hard boundary where Z₁ is much smaller than Z₂. From equation 10 the reflection coefficient becomes 1 which means that the incoming incident pressure wave gets reflected off the interface and its

waveform is not reversed, or its phase does not shift. The transmission coefficient becomes 2 from equation 11 which makes sense mathematically, but does not make sense physically. For an air to water boundary, if sound is produced in air, someone in water is unable to hear any transmitted sound even though mathematically the transmission coefficient is 2. The transmitted sound wave pressure does not get amplified by a factor 2, because no sound is physically transmitted in this scenario. If Z_1 and Z_2 are equal, then from equations 10 and 11 the reflection and transmission coefficients become 0 and 1 respectively. When the specific acoustic impedance of the two media are the same, there is no energy loss from impedance mismatching along the interface. The incoming incident pressure wave gets transmitted across the impedance matching interface and nothing is reflected.

A change in cross sectional area at an interface between two specific acoustic impedance matching mediums also affects how much of the incoming incident pressure wave is transmitted and reflected (Figure 12).

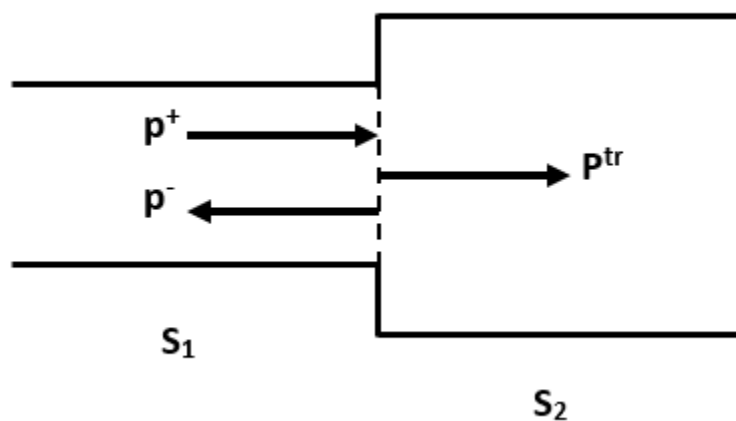


Figure 12 - Reflection and Transmission Sound Pressure at an Impedance matching Interface with different Cross-Sectional Areas

Similar to the assumption made previously, the particle volume velocity across the interface is assumed constant over a given cross section (equation 12) ²⁷.

$$S_1 * u^+ + S_1 * u^- = S_2 * u^{tr}$$

Equation 12 - Surface area boundary condition as a function of incident (u^+), reflection (u^-), and transmission (u^{tr}) particle velocities and the surface area of the incident (S_1) and transmitted (S_2) mediums

Using equations 1, 3, and 4 in equation 12, rearranging, and including a minus sign for the backward traveling wave, a relationship between the cross-sectional areas and the reflection and transmission coefficients is achieved (equation 13) ²⁷.

$$1 - R = \frac{S_2}{S_1} * T$$

Equation 13 – Surface area boundary balance condition expressed as a function of the reflection (R) and transmission (T) coefficients and the surface area of the incident (S_1) and transmitted (S_2) mediums

Combining equations 6 and 13, the reflection and transmission coefficients are solved in terms of cross-sectional areas (equations 14 and 15) ²⁷.

$$R = \frac{S_1 - S_2}{S_1 + S_2}$$

Equation 14 - Reflection coefficient (R) as a function of the incident (S_1) and transmitted (S_2) surface areas

$$T = \frac{2 * S_1}{S_1 + S_2}$$

Equation 15 - Transmission coefficient (T) as a function of the incident (S_1) and transmitted (S_2) surface areas

If the cross-sectional area of the incident medium (S_1) is much greater than the cross-sectional area of the transmitted medium (S_2), then from equations 14 and 15 the reflection and transmission coefficients become 1 and 2 respectively. The incoming incident pressure wave is reflected off the interface of differing cross-sectional areas and its waveform is not reversed, or its phase does not shift. Similar to the specific acoustic impedance mismatching scenario, the transmission coefficient makes sense mathematically, but does not make sense physically. If S_2 is really small compared to S_1 then a

small amount of the incoming incident sound pressure will be transmitted, and most will be reflected. This is a closed end scenario. If the cross-sectional area of the incident medium (S_1) is much smaller than the cross-sectional area of the transmitted medium (S_2), then from equations 14 and 15 the reflection and transmission coefficients become -1 and 0 respectively. This is a soft termination scenario in which the incoming incident pressure wave is reflected off the interface between the cross-sectional areas and the direction of its waveform is reversed or its phase shifts 180°. When the cross-sectional areas of the two impedance matching mediums are the same, there is no energy loss across the interface.

By combining the effects of specific acoustic impedance mismatching between two mediums along an interface of differing cross-sectional areas, the change in sound pressure amplitude across that interface is described (equation 16) ²⁷.

$$1 - R = \frac{S_2 * Z_1}{S_1 * Z_2} * T = \frac{Z_{ac1}}{Z_{ac2}} * T$$

Equation 16 – Combined effects of specific acoustic impedance and surface area for the incident and transmitted mediums boundary balance expressed as a function of the incident (Z_{ac1}) and transmitted (Z_{ac2}) acoustic impedances and the reflection (R) and transmission (T) coefficients

The acoustic impedances of the incident medium (Z_{ac1}) and transmitted medium (Z_{ac2}) are the combined effect of differing cross-sectional areas and specific acoustic impedance mismatching along the interface between the two mediums. By combining equations 6 and 16, the reflection and transmission coefficients are solved in terms of acoustic impedance mismatching and cross-sectional areas (equations 17 and 18) ²⁷.

$$R = \frac{Z_{ac2} - Z_{ac1}}{Z_{ac2} + Z_{ac1}}$$

Equation 17 - Reflection coefficient (R) as a function of the incident (Z_{ac1}) and transmitted (Z_{ac2}) acoustic impedances

$$T = \frac{2 * Z_{ac2}}{Z_{ac2} + Z_{ac1}}$$

Equation 18 - Transmission coefficient (T) as a function of the incident (Z_{ac1}) and transmitted (Z_{ac2}) acoustic impedances

Equations 17 and 18 apply to the scenario where the incident wave is traveling orthogonal to the impedance mismatching interface. This is not always the case. Sometimes the incident wave strikes the interface at an incident angle, θ_i . For this case the boundary dimensions are assumed to be much larger than the wavelength of the sound wave so any energy loss due to a change in cross-sectional area is not considered. After the incident wave impacts the interface at an incident angle θ_i , part of the incident wave transmits across the impedance mismatching boundary at a transmission angle of θ_t , and the rest of the incident wave is reflected off the interface at a reflection angle, θ_r (Figure 13).

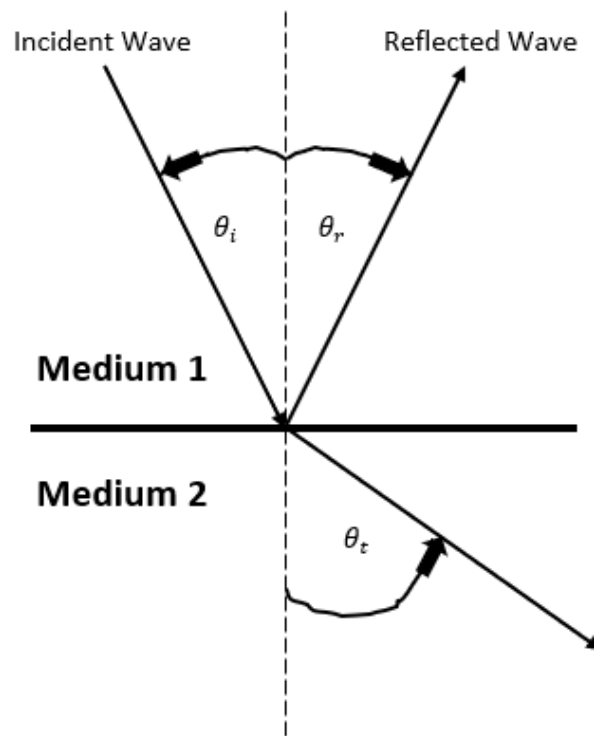


Figure 13 - The behavior of an incident wave striking the boundary between two impedance mismatching mediums

Part of the incident wave reflects off the impedance mismatching interface at a reflection angle (θ_r) which is the same magnitude as the incident angle (θ_i) which is the law of reflection (equation 19) ²⁸.

$$\theta_i = \theta_r$$

Equation 19 - Relationship between the incident (θ_i) and reflection (θ_r) angles of sound waves at an impedance mismatch boundary condition

Snell's law is used to describe the relationship between the incident angle, transmission angle and the speed of sound in in both mediums (equation 20) ²⁸.

$$\frac{\sin \theta_i}{\sin \theta_t} = \frac{c_1}{c_2}$$

Equation 20 - Snell's law as a function of the speed of sound in the incident (c_1) and transmitted (c_2) mediums and the incident (θ_i) and transmitted (θ_t) angles

The normal component of the particle velocity across the interface is assumed to be continuous and is expressed in equation 21 ²⁷.

$$\cos \theta_i * u^+ + \cos \theta_i * u^- = \cos \theta_t * u^{tr}$$

Equation 21 – Normal component of particle velocities boundary condition as a function of incident (u^+), reflection (u^-), and transmission (u^{tr}) particle velocities, and the incident (θ_i) and transmitted (θ_t) angles

Recall that the incident angle is equal to the transmitted angle. Using equations 1, 3, and 4 in equation 21 and including a minus sign for the backward traveling wave, a relationship between the specific acoustic impedance mismatching, incident angle, transmitted angle, and the reflection and transmission coefficients is achieved (equation 22) ²⁷.

$$1 - R = \frac{Z_1 * \cos \theta_t}{Z_2 * \cos \theta_i} * T$$

Equation 22 - Combined effects of specific acoustic impedance and incident and transmitted angles boundary condition expressed as a function of the incident (Z_1) and transmitted (Z_2) specific acoustic impedances and the reflection (R) and transmission (T) coefficients and the incident (θ_i) and transmitted (θ_t) angles

Combining equations 6 and 22, the reflection and transmission coefficients are solved in terms of specific impedance mismatching for both mediums, the incident angle, and transmitted angle (equations 23 and 24) ²⁸.

$$R = \frac{Z_2 \cos \theta_i - Z_1 \cos \theta_t}{Z_2 \cos \theta_i + Z_1 \cos \theta_t} \quad \text{Equation 23}^{28}.$$

$$T = \frac{2 Z_2 \cos \theta_i}{Z_2 \cos \theta_i + Z_1 \cos \theta_t} \quad \text{Equation 24}^{28}.$$

$$R = \frac{Z_2 * \cos \theta_i - Z_1 * \cos \theta_t}{Z_2 * \cos \theta_i + Z_1 * \cos \theta_t}$$

Equation 23 - Reflection coefficient (R) as a function of the incident (Z₁) and transmitted (Z₂) specific acoustic impedances and the incident (θ_i) and transmitted (θ_t) angles

$$T = \frac{2 * Z_2 * \cos \theta_i}{Z_2 * \cos \theta_i + Z_1 * \cos \theta_t}$$

Equation 24 - Transmission coefficient (R) as a function of the incident (Z₁) and transmitted (Z₂) specific acoustic impedances and the incident (θ_i) and transmitted (θ_t) angles

Before calculating the reflection and transmission coefficients, R and T, a critical angle that would cause total internal reflection needs to be checked. When solving for θ_t in equation 20, $\frac{c_1}{c_2} * \sin \theta_i$ needs to be less than or equal to 1 in order for θ_t to be a real number. To find the critical angle $\sin \theta_t$ in equation 20 is set equal to 1 and θ_i becomes the critical angle and is solved for (equation 25) ²⁸.

$$\theta_{critical} = \sin^{-1} \left(\frac{c_1}{c_2} \right)$$

Equation 25 - The critical angle (θ_{critical}) as a function of the speed of sound in the incident (c₁) and transmitted (c₂) mediums

If the incident angle is less than the critical angle, then the wave will transmit at the transmitted angle calculated from equation 20. If the incident angle is equal to the critical angle, then the transmitted angle is 90° and the incident wave is transmitted across the mismatch impedance interface at 90°. If

the incident angle is greater than the critical angle, then total internal reflection occurs and there is no transmission.

1.4.4 Acoustics - Attenuation

Attenuation is the sum of absorption and scattering that occurs in a medium as a sound wave propagates. Absorption is the conversion of ultrasound beam energy into heat²⁸. There are two mechanisms that make up absorption and those are classic and relaxation absorption. In biological tissues, classical absorption contributes the least to the overall absorption of the sound wave and is directly proportional to the square of the operating frequency. Relaxation absorption is a function of the operating frequency and the relaxation time. Tissues have different elastic properties which can quantitatively be described by the relaxation time, τ . Relaxation time is the time it takes for a structure within a tissue to return to its equilibrium position after being displaced by either compression pressure or rarefactional pressure (Figure 14).

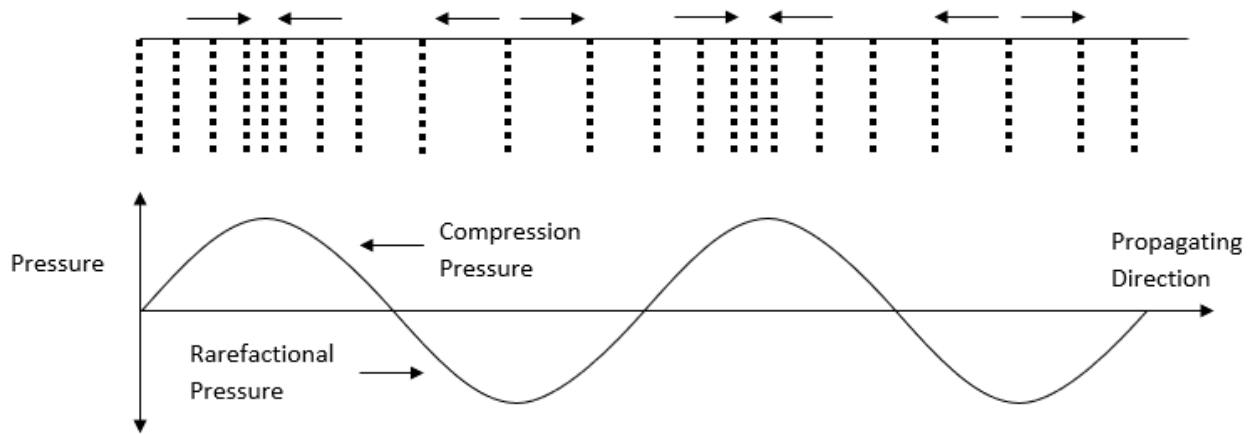


Figure 14 - Compression and Rarefactional Pressure on Particle Vibration Position and Movement (Adapted from²⁸)

Compression pressure is when particles moving about their mean positions as described in section 1.4.1 push against each other and rarefactional pressure is when the particles pull against each other due to their atomic bond. After achieving the maximum positive pressure, elastic forces in the tissue structure

take over and pull the particles backward. As shown in Figure 14, the positive pressure (compression) moves the particles along the positive longitudinal direction (positive – to the right) and the negative pressure pulls them back (negative – to the left). If the maximum negative pressure coincides with the relaxation time of the medium, little energy is lost from the ultrasound beam, but if the relaxation time for the elastic restoring forces is pulling the particles back to the left (negative) at the same time when there is maximum positive pressure, a much larger amount of energy from the ultrasound beam is lost. The relaxation process is described by a relaxation absorption coefficient, β_r (equation 26) ²⁸.

$$\beta_r = \frac{B_0 * f^2}{1 + \left(f/f_r\right)^2}$$

Equation 26 - The relaxation absorption coefficient (β_r) as a function of operating frequency (f), relaxation frequency (f_r) and a constant (B_0)

The relaxation absorption coefficient is β_r , the relaxation frequency which is equal to $1/\tau$ is f_r , the operating frequency is f , and B_0 is a constant. Higher values of β_r correspond to more energy being absorbed from relaxation. Most tissues have multiple relaxation frequencies and relaxation times, so the overall relaxation absorption coefficient is proportional to the sum of the individual relaxation coefficients (equation 27) ²⁸.

$$\beta_{r,tissue} = \sum_n \frac{B_0 * f^2}{1 + \left(f/f_{r,n}\right)^2}$$

Equation 27 - Overall relaxation absorption coefficient ($\beta_{r,tissue}$) as a summation function of “n” iterations, operating frequency (f), “nth” relaxation frequency ($f_{r,n}$) and a constant (B_0)

Measured values of relaxation absorption in many tissues have shown that there is close to a linear relationship between the total absorption coefficient and ultrasound operating frequency. Attenuation

in an ultrasound beam is characterized by an exponential decrease in wave pressure and intensity as a function of propagation distance in a singular direction (equations 28 and 29) ²⁸.

$$I(z) = I(z = 0) * e^{-\mu * z}$$

Equation 28 - Sound intensity (I) as a function of the intensity attenuation coefficient (μ) and depth (z)

$$p(z) = p(z = 0) * e^{-\alpha * z}$$

Equation 29 - Sound Pressure (p) as a function of the sound pressure attenuation coefficient (α) and depth (z)

The intensity attenuation coefficient is μ ($dB * cm^{-1}$), and the pressure attenuation coefficient is α (cm^{-1}) and the value of μ is twice that of α ²⁸. To get μ into just (cm^{-1}), a conversion factor for decibels (dB) must be applied (equation 30) ²⁸.

$$\mu (dB * cm^{-1}) = 4.343 * \mu (cm^{-1})$$

Equation 30 - Unit conversion relationship for the intensity attenuation coefficient

If there is a 3 dB reduction, there is a reduction in intensity by a factor of 2, a 6 dB reduction corresponds with an intensity reduction by a factor of 4, a 9 dB reduction results with an intensity reduction by a factor of 8 and so on ²⁸. There is a frequency dependence of μ for soft tissue and it is $1 dB cm^{-1} MHz^{-1}$. So, at an operating frequency of 2 MHz, the intensity attenuation coefficient is $2 dB * cm^{-1}$. For air and bone, the intensity attenuation coefficients are much higher at $45 dB cm^{-1} MHz^{-1}$ and $8.7 dB cm^{-1} MHz^{-1}$ respectively ²⁸.

For attenuation, if the sound wave is a spherical wave or beyond half of the Rayleigh distance from the source, the pressure of the wave does not decrease exponentially anymore, but decreases by a distance from the sound source. If the pressure radiated by a pulsating sphere of radius R_0 and pressure amplitude at its surface is P_0 , then the pressure amplitude decrease at a distance r from the sound source in the far-field region is described by equation 31 ²⁸.

$$p = \frac{P_0 * R_0}{r}$$

Equation 31 - Pressure amplitude of a spherical wave as a function of radius (r) from the source, pressure amplitude of pulsating sphere (P₀), and pulsating sphere radius (R₀)

This pressure amplitude decrease in the far field region for attenuation is different than calculating the pressure amplitude decrease in the near field region where the sound wave is a plane wave. For this study, since the Rayleigh distance is approximately 1.6m in water, 1.5m in tissue, and 0.6m in bone, and the thicknesses of the media tested was only up to 40mm, the sound waves impacting the spinal fusion interbody composite were plane waves and the intensity and pressure amplitudes would be described by equations 28 and 29 and not by equation 31.

1.4.5 Acoustics - Medical Imaging Ultrasound

Ultrasound is a mechanical wave with a frequency range of 1-15 MHz for clinical imaging use. The speed of sound in tissue is approximately 1540 m/s so the range of wavelengths of ultrasound in tissue is between approximately 0.1mm and 1.5mm²⁸. Ultrasound transducers have arrays of PZT elements that act as individual active sources and are fired sequentially to produce parallel ultrasound beams or pressure waves. These transducers can have up to 512 PZT elements. As sound propagates through tissue, a small fraction of energy is reflected or backscattered to the ultrasound transducer from the boundary between two tissues that have varying acoustic and physical properties. The remaining energy passes through the boundary and continues to propagate deeper into the tissue. The reflected waves are detected by the ultrasound transducer and the distance to each tissue boundary is calculated as a function of time from when the pulse was sent out to when a smaller magnitude of the reflected pulse is received. Once the deepest tissue boundary is detected by the ultrasound probe for that impulse input, the next adjacent beam is emitted. The process repeats to produce an image.

Ultrasound is a small pressure wave that is the passage of energy through a medium which causes individual particles to oscillate about their mean positions in the longitudinal and shear directions as discussed in section 1.4.1. The distance moved from mean starting positions is small for every particle compared to the overall traveled distance of the propagating wave. In Ultrasound imaging, the particle movement and wave velocity are in the same direction which is called a longitudinal wave. Positive pressure of the ultrasonic wave corresponds to compression on the particles interacting with each other and negative pressure corresponds to rarefactional pressure or separation between the particles (Figure 14). This effect causes a cyclic mechanical motion and can be used as a cyclic loading source for PZT energy harvesters.

The active element inside all medical imaging ultrasound transducers is shaped piezoelectric material and is formed from a composite of lead zirconate and titanium (PZT). These powders are mixed and heat treated to high temperatures ($> 120\text{ }^{\circ}\text{C}$) and placed in strong electric fields (kV/cm) to align the dipoles of the PZT material so that an oscillating voltage applied to the PZT material can force changes in physical dimension of the PZT material at the same frequency as the applied voltage²⁸. This also works in reverse where an applied physical change in dimension can generate electric potential out of the PZT material at the same applied physical change frequency. This confers the property of being piezoelectric. The mechanical motion of the PZT elements in an ultrasound transducer is transferred into a medium as a pressure wave through an acoustic impedance matching layer. Thin rods of PZT are embedded in a resin and the combined material is then formed into a desired probe shape and size²⁸. In the case of a single element transducer, the PZT is coated with a thin layer of silver on both faces and connected to wires leading to a power source. PZT has a natural resonant frequency and each probe is optimally built around a certain operating frequency but can still function at others. This natural resonant frequency corresponds to the thickness of the PZT crystal element being one-half of the wavelength of ultrasound in the crystal (equation 32)²⁸.

$$t = \frac{\lambda_{crystal}}{2} = \frac{c_{crystal}}{2 * f_0} \rightarrow f_0 = \frac{c_{crystal}}{2 * t}$$

Equation 32 - Relationship between the thickness of PZT crystals (t), operating frequency (f₀), wavelength (λ_{crystal}), and speed of sound in the crystal (c_{crystal})

The speed of sound in PZT crystal is approximately 4,000 m/s and so the thickness of a crystal for an operating frequency of 4 MHz is 0.0005 meters which is approximately half a millimeter ²⁸.

The acoustic impedance of a PZT elements in ultrasound probes has a Z value of approximately $30 * 10^5 \text{ g cm}^{-2} \text{ s}^{-1}$ ²⁸. Comparing this to Z values for other mediums and knowing that with acoustic impedance mismatching mediums (equation 10) a large amount of energy can be reflected and the efficiency of the transmitted mechanical wave into tissue would be low ²⁸. To improve the efficiency of this mismatched acoustic impedance boundary a 'matching' layer is added to the external face of the PZT element to provide acoustic coupling between the crystal and the tissue medium. The Z value for the 'matching' layer can be described as the geometric mean between the PZT and tissue Z values (equation 33) ²⁸.

$$Z_{\text{matching layer}} = \sqrt{Z_{\text{PZT}} * Z_{\text{tissue/skin}}}$$

Equation 33 - Specific acoustic impedance of a matching layer as a function of PZT (Z_{PZT}) and tissue/skin (Z_{tissue/skin}) specific acoustic impedance

To maximize energy transmission through this 'matching' layer, the thickness of it should be no more than one quarter of the ultrasound wavelength ²⁸. If the thickness of a material is less than the wavelength of the sound wave propagating through it, then energy is conserved ²⁹. Although the matching layer improves acoustic coupling, it does not provide 100% efficiency so multiple 'matching' layers are used in parallel to continue improving the efficiency of mismatched acoustic impedance ²⁸.

Ultrasound signal frequencies sent to the PZT elements in the probe are gated on and off for periods of time typically comprising of two or three cycles of the frequency for each pulse to improve axial spatial resolution. Axial spatial resolution is proportional to the total length of the pulse (Figure 15).

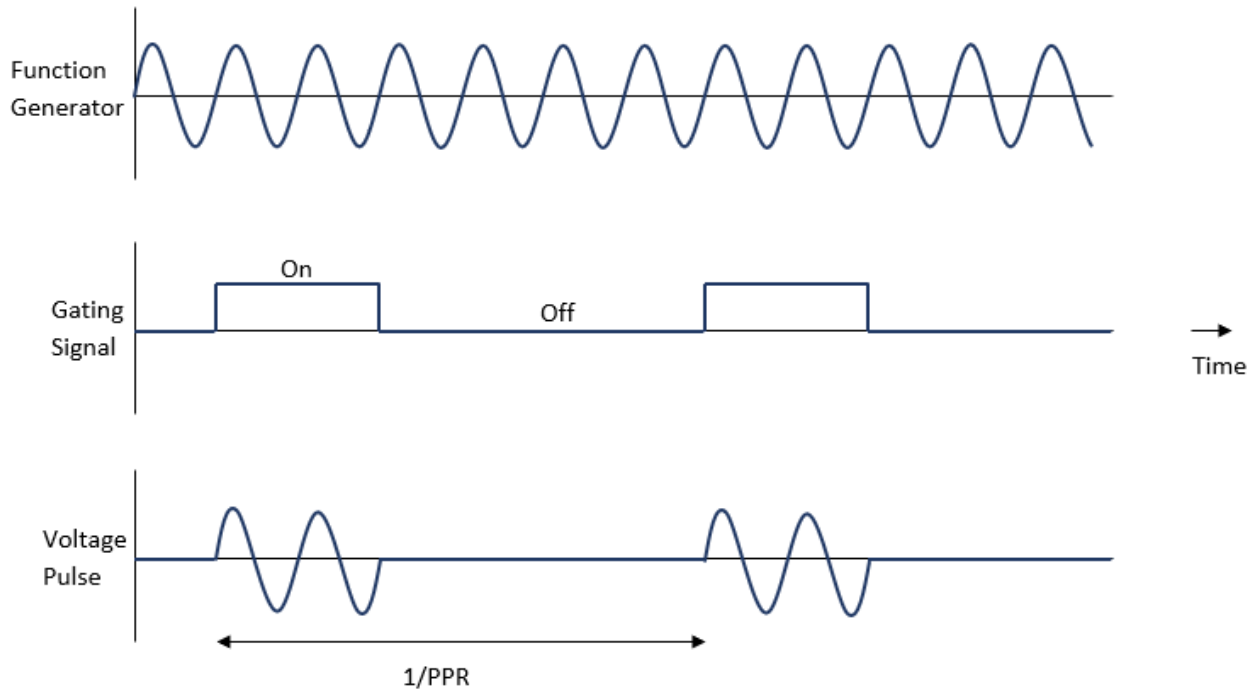


Figure 15 - Gating of Ultrasound Frequency generator and effect on voltage pulse commands to PZT elements and pressure waves generated in low and high transducer damping (Adapted from ²⁸)

The voltage pulses consisting of a couple or a few cycles are produced at a certain rate of $(1/P_{RR})$ ²⁸.

By damping the ultrasound probe, the sound wave pressure duration from the voltage pulse input to the PZT elements is reduced and helps achieve a larger frequency bandwidth for ultrasound probe operation. Materials used for damping are based on epoxies with small added particles like aluminum oxide ²⁸. This prevents the PZT elements from “ringing” after the end of the voltage pulses resulting in poor axial resolution ²⁸. Although this logic to gate the ultrasound frequency signal generator is beneficial for imaging purposes, it decreases the number of mechanical waves propagating in tissue to transfer energy into an implantable energy harvester for biomedical applications over time.

There are two basic ways to focus an ultrasound beam. A concave lens made of plastic can be put in front of the PZT elements, or the layout of the elements can be manufactured as a curved surface. The shape of this curvature is defined by an f-number (equation 34) ²⁸.

$$f\# = \frac{\text{focal distance}}{\text{aperture dimension}}$$

Equation 34 - "F" number (curvature of ultrasound lens with PZT elements) as a function of focal distance and aperture dimension

The aperture dimension corresponds to the size of the PZT element and the focal distance is the distance from the sound source to the focal point or point along ultrasound beam where the lateral beam width is smallest (Figure 16).

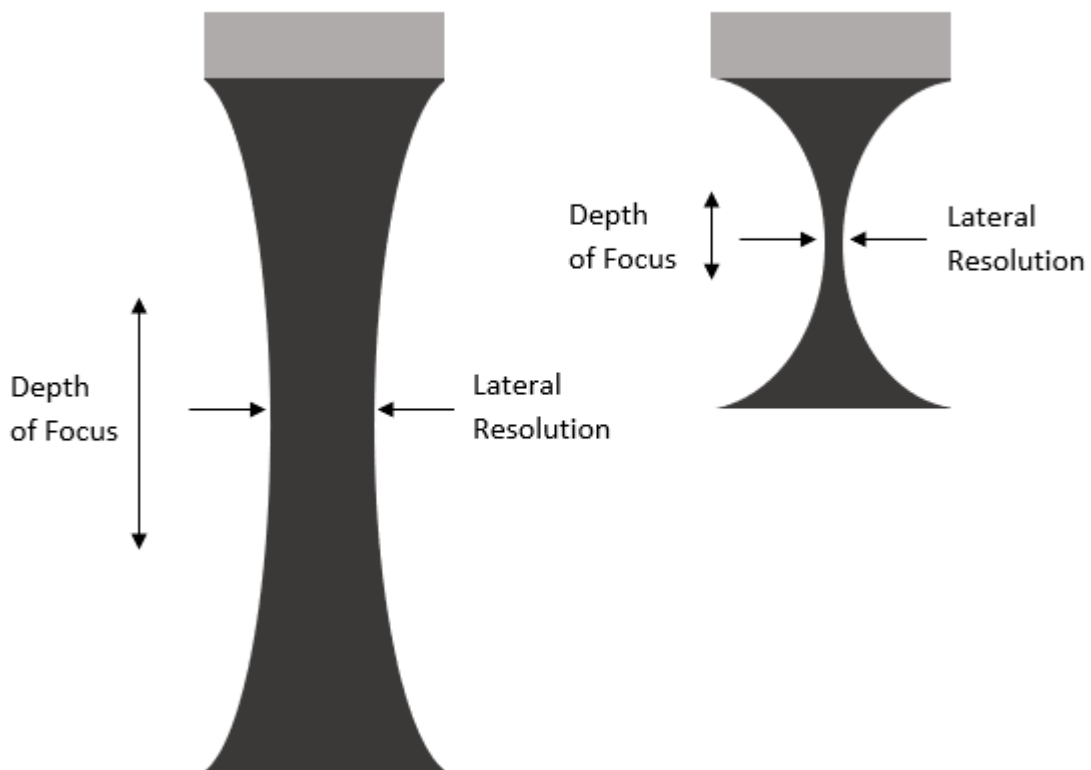


Figure 16 - Weakly focused single element transducer (left) and strongly focused (right) (Adapted from ²⁸)

As the operating frequency increases, the lateral resolution decreases and creates a more “focused” ultrasound beam, but loses depth as seen in Figure 16. A smaller diameter probe will also focus the ultrasound beam more than a larger diameter where the lateral resolution is given by equation 35 ²⁸.

$$\textit{lateral resolution} = \frac{\lambda * f}{D}$$

Equation 35 - Lateral resolution of an circular ultrasound probe as a function of wavelength (λ), frequency (f), and diameter (D) of probe face

In equation 35, λ is the wavelength of the ultrasound wave, f is the operating frequency, and D is the aperture dimension of the probe which is usually a diameter.

Ultrasound PZT element arrays have superseded the use of a single element array for imaging purposes. These arrays enable unique imaging capabilities that through electronic steering the ultrasound beam through the patient, two-dimensional images can be acquired. Linear and phased arrays are two basic types of PZT element array transducers ²⁸. A linear array has about 128-512 rectangular piezoelectric (PZT) elements that have a separation distance between their centers called the pitch and the space in between the elements is called the kerf (Figure 17).

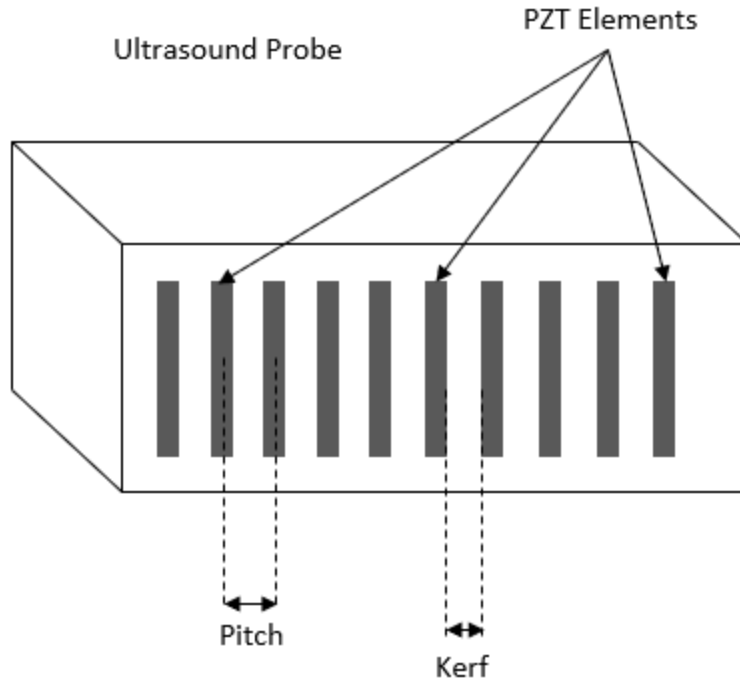


Figure 17 - Ultrasound linear array probe with rectangular PZT elements design (Adapted from ²⁸)

Each of these elements is unfocused and is mechanically and electrically isolated from neighboring elements ²⁸. The pitch is around half or 1.5 times the wavelength of the ultrasound wave coming out of each PZT element. A linear array is typically one centimeter wide and anywhere from a couple of centimeters to 15 centimeters in length. The mode of operation in a linear array is simple. A small amount of the PZT elements are excited or have voltage pulses (Figure 15) sent to them sequentially with the outer array elements excited first and then the inner elements after a certain time delay to produce a curved wave front ultrasound beam at an effective focal point (Figure 18).

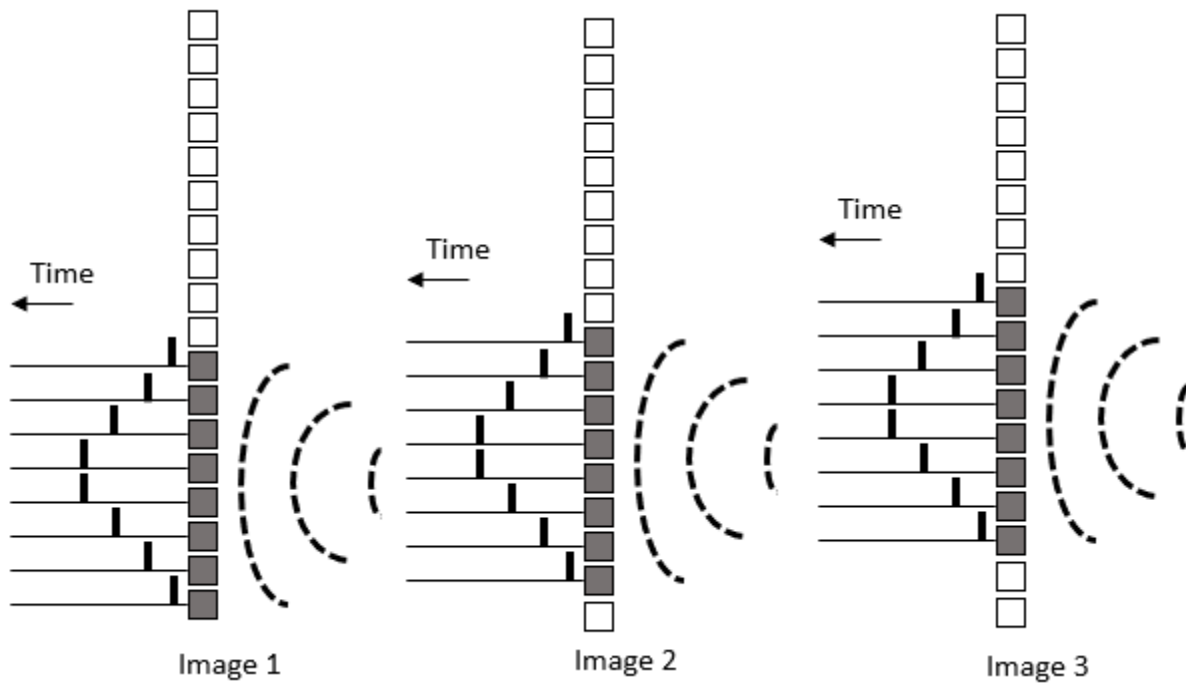


Figure 18 - Operation of linear array. Sequential excitation of small PZT element groups used to produce a two-dimensional image (Adapted from ²⁸)

Once the backscattered pulses have been received by the ultrasound probe, a second beam is sent out in the next group of array elements as shown by Image 2 of Figure 18. This sequence is followed until all PZT elements along the length of the ultrasound probe have been excited. All the backscattered signals received by the ultrasound probe are then converted into intensity and are used to produce a two-dimensional image. For a linear array, focusing can be achieved in the direction parallel to the ultrasound wave front by curving the lens of the ultrasound probe convex, but not in the perpendicular direction. When a large-field-of-view is required close to the surface of the ultrasound probe, linear arrays are used ²⁸.

Phased arrays have fewer PZT elements than linear arrays and have smaller dimensions, typically 1-3 cm in length and 1 cm wide (Figure 19).



Figure 19 - Phased array probe (Adapted from ²⁸)

When there is a small “acoustic window”, or where there is only a small part of the body through which the ultrasound waves can enter without interacting with acoustically hard boundaries like bone to get good images, phased arrays are used ²⁸. For example, in cardiac imaging the phased array ultrasound beams must pass in between the ribs in order to avoid reflections from bone and to produce a good two-dimensional image of the heart. The operation of a phased array ultrasound probe is different than a linear array. Every PZT element in the array is excited by voltage pulses at different times with the

outer array elements being excited first and inner elements are excited some time delay after. The sum of these individual waves across the whole probe makes an effective wave front. Figure 20 shows elements excited symmetrically about the center of the ultrasound probe phased array to produce a focal point at the center of the array.

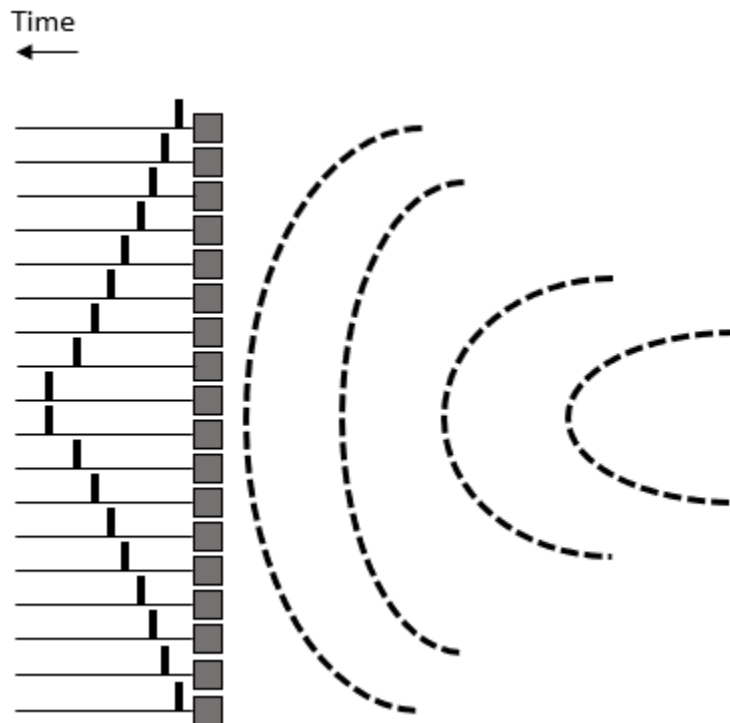


Figure 20 - Beam forming for phased array ultrasound probe. Elements are excited symmetrically in sequence about the center of the array creating a focus point for the ultrasound wave to occur at the center of the array in a medium (Adapted from ²⁸)

In order to form a two-dimensional image, however, the phased array needs to be “steered” by changing the timing delays along the elements in the array (Figure 21).

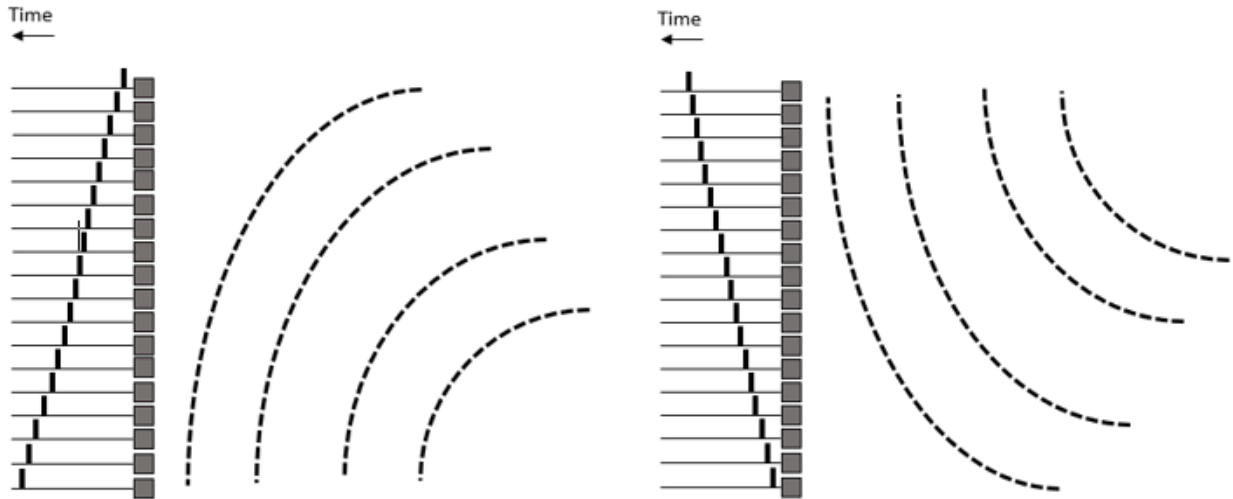


Figure 21 - Beam Steering of phased array ultrasound probe to create different focal points for ultrasound wave by exciting elements at different times (Adapted from ²⁸)

To improve the lateral resolution of an image, “dynamic focusing” is used over the entire depth of the medium being imaged. This involves dynamically exciting a certain number of elements based on a depth setting. If the focal point is close to the probe face only a small number of elements are excited (Figure 22 a).

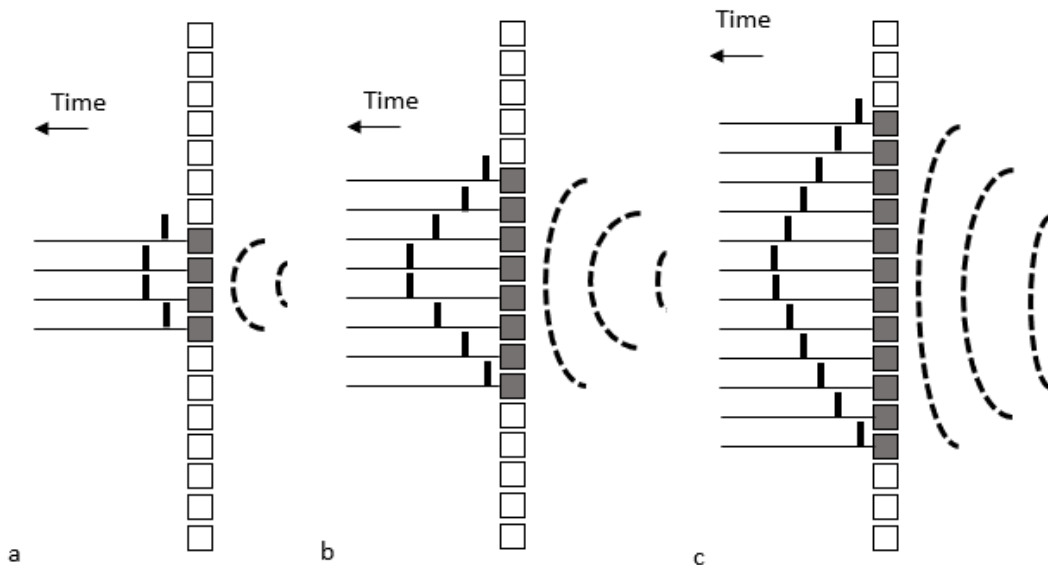


Figure 22 - Dynamic focusing of phased array ultrasound probe used to improve lateral resolution at multiple depths in a medium being imaged. The distance between the elements and the focal point is

small in "a" and more elements are excited in "b" and "c" to achieve a similar focus at greater depths in the medium (Adapted from ²⁸)

At larger depths, the number of excited elements are increased to improve the lateral resolution of an image. This technique is an advantage in medical imaging because it allows for high lateral resolution throughout the depth of the medium that the ultrasound waves are propagating through. For phased arrays, the length of each element defines the "slice thickness" of the image and is typically 2-5 mm ²⁸. If further improved resolution or focusing is required, a curved lens can be incorporated into the ultrasound probe similar to the linear array.

The medical imaging ultrasound system used in this study is an Acuson 128xp with a V4 phased array cardiac ultrasound probe. This probe has 128 individual PZT elements and is in the vector array format (Figure 23).

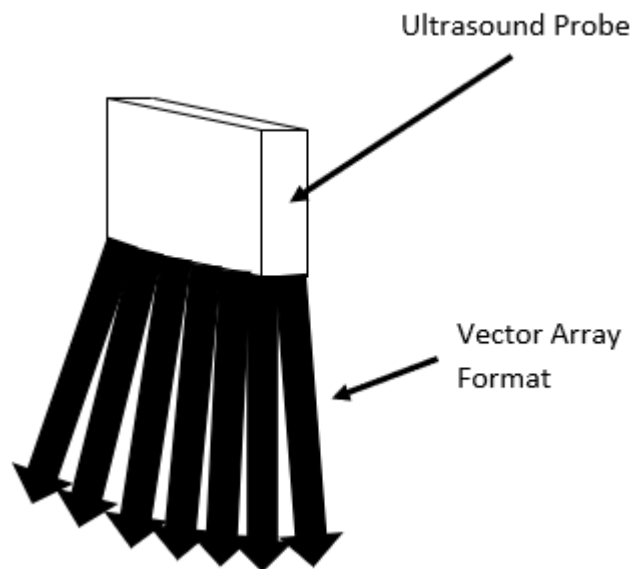


Figure 23 - Acuson 128xp V4 Phased Array Ultrasound Probe Vector Array Ultrasound Scan Format (Adapted from ³⁰)

In a vector array format, element excitation can originate from any point on the transducer face and can be steered in any direction³⁰. The near field image width is as wide as the transducer footprint and then in the far field region, the ultrasound beam begins to spread in all directions³⁰.

Even though ultrasound is considered a safe imaging technique with low power levels and insignificant increases in tissue temperature, there is constant monitoring by various scientific and government bodies²⁸. Several measures of ultrasound energy are monitored and used to form guidelines for different diagnostic protocols, such as spatial average, temporal average, spatial peak, and temporal peak²⁸. During an ultrasound scan, tissue heating and cavitation are two mechanisms that can have destructive bioeffects²⁸. For tissue heating, the intensity of the ultrasound and duration of the scan are contributing parameters, and for cavitation pulse peak rarefactional pressure amplitude is the relevant parameter. Acoustic output in the United States is directly regulated by the FDA and there is an overall maximum intensity limit of 720 mW/cm² for ultrasound imaging. Higher intensities are allowed by the FDA if the imaging system has real-time output display standards (ODS), such as mechanical index (MI) and thermal index (TI). The mechanical index is a function of the axial value for rarefactional pressure, p_r , measured in water at a certain depth, z , and operating frequency, f_0 (equation 36)²⁸.

$$MI = \frac{\max[p_r(z) * e^{-0.0345 * f_0 * z}]}{\sqrt{f_0}}$$

Equation 36 - Mechanical index as a function of operating frequency (f_0), rarefactional pressure (p_r), and depth (z)

The mechanical index and thermal index are only cautious approximations of a risk in biological damage, with values less than 1 indicating safe operation. The mechanical index (MI) has an upper limit of 1.9 defined by the FDA²⁸. The aim of the mechanical index is to predict cavitation, where the critical parameter is peak pressure. The thermal index (TI) estimates thermally induced biological effects in soft tissue and bone.

1.4.6 Acoustics - Powering Medical Devices with Ultrasound in Literature

This section presents ultrasonic wireless powering applications for implantable medical devices from research papers.

One study investigated biocompatible wireless optimum power transfer efficiency between ultrasonic devices, a transmitter and a receiver, in water and pig skin tissue mediums made from 1-3 composite type PZT with a resonance frequency of about 280 kHz³¹. It was not indicated why pig skin tissue was chosen as a tissue medium in the effort to study power transfer efficiency for implantable device applications. In the experimental setup for the water medium an ultrasonic transmitter and receiver were placed 30mm apart in a water tank. For the tissue medium the ultrasonic transmitter and receiver were compressing different pig skin tissue samples of varying depth. A signal generator and power amplifier were used to produce ultrasonic waves out of the transmitter at an operating frequency range of 200-300 kHz and the receiver was hooked up to a battery to see how much power was transferred. It was determined that as you increase the distance the ultrasonic wave travels through a medium, power transfer efficiency decreases. The power transfer efficiency for water at 30mm and 255 kHz driving frequency, 55%, was greater than that of skin at 23mm and 255 kHz driving frequency, 21%, of medium thickness. It was determined that the damping effect of tissue, attenuation plus spherical spreading, on sound waves is higher than water and that was why there was a greater power transfer efficiency in water than in tissue. In medical applications, the distance between the source and receiver is most likely going to be fixed for each patient, so to find the maximum power transfer efficiency it was suggested that the frequency of the source should be adjusted.

The ability of external broadband ultrasound to generate current from small piezoelectric ceramic implants that could be used as devices to stimulate bone healing was studied both in vivo and in vitro³². The small piezoelectric ceramic implants or test coupons were made of PZT-5H with element dimensions of 0.5 x 0.5 x 0.09 cm and a resonance frequency of 2.4 MHz. Each PZT element was coated

with silver on the entire surface and Teflon insulated wires were soldered to the silver electrodes. To complete the assembly, the wired elements were mounted in epoxy on 1-cm² squares of acrylic. In these tests an ultrasonic transducer powered by a function generator via an RF power amplifier at 2.25 MHz operating frequency, 10-30V input and less than 10 mW/cm² intensity was used. It was unspecified whether the ultrasound probe was meant for clinical or non-clinical use. The excitation voltage was adjusted to yield maximum output voltage monitored by an oscilloscope from the test coupons. The current output was measured by a picoammeter after rectification using two Schottky diodes in a voltage-doubling bridge configuration. For in vitro tests, 2.5 cm of water and then 2.5 cm thick polyvinyl chloride (PVC) gel, which is supposed to simulate 10 cm thick of soft tissue, were interposed between the exciting transducer and the receiving test coupon. Next, in a water medium, a sample of hydrated cortical bone 3.5 mm thick with 2.5 cm of PVC gel attached were interposed. For in vivo tests, the test coupons were fixed surgically in laboratory-bred beagles on the subcutaneous fascia of the lateral thigh, the periosteum of the subcutaneous surface of the tibia, and on the anterior surface of the femur. All data points presented were the maximum sustainable output achieved at each excitation voltage. For all three medium configurations compared in vitro, as the excitation voltage from the function generator increased, the short circuit current after rectification also increased. In vitro with an excitation voltage of 10V, the water medium yielded the a much higher current output (1000 microamps) compared to PVC gel (200 microamps) and the Bone plus PVC gel medium (1 microamp). The ultrasound application generated currents from 0.01 microamps to currents exceeding 100 micro amps in vitro. This span exceeds known current values to stimulate osteogenesis and bone resorption around metallic electrodes. In vivo, the test coupon sites that were deeper into the test subjects yielded much lower current output than the subcutaneous location. The peak intensity to generate 20 micro amps from the deep femoral location was approximately 1.5 mW/cm². In general, it is feasible to transmit ultrasonic energy through interposed soft tissue and cortical bone to achieve

high levels of output current in small internal devices designed to stimulate bone healing without the use of invasive implanted batteries, wires or percutaneous leads.

Ultrasonic transcutaneous (measured across a depth of skin) energy transfer (UTET) as a method for powering implanted devices up to a few 100 mW has been explored³³. In this article, external electrical power is converted into a pressure wave in an ultrasonic probe, the acoustic energy is transferred transcutaneously and then is collected and converted back into electrical energy using the piezoelectric effect of the implanted device. This electrical energy can then be used as electrical stimulation for bone healing applications. The UTET link's power transfer efficiency from excitation in the ultrasound probe to the measured output of the implanted device is affected by losses in the amplifier, transducer, tissue absorption, acoustic impedance matching layer, rectification process and the amount of power captured by the receiver. This study used two PZT plane disc transducers as a transmitter and receiver. A test tank was used to house the transmitter and receiver transducers. An ultrasonic absorber material was lined along the inside of the tank to reduce the effect of reflected ultrasonic waves impacting the receiver during testing. The medium used in the tank is distilled water because its acoustic impedance is similar to that of soft biological tissue (1.45-1.55MRayls). A slab of pig muscle tissue was also interposed between the transmitter and receiver with distilled water still in the tank. Water attenuation (0.002 dB/cm @ 1 MHz) is much lower than biological tissue (0.6-1.5 dB/cm @ 1 MHz)³⁴⁻³⁶. Input electrical waveforms to the transmitter probe were generated by a function generator and amplified. Electrical waveforms from the output of the receiver probe were recorded using an oscilloscope and voltage and current probes. At a distance of 30 mm between the ultrasound probe transmitter and receiver in distilled water with a lateral misalignment of 0 mm and power input of 260 mW, the load power was measured to be approximately 95 mW. In pig muscle tissue at the same input parameters, the load power was measured to be approximately 38 mW. From a distilled water medium to a pig muscle tissue medium with other constant input parameters, the load power measure

decreased. For a 15 mm distance at 0 mm lateral misalignment and 260 mW input, the load power measured for distilled water and pig muscle tissue is approximately 92 mW and 55 mW respectively. With a smaller separation distance, the load power measure decreased, but not as much as the larger separation distance. In distilled water with a 0 mm lateral misalignment, the load power for a distance of 5 mm in between the ultrasound probe transmitter and receiver is 100 mW, for a 15 mm and 30 mm distance both were approximately 95 mW. As the separation distance increased in distilled water, the load power barely decreased. In pig muscle tissue with a 0 mm lateral misalignment, the load power for a distance of 5 mm in between the ultrasound probe transmitter and receiver is 70 mW, for 15 mm was 55 mW, and for 30 mm was approximately 38 mW. As the distance increased in pig muscle tissue, the load power decreased more than it did with increasing distance between the transmitter and receiver in distilled water. For optimal power transfer efficiency, the article suggests a few actions. The implantable device should be located at the Rayleigh distance of the ultrasonic beam. The Rayleigh distance is the distance from the transmitter radiating surface where transition from near field to far field regions occur. Over distances longer than the Rayleigh distance, the pressure field from the source starts to diffract and becomes unfocused. It also suggests having acoustic impedance matching between the probe transmitter and medium to improve power transfer efficiency. Impedance mismatch causes part of the pressure wave to reflect at the boundary layers between the PZT elements (31 MRayl) and the distilled water (1.45 – 1.55 MRayl) and pig muscle tissue mediums (1.5 MRayl). This impedance mismatch probably caused a small part of the energy to be reflected at the receiver-medium interface contributing to 15% less power being captured. It is best to have an operating frequency that is close to the resonance frequency of the transducer transmitter to increase the power transfer efficiency of the system. Resonance is determined by the geometry and material constants of the PZT. If a thin receiver is more important than power transfer efficiency, improving rectification components could help minimize energy loss.

In one study, the differences in attenuation of ultrasound by normal, benign, and malignant breast tissue was investigated²⁹. The ultrasonic wavelength used was 0.6 mm for the measurements and 0.25 mm wires held the sample tissues flat against a thin plastic sheet of negligible ultrasonic attenuation for the ultrasound probe to be placed against. To maximize energy transmission through a boundary, the thickness of it should be no more than one quarter of the ultrasound wavelength²⁸. The thin plastic sheet used by C. Calderon et al., is assumed to have been thinner than one quarter of the ultrasound wavelength of 0.6 mm so that no energy loss occurred across the plastic sheet boundary between the ultrasound probe face and the sample tissue. A thin sheet of plastic like Saran Wrap can be used to hold a sample of media so that it won't come in direct contact with an ultrasound probe face or the face of an implantable medical device and still have no energy loss occur across that plastic sheet boundary. This negates an interface boundary loss in measurements.

An ultrasonic and inductive power delivery model was constructed in one study to determine the effects of different separation distances between the transmitter and receiver and different receiver sizes on power transfer efficiency¹². Power transfer efficiency is computed using the voltage source and output of the receiver. The ultrasonic power delivery method model consists of source piezoelectric material, a matching acoustic impedance layer, a tissue sample, another matching impedance layer, and a receiver piezo material. It is stated that the attenuation of ultrasound in human tissue (0.9 dB/cm*MHz) is more than two orders of magnitude higher than in water (0.002 dB/cm*MHz). From the model simulations, it is found that at small separation distances, the ultrasonic power delivery method has worse power transfer efficiency than inductive coupling, but at larger separation distances, or deeply implanted medical devices, the ultrasonic power delivery method outperforms inductive coupling. As a function of separation distance in ultrasonic power delivery from 1 cm to 10 cm with a receiver diameter of 10 mm, the power transfer efficiency decreases from approximately 40 % to 0.2 %. For inductive coupling, the power transfer efficiency decreases from approximately 80 % to 0.0015 %.

For a receiver diameter of 10 mm, the power transfer efficiency of the ultrasonic and inductive power delivery methods is the same at a separation distance of about 3 cm. When the receiver diameter is 5mm and the separation distance is 1 cm to 10 cm, the power transfer efficiency decreases from approximately 30 % to 0.15 % for the ultrasonic power delivery method. For inductive coupling, the power transfer efficiency decreases from approximately 40 % to 0.0008 %. For a receiver diameter of 5 mm, the power transfer efficiency of the ultrasonic and inductive power delivery methods is the same at a separation distance of about 1.4 cm. Although the power transfer decreases quickly as a function of separation distance for both explored methods, this model shows that the ultrasonic power delivery method is better than inductive coupling at larger separation distances (several cm) for smaller implants. The results of this simulation study were not confirmed experimentally.

A miniature ultrasonically powered wireless nerve cuff stimulator has been investigated to excite motor axons in the sciatic nerve of a rat hind limb inducing contraction of lower leg muscles³⁷. It is noted that some have reported a pitfall with ultrasonic transcutaneous energy transfer (UTET) in which precise angular alignment between the transmitting and receiving PZT elements is critically important to effectively transfer energy. To minimize this, the PZT receiver should be relatively small. The incident angle of the ultrasound beam becomes less influential as the dimensions of the receiver are reduced to half of the wavelength of the ultrasound in the medium. A custom-built ultrasound transmitter with a center frequency of 1 MHz and diameter of 26 mm was used in this study. The cylindrical receiver element was made from PZT-5A (1.13 mm diameter x 1 mm length) and in this material the wavelength of sound at 1 MHz is 4mm. Thus, the receiver element was constrained to 2mm in any dimension. A rectifying circuit with one diode (Schottky) and one capacitor (2.2 μ f) were used to convert the AC electrical signal generated by the piezoelectric effect from the mechanical vibrations of the PZT to a DC electrical signal for medical device applications. The Schottky diode was chosen for its low threshold forward voltage and small physical size. The cuff stimulator was designed to

lie parallel to a nerve bundle and thus the ultrasound beam would impact the cylindrical PZT perpendicular to its long axis. The cuff stimulator was tested at a distance of 12 cm to avoid complications with the acoustic near-field measurements and was connected to a 2.2 k Ω resistive load to simulate the in vivo load impedance of the cuff electrode when placed on the sciatic nerve. A rat was anesthetized and the stimulator cuff was placed in the hind leg and a tissue phantom of 8 cm thick bovine striated muscle (0.6 dB/cm/MHz) was positioned over the leg to simulate a more deeply rooted medical device in tissue. Ultrasound tone bursts of 100 micro seconds duration were delivered once a second (duty cycle of 1%) to correspond with cathodic pulses from the stimulator. In the in vivo study, the piezoelectric poling (3-axis) of one cylindrical PZT receiver was oriented axially along its length so that the ultrasound beam impacted it perpendicular to its long axis. In this orientation, it was found that the receiver gave relatively even power output (approximately 0.7 mA) regardless of device rotation (\pm 90 degrees) about the long axis because the ultrasound beam was impinging on the long side of the PZT cylindrical device and thus the poling axis of the PZT cylindrical device remained perpendicular to the ultrasound beam during rotation. Another stimulator was constructed with a poling direction oriented orthogonal to the cylindrical long axis so that at 0 degree rotation the ultrasound beam and the poling direction are parallel and it was found that as the stimulator rotated \pm 90 degrees, the DC current output dropped drastically from approximately 0.7 mA to 0.1 mA at both the -45 degree rotation angle and +45 degree rotation angle. At 0 and 90 degree rotation, the power output was about 0.7 ma. This shows that the alignment of an ultrasound beam with respect the PZT poling axis of an implanted device is crucial to the energy harvesting capability of that device which is difficult to achieve, because the implanted device is not visible from the surface of the medium. It is also found that as ultrasound intensity is increased, so does the DC current output of the device. It is recommended that if higher energy is needed, the power transfer can be improved with a boost in ultrasound intensity, proper

alignment between ultrasound beam and PZT poling axis, populate the implant with multiple PZT elements, and include efficient electrical components and rectifiers.

Another study investigated the effect of mutual orientation of PZT transmitter and receiver in a wireless implantable application using ultrasonic power³⁸. In this paper, a novel ultrasound-based method for powering a battery-free electrical implant was explored. The aim of the study was to find out how the distance between the transmitter and receiver affects power transmission efficiency and how the orientation of the transmitter and receiver affects the output. The ultrasonic transmitter (30 mm diameter) and receiver (25 mm diameter) made of PZT elements had a resonant frequency of 840 kHz. A signal generator and power amplifier were used to generate an ultrasonic wave, and an oscilloscope with a load circuit was used to monitor the power output of the receiver across a 50 Ω load resistance. As distance between the receiver and transmitter increased, power fluctuation reduced and power transfer efficiency steadily increased (21%-25%). The power depended heavily on location due to a standing wave. The power reached a maximum at every half wavelength and a minimum at a quarter wavelength after every maximum. The variation was \pm 60% from the average. As the receiver was turned from 0-15 degrees off orientation from the transmitter, the efficiency plummeted. At an angle of 5 degrees the efficiency was dropped to more than 90 % of the power value at no rotation angle (approximately 27 % to approximately 1 %). This behavior was consistent at a separation distance of 10 mm and 100 mm. As the receiver was moved sideways off alignment with the transmitter (\pm 30 mm), the power efficiency also dropped from approximately 35 % at 0 mm off to 0 % at approximately \pm 20 mm off, forming a gaussian shape. This behavior was also consistent at a separation distance of 10 mm and 100 mm. It was determined in this study that when the receiver face angles away from the transmitter face or when the receiver face is offset from the transmitter face, the power transfer efficiency drops rapidly.

One study explored ultrasonic powering for millimeter-scale implantable devices with specific emphasis on output power levels, efficiency, range, and omnidirectionality (angular alignment insensitivity) of a medical device³⁹. It claimed that due to large acoustic mismatch impedances between soft tissue and air, ultrasonic waves that are transmitted into the human body will reflect back into the body and allow for an increased power transfer efficiency and omnidirectionality with an implanted device. There are two factors that contribute to the omnidirectionality in an ultrasonic powering system; the optimal angular alignment between the incident sound wave and face of implantable device, and large acoustic impedance mismatch at the body tissue air boundary causes reflections of the ultrasound beam so that it stays in the body and has multiple chances to impact the implanted device before it fully attenuates. If the implantable device is omnidirectional, the ultrasound wave can hit the lateral sides and still generate power due to the piezoelectric constant. The input mechanical stress perpendicular to the poling direction of the PZT receiver (3,1) is about half of the mechanical stress parallel to the poling direction (3,3). In the experiment, PZT samples (2 x 2 x 2, 2 x 4 x 2, and 1 x 5 x 1 mm³) were prepared to study the geometric effect on directionality and power output levels. Another set of samples with the same dimensions were created with a thin layer of acrylic coating to reduce the rate at which lead leaches into the body. Two transmitters of two different thicknesses, 1 and 2 mm, and ultrasound frequencies, 2.3 and 1.15 MHz, were coated with impedance matching layers of iron oxide loaded epoxy (6.75 MRayl) and were placed on opposite sides of the testing tank facing towards each other. To ensure a minimum of intensity fluctuations with operation in the near-field region, the dimensions of the probes were chosen so that the far-field region started around 20 cm. A water tank was used in this experiment (50 x 30 x 30 cm²) with the two transmitters attached on the sides of the tank. The receiver was placed 20 cm from the transmitter surfaces with its output connected to an oscilloscope and the axial and transverse angles were adjusted with a manipulator. Two scenarios were tested, one with acoustic absorbing material lining the tank, and another with reflecting boundary

conditions to attempt to simulate boundary condition reflections for a human tissue to outside air interface. The faces of the cubes of PZT were impinged by an ultrasound beam and the poling direction of the PZT was orthogonal to the ultrasound beam direction. For the acoustic absorbing tank, it was found that as the uncoated PZT specimens rotated axially from 0 to 45 degrees, the normalized power dropped from 0.9 to approximately 0.3 for the 2 x 2 x 2 mm³ specimen, from 1 to approximately 0.25 for the 1 x 5 x 1 mm³ specimen, and from 0.9 to approximately 0.1 for the 2 x 4 x 2 mm³ specimen. By continuing to rotate axially from 45 to 90 degrees, all specimen returned to about 70-80 % of their approximate starting normalized power levels seen at 0 degrees axial rotation. The 2 x 2 x 2 mm³ specimen retained the most normalized power as it was axially rotated, because it is the most uniform (cube) and has great omnidirectionality. It is believed that the Poisson ratio helped compensate for the different loading directions by having a relatively constant receiving area throughout the rotation. The deformation was the same at the 0 and 90-degree rotations because of the cubic PZT geometry (omnidirectionality) because in both rotations a flat face of the cube was exposed to the impinging ultrasound wave. The cube was deformed less at the 45-degree rotation because the corner of the cube was facing the ultrasound beam which causes the impinging ultrasound beam to potentially reflect off the angled PZT faces which would reduce deformation. The other specimen had lower normalized power levels when rotated axially because their geometrical dimensions reduce their omnidirectionality. They had smaller surface areas exposed to the ultrasound beam as they were rotated. A similar behavior was observed in the coated PZT specimens and they all dropped to approximately 0.2 – 0.1 normalized power at 45 degrees axial rotation. When the uncoated specimen were rotated transversely in the absorbing tank from 0 to 50 degrees, the normalized power decreased from 1 to 0.4 for the 2 x 2 x 2 mm³ specimen, from 1 to approximately 0.1 for the 1 x 5 x 1 mm³ specimen, and from 1 to approximately 0.2 for the 2 x 4 x 2 mm³ specimen. A similar behavior was observed in the coated PZT specimens and they all dropped to approximately 0.2 – 0 normalized power at 50 degrees transverse

rotation. For the acoustic reflecting tank, it was found that all the uncoated and coated specimen geometries that were rotated axially from 0 to 90 degrees did not have any drop in normalized power. When these uncoated and coated specimen geometries were rotated transversely from 0 to 50 degrees, again little to no drop in normalized power was recorded. This confirms that the omnidirectionality of the specimen was due to reflections and scatterings in the water medium off the water to air acoustic impedance mismatching boundary. Power output of PZT is greatly affected by the relationship between the impinging force direction on the material and the poling axis and by the geometry of the material ²³. If the medium were tissue instead of water, there would be higher attenuation and as the specimen rotated axially and transversely there would be less normalized power. This acoustic reflecting scenario tested in this study is somewhat applicable to the human body in that there is a high impedance mismatch between the tissue ($1.5 \text{ kg/m}^2\cdot\text{s}$) and open air ($429 \text{ kg/m}^2\cdot\text{s}$) boundary layer so most of the incident ultrasound waves on this interface will be reflected back into the body. Also, the power output of the PZT specimen increased linearly with an increase in the ultrasound intensity. It is noted that the FDA limits imaging applications to an intensity of 720 mW/cm^2 to reduce the thermal and non-thermal bioeffects ^{40,41}. The thermal bioeffect is burning of tissue due to high absorption of ultrasonic waves, and the non-thermal bioeffect includes cavitation, rapid collapse of bubbles in acoustic wave propagation, which causes high pressures and temperatures at high ultrasound intensities that are applied for only a few seconds ⁴².

Chapter 2. Journal of Orthopaedic Research Paper (In Progress)

This section contains a manuscript formatted for submission to Journal of Orthopaedic Research (JOR).

2.1 Manuscript for Journal of Orthopaedic Research

Effect of Ultrasound Stimulation of Piezoelectric Composite with Compliant Layers on Power Output for Bone Healing

Kyle Coates¹, Xinmai Yang^{1,2}, Elizabeth A Friis^{1,2,3}

¹University of Kansas, Department of Mechanical Engineering, Lawrence, KS;

²University of Kansas, Bioengineering Graduate Program, Lawrence, KS;

³Evoke Medical LLC, Lawrence, KS

Corresponding Author:

Elizabeth A. Friis
Professor, Mechanical Engineering
University of Kansas
1530 W. 15th St., 3138 Learned Hall
Lawrence, KS 66045
lfriis@ku.edu
785-550-3725

Author Contributions Statement: Each author provided substantial contributions to either research design, data acquisition, analysis or interpretation of data, drafting and revising the paper, and have approved of the submitted version.

2.1.1 Abstract

Direct current (DC) electric stimulation has been shown to increase rates of tissue healing. In a pilot ovine study, piezoelectric composite spinal fusion implants subjected to normal body loading were shown to result in faster and more robust fusion. Methods of providing safe mechanical stimulation of the piezoelectric composite in non-weight-bearing patients are desirable. In this foundational study, standard medical ultrasound as a loading source was used to study the effect of varying compliant layer thicknesses in piezoelectric composites on generated electrical potential and power output in different mediums, medium thicknesses, and loading orientations. Compliant Layer Adaptive Composite Stacks (CLACS) were manufactured with through-thickness pre-poled PZT discs connected electrically in parallel, stacked mechanically in series and four different compliant layer thicknesses interposed. Standard ultrasound used for cardiovascular medical imaging was used as the loading source to mechanically stimulate the PZT elements. Voltage measurements were obtained using an oscilloscope and available power was calculated. Adding an interposed compliant layer between the PZT discs of the CLACS resulted in increased generated electrical potential and power output. As the compliant layer thickness increased, more deformation occurred along the face and edges of the PZT discs, resulting in significant increases in power output. There were also significant effects of varying media type and loading orientations, but little effect with varying media thickness. Future work could lead to a more efficient energy harvester that uses circuit logic to provide electrical stimulation for difficult-to-fuse spinal fusion patients.

2.1.2 Keywords

Bone < Biomaterials, Repair / Therapeutics < Bone Fracture, Mechanics < Spine

2.1.3 Introduction

Spinal fusion devices have up to 50% failure rates for patients who use tobacco or are diabetic ¹. Constant direct current (DC) electrical stimulation applied through a Titanium electrode has been proven to help increase spinal fusion rates, but the present implantable electrical stimulation devices for spinal fusion are powered by a battery ². The battery pack is implanted in the soft tissue around the spine, can be felt under the patient's skin, and eventually requires removal in a second surgery. Many microgenerators use piezoelectric (PZT) material to convert mechanical energy into electrical potential ³⁻¹¹. In a pilot ovine study, composite spinal interbody implants made with stacked layers of piezoelectric (PZT) fibers provided DC electrical stimulation in response to mechanical loading at the interbody site and substantially enhanced fusion under normal loading after six weeks as compared to a control ^{2,12,13}. To improve manufacturability while maintaining material toughness of the interbody implants, alternative manufacturing methods were explored to develop nontraditional piezoceramic composites. Compliant Layer Adaptive Composite Stacks (CLACS) were developed in which compliant layers of epoxy (EPO-TEK® 301) were inserted between serially stacked discs of PZT that were electrically wired in parallel. For patients with limited weight bearing abilities who cannot provide sufficient mechanical energy from human body movement, another method of in vivo mechanical stimulation the PZT discs inside the implant would be beneficial.

Several methods of wirelessly powering medical devices have been developed including electromagnetic waves, thermoelectric devices, inductive coupling and ultrasound. Transmitted ultrasound waves can be used to mechanically activate a medical device with PZT elements that has been implanted into human tissue ^{3-7,10,11}. In this foundational study on the use of a standard medical ultrasound signal as a mechanical loading source for materials used in piezoelectric

spinal fusion implants, the effect of varying compliant layer thicknesses in PZT composite materials on generated electrical potential and power in different media, media thicknesses, and loading orientations was examined.

2.1.4 Methods

Compliant Layer Adaptive Composite Stacks (CLACS) were manufactured with six through-thickness pre-poled PZT-SM111 discs (STEMiNC-0.4mm thickness, 10mm diameter, Part No. SMD10T04F5000S111, Doral, FL) that were connected electrically in parallel (EPO-TEK® H20E, Billerica, MA) with copper strips. Varying compliant layer thicknesses (0, 0.2, 0.4, and 0.8 mm ± 0.02 mm) of medical grade epoxy slices (EPO-TEK® 301, Billerica, MA) were placed in between the PZT discs. The CLACS were then encapsulated in the same type of medical grade epoxy to form specimens of equivalent external dimensions.

An Acuson 128xp/10 Ultrasound Imaging Machine with a V4 probe (128 PZT element phased vector array @ 4MHz, Mountain View, CA) was used as the loading source to mechanically stimulate the PZT elements in the CLACS. Voltage measurements were obtained using a Tektronix DPO 3034 Digital Phosphor Oscilloscope (300 MHz). The media tested were housed in an open plastic container with a rectangular bottom cutout. A plastic film layer (12µm) was placed on top of the media and another sealed the rectangular bottom cutout. Ultrasound PVC gel was placed between the plastic film layers and the ultrasound probe face and CLACS. The system and circuit used in testing are shown in Figures 1 and 2 respectively and the electrical component values of the circuit is shown in Table 1.

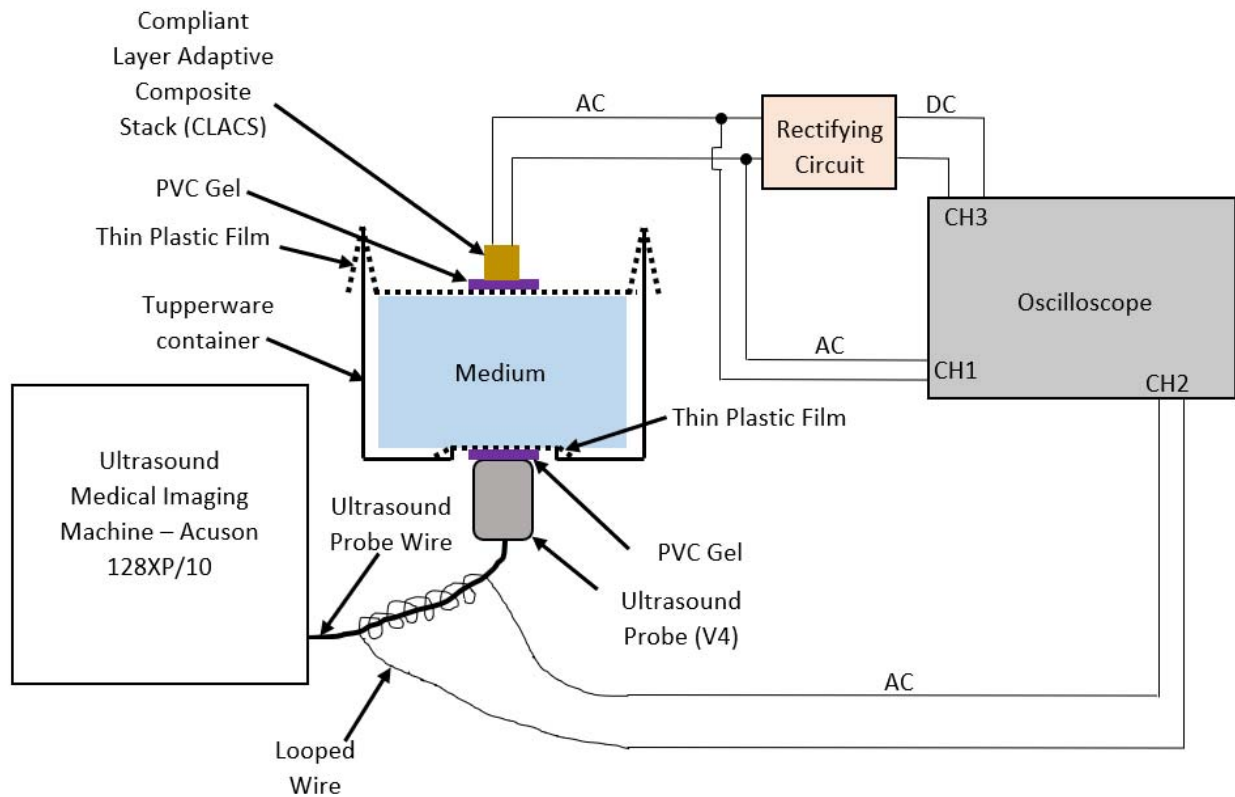


Figure 1 - Schematic of Ultrasound Testing System

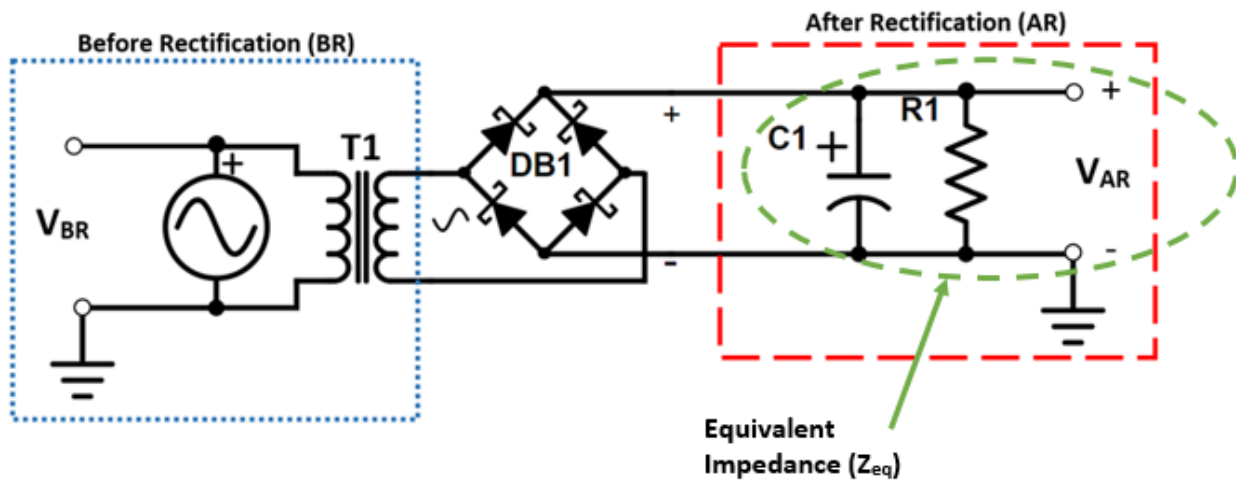


Figure 2 - Rectifying Circuit Diagram. Before rectification measurements are represented by V_{BR} , after rectification measurements are represented by V_{AR} , DB1 represents a full wave rectifier (4 diodes), C1 represents a polarized tantalum capacitor, R1 represents a variable load resistance and T1 represents a 1:1 turns isolation transformer. All values for these electrical components can be seen in Table 1.

Table 1 - Tabulated Values of Rectifying Circuit Components

Circuit Item Description	Value
R1 = Variable Load Resistance (R-C Box, iET Labs Inc. RC-500)	100 Ω – 10 M Ω
VBR = Before rectification measured voltage across Oscilloscope Channel 1 Resistance (Tektronix DPO 3034 Digital Phosphor Oscilloscope)	1 M Ω
VAR = After rectification measured voltage across Oscilloscope Channel 3 Resistance (Tektronix DPO 3034 Digital Phosphor Oscilloscope)	1 M Ω
T1 = High Frequency & High Efficiency Isolation Transformer (Audio Transformer – CyanKen E114)	1:1 \rightarrow (Primary coils = 800 turns, Secondary coils = 800 turns)
DB1 = Full Wave Bridge Rectifier – (4) Schottky Diodes, SEMTECH(ST) DO-35 1N60P 1N60 (Low forward voltage drop, low power consumption, & low noise)	Forward Voltage (each) = 0.2 V
C1 = Tantalum (Pearl) Polarized Capacitor	2.2 μ F
AC Source = Compliant Layer Medical Device – produces AC voltage from ultrasonic acoustic pressure waves	N/A
Ground = Oscilloscope Channel Ground \rightarrow earth	N/A

The CLACS were loaded with ultrasound through different combination of media, media thicknesses, and loading orientations. The three media tested were tap water, fresh bovine muscle tissue, and fresh bovine muscle tissue with dense cancellous bone interposed. The media thicknesses were 20mm and 40mm and the loading orientations were defined by how the ultrasound waves impacted the PZT disc faces in the CLACS (perpendicular or parallel). The specimens were subject to 4MHz ultrasound waves with 1 W (0 dB) of input power. The alternating current (AC) voltage response of the CLACS was observed on Channel 1 of the oscilloscope (Figure 3-a). The impedance of Channel 1 is assumed to be much larger than the internal resistance of the CLACS, therefore nearly all generated voltage is captured (open-circuit). Since the ultrasound machine excitation voltage used to generate sound waves is a

consistent repeating pattern (27 Hz), a looped wire around the ultrasound probe wire was used to capture the generated magnetic field from flowing current. Channel 2 on the oscilloscope was used to detect this magnetic field and its falling edge was used to trigger all Channel waveforms. The rectified direct current (DC) voltage was measured on Channel 3 of the oscilloscope (Figure 3-b).

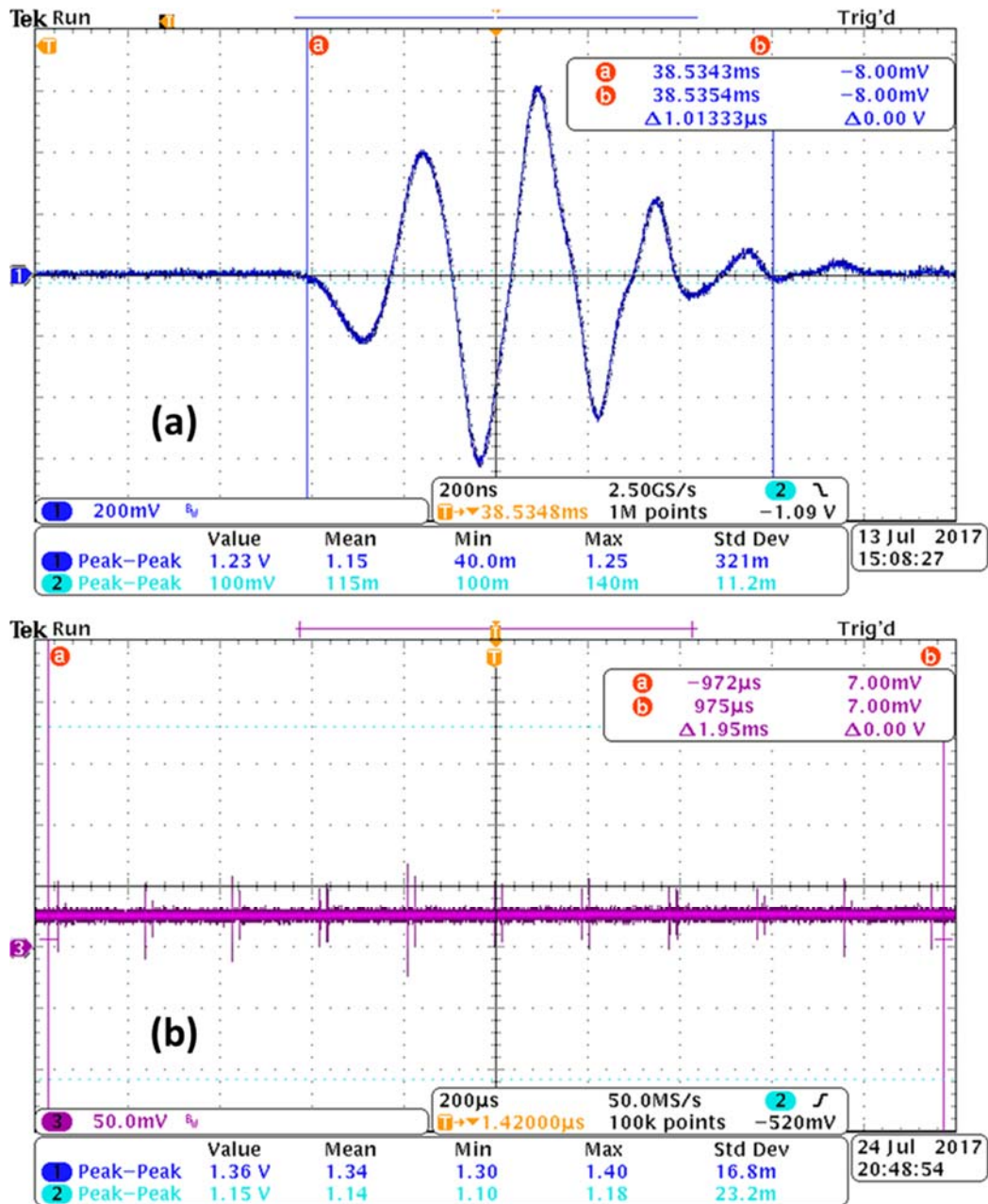


Figure 3 - Voltage signal before rectification (a) and after rectification (b)

Peak AC voltage measurements were obtained by differentiating the maximum and minimum values of the waveform and dividing by two. After rectification, DC voltage waveforms were filtered (Butterworth) to eliminate high frequency noise and then averaged. Electrical power was computed for the equivalent circuit impedance (Z_{eq}) and load resistance

(R1) by combining Joule's and Ohm's law for every resistance in the load resistance sweep (100Ω-10MΩ). During all measurements, the sampling rate was at least 10 times the frequency of the acoustic waves (4MHz) to prevent aliasing and to ensure that the full waveform was captured.

All significant differences presented were found after transforming non-normally distributed data using a Box-Cox transformation function in MATLAB to data that is approximately normal. The data was organized to allow comparison between compliant layer thickness groups (e.g. 0mm, 0.2mm, 0.4mm, and 0.8mm) within each testing parameter (e.g. water) and comparison between testing parameter groups (e.g. media-water, tissue, and tissue plus bone) within each compliant layer thickness (e.g. 0mm). If statistical significance was found using a one-way analysis of variance (ANOVA function in MATLAB), a Tukey-Kramer multiple pairwise comparison function in MATLAB was used to determine significant differences between groups ($p \leq 0.05$).

2.1.5 Results and Discussion

This foundational study was designed to test the influence of common medical ultrasound stimulation on the ability of a piezoelectric composite (CLACS) to produce power needed for electrical stimulation to aid in tissue healing. The power generation ability was tested through various media that could represent varying conditions of external mechanical stimulation for an implanted device. The voltage generated before rectification (AC) represents the maximum or ideal output to be modified by signal conditioning, because tissue healing applications require DC for electrical stimulation. The rectified voltage output (DC) represents a battery source that would be used to power another circuit over time to store and then apply pulsed DC electrical stimulation. These two outputs help characterize the CLACS with ultrasound loading and

provide output specifications needed for future design of implants that provide electrical stimulation for tissue healing.

2.1.5.1 Before Rectification

Average peak voltage as a function of media and compliant layer thickness at 20mm media thickness and perpendicular loading is shown in **Figure 4** (n=5). In water, the 0.2mm average peak voltage is significantly smaller than 0.8mm (*). In tissue plus bone, the average peak voltage for 0.4mm and 0.8mm are significantly greater than 0.2mm (+). Within all compliant layer groups, all media comparisons of average peak voltage are significantly different.

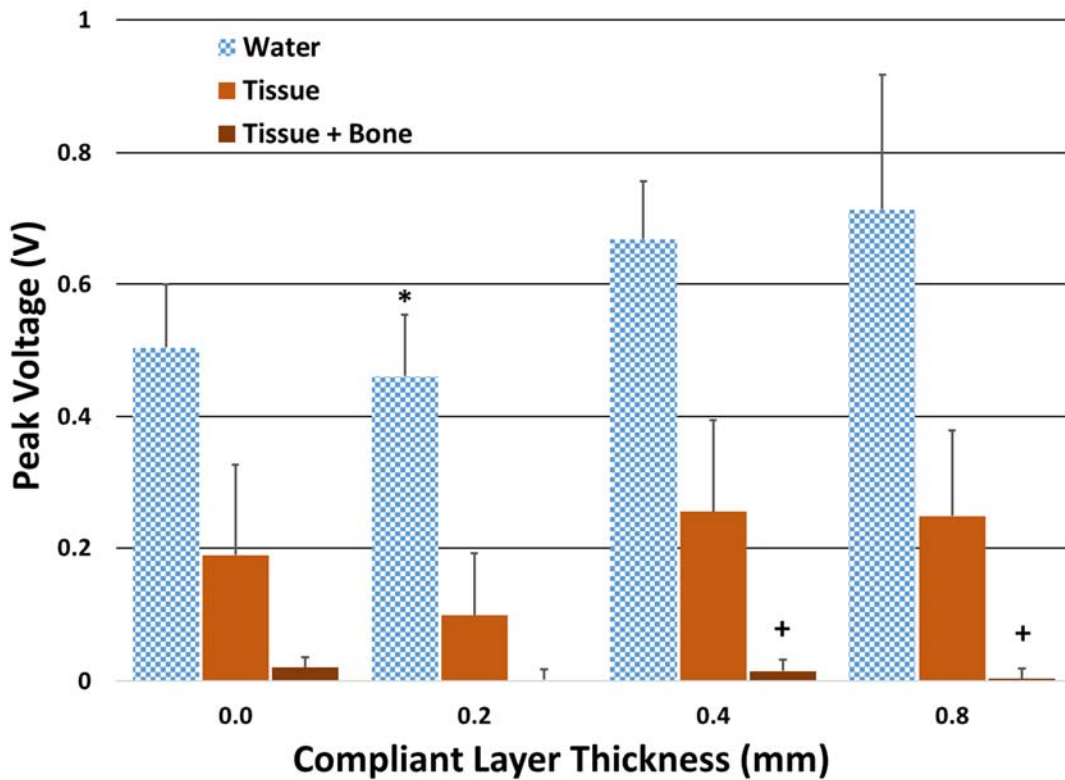


Figure 4 - Average peak voltage (n=5) as a function of media and compliant layer thickness at 20 mm media thickness for loading perpendicular to the PZT disc face. Within compliant layer groups all media comparisons are significantly different. In water: * represents significant difference from 0.8mm. In tissue plus bone: + represents significant difference from 0.2mm. (p<.05 Box-Cox Transformation)

The water media had the highest average peak voltage for all compliant layers and the tissue plus bone media had the lowest in Figure 4. Across all compliant layers in water media at 20mm media thickness and perpendicular loading, the tissue and tissue plus bone media yielded 67% and 98% less average peak voltage respectively. This reduction in average peak voltage might be caused by boundary layer acoustic impedance and surface area mismatching and ultrasound attenuation in the media ¹⁴. The attenuation coefficient of water ($\sim 0.008\text{dB/cm @ 4MHz}$) is much smaller than that of tissue ($\sim 2.4\text{-}6\text{dB/cm @ 4MHz}$) and bone ($2\text{-}15\text{dB/cm*MHz}$) so there is large effect on average peak voltage with different media ^{6,15,16}. The two thicker CLACS yielded higher average peak voltages than the two thinner CLACS in water and tissue media. However, in tissue plus bone media, the 0mm group had the highest average peak voltage followed by the 0.4mm, 0.8mm, and 0.2mm groups in descending order. This behavior trend may have been caused by an outlier in the 0mm samples that pushed the average peak voltage above the 0.4mm and 0.8mm groups and may be different with a larger sample size. The effect of compliant layers on average peak voltage is evident in water and tissue media.

Average peak voltage as a function of media thickness and compliant layer thickness in water with perpendicular loading is shown in **Figure 5** (n=5). At 20mm media thickness, the 0.2mm average peak voltage is significantly smaller than the 0.8mm (*). Within the 0.4mm group, the 20mm media thickness average peak voltage is significantly higher than 40mm (+).

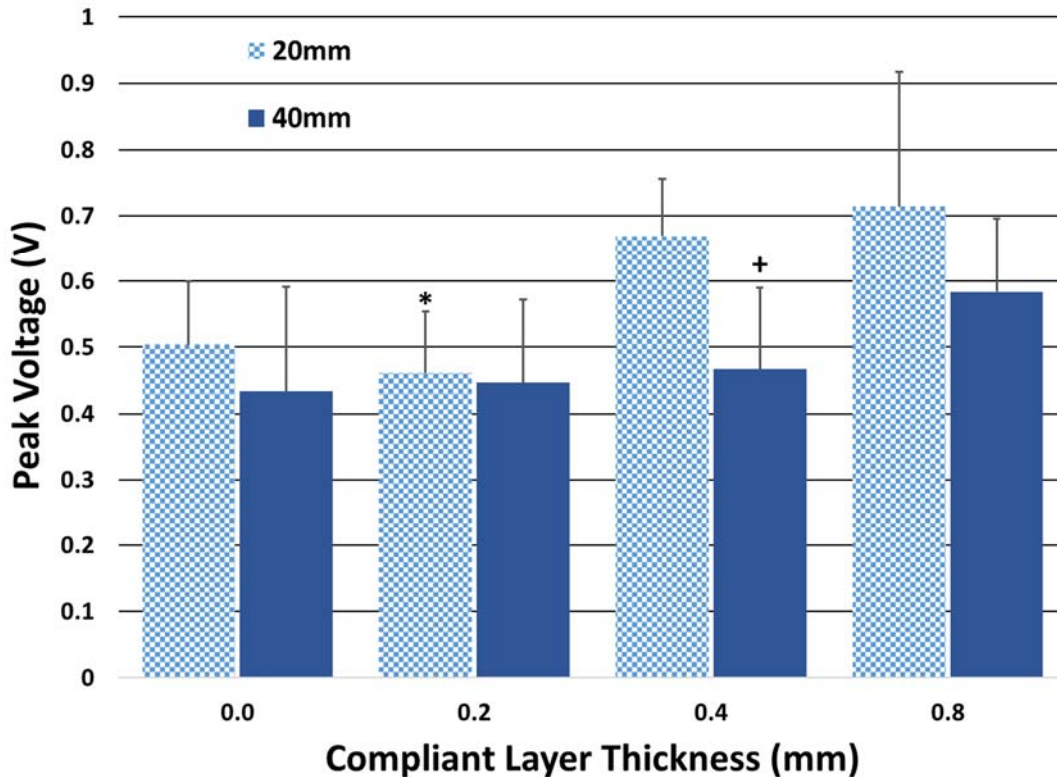


Figure 5 - Average peak voltage output ($n=5$) as a function of media thickness and compliant layer thickness in water media for loading perpendicular to the PZT disc face. At 20mm media thickness: * represents significant difference from 0.8mm. In 0.4mm: + represents significant difference from 20mm. ($p < .05$ Box-Cox Transformation)

In Figure 5, the 20mm media thickness in water media and perpendicular loading for CLACS had the highest average peak voltage. The two thicker CLACS yielded higher average peak voltages than the two thinner CLACS for both media thicknesses. When the media thickness doubled, the peak voltage decreased by an average of 26% across all CLACS. This behavior is most likely caused by ultrasound attenuation because with increasing media thickness the ultrasonic wave will attenuate more decreasing its pressure amplitude¹⁷. Because the attenuation coefficient of water is small, there is little effect on average peak voltage in doubling the water media thickness (Figure 5)¹⁸. In addition, the pressure amplitude of the ultrasonic wave will decrease due to acoustic impedance and surface area mismatching boundaries. If a material

thickness is much less than the wavelength of the ultrasonic wave, it becomes transparent for ultrasound propagation. Thus, it is assumed that the pressure amplitude does not decrease as it passes through thin PVC gel and plastic film (~12.5 μm) layers used in this study to separate the ultrasound probe face from touching the media and the media from touching the CLACS¹⁹.

Figure 6 shows average peak voltage as a function of loading orientation and compliant layer thickness in water at 20mm media thickness (n=5). In the perpendicular loading orientation, the 0.2mm average peak voltage is significantly smaller than 0.8mm (*). Within all compliant layer groups, all loading orientation comparisons of average peak voltage outputs are significantly different.

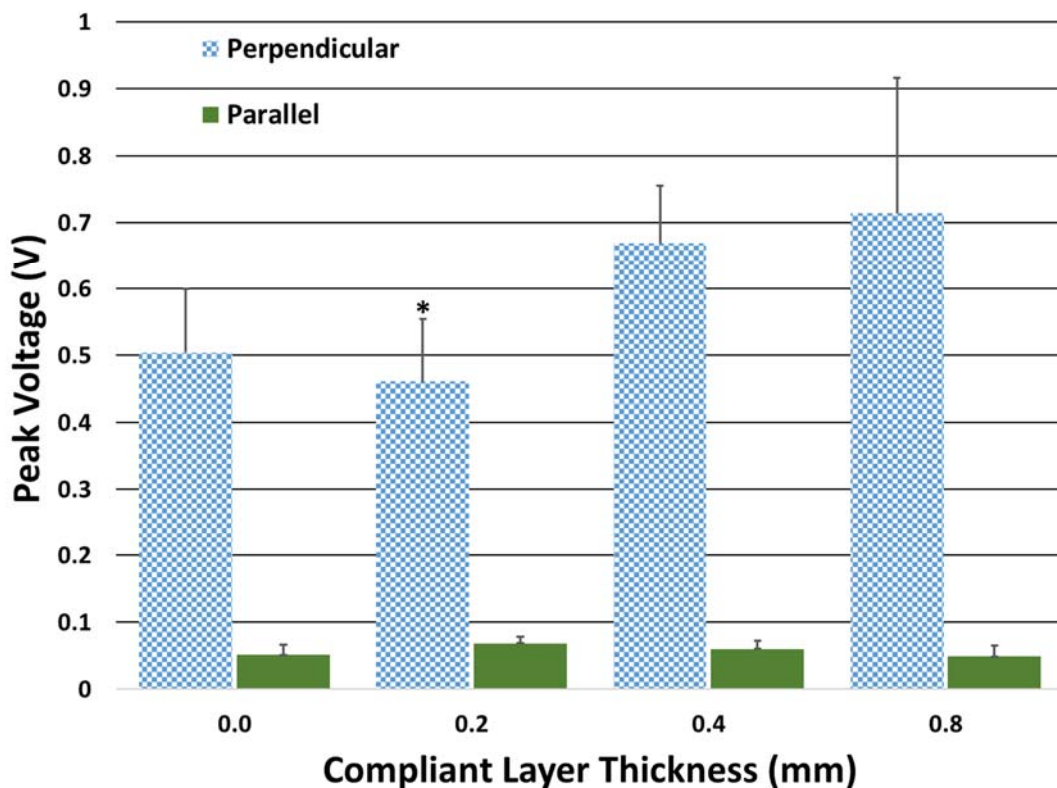


Figure 6 - Average peak voltage output (n=5) as a function of loading orientation and compliant layer thickness in water media at 20mm media thickness. Within compliant layer groups all loading orientation

*comparisons are significantly different. Perpendicular: * represents significant difference from 0.8mm. (p<.05 Box-Cox Transformation)*

The perpendicular loading orientation had the highest average peak voltage for CLACS in water at 20mm media thickness in Figure 6. The two thicker CLACS yielded higher average peak voltages than the two thinner CLACS in the perpendicular loading orientation. In the parallel loading orientation however, the 0.2mm group had the higher average peak voltage followed by the 0.4mm, 0mm and 0.8mm groups in descending order. This behavior trend may have been caused by an outlier in the 0.2mm samples that pushed the average voltage output above both the 0.4mm and 0.8mm compliant layers and may be different with a larger sample size. The average peak voltage across all the CLACS dropped by an average of 89% from perpendicular to parallel loading. In the perpendicular loading orientation, the ultrasonic wave is impacting the PZT disc faces (33 mode) and deformation is occurring along the through-thickness poling direction which is expected to produce more electrical potential ²⁰.

The thicker CLACS produced more electrical potential than the thinner CLACS before rectification. There is an effect of adding a compliant layer in between the PZT discs on generated electrical potential (AC). This allows for more generated electrical potential to be rectified, stored, and then used to produce electrical stimulation to induce bone growth for spinal fusion applications.

2.1.5.2 After Rectification

In the rectification circuit, the impedance of the capacitor and oscilloscope are constant, and the load resistance is varied. The load resistance values were chosen to represent the lumped electrical impedance of another circuit that would perform pulsed DC electrical stimulation logic

for spinal fusion applications. This circuit would store energy (DC) over time and release the stored energy in sequence with the cyclic mechanical loading felt in the lumbar spine while walking. Since the capacitor has lower impedance than the Oscilloscope and smallest load resistance, and all three are connected in parallel (Figure 2), the equivalent impedance is smaller than the component with the smallest impedance (capacitor). As the load resistance increases, the equivalent impedance approaches the impedance value of the capacitor. In this study, the equivalent impedance is essentially constant for all load resistances.

Average total power as a function of load resistance and compliant layer thickness after rectification in water media at 20mm media thickness and loading perpendicular to the PZT face is shown in **Figure 7** (n=5). For the last four resistances of the load resistance sweep (500K Ω – 10M Ω), the 0.8mm and 0.4mm groups are significantly larger than the 0mm and 0.2mm groups (p<.05 Box-Cox Transformation).

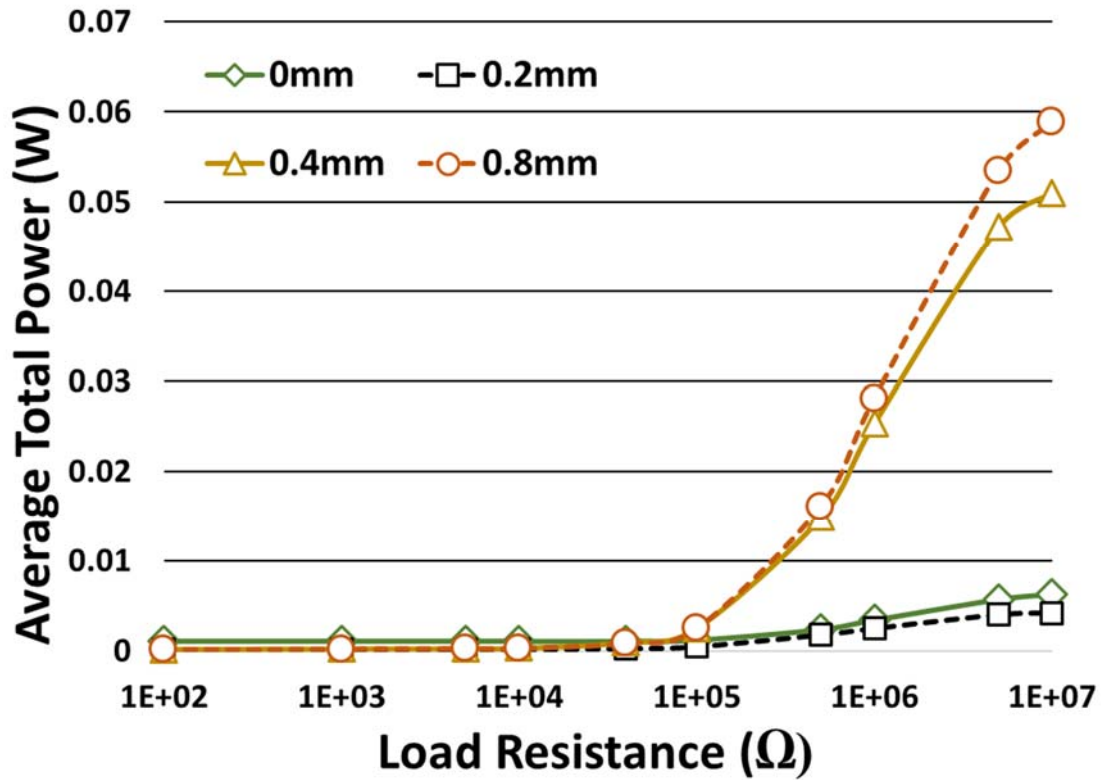


Figure 7 - Average Total Power (W) as a function of Load Resistance (Ω) and compliant layer thickness at 20mm media thickness and loading perpendicular to the PZT disc face in water media after rectification ($n=5$). For the last four resistances of the load resistance sweep (500K Ω – 10M Ω), the 0.8mm and 0.4mm compliant layer groups are significantly larger than the 0 and 0.2mm groups and the 0.8mm and 0.4mm compliant layer groups are not significantly different compared to each other as well as the 0mm and 0.2mm groups ($p<.05$ Box-Cox Transformation). Error bars excluded for visual clarity.

The total power of all the CLACS increases as load resistance increases (Figure 7). The thicker CLACS generate significantly more total power at higher load resistances (500K Ω to 10M Ω) than the thinner CLACS (BoxCox Transformation $p<0.05$). The 0.8mm and 0.4mm CLACS power curves rapidly increase from 100K Ω to 5M Ω and then begin to plateau at 10M Ω . The 0.2mm and 0mm CLACS total power curves behave similarly to the 0.8mm and 0.4mm CLACS total power curves, but at a smaller scale ($\sim 1/10$). From the mechanical vibrations of the ultrasonic waves, the PZT discs deform and convert that mechanical energy into electrical potential. In addition, the compliant layers allow for more deformation to occur along the face

and edges of the PZT discs which is more deformation than if it were a monolithic chunk of PZT. With thicker compliant layers, this effect increases because in addition to deformation that occurs in the center of the disc from ultrasonic waves, the thicker compliant layers are stiffer and allow the edges of the PZT discs to deform more than the thinner compliant layers. Since compliant layers allow the PZT in the CLACS to experience higher displacements and strains, there is an increase in electrical potential before rectification and thus an increase in power after rectification because more mechanical energy is converted into electrical potential²⁰. In conjunction with the compliant layer design, the electrical components used in the rectification circuit also affected the total power of the CLACS. Four diodes were used to rectify or convert the generated AC voltage from the CLACS to DC voltage in a full wave rectifier configuration (Figure 2). Diodes have a unique voltage and current relationship such that they need a certain amount of “forward voltage” in order for larger magnitudes of current to flow through them. The diodes used in this study needed at least 0.2V of forward voltage each in order for larger amounts of current to flow through them. A slightly higher forward voltage than 0.2V would yield an exponentially increasing current that flows through the diode²¹. However, if the forward voltage was below 0.2V, some but little current would pass through the diode because in the 0-0.2V forward voltage range, the current would gradually increase with an increasing input forward voltage, but not exponentially. Since a full wave rectifier configuration was used in this study, at any given time whether the current was traveling in one direction through the circuit or alternated and traveled in the other direction, it needed to pass through two diodes and thus a 0.4V forward voltage was required for larger amounts of current to pass through towards the equivalent parallel circuit components. With forward voltages higher than 0.4V, an exponential increase in current would pass across the diodes and more current would then flow to the

equivalent parallel circuit components allowing more voltage to be measured after rectification. With forward voltages around 0.4V, less voltage would be measured after rectification. Before rectification for all testing parameter combinations in the parallel loading orientation and in the tissue and tissue plus bone media, the AC peak voltage samples measured were less than 0.4V. For the 0mm and 0.2mm CLACS in water media, loading in the perpendicular loading orientation, and at a 20mm media thickness, the average AC peak voltages before rectification hovered around 0.4V. This means barely enough meaningful current passed through the diodes towards the equivalent parallel circuit components for voltage to be measured. Only 31 out of the 240 total combinations tested (3 media x 2 media thicknesses x 2 loading orientations x 20 CLACS samples) had AC peak voltages of 0.4V or higher. As the load resistance increased, there was a small and gradual increase in voltage and therefore power, but not a significant amount because the forward voltage was only around 0.4V (Figure 7). On the other hand, the 0.4mm and 0.8mm CLACS AC average peak voltages in the same parameter configuration before rectification were higher than 0.4V, so a larger amount of current was passing through the diodes. Because the forward voltage was higher than 0.4V, as the load resistance increased, there was a larger increase in voltage measured and therefore a more exponential increase in power (Figure 7). The addition of a compliant layer in conjunction with this diode behavior had an effect on total power output of the CLACS.

Total power curves for the tissue and tissue plus bone media at 20mm media thickness and perpendicular loading orientation are extremely small compared to the water media total power curve. The values of these tissue and tissue plus bone total power curves are consistent across the load resistance sweep for all CLACS because little electrical potential was produced

and only some current passed through the rectification circuit diodes, thus little voltage was measured. The total power curve in the water media displayed the same behavior described previously for total power in Figure 7 for all CLACS. The total power curves for the thinner CLACS in water media have a smaller magnitude but similar behavior to the thicker CLACS. Therefore, enough forward voltage was generated by all CLACS in the water media and a thicker compliant layer yielded an increase in total power. Average power reduction between water and tissue is 89%, 91%, 96%, and 98% for the 0mm, 0.2mm, 0.4mm, and 0.8mm CLACS respectively for 500K Ω -10M Ω . Between water and tissue plus bone there is an 80%, 89%, 98%, and 99% average power reduction for the 0mm, 0.2mm, 0.4mm, and 0.8mm CLACS respectively for 500K Ω -10M Ω . In two studies, one showed a %60 reduction in power between water and pig tissue media, and the other presented a 99% reduction in power between water and bone plus PVC gel ^{4,5}.

Figure 8 shows average total power as a function of load resistance (Ω) and media thickness in water media and loading perpendicular to the PZT face. For the 0.4mm compliant layer thickness (c), there is a significant difference between the 20mm and 40mm distances for the 40K Ω -10M Ω load resistances and the remaining load resistances are not significantly different ($p < .05$ Box-Cox Transformation). For the remaining compliant layer types, there is no significant difference between the 20mm and 40mm media thicknesses across all load resistances ($p < .05$ Box-Cox Transformation).

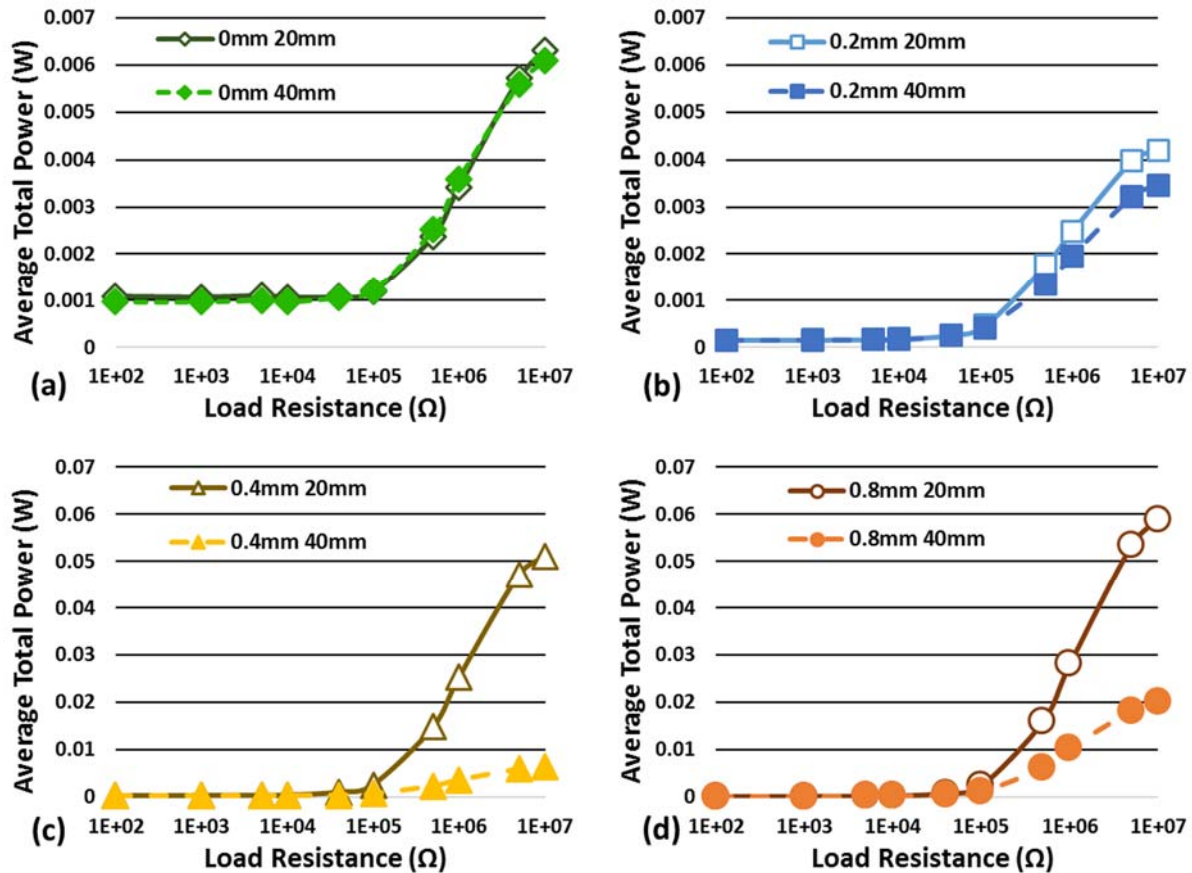


Figure 8 - Average total power (W) as a function of load resistance (Ω) and media thickness in water media and loading perpendicular to the PZT face ($n=5$). (a) represents 0mm, (b) represents 0.2mm, (c) represents 0.4mm and (d) represents 0.8mm compliant layer media thickness comparisons. Note that (a,b) is on a scale that is 1/10th of (c,d). Error bars excluded for visual clarity.

In Figure 8, the 20mm and 40mm thickness total power curves for the thinner CLACS in water media at the perpendicular loading orientation were essentially the same, but the thicker CLACS total power curves had significant differences between the 20mm media thickness across the higher end of the load resistance sweep ($500K\Omega$ - $10M\Omega$) ($p < .05$ Box-Cox Transformation). For the 0mm and 0.2mm CLACS, the 20mm and 40mm thickness total power curves did not differ and both behaved similarly across the load resistance sweep (Figure 8.a & b). This behavior for the thinner CLACS total power curves in Figure 8 is also seen in Figure 5 where an increase in water media thickness yielded a small change in AC peak voltage. With little change in AC peak

voltage, there is little change in DC voltage after rectification. Attenuation in media will cause the ultrasound wave pressure amplitude to decrease. However, the attenuation coefficient in water is low, so an increase in water media thickness will not affect the generation of electrical potential (AC peak voltage) in the CLACS and thus DC voltage will not be affected. The 20mm thickness total power curve increased more quickly than the 40mm total power curve for the thicker CLACS because with the effect of a compliant layer, more power is produced (Figure 8.c and d). At the higher end of the load resistance sweep (500K Ω -10M Ω), average power reduction between 20mm and 40mm media thicknesses in water is 3%, 20%, 86%, and 64% for the 0mm, 0.2mm, 0.4mm, and 0.8mm CLACS respectively. The average power reduction percentages are higher for the thicker CLACS than the thinner CLACS because with the effect of a compliant layer more electrical potential (AC peak voltage) is generated and thus more power is produced. In one study, 7% power reduction from 5mm to 15mm water thickness was observed⁵. The thinner CLACS have a smaller magnitude but similar behavior to the thicker CLACS (Figure 8.a and b). An increasing compliant layer thickness yields higher total power for both media thicknesses across all load resistances.

The parallel loading orientation of the total power curve for all CLACS as a function of load resistance and loading orientation in water media at 20mm media thickness is extremely small compared to the perpendicular loading orientation and is consistent across the load resistance sweep for all CLACS. At the higher end of the load resistance sweep (500K Ω -10M Ω), there is an average power reduction of 76%, 86%, 99%, and 99% for the 0mm, 0.2mm, 0.4mm and 0.8mm CLACS respectively from the perpendicular to parallel loading orientations. Since the PZT discs are through thickness poled, the perpendicular loading orientation means

that the poling axis is in the same direction as the impinging ultrasound beam and in the parallel loading orientation the poling axis is perpendicular to the ultrasound beam. In Larson et. al, ultrasound was loaded onto the long side of two cylindrical PZT devices used for neural stimulation and during testing they were rotated about their long axes. For the first device, the poling axis of the cylindrical PZT was in the same direction as the propagating ultrasound beam and as the device was rotated about the cylindrical long axis, there was a 90% power reduction at 45-degrees rotation and roughly 0% reduction at 90-degrees rotation. For the second device, the poling axis of the cylindrical PZT was along the long axis of the cylinder and there was essentially no power reduction as the device was rotated²². In Song et. al, the face of a cube of PZT was impacted by an ultrasound beam orthogonal to the poling direction of the¹⁶. There was a 90% reduction in power with 45-degree rotation of the poling axis and roughly 0% reduction at 90-degree rotation. The deformation was the same at the 0 and 90-degree rotations because of the cubic PZT geometry (omnidirectionality) and in both rotations a flat face of the cube was exposed to the incoming ultrasound wave. The cube was deformed less at the 45-degree rotation while the corner of the cube was facing the ultrasound beam. Arra et. al had a 90% reduction with a 15 degree rotation of a receiving PZT face off a transmitting PZT face⁷.

The deformation of the through thickness poled PZT discs was greater when the ultrasound wave front impacted the face of the discs (parallel to the poling axis) than when impacting the thickness of the discs (perpendicular to the poling axis). Because the thickness of the PZT discs is small compared to the diameter in the parallel loading orientation, the ultrasound wave is attempting to deform a “rod-like structure”. Due to this inconvenient geometry, less deformation occurs under loading (less deformation=less power). In the perpendicular loading orientation however, the ultrasound wave is attempting to deform a “plate”

which has a more favorable geometry for deformation to occur under loading (disc diameter >> disc thickness). Power output of PZT is greatly affected by the geometry of the material and by the relationship between the direction of deformation in the PZT due to mechanical loading and the poling direction of the PZT²⁰. The total power curve in the perpendicular loading orientation displayed similar behavior described previously for the total power in Figure 7 for all CLACS. The thinner CLACS in the perpendicular loading orientation, have a smaller total power magnitude but similar behavior to the thicker CLACS. Therefore, enough forward voltage was generated by all the CLACS in the perpendicular loading orientation and a thicker compliant layer yields an increase in total power. The average power production in the perpendicular direction is larger for the thicker CLACS than the thinner CLACS because with the effect of a compliant layer more deformation occurs along the entire face and edges of the PZT disc and thus more power is generated.

Average load resistance power as a function of load resistance and compliant layer thickness after rectification in water media at 20mm media thickness and loading perpendicular to the PZT face is shown in **Figure 9** (n=5). For the last four load resistances (500K Ω – 10M Ω), the 0.8mm and 0.4mm groups are significantly larger than the 0mm and 0.2mm groups (p<.05 Box-Cox Transformation).

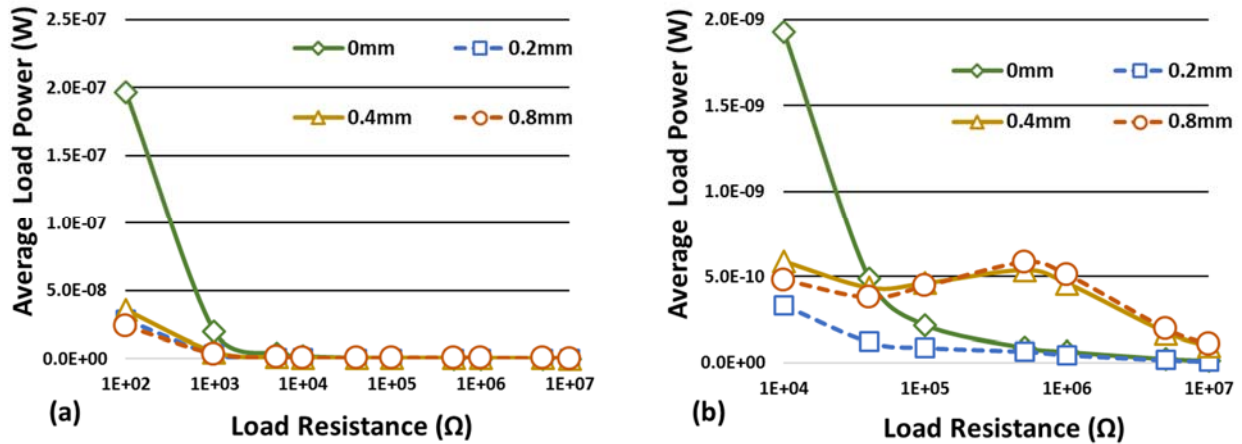


Figure 9 - Average Load Resistance Power (W) as a function of Load Resistance (Ω) and compliant layer thickness at 20mm media thickness and loading perpendicular to the PZT disc face in water media after rectification ($n=5$). (a) represents the average load resistance power across the whole resistance sweep. (b) represents the average load resistance power across the higher end of the resistance sweep (10K Ω – 10M Ω). For the last four resistances of the load resistance sweep (500K Ω – 10M Ω), the 0.8mm and 0.4mm compliant layer groups are significantly larger than the 0 and 0.2mm groups and the 0.8mm and 0.4mm compliant layer groups are not significantly different compared to each other as well as the 0mm and 0.2mm groups ($p < .05$ Box-Cox Transformation). Error bars excluded for visual clarity.

Power across the load resistance behaves differently than total power across the equivalent impedance of the rectification circuit. In Figure 9.a, the load resistance power in water media at 20mm and perpendicular loading orientation for all CLACS appears to exponentially decrease as load resistance increases. The load resistance power of the 0mm CLACS at 100 Ω appears larger than the other CLACS, but is not significantly different ($p < .05$ Box-Cox Transformation). In Figure 9.b at the 40K Ω load resistance for the thicker CLACS, the load power curve begins to increase because the squared DC voltage increases faster than the load resistance. At 500K Ω , the load power curve peaks for the thicker CLACS and after begins to decrease because the load resistance value begins to increase more quickly than the squared DC voltage. This behavior at 500K Ω load resistance may have been caused by electrical impedance matching in the circuit. If there is impedance mismatch between electrical components in the circuit, then some electrical

energy gets reflected and is essentially lost. To help minimize this all components of a circuit need to have similar electrical impedances⁷. The 500K Ω load resistance may be an impedance match to the rest of the circuit causing a peak in power, but is only evident in the thicker compliant layers.

2.1.6 Conclusion

By adding a compliant layer thickness in between the PZT discs of the CLACS, generated electrical potential and power output increased. As the compliant layer thickness increased there were significant increases in power output due to more deformation that occurred along the entire face and edges of the PZT discs. Also, there were significant effects of varying media type and loading orientations, but little effect with varying media thickness. Future work could build off this foundational study to further characterize the CLACS power output behavior. These future studies would include focused vs. unfocused ultrasound loading sources, differing operating frequencies to match and mismatch the resonant frequency of the PZT discs, testing more varied loading orientations, differing ultrasound intensity levels, using a combination of radially and through-thickness poled PZT discs, designing circuit components to improve electrical energy transfer efficiency and implementing pulsed DC circuit logic after rectification to approach a more realistic application of DC electrical stimulation in tissue healing. After conducting these future studies, a more efficient energy harvester that is powered by ultrasound and uses electrical stimulation for hard-to-heal patients in spinal fusion applications could be achieved.

2.1.7 Acknowledgements

This study was supported by the NIH grant R44AR070088. We thank Ember Krech for manufacturing specimens tested in this study

2.1.8 References

1. Kucharzyk DW. 1999. A Controlled Prospective Outcome Study of Implantable Electrical Stimulation With Spinal Instrumentation in a High-Risk Spinal Fusion Population: *Spine* 24(5):465–468.
2. Goetzinger NC, Tobaben EJ, Domann JP, et al. 2016. Composite piezoelectric spinal fusion implant: Effects of stacked generators. *J. Biomed. Mater. Res.* 104(1):158–164.
3. Wei X, Liu J. 2008. Power sources and electrical recharging strategies for implantable medical devices. *Frontiers of Energy and Power Engineering in China* 2(1):1–13.
4. Cochran GVB, Kadaba MP, Palmieri VR. 1988. External ultrasound can generate microampere direct currents in vivo from implanted piezoelectric materials. *J. Orthop. Res.* 6(1):145–147.
5. Ozeri S, Shmilovitz D. 2010. Ultrasonic transcutaneous energy transfer for powering implanted devices. *Ultrasonics* 50(6):556–566.
6. Denisov A, Yeatman E. 2010. Ultrasonic vs. Inductive Power Delivery for Miniature Biomedical Implants. In: 2010 International Conference on Body Sensor Networks. p 84–89.
7. Arra S, Leskinen J, Heikkila J, Vanhala J. 2007. Ultrasonic Power and Data Link for Wireless Implantable Applications. *IEEE* [cited 2017 Nov 13] Available from: <http://ieeexplore.ieee.org/document/4147127/>.
8. Martins M, Correia V, Cabral JM, et al. 2012. Optimization of piezoelectric ultrasound emitter transducers for underwater communications. *Sensors and Actuators A: Physical* 184:141–148.
9. Lee SQ, Youm W, Hwang G. 2013. Biocompatible wireless power transferring based on ultrasonic resonance devices. *Proceedings of Meetings on Acoustics* 19(1):030030.

10. Charthad J, Weber MJ, Chang TC, Arbabian A. 2015. A mm-Sized Implantable Medical Device (IMD) With Ultrasonic Power Transfer and a Hybrid Bi-Directional Data Link. *IEEE Journal of Solid-State Circuits* 50(8):1741–1753.
11. Mazzilli F, Lafon C, Dehollain C. 2014. A 10.5 cm Ultrasound Link for Deep Implanted Medical Devices. *IEEE Transactions on Biomedical Circuits and Systems* 8(5):738–750.
12. Tobaben EJ, Goetzinger NC, Domann JP, et al. 2015. Stacked macro fiber piezoelectric composite generator for a spinal fusion implant. *Smart Mater. Struct.* 24(1):017002.
13. Friis, Elizabeth A, Galvis, Sarah N, Cadel, Eileen, Sis, Hadley L, Wong, Benjamin M, and Arnold, Paul M, "DC Stimulation for Spinal Fusion with a Piezoelectric Composite Material Interbody Implant: A Pilot Ovine Study," Society For Biomaterials, Charlotte, NC. Transactions of the 2015 Society For Biomaterials Meeting: (April 15, 2015 - April 17, 2015).
14. Christensen DB, Roundy S. 2016. Ultrasonically powered piezoelectric generators for bio-implantable sensors: Plate versus diaphragm. *Journal of Intelligent Material Systems and Structures* 27(8):1092–1105.
15. Hoskins PR, Martin K, Thrush A. 2010. *Diagnostic Ultrasound: Physics and Equipment*. Cambridge, UNKNOWN: Cambridge University Press. [cited 2017 Dec 5] Available from: <http://ebookcentral.proquest.com/lib/ku/detail.action?docID=534730>.
16. Song SH, Kim A, Ziaie B. 2015. Omnidirectional Ultrasonic Powering for Millimeter-Scale Implantable Devices. *IEEE Transactions on Biomedical Engineering* 62(11):2717–2723.
17. Smith NB, Webb A. 2010. *Introduction to Medical Imaging: Physics, Engineering and Clinical Applications*. Cambridge University Press. 299 p.
18. White SM. 2005. *Diagnostic Ultrasound: Physics and Equipment*. *European Journal of Anaesthesiology* 22(9):734.
19. Calderon C, Vilkomerson D, Mezrich R, et al. 1976. Differences in the attenuation of ultrasound by normal, benign, and malignant breast tissue. *J. Clin. Ultrasound* 4(4):249–254.
20. Anton SR, Sodano HA. 2007. A review of power harvesting using piezoelectric materials (2003–2006). *Smart Mater. Struct.* 16(3):R1.
21. [date unknown]. 1N60P pdf, 1N60P description, 1N60P datasheets, 1N60P view ::: ALLDATASHEET ::: [cited 2017 Dec 7] Available from: http://pdf1.alldatasheet.com/datasheet-pdf/view/281737/SEMTECH_ELEC/1N60P.html.
22. Larson PJ, Towe BC. 2011. Miniature ultrasonically powered wireless nerve cuff stimulator. *IEEE*. p 265–268 [cited 2017 Nov 13] Available from: <http://ieeexplore.ieee.org/document/5910538/>.

2.2 Additional Figures and Information

This section contains additional figures and figure captions not used to present results in the manuscript because of the Journal word count limit. These figures are for after rectification total power and load resistance power results that show the effect of a compliant layer, media type, media thickness, and loading orientation across a resistant sweep for the equivalent impedance after rectification and for the load resistance.

2.2.1 After Rectification Total Power Figures

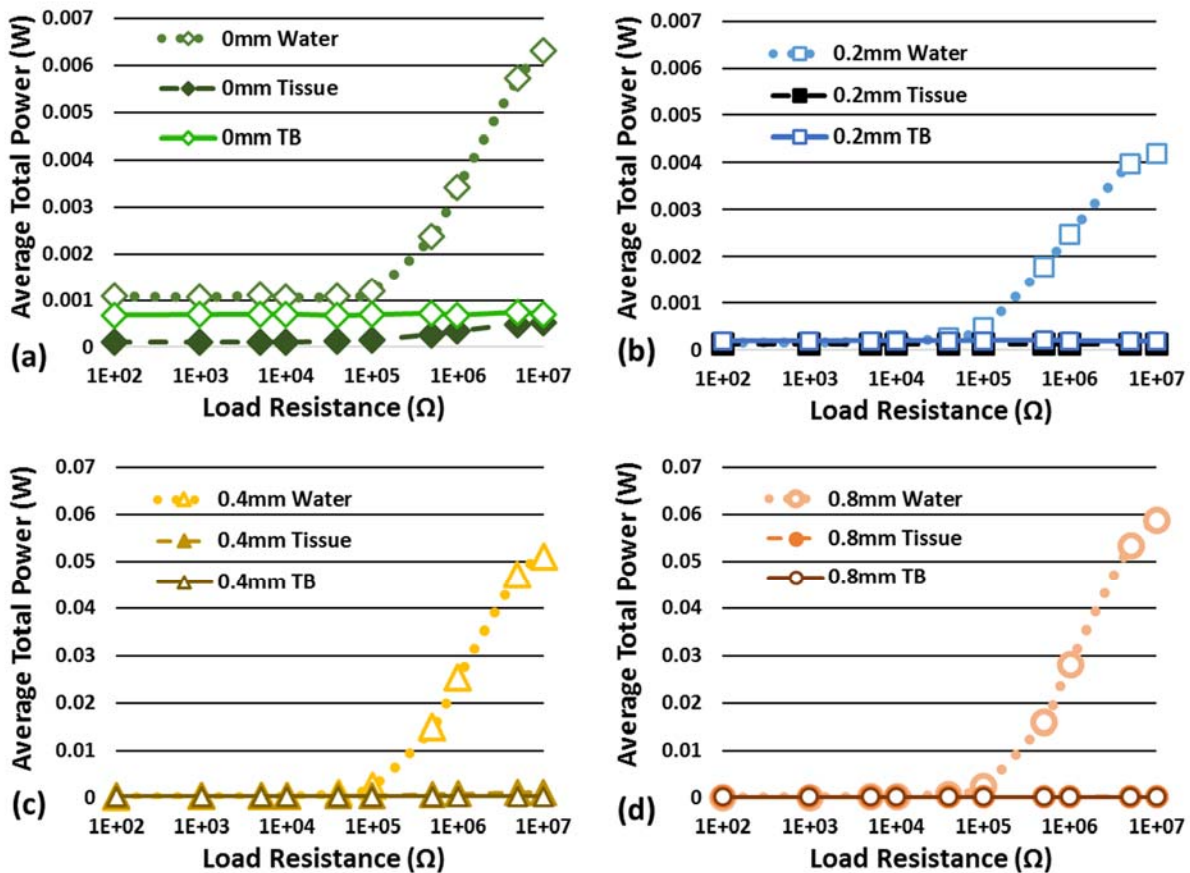


Figure 10 - Average total power (W) as a function of load resistance (Ω) and media at 20mm media thickness and loading perpendicular to the PZT disc face ($n=5$). (a) represents 0mm, (b) represents 0.2mm, (c) represents 0.4mm and (d) represents 0.8mm compliant layer media comparisons. Note that (a,b) is on a scale that is 1/10th of (c,d). Error bars excluded for visual clarity.

Figure 10 shows average total power as a function of load resistance and media at 20mm media thickness and loading perpendicular to the PZT disc face (n=5). For 0.2mm (b), there is a significant difference between all media types for the 100Ω load resistance, and the last four load resistances (500KΩ-10MΩ). For the remaining load resistances (1KΩ-100KΩ) there is a significant difference between the water and tissue media and the tissue and tissue plus bone media. For 0.4mm (c), there is a significant difference between the water and tissue media and the water and tissue plus bone media for the 40KΩ-100KΩ load resistances and for the 500KΩ-10MΩ load resistances there is a significant difference between all media types. For 0.8mm (d), there is a significant difference between all media types for the 10KΩ and last four load resistances (500KΩ-10MΩ). For the 100Ω and the 40KΩ-100KΩ load resistances there is a significant difference between water and tissue media and water and tissue plus bone media. For the 5KΩ load resistance the water and tissue plus bone media are significantly different ($p < .05$ Box-Cox Transformation).

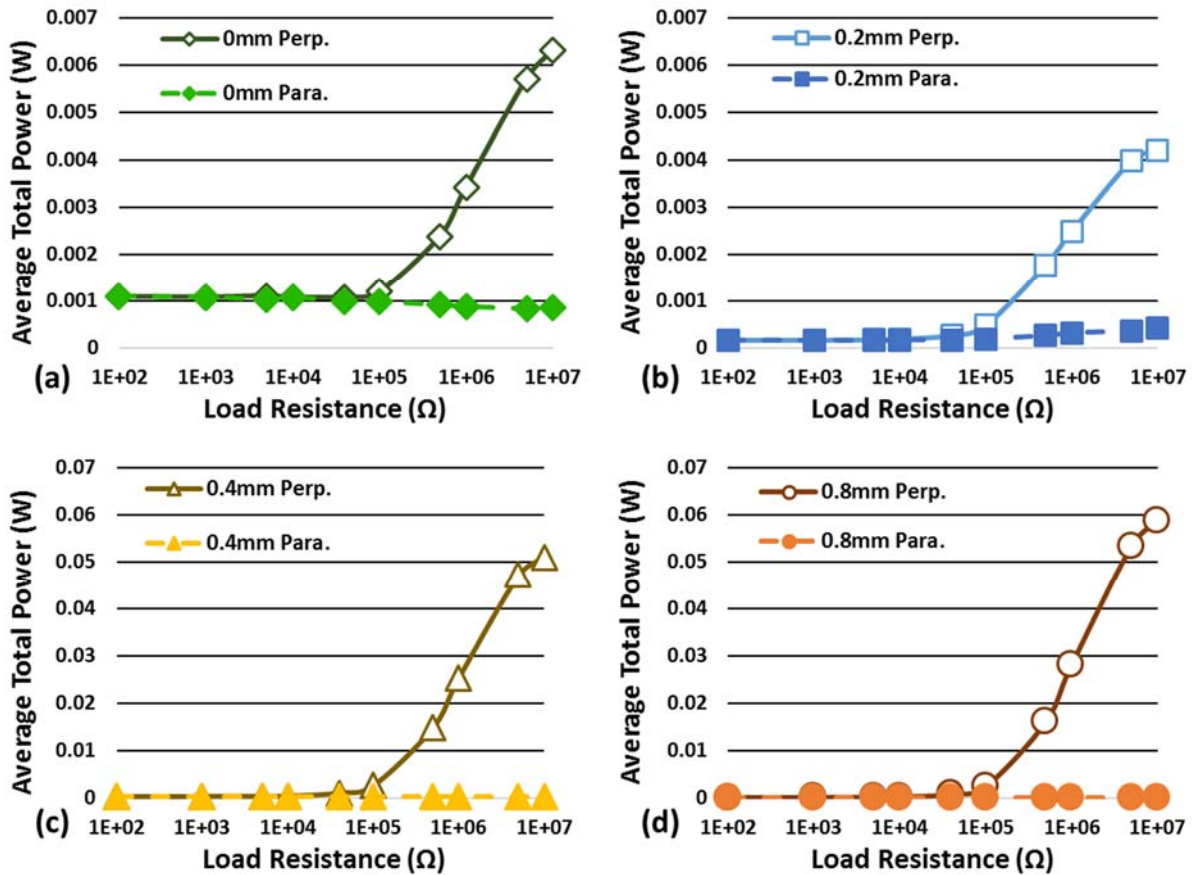


Figure 11 - Average total power (W) as a function of load resistance (Ω) and loading orientation in water media at 20mm media thickness ($n=5$). (a) represents 0mm, (b) represents 0.2mm, (c) represents 0.4mm and (d) represents 0.8mm compliant layer loading orientation comparisons. Note that (a,b) is on a scale that is 1/10th of (c,d). Error bars excluded for visual clarity.

Figure 11 shows average total power as a function of load resistance (Ω) and loading orientation in water media at 20mm media thickness. For the 0.4mm compliant layer type (c), there is a significant difference between the loading orientations for the 40K Ω -10M Ω load resistances. For the 0.8mm compliant layer type (d), there is a significant difference between the loading orientations across the entire load resistance sweep. For the 0mm and 0.2mm compliant layers there is no significant difference between the loading orientations across the entire load resistance sweep ($p < .05$ Box-Cox Transformation).

2.2.2 After Rectification Load Power Figures

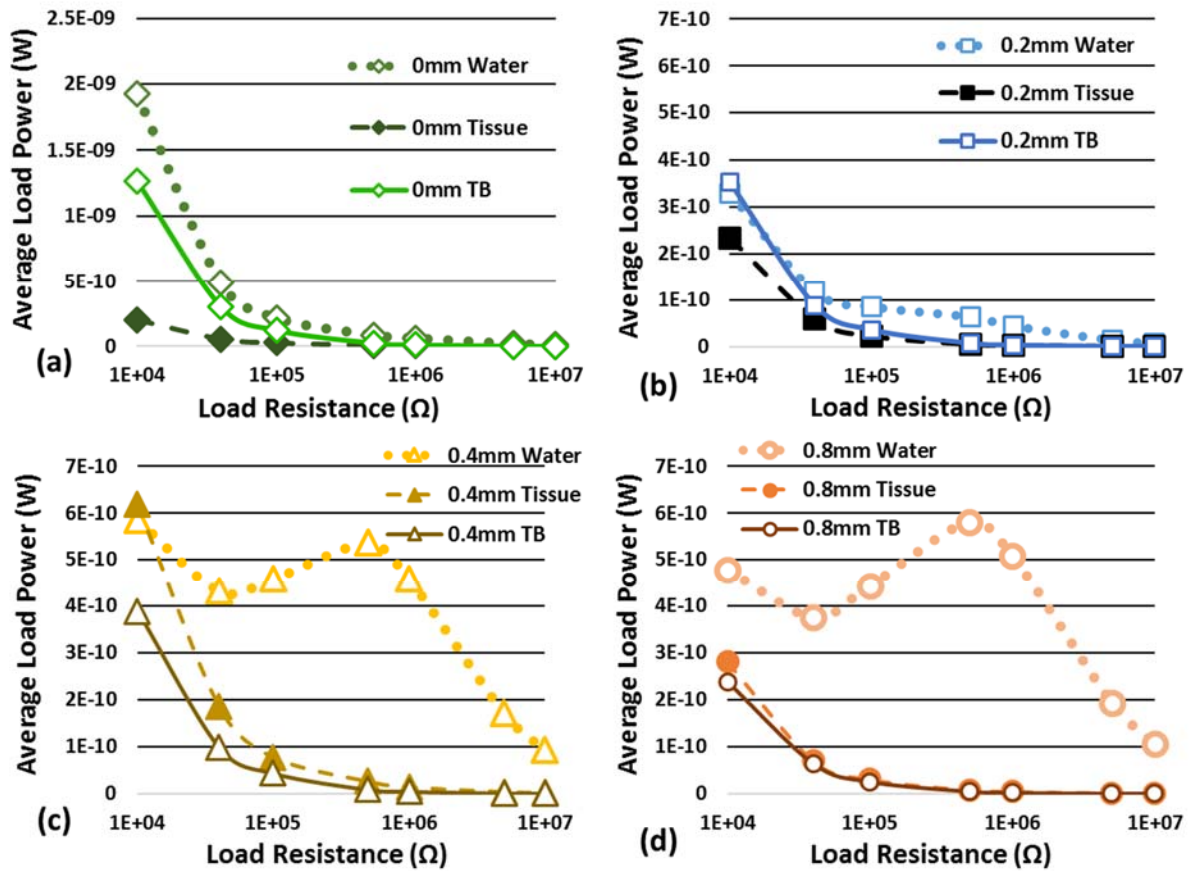


Figure 12 - Average load resistance power (W) as a function of load resistance (Ω) and media at 20mm media thickness and loading perpendicular to the PZT disc face ($n=5$). (a) represents 0mm, (b) represents 0.2mm, (c) represents 0.4mm and (d) represents 0.8mm compliant layer media comparisons. Note that (b,c,d) are on a scale that is a magnitude less than (a). Error bars excluded for visual clarity.

Figure 12 shows average load resistance power (W) as a function of load resistance (Ω) and media at 20mm media thickness and loading perpendicular to the PZT disc face. The same significant difference behavior between the media types for the average total power in Figure 10 is also exhibited in Figure 12 ($p < .05$ Box-Cox Transformation).

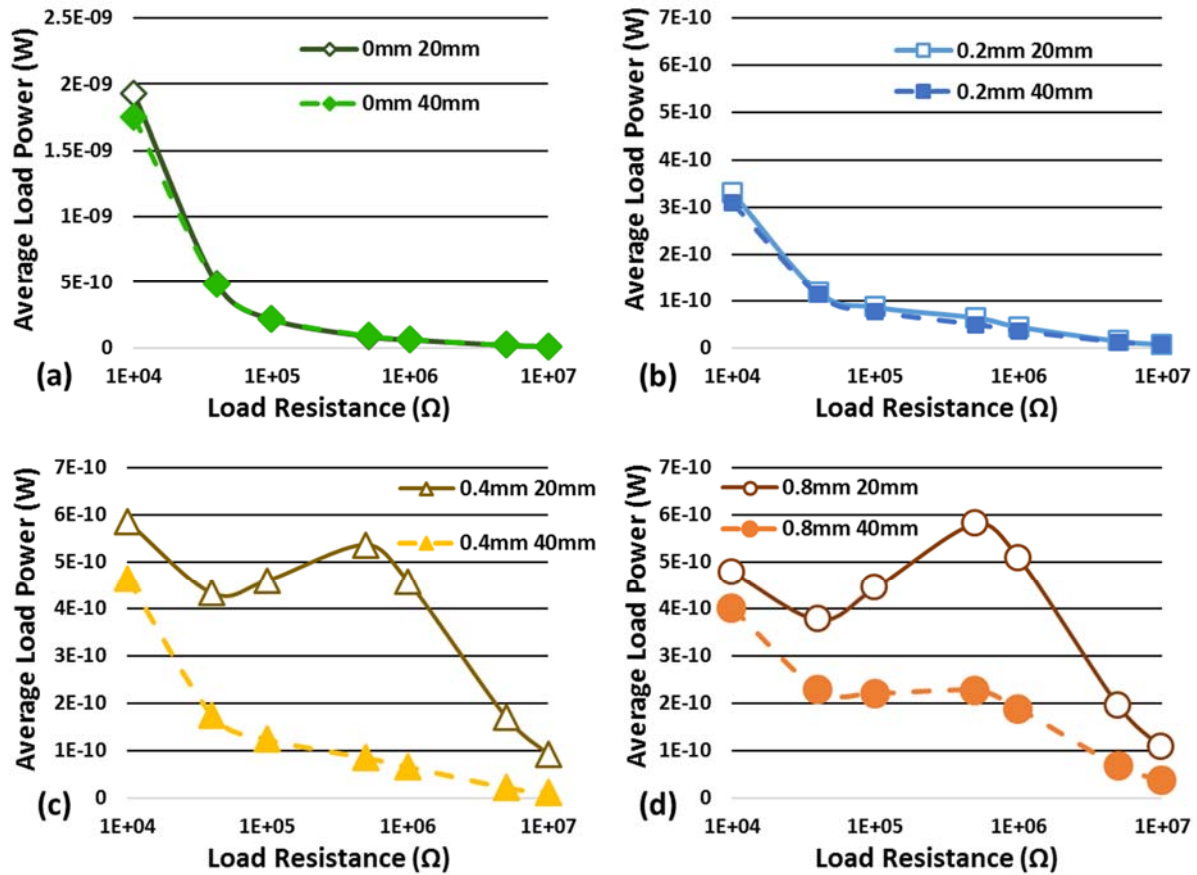


Figure 13 - Average load resistance power (W) as a function of load resistance (Ω) and media thickness in water media and loading perpendicular to the PZT face ($n=5$). (a) represents 0mm, (b) represents 0.2mm, (c) represents 0.4mm and (d) represents 0.8mm compliant layer distance comparisons. Note that (b,c,d) are on a scale that is a magnitude less than (a). Error bars excluded for visual clarity.

Figure 13 shows average load power (W) as a function of load resistance (Ω) and distance in water media and loading perpendicular to the PZT face. The same significant difference behavior between the 20mm and 40mm distances for the average total power in Figure 8 is also shown in Figure 13 ($p < .05$ Box-Cox Transformation).

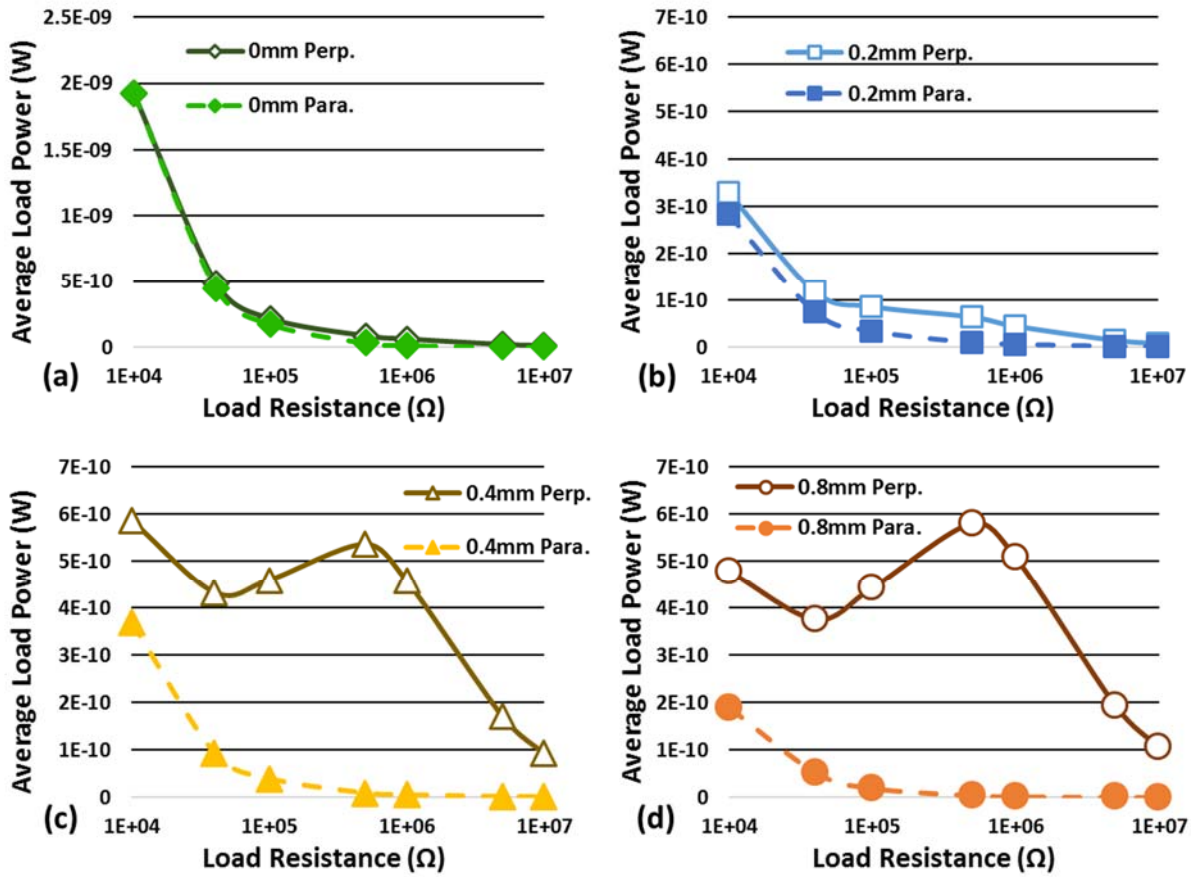


Figure 14 - Average load resistance power (W) as a function of load resistance (Ω) and loading orientation in water media at 20mm media thickness ($n=5$). (a) represents 0mm, (b) represents 0.2mm, (c) represents 0.4mm and (d) represents 0.8mm compliant layer loading orientation comparisons. Note that (b,c,d) are on a scale that is a magnitude less than (a). Error bars excluded for visual clarity.

Figure 14 shows average load resistance power (W) as a function of load resistance (Ω) and loading orientation in water media at 20mm distance. The same significant difference behavior between the loading orientations for the average total power in Figure 11 is also shown in Figure 14 ($p < .05$ Box-Cox Transformation).

2.2.3 Capacitor and Oscilloscope Power Curves

Power curves across the capacitor and oscilloscope lumped internal impedance were not presented in this study. The distribution of the total power across the three electrical components in parallel were computed. The maximum percentage amount of the total power consumed by the capacitor was 99.999998 % and the minimum percent power amount consumed was 99.9663367 %. In every combination of CLACS, media type, media thickness, loading orientation, and load resistance value the capacitor consumed almost all the available power after rectification. This makes sense, because the capacitor has a much lower impedance than the oscilloscope lumped impedance and lowest load resistance value and since current will take the path of least resistance, most of the current traveled across the capacitor. Since the capacitor essentially consumed most of the total power after rectification, the behavior of a power curve for the capacitor would be extremely similar to the total power curve. Since the oscilloscope lumped impedance did not change during testing and the equivalent impedance was essentially constant during testing, the behavior of a power curve for the oscilloscope lumped impedance would be extremely similar to the total power curves presented in this study but magnitudes lower. The maximum percentage amount of the total power consumed by the oscilloscope lumped internal impedance was 0.00000203200 % and the minimum percentage power amount consumed was 0.00000169788 %. Lastly, the maximum percentage amount of the total power consumed by the load resistance was 0.03366140549 % and the minimum percentage power amount consumed was 0.00000018098 %. These maximum and minimum percentages of total power consumed were computed using Excel “max” and “min” functions.

Chapter 3. Detailed Methods

Using medical imaging ultrasound to mechanically load piezoelectric composite discs in a compliant layer adaptive composite stack (CLACS), the effect of varying compliant layer thicknesses on generated electrical potential (V) and power output (W) was studied through various mediums (3 – water, tissue, and tissue plus bone), media thicknesses or distance between the ultrasound probe face and CLACS (20mm, 40mm), and loading orientations that the ultrasonic waves impact the face of the PZT discs in the CLACS (perpendicular, parallel). This chapter explains the manufacturing process of the CLACS, the experimental setup, and methods used to collect and analyze data in this foundational study.

3.1 Manufacturing of Spinal Fusion Devices with varying Compliant Layers

The manufacturing methods of the CLACS were produced by Ember Krech, a PhD graduate student in the spine biomechanics lab at the University of Kansas. All manufacturing steps and the manufacturing of the CLACS was done by Ember Krech. These manufacturing methods were documented by Ember Krech in a spine biomechanics lab protocol document and a summary of these methods is discussed in this section.

Six through thickness pre-poled PZT discs that are 10mm in diameter and 0.4mm thick (STEMiNC, Part No. SMD10T04F5000S111, Doral, FL) were used in each of the CLACS. First, the PZT disc poling direction needed to be checked and this was done with a voltmeter and an aluminum metal sheet. The voltmeter was set to the DC voltage setting and the PZT disc bottom electrode was placed on an aluminum sheet. One of the voltmeter leads was gently placed on top of the disc and the other on the aluminum sheet. The manufacturer proceeded by exhaling and creating a “puff” of air over the disc to create a small deviation in pressure in air that would impact the disc. This small deviation in pressure would deform the PZT disc slightly and this deformation or mechanical energy would be converted into electrical potential. While exhaling, a voltage was read off the voltmeter and if the voltage was positive

and the black lead of the voltmeter was touching the top of the disc, then a mark was made on top of the disc to indicate that it is the positive side (Figure 24).

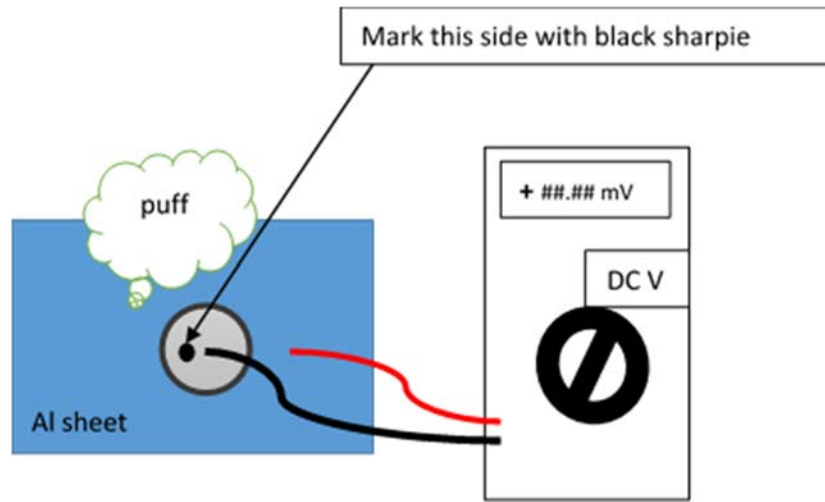


Figure 24 - Testing the poling direction of a PZT disc (Ember Krech Compliant Layer Thickness Study Protocol – used with permission)

If the voltage was negative and the black lead of the voltmeter was touching the top of the disc, then a mark was made on the bottom of the disc to indicate that it is the positive side. This was done for all PZT discs before further manufacturing procedures were followed. Two cut copper strips of 6-8 inches long, 1/16 inches thick and 1/4 inches wide were straightened and then cleaned with rubbing alcohol. A silicone sheet with holes punched in them, a plain silicone sheet, and a piece of Delrin were used to help electrically connect the PZT discs in parallel and these were also cleaned with rubbing alcohol. One of the copper strips was placed between the two silicone sheets that are on top of the piece Delrin and tape was used to secure the copper strip on the ends touching the Delrin. (Figure 25).

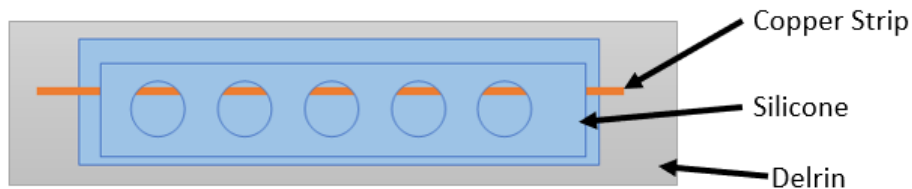


Figure 25 - Placing a copper strip in between two silicone sheets on a piece of Delrin (Ember Krech Compliant Layer Thickness Study Protocol – used with permission)

Enough conductive epoxy (EPO-TEK® H20E, Billerica, MA) was spread on the copper strip within the bounds of each hole cutout of the top silicone sheet to ensure that the PZT discs would adhere to the copper strip, but also not too much was applied so that epoxy would get on the edges of the hole cutout (Figure 26).

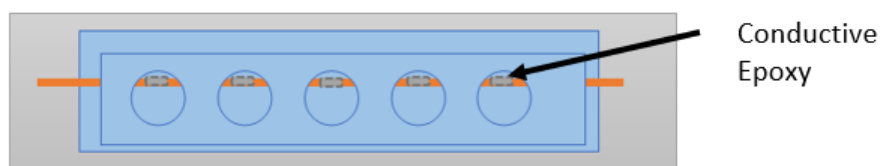


Figure 26 - Placing conductive epoxy (EPO-TEK® H20E, Billerica, MA) on the copper strip within the hole cutouts (Ember Krech Compliant Layer Thickness Study Protocol – used with permission)

If the epoxy would get on the edges of the hole cutout, the PZT disc top and bottom face could then be electrically connected. This would ruin the production and electrical function of the PZT discs in the CLACS. The PZT discs were then carefully placed inside the hole cutouts onto the conductive epoxy and it was made sure that all the marked sides of the discs from the poling direction part of the protocol were facing up. Because of the large size of the hole cutouts compared to the PZT disc diameter, the discs were able to be placed in-line with each other on the copper strip (Figure 27).

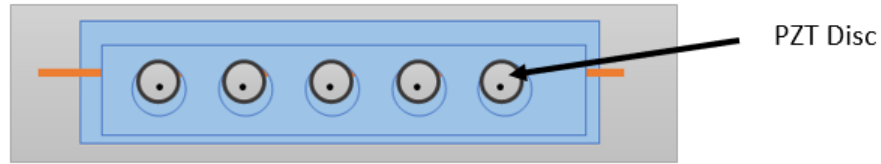


Figure 27 - Placing PZT discs in hole cutouts (Ember Krech Compliant Layer Thickness Study Protocol – used with permission)

Tweezers were gently used to lightly press on the PZT discs to help them adhere to the conductive epoxy. Next, some conductive epoxy was applied on top of the PZT discs again with enough for proper adhering, but not too much so that conductive epoxy does not get on the edges of the hole cutouts. The second copper strip was then placed on top of the conductive epoxy on top of the PZT discs in a straight line (Figure 28).

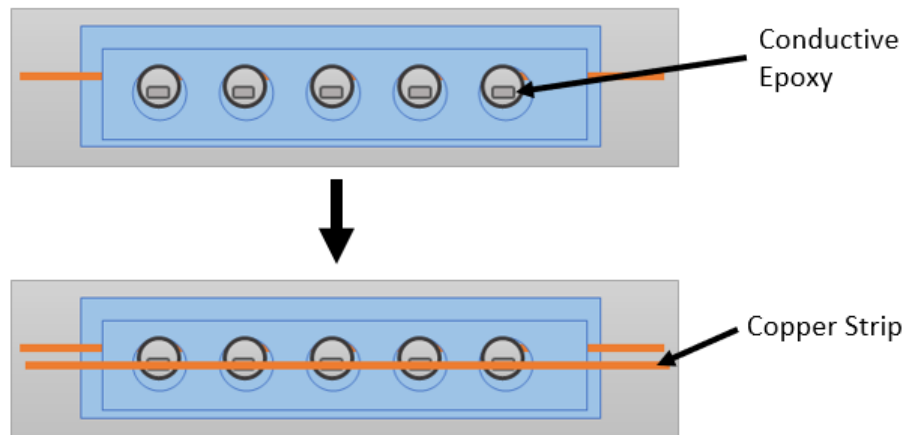


Figure 28 - Placing conductive epoxy on top of PZT discs and placing copper strip on top of conductive epoxy (Ember Krech Compliant Layer Thickness Study Protocol – used with permission)

Silicone circles were then placed on top of the hole cutouts and then a weight that covers the whole assembly was placed on top of the whole assembly. The assembly was then air cured for 24 hours and then cured in an oven at 100°C for 2 hours. After curing, the assembly was tested for electrical connections by using a voltmeter on the resistance setting. When the leads of the voltmeter were placed on the copper strips the and overload resistance was measured indicating that there was no electrical connection between the copper discs (Figure 29).

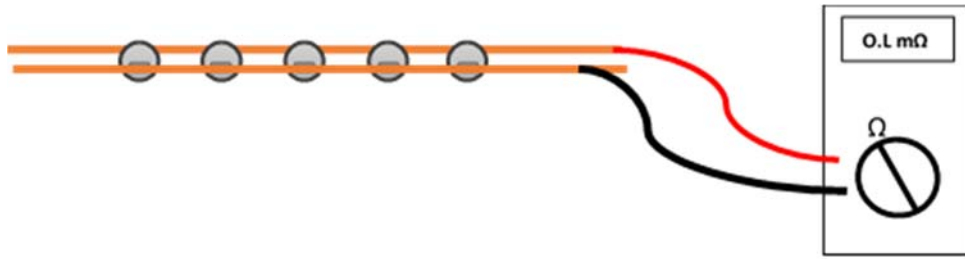


Figure 29 - Electrical connection testing across PZT disc thickness after assembly curing (Ember Krech Compliant Layer Thickness Study Protocol – used with permission)

The black lead of the voltmeter in Figure 29 was then placed on top of each individual disc while the red lead remained on the bottom copper strip to make sure that there was no electrical connection such that the voltmeter measures an overload resistance. Then the black lead was then placed on top of the top copper strip and the red lead was placed on top of each individual disc to check for an electrical connection such that the voltmeter measures a small amount of resistance which indicates that there is an electrical connection (Figure 30).

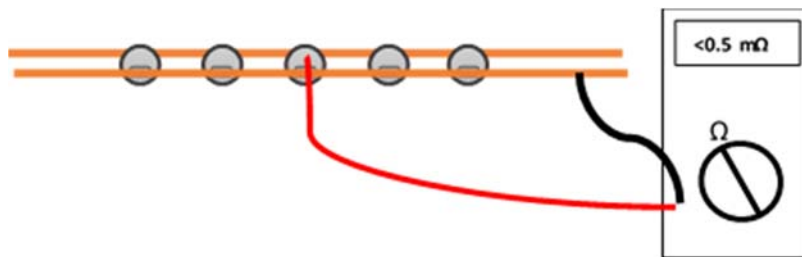


Figure 30 - Electrical connection on one side of each PZT disc after assembly curing (Ember Krech Compliant Layer Thickness Study Protocol – used with permission)

The next step of the manufacturing process is to mechanically stack the electrically connected PZT discs in series. Using a medical spatula, the electrically connected PZT discs were folded in an accordion style (Figure 31).

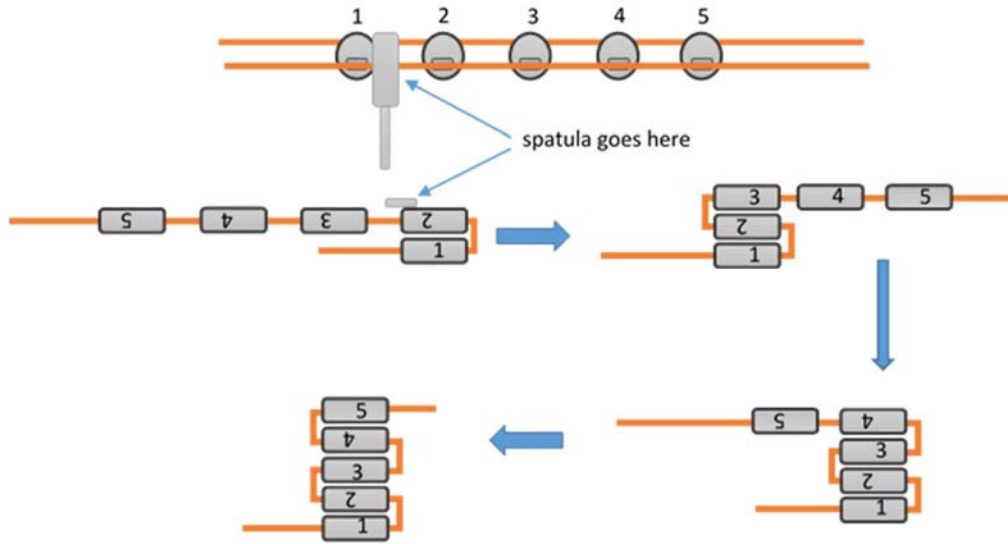


Figure 31 - Stacking electrically connected PZT discs in an accordion style (Ember Krech Compliant Layer Thickness Study Protocol – used with permission)

Slices of pre-made cured epoxy (EPO-TEK® 301, Billerica, MA) of varying thicknesses of 0, 0.2, 0.4, and 0.8mm ($\pm 0.02\text{mm}$) were inserted and adhered between each PZT disc with more epoxy (EPO-TEK® 301, Billerica, MA) that was in a “goopy” or viscous state. “Goopy” epoxy was achieved by letting epoxy air cure for about 2 hours before applying in the assembly with a spatula. Silicone pieces were placed on the top and bottom of the assembly so that the epoxy would not adhere in the oven during heat curing. A couple of metal nuts were used as weights to help compress the assembly to have epoxy flow in between all interfaces and eliminate air bubbles (Figure 32).

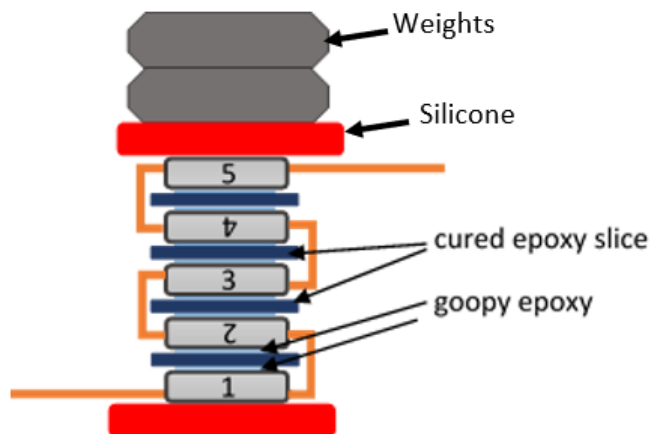


Figure 32 – Stacked assembly of electrically connected PZT discs with varying compliant layer thicknesses (cured epoxy slices) and goopy epoxy interposed for oven curing. Pieces of silicone placed on the top and bottom of the assembly and weights (metal nuts) placed on top of the assembly (Ember Krech Compliant Layer Thickness Study Protocol – used with permission)

The assembly was then left to cure for approximately five to six hours in air. After silicone pieces and weights were placed on top of the assembly. To encapsulate the assembly, silicon rubber molds (Dragon Skin, Smooth-On, Macungie, PA) were used. These molds were first cleaned with rubbing alcohol and then filled with epoxy using a syringe or pipette. The assembly was then placed into the mold with the long copper tabs pointing up and the PZT discs parallel to the top and bottom of the mold (Figure 33).

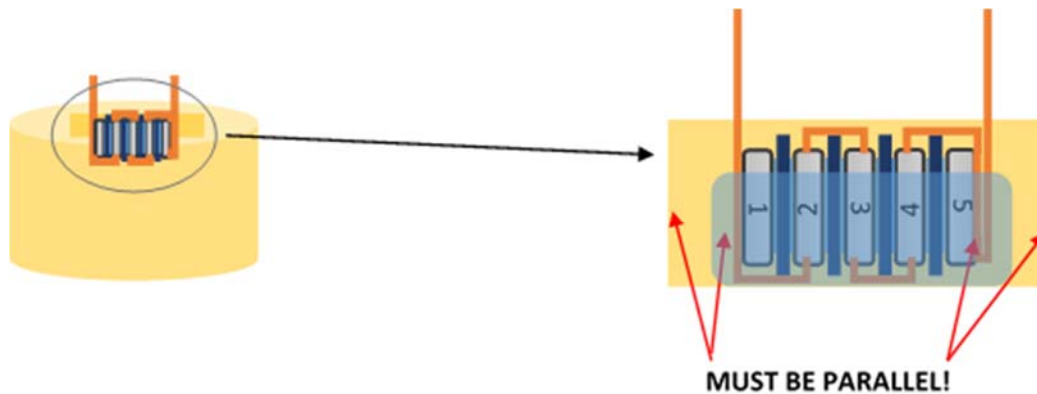


Figure 33 - Encapsulating the stacked in series PZT disc assembly in a dragon skin mold (Ember Krech Compliant Layer Thickness Study Protocol – used with permission)

Air bubbles in the epoxy in the mold were popped using a T-pin or tweezers. The assembly was then air cured for 24 hours and then cured in an oven for 2 hours at 65°C. After curing, any excess epoxy was removed carefully with a handheld Dremel tool (Racine, WI) so that all the faces of the cube of epoxy encapsulating the assembly are as flat as possible (Figure 34).

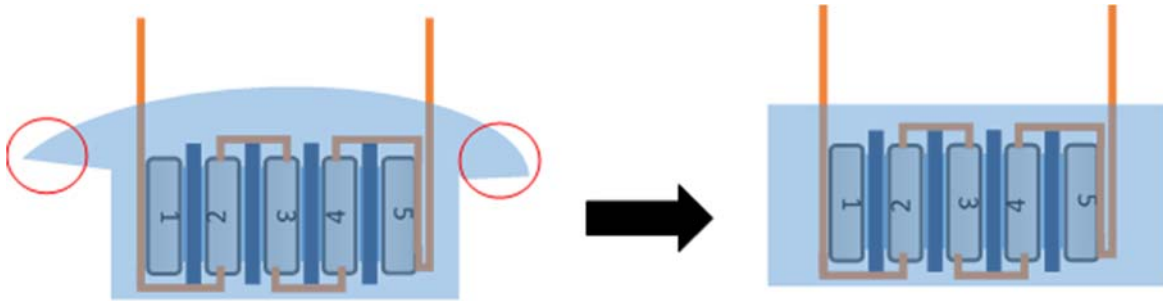


Figure 34 - Excess epoxy was carefully removed using a Dremel so that the epoxy encapsulating the assembly had faces that are as flat as possible (Ember Krech Compliant Layer Thickness Study Protocol – used with permission)

After encapsulation and removal of excess epoxy, the assembly has become a compliant layer adaptive composite stack (CLACS) and is ready for testing. This manufacturing process was repeated for each specimen made. Four groups of specimens were made each with a sample size of 5. One group had 0mm compliant layer thicknesses, another with 0.2mm, another with 0.4mm, and the last with 0.8mm compliant layer thicknesses ($\pm 0.02\text{mm}$).

3.2 Experimental Setup

The schematic and physical ultrasound system setup used in this study can be seen in Figures 35 and 36 respectively.

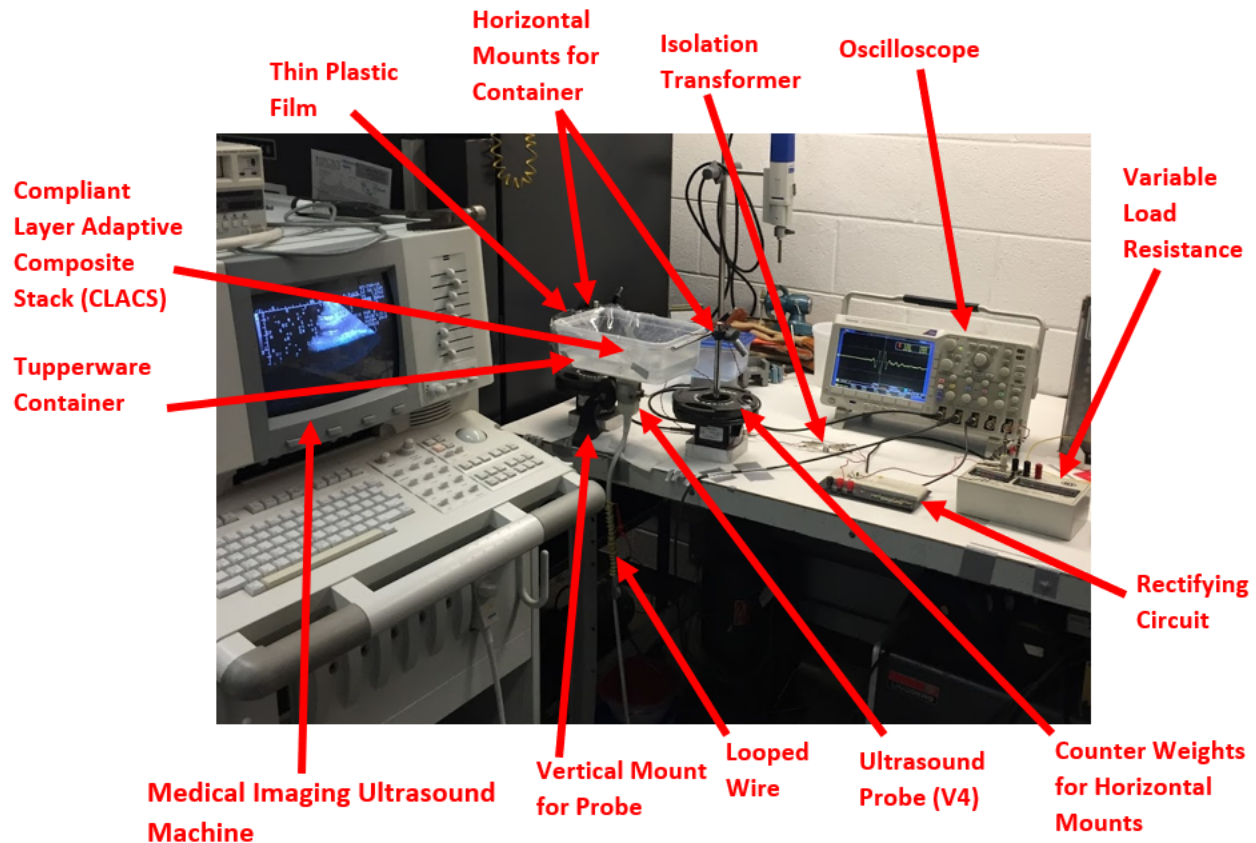


Figure 36 - Ultrasound Testing System Setup

An Acuson 128xp Ultrasound Imaging Machine (Mountain View, CA) with a V4 cardiac phased vector array probe was used as the sound source. The probe face area is approximately a 3.2cm x 1.9cm rectangle. More information about the Medical imaging ultrasound machine and probe is in section 3.4. A rectangular Ziploc Tupperware container (23cm x 15cm x 8cm) was used to house the media in the experiment. A hole (6cm x 3.3cm) was cut in the bottom of the Tupperware container so that the ultrasound V4 probe face area would fit inside of it. This hole was covered with a thin plastic film which is approximately 12 μ m in thickness and another piece of the same type of plastic film was placed on top of the media and hung over the rim of the Tupperware container. Duct tape was used to fix the thin plastic film layers to the Tupperware container so that the thin plastic film was slightly taut. This allowed for the CLACS to be placed on top of the water media tested in this study and not sink. The

CLACS were placed on top of the thin plastic film layer above the media and the ultrasound probe was fixed in place with an adjustable circular grip so that the probe face was essentially fixed, was pointing up and made contact with the bottom thin plastic film layer below the media. A thin PVC gel layer was applied in between the ultrasound probe face and bottom thin plastic film, and in between the CLACS and top thin plastic film so that the sound waves did not have any air media to travel through from the probe face up to the CLACS (Figure 37).



Figure 37 - Thin PVC gel film placed on top of the V4 cardiac phased vector array ultrasound probe face

The PVC gel serves as an acoustic impedance matching layer for medical imaging that is extremely thin, so sound waves do not attenuate or lose energy as they travel through it. Since the PVC gel and thin plastic film layer thicknesses are smaller than the wavelength of the ultrasonic waves for all media (water - $\sim 0.375\text{mm}$, tissue - $\sim 0.4\text{mm}$, bone - $\sim 1\text{mm}$), energy will not be lost due to attenuation in through those thicknesses^{28,29}. The CLACS copper strips were connected to an Oscilloscope and rectifying circuit for voltage measurements to be taken before and after rectification. More information

about the Oscilloscope testing parameters and rectifying circuit components can be found in sections 3.5 and 3.6 respectively.

3.3 Parameters Tested

The different compliant layer thicknesses tested were 0mm, 0.2mm, 0.4mm, and 0.8mm with a sample size of 5 for each. The effect of these compliant layers on electrical potential and power output were tested with varying testing parameters such as media type, distance between the ultrasound probe face and the CLACS (media thickness), and the orientation of the PZT disc faces relative to the direction of the propagating ultrasound wave to study their effects as well. The varying media types tested were tap water, tissue, and tissue plus bone and are shown in Figures 38-40 respectively.



Figure 38 - Water media used in testing



Figure 39 - Tissue media used in testing



Figure 40 - Tissue plus bone media used in testing

Water was chosen as the baseline media and the tissue and tissue plus bone media were chosen to resemble a medium similar to human body tissue surrounding the intervertebral space of the lumbar spine that ultrasonic waves would have to propagate through. Different distances between the ultrasound probe and the CLACS (medium thicknesses) of 20mm and 40mm were tested. An effort was made to determine an average distance from the exterior surface of a person's back to the center of the intervertebral body space where the CLACS would be located, but this distance measurement (tissue medium thickness) would vary depending on where you measure from on the exterior of a person's back to the center of the intervertebral space (Figure 41).

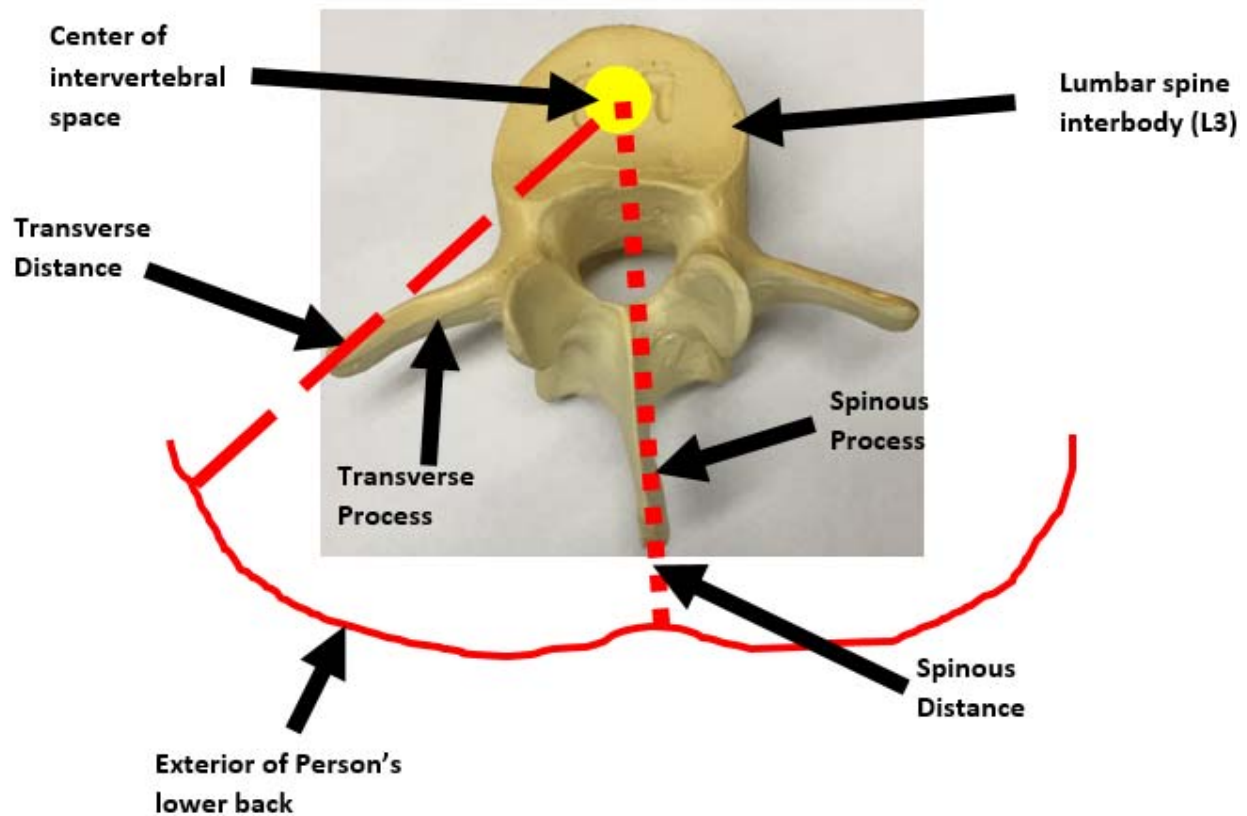


Figure 41 - Tissue thicknesses at two different spots on the exterior of a person's back to the center of the intervertebral body in the lower back (Lumbar spine L3)

Since the distance measurement (media thickness) along the spinous process from the exterior of a person's back to the center of the intervertebral space in the lumbar spine is less than the measurement

along the transverse process and since ultrasonic waves attenuate as a function of distance through a media, pressure amplitudes of the ultrasonic waves would decrease less along spinous process distance compared to the transverse process distance. However, if the ultrasound probe was placed slightly off of the transverse process direction so that the bone of the transverse process would not interfere with the incoming ultrasonic waves, there would be more bone present along the spinous process distance than the transverse process distance. Bone has a higher acoustic impedance than tissue and would create an acoustic impedance mismatch along the spinous process which would reduce the pressure amplitude of the ultrasonic wave to the point where the pressure amplitude may be equivalent to nothing by the time the ultrasonic wave travels to the center of the intervertebral space. In addition, every person has different amounts of tissue surrounding their lumbar spine region and has slightly different bone structures which would be difficult to create test cases for all ranges of media thickness. Because of the media thickness variation and the multiple locations that a probe face could be placed on the exterior of a person's back and since this is a foundational study, two media thickness of 20mm and 40mm were chosen to simplify the experiment. The two orientations of the CLACS are described by how the PZT circular disc faces within were impacted by the ultrasound wave front; perpendicular and parallel (Figure 42).

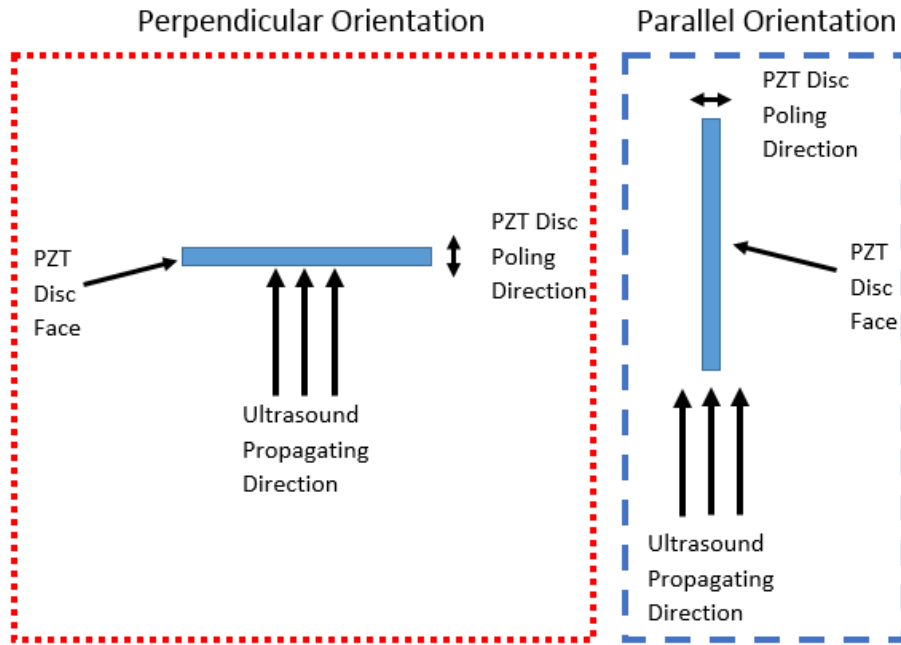


Figure 42 - Perpendicular and Parallel Loading Orientations

These were chosen to represent the two different orientations that the CLACS could rest in the intervertebral space of the lumbar spine.

3.4 Medical Imaging Ultrasound Machine and Probe – Acuson 128xp, V4

An Acuson 128xp Ultrasound Imaging Machine (Mountain View, CA) with a V4 probe was used as the sound source (Figure 43).



Figure 43 - Acuson 128XP/10 Ultrasound Medical Imaging Machine (Mountain View, CA)

This machine was used to market the idea that a CLACS could be powered by a medical imaging ultrasound machine so that if this idea became a product, hospitals would not have to purchase a specialized ultrasound machine to conduct electrical stimulation with a CLACS but could use the ultrasound machines that already exist in the hospital. The V4 ultrasound probe is a cardiac phased vector array (Mountain View, CA) with 128 PZT elements and produced sound at 4MHz (Figure 44).



Figure 44 - Acuson V4 Ultrasound cardiac phased vector array probe (Mountain View, CA)

This probe was chosen because of its imaging application. It was designed to have a more focused wave front of sound to image the heart because the sound waves must travel from the surface of a person's chest, in between the ribs, impact the heart, reflect off the heart, and travel back to the probe face. This more focused probe allows for the heart to be imaged. The more focused channel of sound waves of this probe travel outward in an approximate rectangular profile that is slightly larger than the dimensions of the probe face. Eventually, the sound waves will propagate a certain distance through the media called the Rayleigh distance in which the rectangular profile of sound will begin to spread out. The ultrasound machine was set to image at a depth of 100mm at 4MHz frequency with a power input level of 0 dB or 1 W by flipping the depth switch and toggling through the multi-frequency and transformer power buttons for all tests. The V4 probe can image at 2.5MHz, 3.5MHz, and 4MHz frequencies and since the resonance frequency of the PZT (SM111) is 5MHz, the 4MHz setting was used. The 4MHz setting was chosen because it is the closest frequency to the resonant frequency of the PZT. This will cause more deformation to happen in the PZT discs because when the PZT discs operate at their

resonant frequency, they deform the most. When the PZT discs mechanically deform more, more electrical potential is generated due to the piezoelectric effect. An increase in electrical potential yields more power output after rectification. The imaging depth of 100mm was chosen so that the sound waves could travel farther into a medium and maintain the rectangular profile of sound that is similar to the geometry of the probe face. If the imaging depth setting was chosen to be less than 100mm, the ultrasound wave front would be more focused at a certain depth, but would not travel as far into the medium being tested. The 0 dB or 1 W power setting was chosen because it was the highest power level that could be used with this machine. All other power levels were negative dB meaning the pressure of the ultrasound waves would be less than if the power level was set at 0 dB. The intensity of the sound wave with these settings is approximately $165\text{mW}/\text{cm}^2$ which is still well below the FDA limit of $720\text{mW}/\text{cm}^2$. With all these settings, the ultrasound probe PZT elements were excited at specific time intervals to produce sound waves with amplitudes in a Gaussian shape 27 times a second (27 Hz) for heart imaging applications (Figure 45).

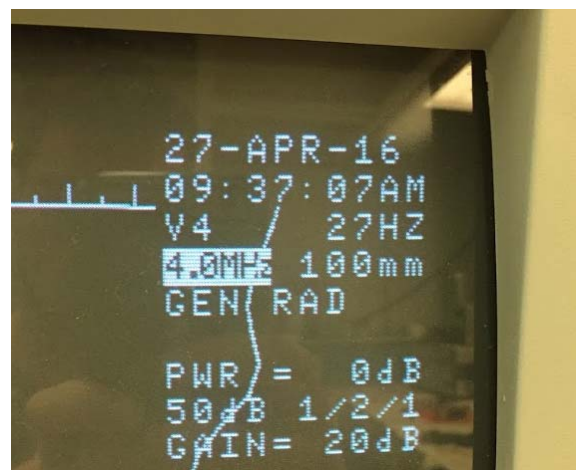


Figure 45 - Ultrasound machine screen showing set parameter values for medical imaging

The “50dB” and “Gain” items in Figure 45 had to do with how the intensities of the reflected sound waves were seen on the screen. These items did not affect the ultrasound waves produced by the ultrasound machine and probe. The imaging screen also has distance marks and a cursor function that

were used to determine the depth of the water media used in testing. This tissue and tissue plus bone media were measured with calipers to be approximately 20mm and 40mm thicknesses.

3.5 Measuring Device – Tektronix DPO 3034 Digital Phosphor Oscilloscope

A Tektronix DPO 3034 Digital Phosphor Oscilloscope (Beaverton, OR) was used as the measurement device in this study (Figure 46).

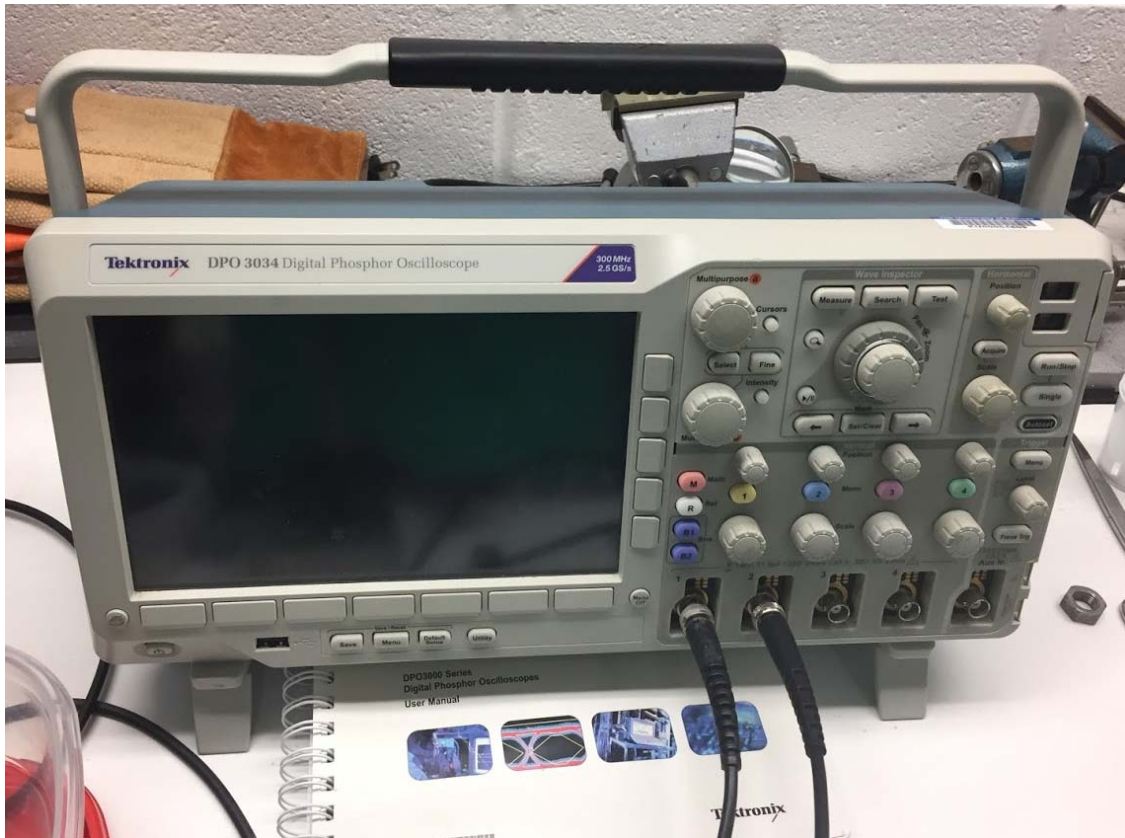


Figure 46 – Tektronix DPO 3034 Digital Phosphor Oscilloscope (Beaverton, OR) used to take measurements in this study

This Oscilloscope has the capability to measure signals with a bandwidth of up to 300MHz and during testing it was set to view signals below a bandwidth of 20MHz to help eliminate high frequency electrical noise. Each time a waveform was saved, the window was set so that the sampling rate was at least ten times the acoustic 4MHz frequency signal. It is important to have a higher sampling rate than

the frequency of the measured signal to fully capture the waveforms. If the sampling rate is not high enough, the full waveform may not be captured. As current was sent to the V4 probe PZT elements by the ultrasound machine along the probe wire, a magnetic field was generated around the insulated wire because of moving electrons. Solid 18-gauge wire was wrapped around the probe insulated wire connecting the V4 probe to the ultrasound machine so that the magnetic field generated by the insulated wire was captured (Figure 47).



Figure 47 - Looped wire wrapped around the Ultrasound probe wire to capture the magnetic field generated by moving electrons in the probe wire

This wrapped wire was attached to a split co-axial cable that was connected to one of the Oscilloscope channels at the other end. The accuracy of this waveform magnitude from the ultrasound probe wire was not being measured, but the timing at which it took place relative to the waveform responses seen out of the CLACS was of importance to help identify the waveform signals seen on the other Oscilloscope channels. Since the magnetic field waveform signal coming off the probe wire consistently occurred 27 times a second (27Hz) and its magnitude remained unaffected by changing the testing parameters of the setup, a falling edge trigger was used on it to gather the shape and timing of the AC signal that was being sent to the PZT elements in the ultrasound probe. The Oscilloscope trigger would stop the waveform at the triggered point and made that spot 0 time. The rest of the waveform was then built around that time equals 0 point on the Oscilloscope screen. The trigger allows for a time

frame of reference to compare other measured signals in this experiment. By triggering the signal going to each PZT element in the ultrasound probe, it is made at time equals 0 seconds and the other electrical signals measured by the Oscilloscope are placed accordingly along the time axis. This is another way to compute the distance between the ultrasound probe and spinal fusion device (media thickness). Since the speed of sound in the mediums tested is known and the time between signal peaks is known, the distance (media thickness) between those signals can be calculated. All signals were measured by the Oscilloscope's Channel resistances which were set at 1 M Ω each to serve as an "open-circuit" resistance so that almost all the electrical potential of the incoming waveform signals was captured. The signal waveform data points, settings, and a picture of the waveform were recorded as a CSV file, set file, and PNG file respectively on a USB drive.

3.6 Rectifying Circuit

For bone healing applications involved with electrical stimulation, direct current (DC) is known to work which is described in the Background and Literature review section. As the CLACS in this study are mechanically deformed in a cyclic pattern by ultrasonic waves, electrical potential is generated as an alternating current (AC) electrical signal from the CLACS. This AC electrical signal must be converted to a DC electrical signal for bone healing applications. The AC signal coming off the spinal fusion devices in this study was rectified to become DC signals. A full wave bridge rectifier was constructed using a universal breadboard (Radio Shack, Cat. No. 276-169A, Fort Worth, TX), solid 18-gauge wires, a tantalum polarized capacitor (2.2 μ f), and Schottky diodes (SEMTECH DO-35 1N60P 1N60, Camarillo, CA). The rectifying circuit schematic used in this study is shown in Figure 48.

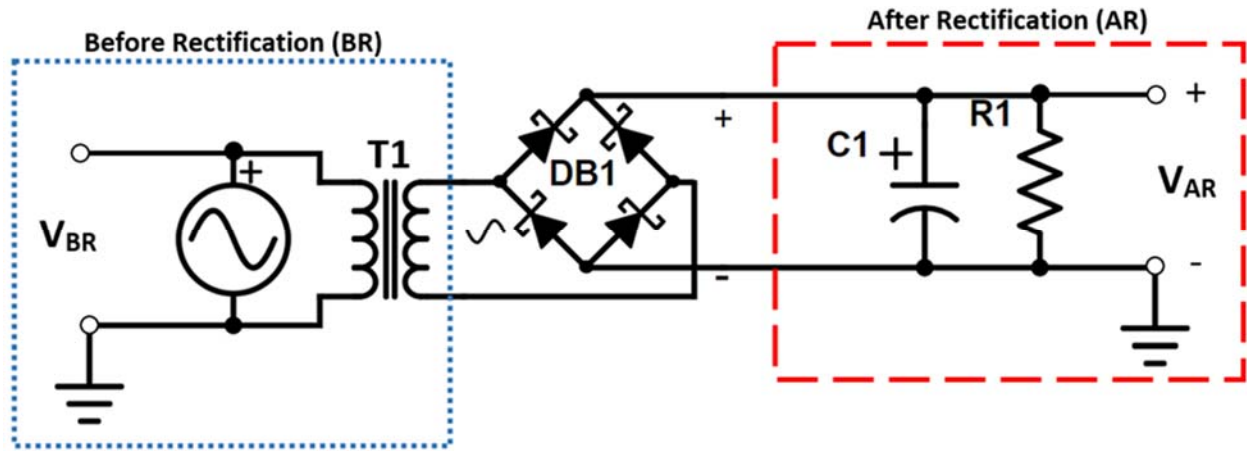


Figure 48 - Rectifying Circuit Diagram. Before rectification measurements are represented by V_{BR} , after rectification measurements are represented by V_{AR} , DB1 represents a full wave rectifier (4 diodes), C1 represents a polarized tantalum capacitor, R1 represents a variable load resistance and T1 represents a 1:1 turns isolation transformer. All values for these electrical components can be seen in Table 1

In Table 1, the rectifying circuit components and their corresponding values are tabulated.

Table 1 - Tabulated Values of Rectifying Circuit Components

Circuit Item Description	Value
R1 = Variable Load Resistance (R-C Box, iET Labs Inc. RC-500)	100 Ω – 10 M Ω
VBR = Before rectification measured voltage across Oscilloscope Channel 1 Resistance (Tektronix DPO 3034 Digital Phosphor Oscilloscope)	1 M Ω
VAR = After rectification measured voltage across Oscilloscope Channel 3 Resistance (Tektronix DPO 3034 Digital Phosphor Oscilloscope)	1 M Ω
T1 = High Frequency & High Efficiency Isolation Transformer (Audio Transformer – CyanKen EI14)	1:1 \rightarrow (Primary coils = 800 turns, Secondary coils = 800 turns)

DB1 = Full Wave Bridge Rectifier – (4) Schottky Diodes, SEMTECH(ST) DO-35 1N60P 1N60 (Low forward voltage drop, low power consumption, & low noise)	Forward Voltage (each) = 0.2 V
C1 = Tantalum (Pearl) Polarized Capacitor	2.2 μ F
AC Source = Compliant Layer Adaptive Composite Stack (CLACS) – produces AC voltage from ultrasonic acoustic pressure waves	N/A
Ground = Oscilloscope Channel Ground → earth	N/A

The Schottky diodes were chosen for their low power dissipation, high operating frequency, and low forward voltage properties that would use up little electrical potential during the rectification process. These diodes require a forward voltage of 0.2 V for any meaningful current to pass through them⁴³. Forward voltage slightly higher than 0.2V would yield an exponentially increasing current that flows through the diode. However, if the forward voltage was below 0.2V, some but little current would pass through the diode because in the 0-0.2V forward voltage range the current would gradually increase with an increasing input forward voltage, but not exponentially. Since a full wave rectifier configuration was used in this study, at any given time whether the current was traveling in one direction through the circuit or alternated and traveled in the other direction, it needed to pass through two diodes and thus a 0.4V forward voltage was required for larger amounts of current to pass through towards the equivalent parallel circuit components. With forward voltages higher than 0.4V, an exponential increase in current would pass across the diodes and more current would then flow to the equivalent parallel circuit components allowing more voltage to be measured after rectification. With forward voltages around 0.4V, less voltage would be measured after rectification. The diodes effectively convert all the negative AC signal to positive values and the waveform then becomes a DC Bias electrical signal. A tantalum polarized capacitor (C1 in Figure 48) was connected in parallel to the varying load resistance (R1 in

Figure 48) to help convert the DC Bias electrical signal into a DC electrical signal. As you increase your capacitance and resistance in the rectifying circuit, the positive DC Bias electrical signal “humps” start to connect to each other with their peaks slowly decreasing and eventually a flat line of DC voltage is formed. Since the ultrasound waves in this study were impacting the PZT stacks with pressure amplitude profiles resembling a Gaussian shape and not a sine or cosine wave, the typical simple method of converting an AC signal to DC using RMS voltage cannot be used. Typically, an AC electrical signal can be mathematically converted into a DC electrical signal by taking the peak difference between the maximum and minimum values of the AC electrical signal, dividing that difference by two to get a peak voltage value, and then dividing that peak voltage value by the square root of two to give an RMS voltage. However, with this study the AC electrical signal is a Gaussian shape, so designing a circuit to rectify the signal was necessary because the AC electrical signal was not predictable, and an RMS voltage could not be properly calculated. In the test, if the maximum of the peak voltage value before rectification was at least 0.4 V, then there was a noticeable difference in the DC signal magnitude as the load resistance increased. As the load resistance increased, the equivalent resistance (Z_{eq} in Figure 55) increased and more voltage was measured by the Oscilloscope’s channel resistance (V_{AR}). Since the electrical components after rectification are connected in parallel and the capacitor (C1 in Figure 48) has lower impedance than the Oscilloscope (V_{AR} in Figure 48) and the smallest load resistance (R1 in Figure 48), the equivalent impedance cannot be larger than the component with the smallest impedance (capacitor). As the load resistance increased, the equivalent impedance approached the impedance value of the capacitor. In this study, the equivalent impedance is essentially constant for all load resistances. More information about how the equivalent impedance was calculated can be seen in section 3.6.2. A Faraday cage was available but not used in testing to reflect incoming magnetic fields around the testing location that could affect Oscilloscope measurements because the setup was too large to be housed in the Faraday cage. To minimize and reflect incoming magnetic fields, all the long

connecting wires used in the circuit were braded using a hand drill. Some of the long connecting wires were coaxial cable wires which are shielded and protect against incoming magnetic fields around the testing location. A one-to-one turns ratio high frequency isolation transformer (CyanKen EI14) was used to separate Oscilloscope channel grounds during rectification so that the full waveform after rectification could be measured. Without this isolation transformer, only half of the AC electrical signal waves would be rectified and the other half would become zero because current will take the path of least resistance. More detail about this isolation transformer can be seen in section 3.6.1.

3.6.1 Isolation Transformer – CyanKen EI14 (1:1)

In order for the full waveform of the rectified AC acoustic response to be measured, an isolation transformer was used to separate the common Oscilloscope ground in Channel 1 and Channel 3 from the un-rectified and rectified circuits. A CyanKen EI14 high frequency, high efficiency, one to one audio isolation transformer with 800 primary and secondary turns was used in this study (Figure 49).



Figure 49 - CyanKen Audio Isolation Transformer

If an isolation transformer was not used, half of the AC waveform would essentially bypass the Oscilloscope Channel 3 lumped resistance and no voltage would be measured. The rectifying circuit used in this study can be seen in Figure 48. In Table 1, the rectifying circuit components and their corresponding values are tabulated. Voltage before rectification was measured across the Oscilloscope channel lumped impedance ($1M\Omega$) and is represented as R2 and voltage after rectification was also measured across the Oscilloscope channel lumped impedance ($1M\Omega$) is represented as R3 for Figures 50-53. Figure 50 and 51 show what the current path would be if the rectifying circuit did not have an isolation transformer to separate the common Oscilloscope ground from the un-rectified and rectified circuits as the current travels in one particular direction (green arrows) and then alternates and travels in the opposite direction (red arrows).

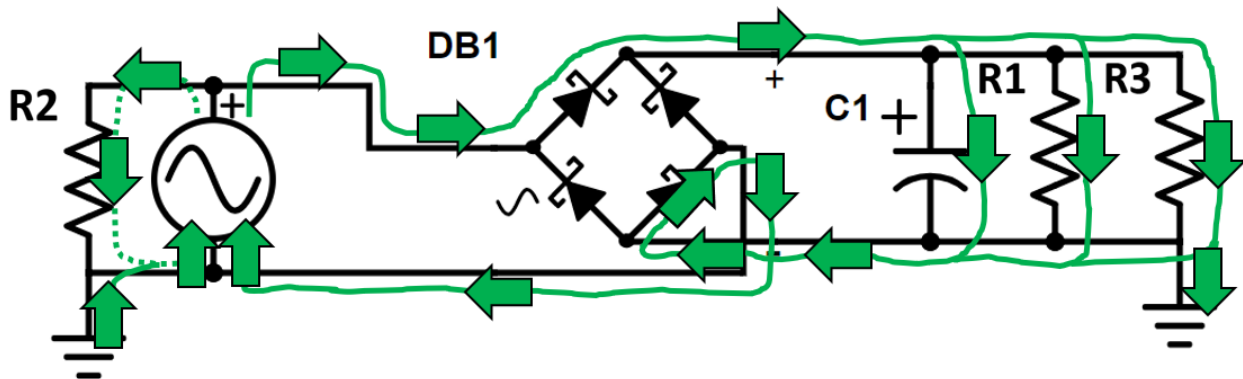


Figure 50 - Rectifying circuit without an isolation transformer where the current travels in one particular direction (green arrows) out of the symbolized Compliant Layer Adaptive Composite Stack (CLACS)

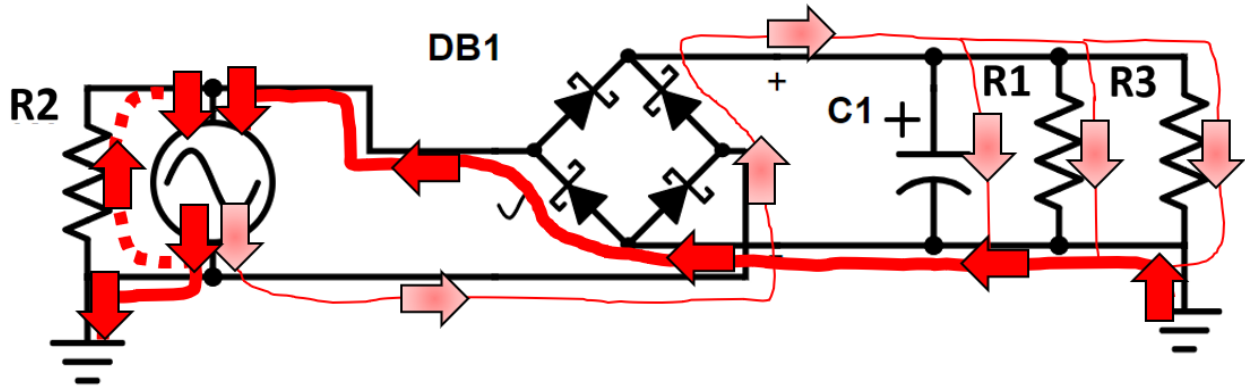


Figure 51 - Rectifying circuit without an isolation transformer where the current alternates and travels in the opposite direction (red arrows) out of the symbolized Compliant Layer Adaptive Composite Stack (CLACS) compared to the current path in Figure 50.

The dotted paths represents current that travels to the Oscilloscope Channel 1 lumped resistance for measuring the AC acoustic response before rectification in both Figure 50 and 51. In Figure 50, the current path travels across the rectified components which are a smoothing polarized capacitor, load resistance, and Oscilloscope Channel 3 lumped resistance. Because the current travels across the Oscilloscope Channel 3 lumped resistance, voltage can be measured. However, in Figure 51 when the current path alternates compared to the current path in Figure 50, most of the available current travels along the bolded and dotted red paths and a small amount travels across the rectified components. The current travels this way because current takes the path of least resistance. It will take advantage of travelling across the Oscilloscope common ground from Channel 1 (R1) to Channel 3 (R3) and then across one diode instead of going across all the rectified components and two diodes (skinny red path). Due to ohm's law, with little current traveling across a resistance, little voltage is measured across that resistance. Because of this, little voltage if any would be measured across the Oscilloscope Channel 3 lumped resistance while the current travels in the alternative direction (Figure 51 – red) compared to the path traveled (green) in Figure 50. Without an isolation transformer only half of the rectified waveform is measured so there would be period of time on the triggered Oscilloscope screen where the measured voltage would be zero and then the other corresponding periods would measure some

voltage value. For this study full wave rectification is desired because more energy needs to be stored over time after rectification so it can be used in a potential future application where electrical stimulation is used to induce bone growth with DC signals that have a particular duty cycle (controlled pulse). If half of the rectified waveform isn't stored, then intuitively it would take twice as long to store the required electrical energy to apply pulsed DC stimulation. This lag might only allow the applied DC pulse to be applied every other mechanical loading cycle (walking) in the spine which may not grow bone as quickly or as well. Figures 52 and 53 show the rectification circuit with an isolation transformer with the current traveling in one particular direction (green) and with current traveling in the opposite (alternative) direction (red), respectively.

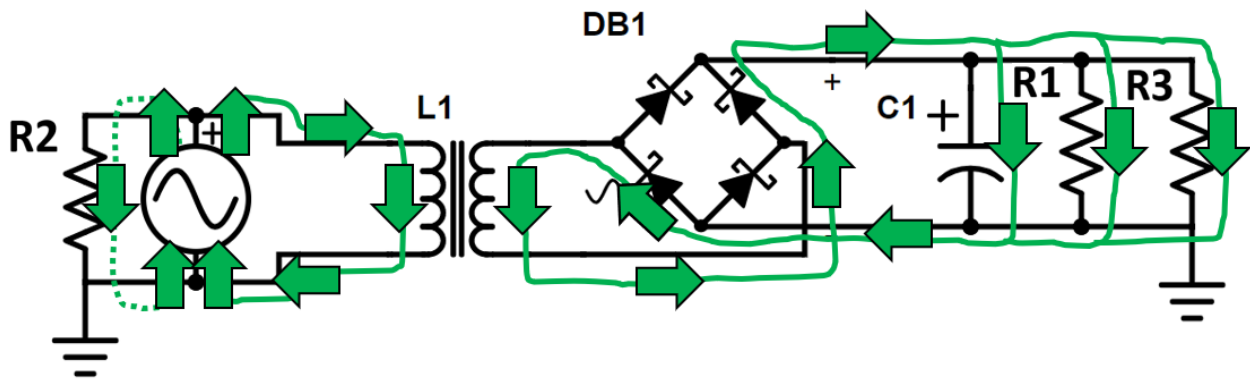


Figure 52 - Rectifying circuit with an isolation transformer where the current travels in one particular direction (green arrows) out of the symbolized Compliant Layer Adaptive Composite Stack (CLACS)

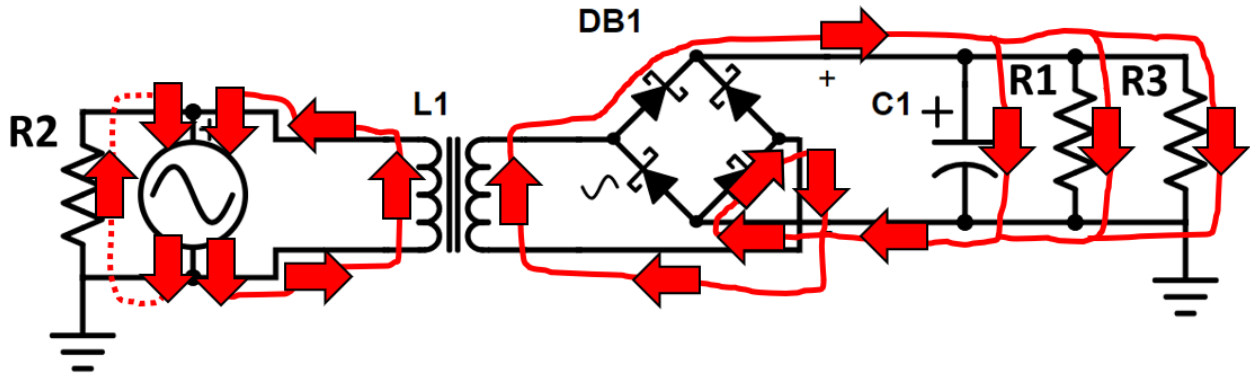


Figure 53 - Rectifying circuit with an isolation transformer where the current alternates and travels in the opposite direction (red arrows) out of the symbolized Compliant Layer Adaptive Composite Stack (CLACS) compared to the current path in Figure 52.

With an isolation transformer, whether current is traveling in one particular direction (green arrows) or in an alternative direction (red arrows), the full waveform travels across the rectified components and can then be measured as a DC voltage.

In theory, a one to one isolation transformer should have the same number of coil turns on the primary and secondary sides of the transformer and the amplitude of the voltage on the secondary side should be the same as the primary side and there is no power loss that occurs. However, in reality, there is either a little step up voltage or step down voltage that occurs from the primary side to the secondary side of the transformer and there is power loss due to core losses, winding losses, and parasitic capacitance⁴⁴. The core losses include hysteresis losses which are due to nonlinear voltage in the transformer core and eddy current losses which are due to joule heating (generation of heat by passing electric current) that occurs in the core and is proportional to the square of the transformer's applied voltage. The winding losses include joule heating in the wires on the primary and secondary sides of the transformer and leakage flux that escapes from the core and passes only through one side of the transformer (one winding) which results in primary and secondary reactive impedance. There are three kinds of parasitic capacitance phenomenon due to the electric field distribution which include capacitance between adjacent turns, layers, and between the core and the layers adjacent to the core.

In this study, a CynKen audio EI14 isolation transformer was used. This transformer is labeled as a high frequency and high efficiency transformer that has 800 turns on both the primary and secondary sides of the transformer. Before running any tests, the validity of the one to one turns label for these transformers was tested. A BK Precision 3011 MHz Function Generator was used to output a sine wave of varying voltage amplitudes at a 2.52MHz frequency. A coaxial cable with a coaxial splitter was connected to the output of the Function generator and to the primary side leads of the isolation transformer. Another coaxial cable with a coaxial splitter was also connected to the primary side leads of the isolation transformer and to Channel 1 of the Oscilloscope. A third coaxial cable with a coaxial splitter was connected to the secondary side of the isolation transformer and to Channel 2 of the Oscilloscope so that the waveform on the secondary side of the isolation transformer could be captured. A built-in peak-to-peak measurement was used to calculate the peak-to-peak voltages of Channel 1 (primary side) and Channel 2 (secondary side) on the Oscilloscope and these values were manually recorded and tabulated for all isolation transformers. Six isolation transformers were tested at an input voltage peak-to-peak amplitude (AC) of 10V and 2.5MHz from the Function generator. Of the six, three showed voltage drops of 5.6%, 8.8% and 27.2% that would not be characteristic of a labeled one to one isolation transformer. The other three were determined to be reasonable and one of these four showed only a 2% voltage drop. This transformer was then tested at other lower voltages because a prediction was made that the composite would produce lower peak-to-peak voltages than 10V with ultrasound as the loading source because it applies less stress on the material compared to simulated mechanical loading (walking) at 2Hz using an MTS uniaxial machine. Ultrasonic pressure that is used to imaging inside the human body is extremely small compared to 1000N load from the MTS. Using the MTS as the loading source, maximum peak-to-peak voltage levels of 10V and higher were seen. This isolation transformer was then tested with input (primary side – CH1) peak-to-peak (AC) voltage levels of 0.8-5.0V

from the Function generator and the secondary side (CH2) peak-to-peak (AC) voltage levels were recorded (Figure 54).

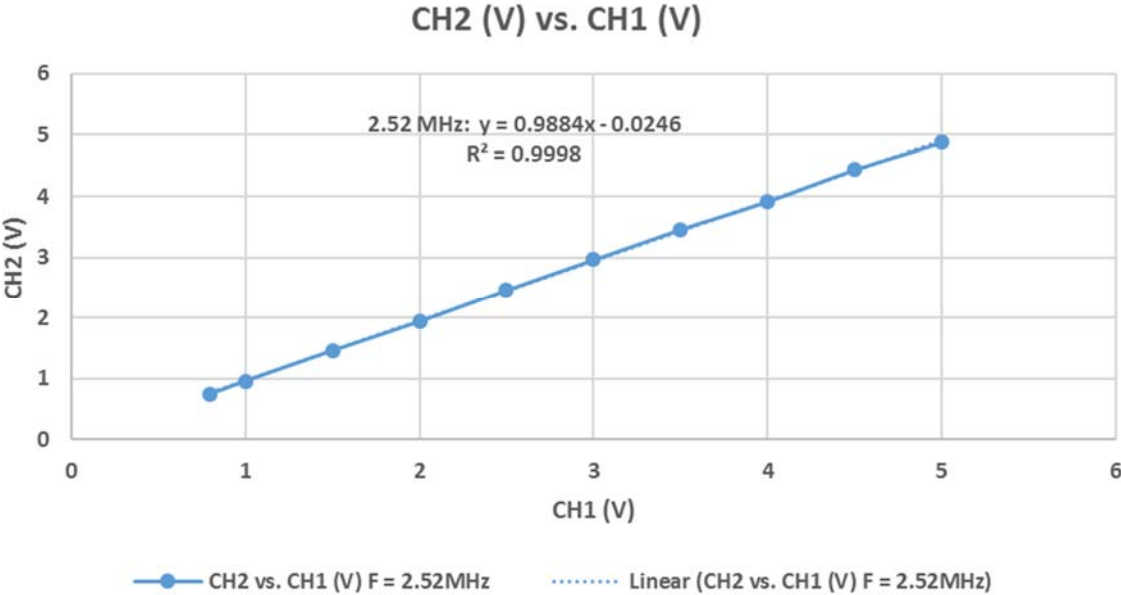


Figure 54 – CH1 vs. CH2 peak-to-peak voltage (AC)

After plotting this relationship in excel, a linear trend line was used to determine the slope of the data. In Figure 54 the slope of the trend line is 0.9884 which is close to a slope of 1 which means that almost all the input peak-to-peak amplitude (AC) voltage was transformed across the transformer. This isolation transformer was used for testing.

3.6.2 Equivalent Impedance of the Rectifying circuit

This section contains the equation to find the equivalent impedance used in electrical power calculations for total power after rectification (Figure 55).

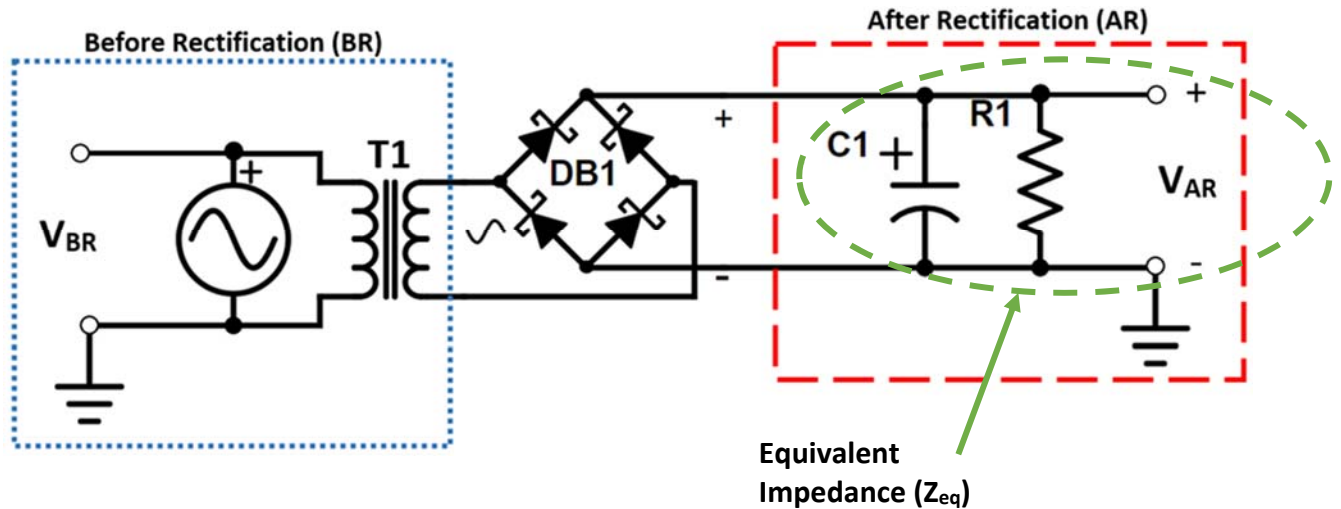


Figure 55 - Rectification Circuit used in Testing. The green circled area represents the lumped impedance (Z_{eq}) of a capacitor (C1) in parallel with a variable load resistance (R1) in parallel with the lumped Oscilloscope Channel 3 resistance ($1M\Omega$) in which after rectification measurements were taken (V_{AR})

The green circled area in Figure 55 represents the lumped impedance (Z_{eq}) of a capacitor (C1) in parallel with a variable load resistance (R1) in parallel with the lumped Oscilloscope Channel 3 impedance ($Z_{osc} = 1M\Omega$) in which after rectification measurements were taken (V_{AR}). Impedances in parallel are added up by taking the reciprocal of each component summing them up, and then taking the reciprocal of the sum (equation 37).

$$Z_{eq} = \left(\frac{1}{\frac{-j}{Z_{c1}} + \frac{1}{Z_{R1}} + \frac{1}{Z_{osc}}} \right)$$

Equation 37 – Equivalent impedance (Z_{eq}) as a function of the oscilloscope lumped channel impedance (Z_{osc}), load resistance impedance (Z_{R1}), and capacitor impedance (Z_{c1}) which has a -j because it is purely imaginary impedance (reactance)

In this study the oscilloscope channel lumped impedances were all set to $1M\Omega$ and the load resistance varied from 100Ω to $10M\Omega$. The capacitors impedance is described by equation 38, where j is an imaginary number because capacitors have purely imaginative impedance (reactance), ω represents the

angular frequency which is a function of input signal frequency, f , and 2π radians, and C represents the capacitance.

$$-j * Z_{C1} = \frac{-j}{\omega * C} = \frac{-j}{2 * \pi * f * C}$$

Equation 38 - Impedance of a capacitor as a function of operating frequency (f) and capacitance (C)

The signal frequency used in this calculation is 4MHz because the frequency of the ultrasound probe is 4MHz and the acoustic response before rectification was measured to be 4MHz using built-in Oscilloscope functions and the capacitance of this tantalum polarized capacitor is 2.2 μ f. Using a 4MHz frequency and 2.2 μ f the impedance of the capacitor is computed in equation 39.

$$Z_{C1} = \frac{1}{2 * \pi * f * C} = \frac{1}{2 * \pi * (4E6) * (2.2E - 6)} = 0.0180857889877154$$

Equation 39 - Capacitor impedance at 4MHz operating frequency (f) and 2.2 μ f capacitance (C)

To add components in parallel, they need to all have a common denominator (equations 40, 41, and 42).

$$Z_{R1} \rightarrow \left(\frac{1}{Z_{R1} + j * 0} \right) * \left(\frac{Z_{ocs} + j * 0}{Z_{ocs} + j * 0} \right) * \left(\frac{-j * Z_{C1}}{-j * Z_{C1}} \right) = \frac{Z_{ocs} * Z_{C1}}{Z_{R1} * Z_{ocs} * Z_{C1}}$$

Equation 40 – Common denominator for load resistance component impedance (Z_{R1}) as a function of the oscilloscope channel lumped impedance (Z_{osc}), load resistance impedance (Z_{R1}), and capacitor impedance (Z_{C1})

$$Z_{osc} \rightarrow \left(\frac{1}{Z_{osc} + j * 0} \right) * \left(\frac{Z_{R1} + j * 0}{Z_{R1} + j * 0} \right) * \left(\frac{-j * Z_{C1}}{-j * Z_{C1}} \right) = \frac{Z_{R1} * Z_{C1}}{Z_{R1} * Z_{osc} * Z_{C1}}$$

Equation 41 - Common denominator for oscilloscope channel lumped impedance component (Z_{osc}) as a function of the oscilloscope channel lumped impedance (Z_{osc}), load resistance impedance (Z_{R1}), and capacitor impedance (Z_{C1})

$$Z_{C1} \rightarrow \left(0 + \frac{j}{Z_{C1}}\right) * \left(\frac{Z_{R1} + j * 0}{Z_{R1} + j * 0}\right) * \left(\frac{Z_{osc} + j * 0}{Z_{osc} + j * 0}\right) = \frac{j * Z_{R1} * Z_{osc}}{Z_{R1} * Z_{osc} * Z_{C1}}$$

Equation 42 - Common denominator for capacitor component impedance (Z_{C1}) as a function of the oscilloscope channel lumped impedance (Z_{osc}), load resistance impedance (Z_{R1}), and capacitor impedance (Z_{C1})

By combining equations 40-42 into equation 37, Z_{eq} can be expressed with a common denominator (equation 43).

$$Z_{eq} = \left(\frac{1}{\left(\frac{Z_{ocs} * Z_{C1} + Z_{R1} * Z_{C1} + j * Z_{R1} * Z_{osc}}{Z_{R1} * Z_{ocs} * Z_{C1}} \right)} \right) = \frac{Z_{R1} * Z_{ocs} * Z_{C1}}{(Z_{ocs} * Z_{C1} + Z_{R1} * Z_{C1}) + j * (Z_{R1} * Z_{osc})}$$

Equation 43 - Equivalent impedance (Z_{eq}) as a function of the oscilloscope lumped channel impedance (Z_{osc}), load resistance impedance (Z_{R1}), and capacitor impedance (Z_{C1}) which has a -j because it is purely imaginary impedance (reactance)

Now Z_{eq} has an imaginary term in the denominator and it needs to be multiplied by the complex conjugate to bring the imaginary term to the numerator, so the numerator terms can be divided by a term that is not imaginary (equation 44).

$$Z_{eq} = \frac{(Z_{C1}^2 * Z_{osc}^2 * Z_{R1} + Z_{C1}^2 * Z_{R1}^2 * Z_{osc}) - j * (Z_{C1} * Z_{osc}^2 * Z_{R1}^2)}{(Z_{C1}^2 * Z_{osc}^2 + 2 * Z_{C1}^2 * Z_{osc} * Z_{R1} + Z_{C1}^2 * Z_{R1}^2 + Z_{osc}^2 * Z_{R1}^2)}$$

Equation 44 - Equivalent impedance (Z_{eq}) as a function of the oscilloscope lumped channel impedance (Z_{osc}), load resistance impedance (Z_{R1}), and capacitor impedance (Z_{C1}) which has a -j because it is purely imaginary impedance (reactance) after performing the complex conjugate

The equivalent impedance, Z_{eq} , can now be expressed in terms of other variables that represent sections of equation 44 (equations 45, 46, 47, and 48).

$$Z_{eq} = \frac{b - j * c}{a}$$

Equation 45 - Equivalent impedance (Z_{eq}) as a function of three variables, a, b, and c which represent parts of equation 44

$$b = (Z_{C1}^2 * Z_{osc}^2 * Z_{R1} + Z_{C1}^2 * Z_{R1}^2 * Z_{osc}) = Z_{C1}^2 * (Z_{osc}^2 * Z_{R1} + Z_{R1}^2 * Z_{osc})$$

Equation 46 - "b" variable part of equation 45 as a function of the oscilloscope lumped channel impedance (Z_{osc}), load resistance impedance (Z_{R1}), and capacitor impedance (Z_{C1})

$$c = (Z_{C1} * Z_{osc}^2 * Z_{R1}^2)$$

Equation 47 - "c" variable part of equation 45 as a function of the oscilloscope lumped channel impedance (Z_{osc}), load resistance impedance (Z_{R1}), and capacitor impedance (Z_{C1})

$$\begin{aligned} a &= Z_{C1}^2 * Z_{osc}^2 + 2 * Z_{C1}^2 * Z_{osc} * Z_{R1} + Z_{C1}^2 * Z_{R1}^2 + Z_{osc}^2 * Z_{R1}^2 \\ &= Z_{C1}^2 * (Z_{osc}^2 + 2 * Z_{osc} * Z_{R1} + Z_{R1}^2) + (Z_{osc}^2 * Z_{R1}^2) \end{aligned}$$

Equation 48 - "a" variable part of equation 45 as a function of the oscilloscope lumped channel impedance (Z_{osc}), load resistance impedance (Z_{R1}), and capacitor impedance (Z_{C1})

To find the magnitude of Z_{eq} , equation 49 was used.

$$|Z_{eq}| = \sqrt{\left(\frac{b}{a}\right)^2 + \left(\frac{c}{a}\right)^2}$$

Equation 49 - Equivalent impedance magnitude ($|Z_{eq}|$) as a function of, b, c, and a from equations 46, 47, and 48 respectively

Equations 50, 51, 52, and 53 are sample calculations for the circuit equivalent impedance, Z_{eq} , with a load resistance, Z_{R1} , value of 100Ω.

$$\begin{aligned} b &= Z_{C1}^2 * (Z_{osc}^2 * Z_{R1} + Z_{R1}^2 * Z_{osc}) \\ &= (0.0180857889877154\Omega)^2 * ((1E6\Omega)^2 * (100\Omega) + (100\Omega)^2 * (1E6\Omega)) \\ &= 3.271284729E10\Omega^5 \end{aligned}$$

Equation 50 - Example calculation of equation 46 using the result from equation 39, a 100Ω load resistance and the oscilloscope channel lumped impedance of 1,000,000Ω

$$c = (Z_{C1} * Z_{osc}^2 * Z_{R1}^2) = (0.0180857889877154\Omega * (1E6\Omega)^2 * (100\Omega)^2) = 1.8085789E14\Omega^5$$

Equation 51 - Example calculation of equation 47 using the result from equation 39, a 100Ω load resistance and the oscilloscope channel lumped impedance of 1,000,000Ω

$$\begin{aligned}
a &= Z_{C1}^2 * (Z_{osc}^2 + 2 * Z_{osc} * Z_{R1} + Z_{R1}^2 * Z_{osc}) + (Z_{osc}^2 * Z_{R1}^2) \\
&= (0.0180857889877154\Omega)^2 \\
&\quad * [(1E6\Omega)^2 + 2 * (1E6\Omega) * (100\Omega) + (100\Omega)^2 * (1E6\Omega)] + ((1E6\Omega)^2 * (100\Omega)^2) \\
&= 1E16\Omega^4
\end{aligned}$$

Equation 52 - Example calculation of equation 48 using the result from equation 39, a 100Ω load resistance and the oscilloscope channel lumped impedance of 1,000,000Ω

$$|Z_{eq}| = \sqrt{\left(\frac{3.271284729E10\Omega^5}{1E16\Omega^4}\right)^2 + \left(\frac{1.8085789E14\Omega^5}{1E16\Omega^4}\right)^2} = 0.018085788691867\Omega$$

Equation 53 - Example calculation of equation 45 using the results from equations 50, 51, and 52

Another method of calculating the equivalent impedance was explored to validate the equivalent impedance determined in equation 53. This second method first calculates an equivalent impedance of the load resistance and oscilloscope resistance, R_{eq} (equation 54), and then calculates an equivalent impedance of R_{eq} and the capacitor in parallel, Z_{eq} (equation 55).

$$R_{eq} = \left(\frac{1}{Z_{R1}} + \frac{1}{Z_{osc}}\right)^{-1}$$

Equation 54 - Equivalent resistance as a function of the oscilloscope channel lumped impedance (Z_{osc}) and the load resistance impedance (Z_{R1})

$$Z_{eq} = \left(\frac{1}{R_{eq}} + \frac{1}{-j * Z_{C1}}\right)^{-1}$$

Equation 55 - Equivalent impedance (Z_{eq}) as a function of the equivalent resistance (R_{eq}) and the capacitor impedance (Z_{C1}) which has a -j because it is purely imaginary impedance (reactance)

To add components in parallel, they need to all have a common denominator (equation 56).

$$Z_{eq} = \left(\left(\frac{1}{R_{eq}} \right) * \left(\frac{-j * Z_{C1}}{-j * Z_{C1}} \right) + \left(\frac{1}{-j * Z_{C1}} \right) * \left(\frac{R_{eq}}{R_{eq}} \right) \right)^{-1} = \frac{-j * Z_{C1} * R_{eq}}{R_{eq} - j * Z_{C1}}$$

Equation 56 - Equivalent impedance (Z_{eq}) as a function of the equivalent resistance (R_{eq}) and the capacitor impedance (Z_{C1}) which has a -j because it is purely imaginary impedance (reactance)

Now Z_{eq} has an imaginary term in the denominator and it needs to be multiplied by the complex conjugate to bring the imaginary term to the numerator, so the numerator terms can be divided by a term that is not imaginary (equation 57).

$$Z_{eq} = \frac{-j * Z_{C1} * R_{eq}}{R_{eq} - j * Z_{C1}} * \left(\frac{R_{eq} + j * Z_{C1}}{R_{eq} + j * Z_{C1}} \right) = \frac{(Z_{C1}^2 * R_{eq}) - j * (Z_{C1} * R_{eq}^2)}{(Z_{C1}^2 + R_{eq}^2)}$$

Equation 57 - Equivalent impedance (Z_{eq}) as a function of the equivalent resistance (R_{eq}) and the capacitor impedance (Z_{C1}) which has a -j because it is purely imaginary impedance (reactance) after performing the complex conjugate

The equivalent impedance, Z_{eq} , can now be expressed in terms of other variables that represent sections of equation 58 (equations 59, 60, and 61).

$$Z_{eq} = \frac{b - j * c}{a}$$

Equation 58 - Equivalent impedance (Z_{eq}) as a function of three variables, a, b, and c which represent parts of equation 57

$$b = Z_{C1}^2 * R_{eq}$$

Equation 59 - "b" variable part of equation 45 as a function of the equivalent resistance (R_{eq}) and capacitor impedance (Z_{C1})

$$c = Z_{C1} * R_{eq}^2$$

Equation 60 - "c" variable part of equation 45 as a function of the equivalent resistance (R_{eq}) and capacitor impedance (Z_{C1})

$$a = Z_{c1}^2 + R_{eq}^2$$

Equation 61 - "a" variable part of equation 45 as a function of the equivalent resistance (R_{eq}) and capacitor impedance (Z_{c1})

To find the magnitude of Z_{eq} , equation 49 was used. Equations 62, 63, 64, 65, and 66 are sample calculations for the circuit equivalent impedance, Z_{eq} , with a load resistance, Z_{R1} , value of 100Ω.

$$R_{eq} = \left(\frac{1}{Z_{R1}} + \frac{1}{Z_{osc}} \right)^{-1} = \left(\frac{1}{100\Omega} + \frac{1}{1E6\Omega} \right)^{-1} = 99.990001\Omega$$

Equation 62 - Example calculation of equation 54 at 100Ω load resistance and oscilloscope channel lumped impedance of 1,000,000Ω

$$b = Z_{c1}^2 * R_{eq} = (0.0180857889877154\Omega)^2 * (99.990001\Omega) = 0.032706306\Omega^3$$

Equation 63 – Example calculation of equation 59 using the result from equation 39, a 100Ω load resistance and the oscilloscope channel lumped impedance of 1,000,000Ω

$$c = Z_{c1} * R_{eq}^2 = (0.0180857889877154\Omega) * (99.990001\Omega)^2 = 180.8217238\Omega^3$$

Equation 64 – Example calculation of equation 60 using the result from equation 39, a 100Ω load resistance and the oscilloscope channel lumped impedance of 1,000,000Ω

$$a = Z_{c1}^2 + R_{eq}^2 = (0.0180857889877154\Omega)^2 + (99.990001\Omega)^2 = 9998.000627\Omega^2$$

Equation 65 – Example calculation of equation 61 using the result from equation 39, a 100Ω load resistance and the oscilloscope channel lumped impedance of 1,000,000Ω

$$|Z_{eq}| = \sqrt{\left(\frac{0.032706306\Omega^3}{9998.000627\Omega^2} \right)^2 + \left(\frac{180.8217238\Omega^3}{9998.000627\Omega^2} \right)^2} = 0.018085788691867\Omega$$

Equation 66 - Example calculation of equation 45 using the results from equations 63, 64, and 65

The results of equation 53 and 66 are the same so the second method was used in the MATLAB code to calculate electrical power because it requires fewer variables and a little less computation time.

Electrical power is a combination of Ohm’s law and Joule’s law where voltage (V) and impedance (Z) are inputs (equation 68).

$$\text{Electrical Power} = I * V = I^2 * Z = \frac{V^2}{Z}$$

Equation 67 - Electrical power as a function of voltage and impedance

An equivalent impedance was calculated for each load resistance value (100Ω to 10MΩ) using equations 54 to 67 in MATLAB (Table 2).

Table 2 - Equivalent Impedance Values calculated using Load Resistance Sweep values and the Oscilloscope lumped internal impedance value

Load Resistance Sweep (Ω)	Oscilloscope Lumped Impedance (Ω)	Equivalent Resistance (Ω)	Equivalent Impedance (Ω)
10	1000000	99.990001	0.01808578869186700000
1000	1000000	999.000999	0.01808578898475160000
5000	1000000	4975.124378	0.01808578898759590000
10000	1000000	9900.990099	0.01808578898768520000
40000	1000000	38461.53846	0.01808578898771340000
100000	1000000	90909.09091	0.01808578898771500000
500000	1000000	333333.3333	0.01808578898771540000
1000000	1000000	500000	0.01808578898771540000
5000000	1000000	833333.3333	0.01808578898771540000
10000000	1000000	909090.9091	0.01808578898771540000

As the load resistance value increased, the equivalent impedance, Z_{eq} , more closely approached the capacitor impedance because when an equivalent impedance is calculated for circuit components in parallel, it cannot be greater than the component with the smallest impedance.

3.7 Generic Testing Procedure

This section describes a general testing procedure that was followed during the testing for this study. The Acuson 128xp ultrasound machine start-up procedure was followed (Appendix B) and all the settings described in section 3.4 were selected. Next, the Tektronix DPO 3034 Digital Phosphor Oscilloscope was turned on and all the settings described in section 3.5 were selected. The V4 ultrasound probe was then placed upright into the vertical fixed grip on the table. After that, the rectification circuit connections were checked to make sure that there was metal contact between all the wires and electrical components. Details of the electrical components can be seen in section 3.6.

Looped wire around the ultrasound probe wire was wrapped and connected to test clips that were wired into a co-axial cable connected to Channel 2 on the Oscilloscope. Another coaxial cable connected to Channel 1 on the Oscilloscope with a coaxial cable splitter on the other end was connected to two alligator clips that were soldered onto two braded wires. On the other end of those braded wires were two more alligator clips that were soldered on and these alligator clips were attached to the primary leads one side of the isolation transformer. Another two alligator clips soldered onto two braded wires were attached to the primary leads of the isolation transformer and on the other end of the two braded wires were two more alligator clips that were soldered on and these two alligator clips were attached to the copper strips of the CLACS. Two alligator clips soldered onto two braded wires were attached to the leads on the secondary side of the isolation transformer and the other end of those braded wires were attached to the breadboard as the alternating current (AC) voltage input to the rectification circuit on the breadboard. On the breadboard were short wires, a capacitor, and four

diodes were connected in specific locations on the breadboard to perform rectification logic. Two more braded wires were attached to specific breadboard locations in which measuring across those locations would resemble rectified AC voltage or direct current (DC) voltage. On the other end of these two braded wires were two soldered on alligator clips. These alligator clips were attached across the terminals of a variable resistance on a resistance and capacitance box (IET Labs Inc., RCS Series Resistance and Capacitance Box, Boston MA) (Figure 56).

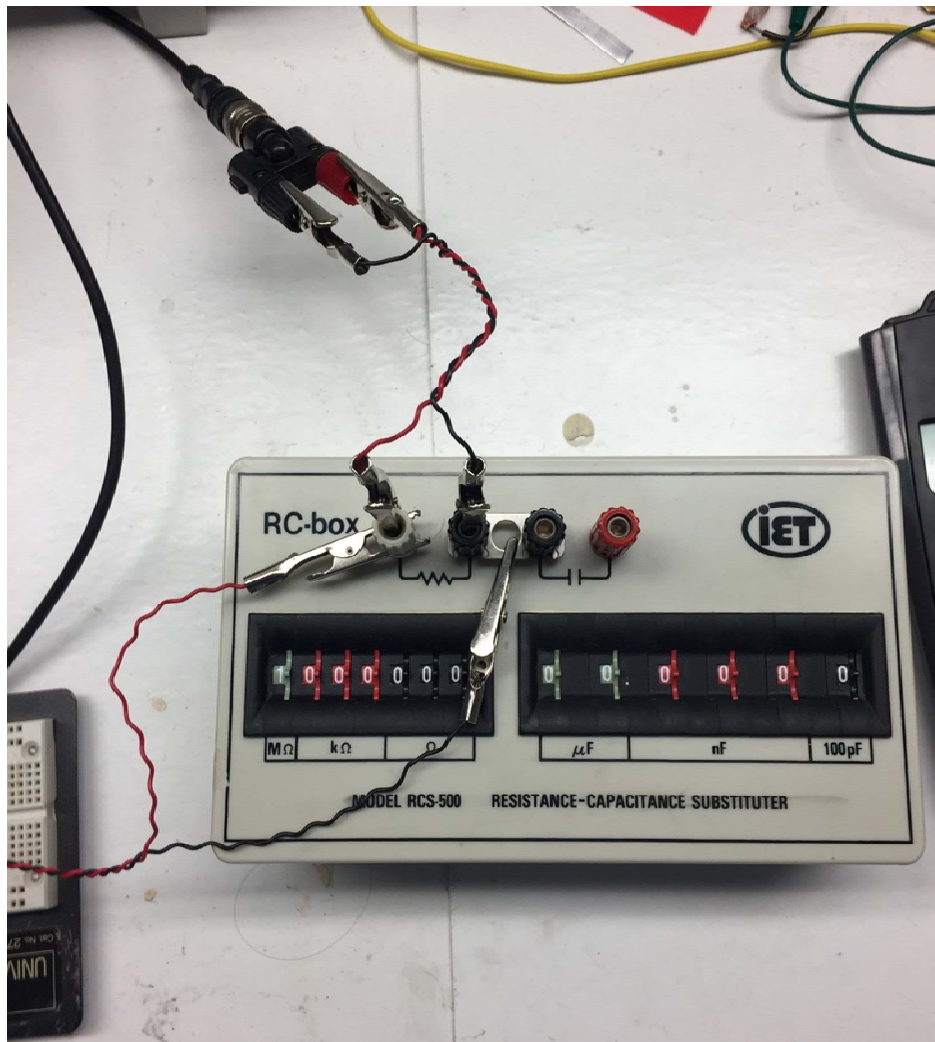


Figure 56 - RCS box used as a variable load resistance

Two more alligator clips that were soldered onto two more braded wires were also connected across the variable resistance of the RCS box. On the other end of the two braded wires were two more

alligator clips that were attached to a co-axial cable splitter connected to a co-axial cable which was connected to Channel 3 on the Oscilloscope. To limit the amount of influence phantom signals have on the testing circuit, all wires were braded and all wire lengths were minimized where possibly, and all items on the breadboard were connected with small wire lengths and height (Figure 57).

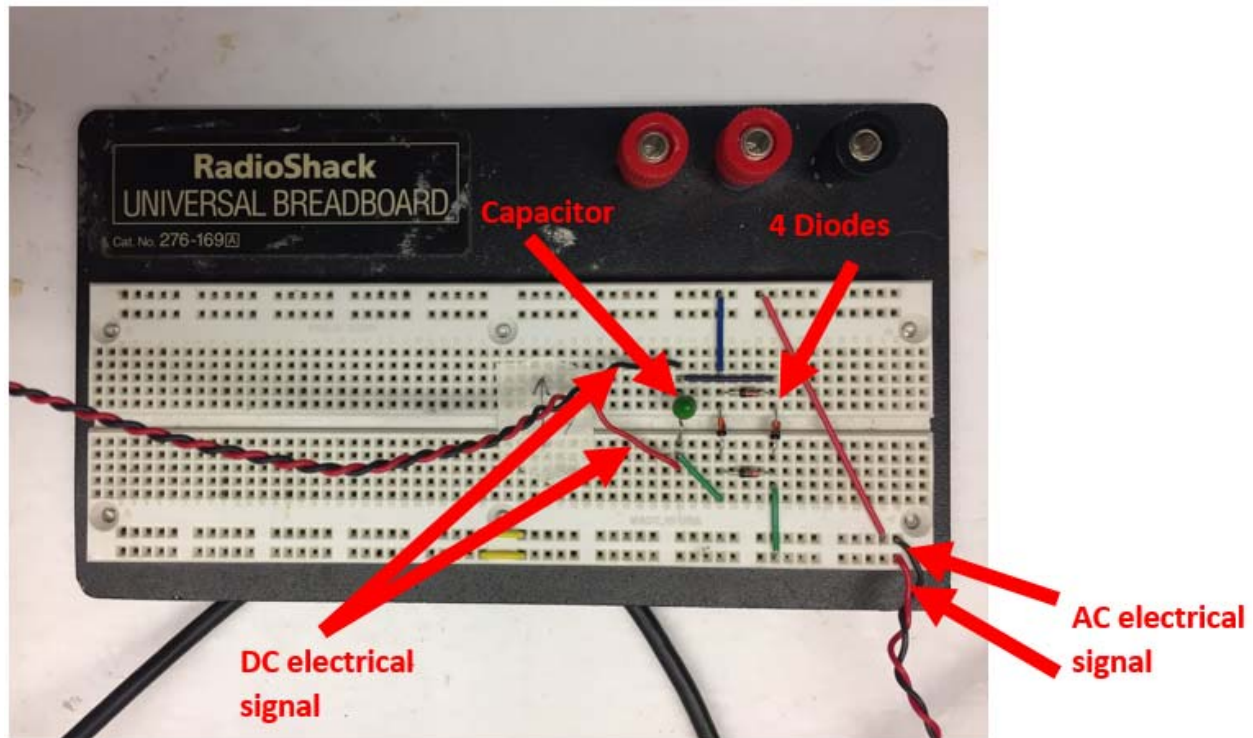


Figure 57 - Physical layout of rectification circuit

Two stands with cantilevered horizontal metal rods were placed on opposite sides of the vertical fixed grip and V4 ultrasound probe. These cantilever metal rods could be moved vertically and angled by loosening a side knobs on the stand. The two cantilever metal rods were positioned so that they were level and parallel to each other using a level. Next, the Tupperware container was filled up with approximately 20mm of water in height to match with the first media thickness testing parameter. This media thickness was confirmed once the container was placed on top of the V4 probe using the Ultrasound medical imaging machine to locate a higher intensity of reflected sound waves on the machine screen and using built-in functions (cursor). Before placing the Tupperware container on the

two stands with cantilevered horizontal metal rods, PVC gel was placed on the ultrasound probe face and on one of the flat sides of the CLACS. The rim of the Tupperware container was then set on top of cantilever horizontal metal rods that are a part of the two stands. Contact between the thin plastic film attached to the bottom hole of the Tupperware container and the ultrasound probe face was checked. If not enough or too much tension was in the thin plastic film, then the height of the metal cantilever rods attached to the two stands was adjusted by using the side knobs. There should be slight tension in the thin plastic film as it is placed on the ultrasound probe, but not enough to rip or pull it up off of the Tupperware container around the cutout hole. Once the right amount of tension was found, the testing parameter media thickness was verified again by using the built-in depth imaging capabilities of the ultrasound machine. For example, if the distance measured by the ultrasound machine was less than 20mm, then more water media was added and if the distance was greater than 20mm, then water media was removed until 20mm media thickness was achieved. Another layer of thin plastic film was then placed on top of the water media in the Tupperware container. This thin plastic film was taped to the sides of the Tupperware container with duct tape so that when the CLACS were placed on top of the thin plastic film, they would not sink into the water medium. The CLACS were placed on top of the thin plastic film at relatively the same location for every test by eye, but the exact spot was not documented or controlled. This approximate location was found by doing some preliminary location testing on the ultrasound probe face. One CLACS was moved around along and within the profile the ultrasound probe face with water as the medium and a medium thickness of 20mm and a perpendicular loading orientation until the maximum AC amplitude was seen on the Oscilloscope. The sound pressure output of the V4 phased vector array seemed to be located in the middle of the probe face. The CLACS for all testing parameters were then placed to the best of the user's eye in the middle of the probe face. The exact location of the CLACS was difficult to determine with tissue and tissue plus bone media, but was estimated by observing where the CLACS was located compared to the sides of the probe face. If the

medium was tissue or tissue plus bone, a layer of thin plastic film was laid tightly around the medium to ensure full surface contact between the thin plastic film and medium so that there was no air gaps between the thin plastic film and the medium. If there were air gaps, the ultrasound waves would reflect off the air gap and never propagate through to the CLACS, because of acoustic impedance mismatching between the tested mediums and air. The tissue medium 20mm depth was used in the same piece that was used for the tissue plus bone medium, but the CLACS was placed only on tissue and not the “T” bone on the “T” bone tissue assembly (Figure 58).



Figure 58 - CLACS placed on top of 20mm tissue thickness media for testing

Another slab of tissue was cut another 20mm depth and this was placed on top of the tissue part of the “T” bone tissue assembly to achieve a distance of 40mm media thickness. The tissue plus bone medium had the bottom part of the “T” resting over the ultrasound probe face with a little slab of tissue above it to achieve 20mm depth (Figure 59).



Figure 59 - Tissue plus bone media with a little slab of tissue placed above the small part of the "T" bone to achieve 20mm media thickness.

When testing the second media thickness parameter in the tissue plus bone media, another slab of the tissue was cut so that when it was stacked on top of the "T" bone tissue assembly a 40mm of depth or media thickness was achieved.

Since the CLACS were encapsulated in a cube of epoxy the CLACS could be rotated 90 degrees on top of the top thin plastic film above the media to achieve the perpendicular and parallel loading orientations. These orientations are described in section 3.3.

During testing, data was recorded for each CLACS of varying compliant layer thicknesses. All combinations of compliant layer thicknesses (4 - 0mm, 0.2mm, 0.4mm, and 0.8mm), media type (3 – water, tissue, and tissue plus bone), media thickness (2 - 20mm and 40mm), and loading orientation (2 - perpendicular and parallel) were tested for before rectification measurements. For after rectification measurements, all the previously listed testing parameters were tested with the addition of varying load resistances (10). Once data for all combinations of the testing parameters (media type, media thickness, loading orientation, and load resistance) had been recorded before and after rectification for one compliant layer thickness CLACS, the process was repeated for the remaining CLACS of that compliant

layer thickness. When data for all CLACS of a particular compliant layer thickness had been recorded, the process was repeated for the remaining CLACS of their respective compliant layer thicknesses.

3.7.1 Measurements Before Rectification (V_{BR})

For before rectification measurements, a global perspective was observed at first by identifying and locating the peak of the gaussian responses on the Oscilloscope after triggering (Figure 60).

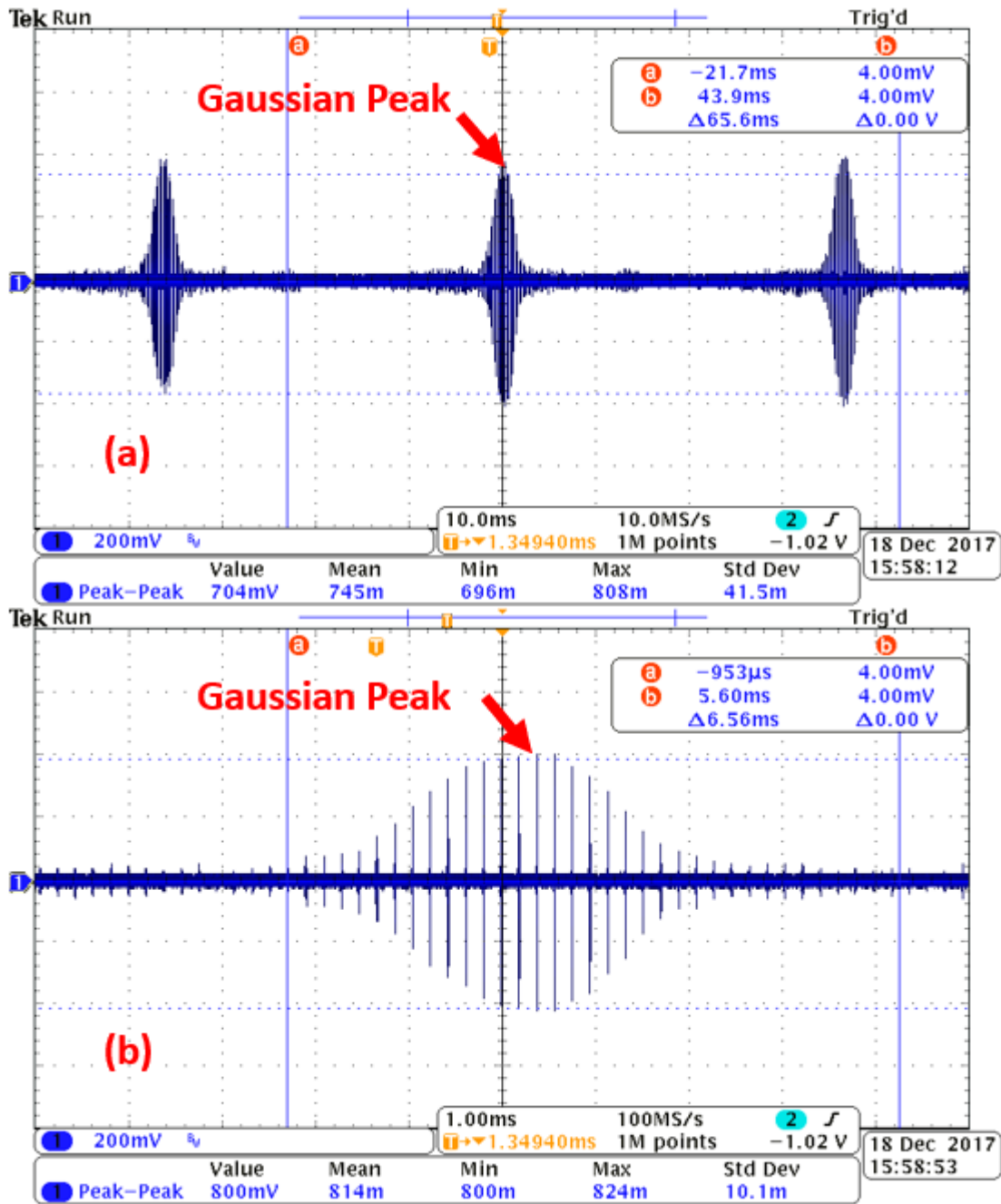


Figure 60 - Global perspective identifying peak of Gaussian responses (a) and then zooming in on one Gaussian shape to find its peak and take measurements (b)

For all combinations of compliant layer thicknesses, media type, media thickness, and orientation before rectification, there were three different types of electrical responses measured after finding the peak of the Gaussian response with the Oscilloscope (Figure 61).

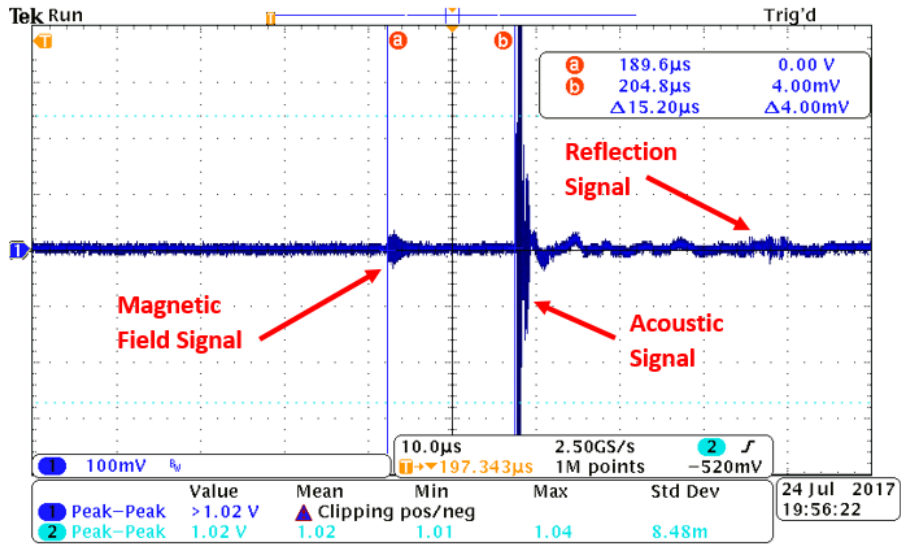


Figure 61 – Example of before rectification electrical responses from the magnetic field of the Ultrasound probe wire, acoustic response of the incident ultrasonic waves, and the acoustic reflection

One was the electrical response from the incident ultrasound wave impacting the PZT discs within the CLACS and was categorized as the Acoustic response (Figure 62).

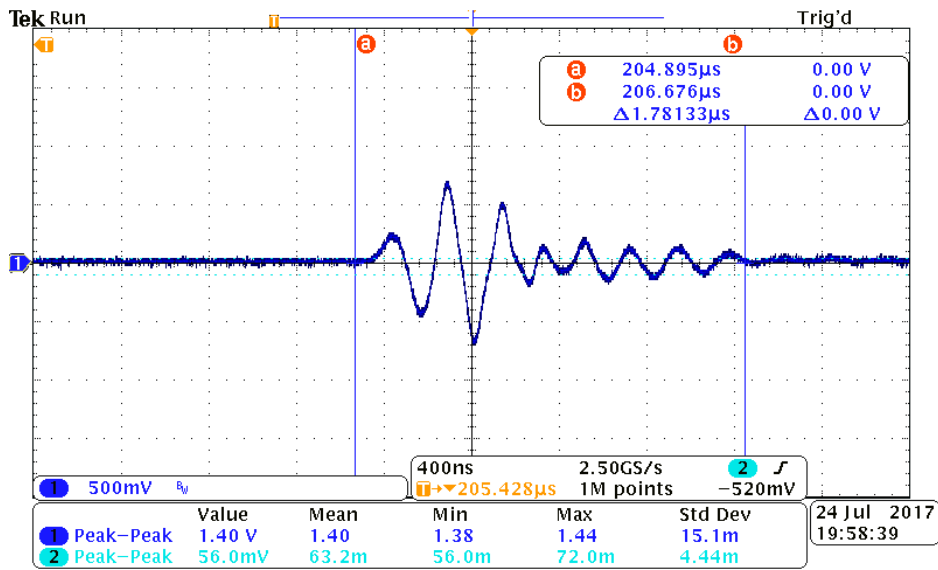


Figure 62 – Example of before rectification acoustic response measurement

Another measured electrical response on the Oscilloscope screen was from part of the incident ultrasound wave reflecting off either the PZT discs within the CLACS or the outer epoxy layer of the CLACS (Figure 63).

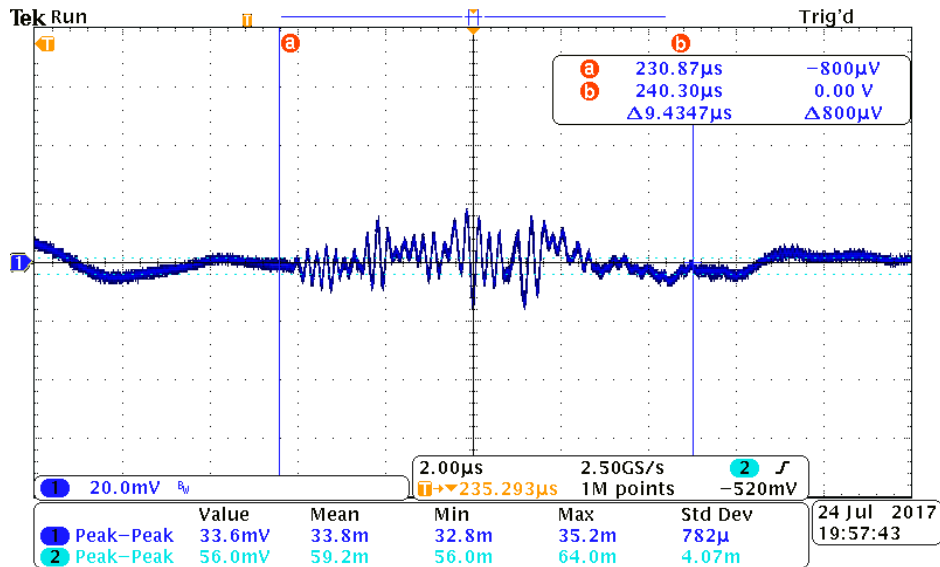


Figure 63 – Example of before rectification reflection response measurement

The ultrasound wave would impact a PZT discs, reflect back to the probe face, part of it would then reflect back up to the CLACS and impact the PZT discs again. This electrical response generated by acoustic reflection on the PZT discs within the CLACS was called the Reflection response. The last electrical response that was recorded was from a magnetic field generated by current being drawn from the ultrasound machine to each of the PZT elements in the ultrasound probe (Figure 64).

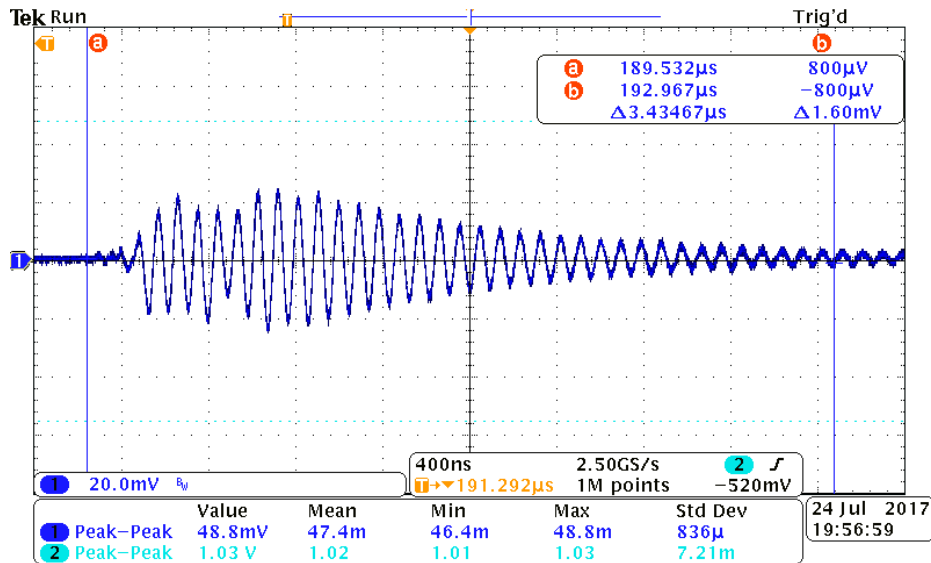


Figure 64 – Example of before rectification magnetic field response measurement

This electrical response was in sync with the triggered electrical response of the looped wire wrapped around the ultrasound probe wire to capture the magnetic field so this signal had to be the magnetic field response. Even though the wires in the circuit system were braided to help shield the current flowing through them from outside magnetic field disturbances, the magnetic field from the ultrasound probe wire induced an electrical response that was measured. It is unclear if the magnetic field from the ultrasound probe wire influenced the PZT discs within the device, or if it generated current to flow in the circuit wires that were not co-axial cables, or both. Once each electrical response was identified before rectification, measurements could be taken for each before rectification electrical response for data analysis. The sampling rate of the Oscilloscope was set to be at least 10 times higher than the acoustic response signal to ensure that the full waveform was being captured.

3.7.2 Measurements After Rectification (V_{AR})

After rectification, all combinations of compliant layer thicknesses, media types, media thicknesses, loading orientations, and load resistances were tested, and for each combination there was only one type of electrical response to be recorded by the Oscilloscope's Channel 3 lumped impedance

(1MΩ). Because of the rectifying circuit, the acoustic (AC), reflection (AC), and magnetic field (AC) responses all became one line of voltage (DC) that was measured over time (Figure 65).

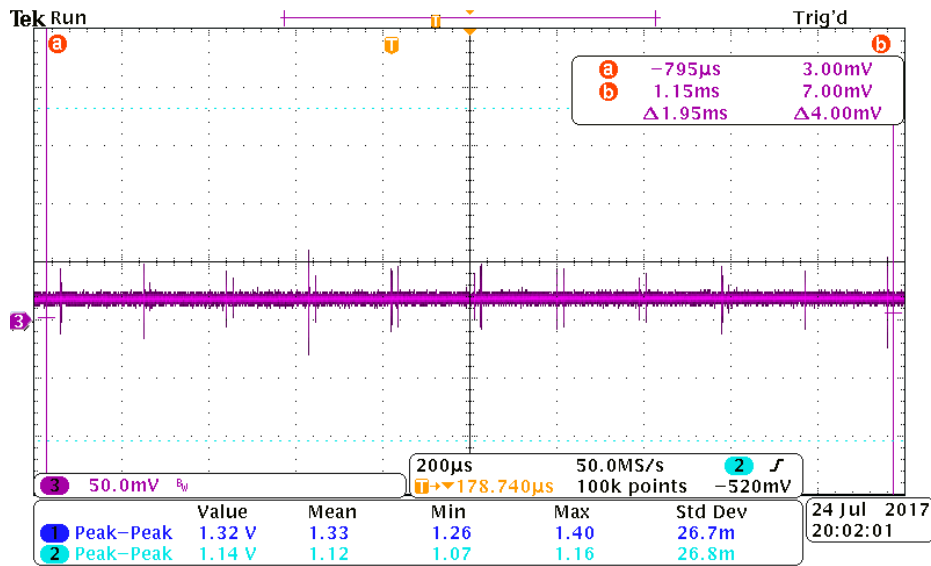


Figure 65 – Example of after rectification DC voltage measurement

Methods were used to filter out high frequency signals in the measured DC voltage and these are detailed in section 3.8.1. The DC voltage measured was across the Oscilloscope's lumped impedance for Channel 3 (1MΩ) which is in parallel with the rectification diodes, tantalum polarized capacitor, and a varying load resistance (RCS box) in which 10 different resistance values were selected. The different load resistance values chosen represent the load resistance sweep and these values were 100Ω, 1,000Ω, 5,000Ω, 10,000Ω, 40,000Ω, 100,000Ω, 500,000Ω, 1,000,000Ω, 5,000,000Ω, and 10,000,000Ω. The load resistance sweep after rectification represent different resistances that a logic circuit used to apply pulsed DC electrical stimulation could be. The CLACS is being mechanically loaded in a cyclic pattern by ultrasound waves to generate electrical potential (AC), rectify it (DC), and then use that rectified voltage to power the pulsed DC electrical stimulation logic part of the circuit. The sampling rate of the Oscilloscope was set to be at least 10 times higher than the acoustic response signal to ensure that the full waveform was being captured.

3.7.3 Recording Data

For data before and after rectification, the waveform setup file (set), waveform data file (CSV), and waveform image file (PNG), for each combination of media type, media thickness, loading orientation, type of electrical signal (before rectification), and load resistance (after rectification) using the Oscilloscope's "save all" feature. A file folder for each CLACS was created. Within each CLACS folder are folders for different media types (3 – water, tissue and tissue plus bone), within each media type folder are folders for different media thicknesses (2 - 20mm and 40mm), within each media thickness folder are folders for different loading orientations that describe how the ultrasound wave impacts the PZT disc faces in the CLACS (2 – perpendicular, parallel), and within each loading orientation folder are folders to separate voltage measurements for before and after rectification. In the before rectification (AC) folder are folders for the different electrical responses (3 – acoustic, reflection, magnetic field), and within each electrical response folder is where the waveform setup file (set), waveform data file (CSV), and waveform image file (PNG) were saved to. These voltage waveforms were measured by the Oscilloscope's Channel 1 lumped impedance (1 M Ω). A waveform setup file (set), waveform data file (CSV), and waveform image file (PNG) were saved in the before rectification (AC) folder in which the acoustics, reflection, and magnetic field electrical responses are all included in one electrical response. In the after rectification (DC) folder are folders for the 10 load resistance values of the load resistance sweep, and within each load resistance folder is where the waveform setup file (set), waveform data file (CSV), and waveform image file (PNG) were saved to. These voltage waveforms were measured by the Oscilloscope's Channel 3 lumped impedance (1 M Ω). For each CLACS, once data for all combinations of the testing parameters (media, media thickness, loading orientation, and load resistance) had been recorded before and after rectification, the process was repeated for each remaining CLACS of that compliant layer thickness. When data for all samples of a particular compliant layer thickness had been recorded, the process was repeated for the remaining compliant layer thicknesses.

3.8 Data Analysis Methods

In this section, methods of analyzing the waveform excel data files (CSV) for before and after rectification measurements for each compliant layer adaptive composite stack (CLACS) at every combination of media type, thickness of media, loading orientation, and load resistance (section 3.7.3) and statistical methods used to show significance are discussed. MATLAB was used to read in waveform data files (CSV) for each CLAC at every combination of media type, thickness of media, loading orientation direction, and load resistance to calculate peak voltage for before rectification measurements and average DC power for after rectification measurements (Section 3.8.1). Once these calculations were complete, they were tabulated in excel and averages and standard deviations were then computed for each CLACS and pivot tables were used to organize all tabulated sample data and average data (Section 3.8.2). MATLAB was then used to perform statistical analysis using ANOVA and Tukey-Kramer to compare each CLACS within each testing parameter combination of media type, thickness of media, loading orientation, and load resistance for before and after rectification. In addition the MATLAB code compared testing parameters within each CLACS using ANOVA and Tukey-Kramer (Section 3.8.3).

3.8.1 Data Analysis Methods - MATLAB

The methods of analyzing waveform excel data files (CSV) with MATLAB for each compliant layer adaptive composite stack (CLACS) at every combination of media type, thickness of media, loading orientation, and load resistance is discussed in this section. In MATLAB, an appropriately sized array was created to display before rectification computed peak voltage and average voltage, for the acoustic, magnetic field, and reflection waveforms for all parameter combinations tested. Another appropriately sized array was created to display after rectification average voltage values for all parameter combinations tested.

For before rectification (AC), the code ran through the CLACS folder paths as described in section 3.7.3. For each of these CLACS folders, the CSV waveform data file was opened and read into the MATABL workspace if it existed in the current folder. Since the Oscilloscope trigger stops the incoming waveform at time equals zero seconds and builds the waveform around that time, each of the waveforms have voltage values on the y-axis with negative time on the x-axis and also have voltage values on y-axis with positive time on the x-axis. The code made all of the time coordinates of each data point in the waveform positive by changing the most negative time data point to start at time zero and all other time data points were made positive time values by taking the difference between the time of a data point and the starting time of the waveform (i.e. -2 to 2 seconds becomes 0 to 4 seconds). Next, the maximum and minimum values of the waveform was found using MATLAB's "max()" and "min()" functions. The maximum value was then subtracted by the minimum value and divided by two to compute peak voltage of the before rectification waveform (equation 68).

$$Peak Value = \frac{max - min}{2}$$

Equation 68 - Peak value as a function of the max and min values of before rectification waveforms

In Figure 66, the before rectification acoustic response waveform (AC) for the 0.8mm CLACS sample in water medium, at 20mm media thickness, and perpendicular loading orientation is shown.

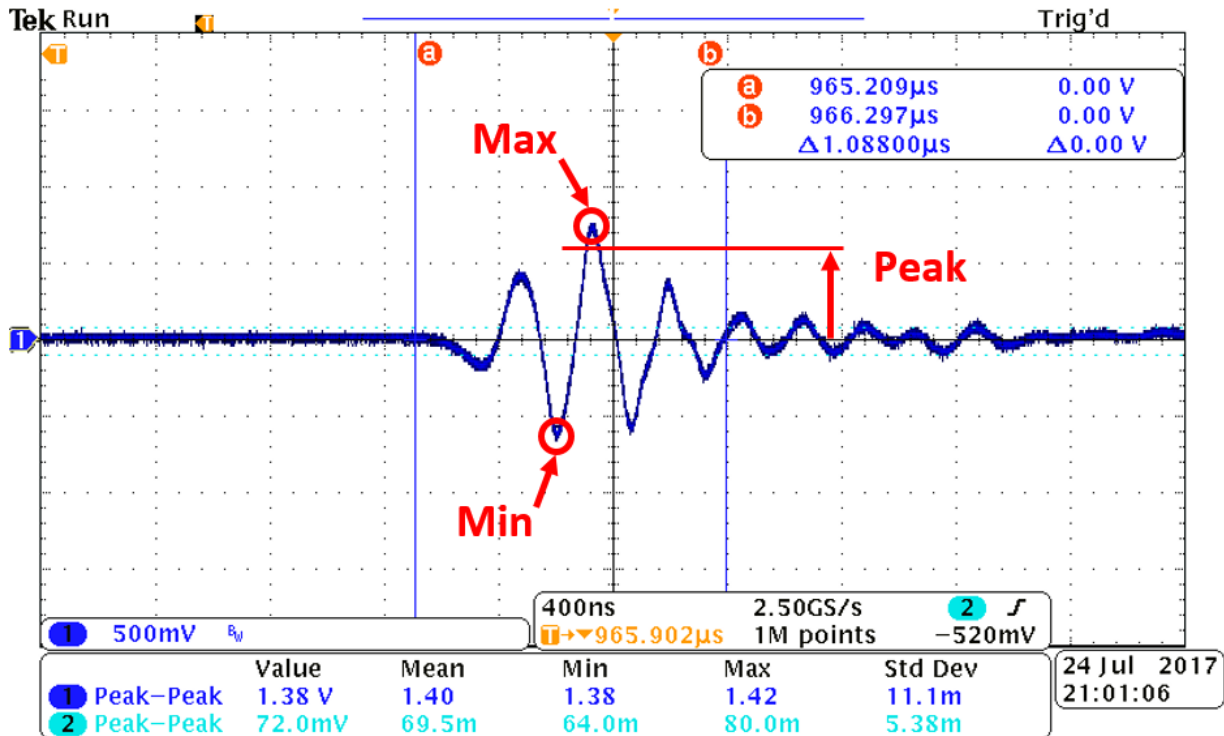


Figure 66 - Before rectification waveform (AC) for the TS85 sample in water medium, at 20mm media thickness, and perpendicular loading orientation

The collected waveform data is made up of the data points between the “a” and “b” lines in Figure 66 and the maximum, minimum, and peak voltage values are shown. An average voltage for the waveform was also computed by integrating the waveform and dividing by the duration of the waveform (equation 69).

$$\text{Average Value} = \frac{1}{u-l} * \int_l^u f(x)dx$$

Equation 69 - Average value of a waveform as a function of the upper and lower bounds of the waveform

In equation 69, “u” represents the upper bound, “l” represents the lower bound, “dx” represents the small change in time, and “f(x)” represents the function of the waveform. For the analysis in MATLAB, “u” was be the last data point and “l” was the first data point of the waveform. In order to appropriately integrate the waveform that has both positive and negative values, all waveform values were made

positive by using MATLAB's "abs()" function. If the values were not made positive, the waveform positive and negative areas would cancel each other out and the average would be zero. To find the average value of an AC signal, the waveform must be made all positive first. To numerically integrate the waveform, the trapezoidal summation method was used which adds up a large amount of small trapezoids that were made from the data points of the waveform to calculate the "area under the curve" (equation 70).

$$\int_l^u f(x)dx \approx \sum_{n=1}^N \left[\left(\frac{f(x_{n-1}) + f(x_n)}{2} \right) * \Delta x_n \right] = \text{sum}$$

Equation 70 - Trapezoidal Rule approximating the area under a curve

In equation 71, N represents the total number of data points, x_n represents the "nth" data point, and Δx_n represents the change in time from one data point to the next. The waveform was then divided by its time duration to get an average voltage value (equation 71).

$$\text{Average Value} = \frac{\text{sum}}{u - l}$$

Equation 71 - Average value of a curve as a function of the approximated sum using the trapezoidal rule (equation 70) and the upper and lower bounds of the curve

This was done for each combination tested before rectification on the CLACS and was tabulated into the pre-sized data array.

For after rectification, the code ran through the CLACS folder paths as described in section 3.7.3. For each of these, the CSV waveform data file was opened and read into the MATALB workspace if it existed in the current folder. In the same way as in before rectification, the code manipulated the time axis of each waveform so that all time on the x-axis was positive with the most negative time data point as time zero. Next, the code computed the average voltage for the waveform in a similar way to the before rectification section. This time the waveform values were not made to all be positive when

finding the average value of the waveform. When trying to find the average value of a DC voltage that is noisy, it was found that by taking the absolute value of the waveform before using equation 38 the average value was overestimated, especially when the waveform voltage average hovered a little above 0. As the DC voltage waveform moved higher above zero and eventually when all data points were above zero, it did not matter whether the absolute value of the waveform was performed or not because all values were positive. The average values became closer as the DC voltage waveform moved higher above zero.

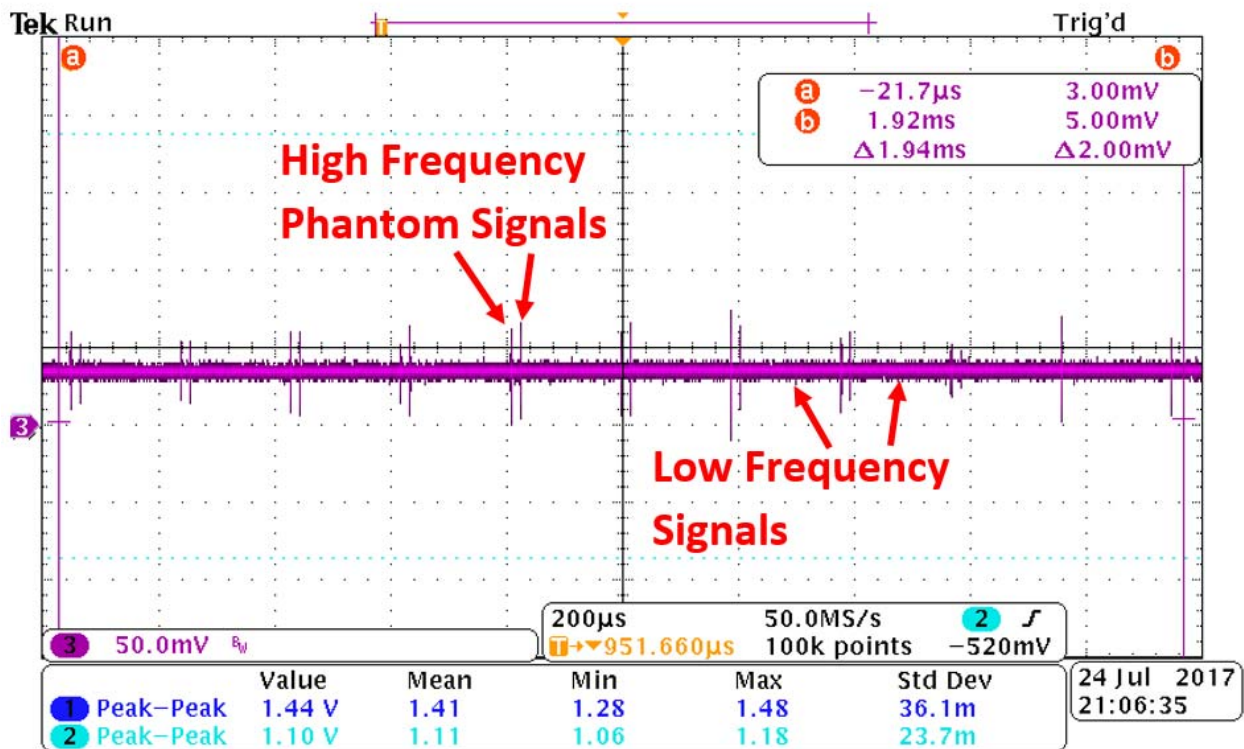


Figure 67 - After rectification waveform (DC) for the TS85 sample in water medium, at 20mm media thickness, perpendicular loading orientation, and 10MΩ load resistance

In Figure 67, high frequency noise and pulses are present in the after rectification waveform (DC) in addition to lower frequency signals that make up the bulk of the waveform. There seems to be two “phantom” signals where one occurs every 190 μs (approximately) which is confirmed to be the response that is generated by the magnetic field of the ultrasound probe wire and the other signal that

occurs a small amount of time after the first phantom signal seems to be a reflection or repetition of the first. Regardless of the origin of these “phantom” signals they needed to be removed from the after rectification waveform (DC) so a more accurate average could be computed. An effort was made to reduce the effect of these “phantom” impulses by braiding and shortening the circuit wires (Figure 68).

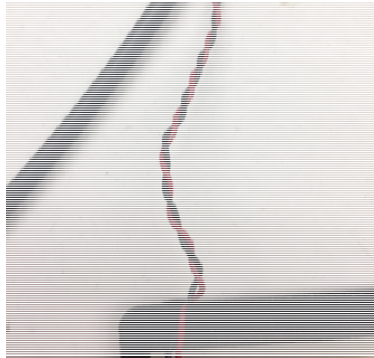


Figure 68 - Braided wire used throughout rectification circuit for testing in an attempt to reduce the effect of unwanted magnetic fields

Unfortunately, these “phantom” signals still showed up in the after rectification waveform (DC) so a mathematical method to remove them was followed. A Fast Fourier Transform (FFT) was performed in MATLAB on the waveform data to highlight the amplitudes of various frequencies that are present in the after rectification waveform (Figure 69).

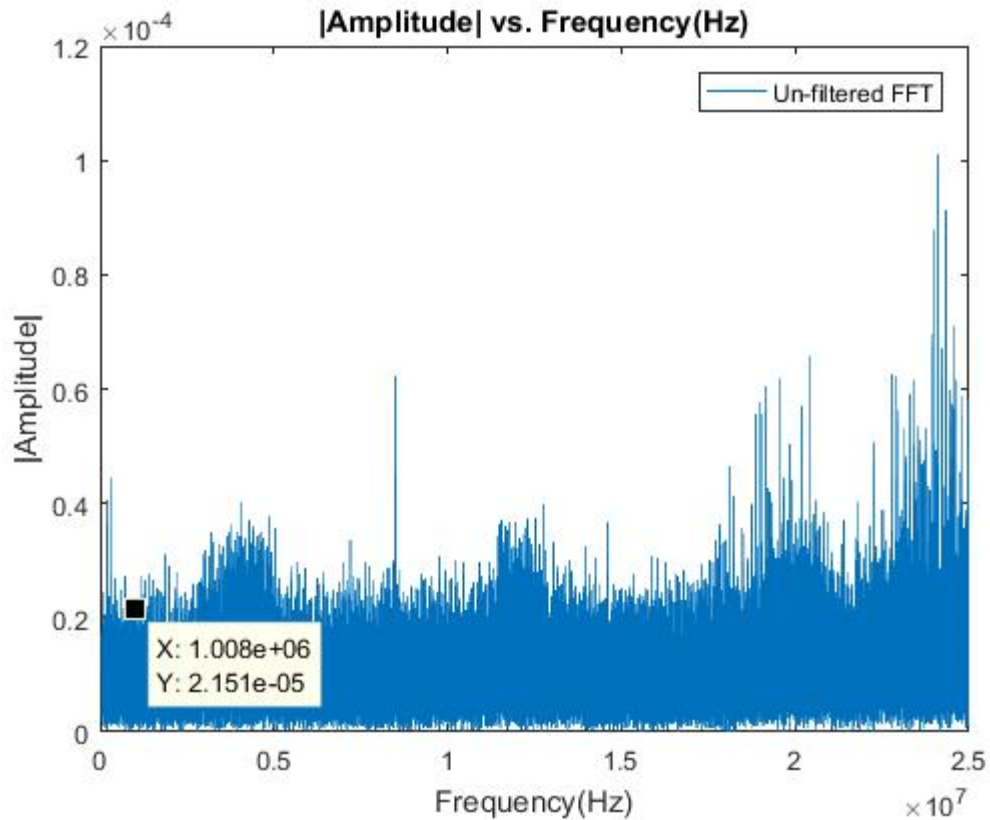


Figure 69 - Fast Fourier Transform (FFT) Response of after rectification waveform (DC) in Figure 67

In Figure 66, there are high frequency signals with higher amplitudes than the smaller frequency signals which is shown in Figure 66 with the “phantom” impulses having a much larger amplitude compared to the lower frequency signals. A 6th order Butterworth filter was used in MATLAB to filter the after rectification waveforms by removing the high frequency signals and their amplitudes. The high order was chosen to have a sharper cutoff occur at the cutoff frequency because lower order cutoff frequencies have a gradual cutoff. A sampling frequency of 50MHz was used in the Butterworth filter because this was the sampling frequency of all the after rectification waveforms. Lastly, a cutoff frequency of 1MHz was used to eliminate any higher frequency signals from the after rectification waveform (Figure 70).

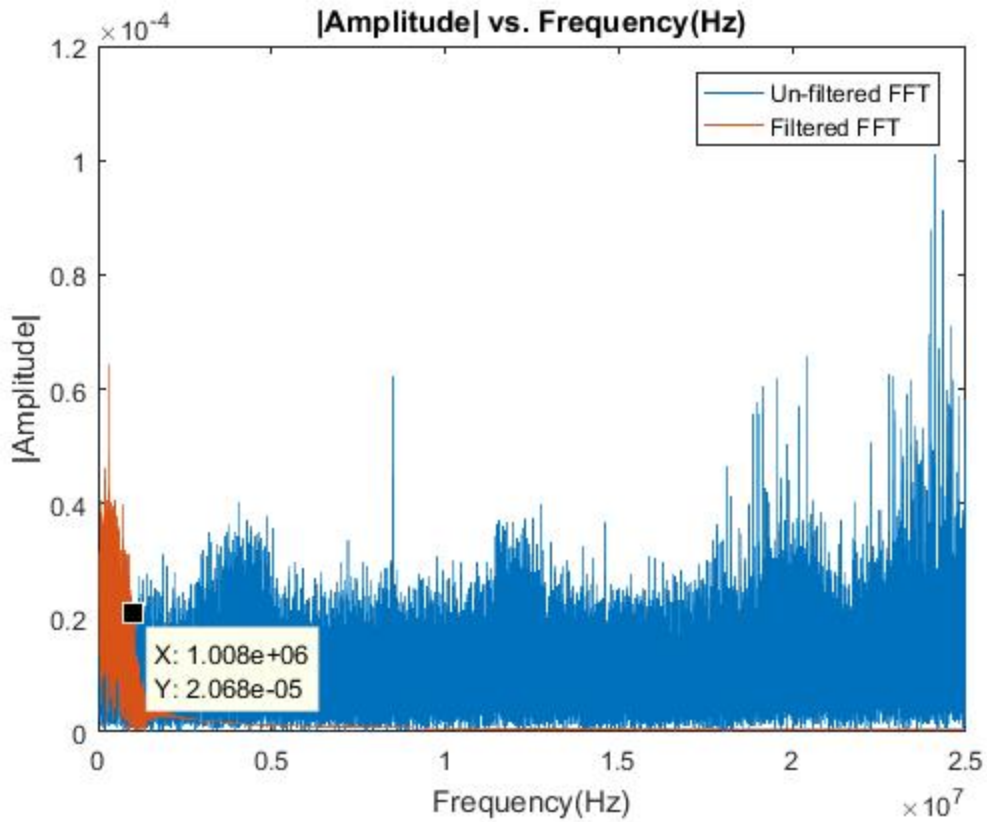


Figure 70 - Fast Fourier Transform (FFT) Response of after rectification waveform (DC) in Figure 67 and of filtered after rectification waveform

After designing the Butterworth filter and applying it to the after rectification waveform data, the signal (DC) was less noisy and more reasonable to be used to compute an average voltage (Figure 71).

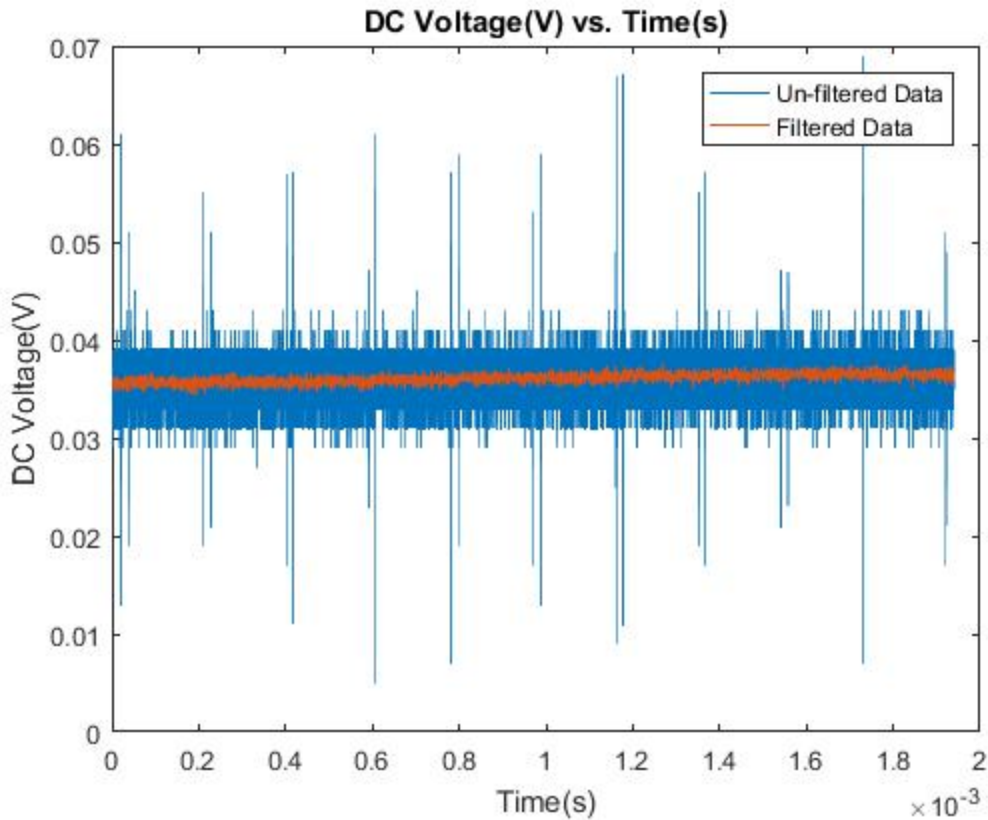


Figure 71 – Unfiltered and filtered after rectification waveform (DC) for the TS85 sample in water medium, at 20mm media thickness, perpendicular loading orientation, and 10M Ω load resistance

This average voltage was then converted into electrical power by combining Joule’s and Ohm’s law that uses voltage (V) and impedance (Z) as inputs (equation 67). Electrical power was calculated across the lumped impedance of the electrical components after rectification (capacitor, load resistance, and lumped oscilloscope resistance connected in parallel), and across each individual component. This was done for each combination tested after rectification for one of the CLACS and was tabulated into the pre-sized data array for after rectification.

Now each CLACS had two data arrays for each combination tested in before and after rectification measurements that contain peak voltage and power values respectively. These two data arrays for the CLACS were then copied into an excel workbook to consolidate all data into one source. This MATLAB code was run for each CLACS (n = 20) and can be seen in section A.1 of the Appendix.

3.8.2 Data Analysis Methods – Organization in Excel

After the MATLAB code was run for each CLACS to calculate peak voltage for before rectification measurements and average DC power for after rectification measurements, the data arrays for before and after rectification were copied into an excel workbook to consolidate all data into one source. Each CLACS data was compiled into two universal data tables for before and after rectification measurements. Once these two universal data tables were built, averages and standard deviations were computed for each CLACS with a sample size of 5 at each testing parameter combination of media type, media thickness, loading orientation, and load resistance. Two more data tables were created which contain the averages and standard deviations of each testing parameter combination of media type, media thickness, and loading orientation. Pivot tables were created for each of the four data arrays and were used to organize select portions of the data to be observed and then graphed.

3.8.3 Statistical Analysis Methods – MATLAB

In this section, statistical methods that were used to determine significance between CLACSs within each testing parameter and between testing parameters within each CLACS is discussed. The pivot tables in excel allowed for easy data organization for statistical analysis and was done for each testing parameter configuration before and after rectification to fully compare the entire data set. An example set of organized data is shown in Figure 72.

	A	B	C	D
1	Specimen	Water	Tissue	TB
2	0mm	0.464	0.00608	0.0104
3	0mm	0.456	0.186	0.02
4	0mm	0.392	0.114	0.0021
5	0mm	0.592	0.282	0.0312
6	0mm	0.616	0.356	0.0392
7	0.2mm	0.576	0.083	0.00192
8	0.2mm	0.444	0.168	0.00212
9	0.2mm	0.628	0.077	0.00196
10	0.2mm	0.324	0.079	0.00204
11	0.2mm	0.332	0.089	0.00152
12	0.4mm	0.528	0.262	0.0044
13	0.4mm	0.528	0.0148	0.0054
14	0.4mm	1.01	0.26	0.022
15	0.4mm	0.616	0.34	0.0248
16	0.4mm	0.664	0.404	0.0196
17	0.8mm	0.94	0.2	0.0054
18	0.8mm	0.7	0.292	0.002
19	0.8mm	0.556	0.278	0.0027
20	0.8mm	0.676	0.224	0.0032
21	0.8mm	0.7	0.252	0.0055

Figure 72 - Example organized data set for statistical analysis. This data set is organized for comparing different CLACS types within each media parameter and for comparing each media parameter within each CLACS.

This was done for each testing parameter configuration before and after rectification to fully compare the entire data set. Once all data sets were organized, MATLAB code was used to assess normality and perform statistical significance test. One-way ANOVA and Tukey-Kramer pair-wise multi-comparison tests were run in MATLAB and each assumes a normal distribution of data. Each data set was checked for normality by plotting a box and whisker, histogram, QQ, and residual plot using MATALB functions. For the QQ plot, a linear model was made for each data set and was used as an input to the QQ plot MATLAB function. All checks for normality were done by the user and it was determined by the user if the data was normal or not. If the data was not normal, then a transformation was performed on the data to normalize it. Five different transformations were performed on the data sets to determine which one across all data sets would produce the most normal data sets. These include a square-root, squared, reciprocal, logarithm (base e), and BoxCox transformation. The BoxCox transformation is a data transformation that transformers non-normal data to an approximately normal distribution by using equations 72 and 73 ⁴⁵.

$$data(\lambda) = \frac{data^\lambda - 1}{\lambda}$$

Equation 72 - Transforming data using the BoxCox method as a function of λ , which is determined by the MATLAB program

If λ was equal to zero, then the BoxCox transformation became a logarithm (base e) transformation (equation 73).

$$data(\lambda) = \log(data)$$

Equation 73 - If λ is equal to 0 then the log transformation is performed

Since the original data sets were not normally distributed, all five transformations were run for data sets before rectification and some data sets after rectification for the 500 kilo-ohm and 10 mega-ohm load resistance data sets to determine which transformation to use before performing statistical analysis. The user determined which of the five transformations made the data the most normal and that transformation was counted. After running the transformations across the data sets described previously, the BoxCox transformation made the data sets the most normal. This transformation was then used for the rest of the data set combinations to be compared.

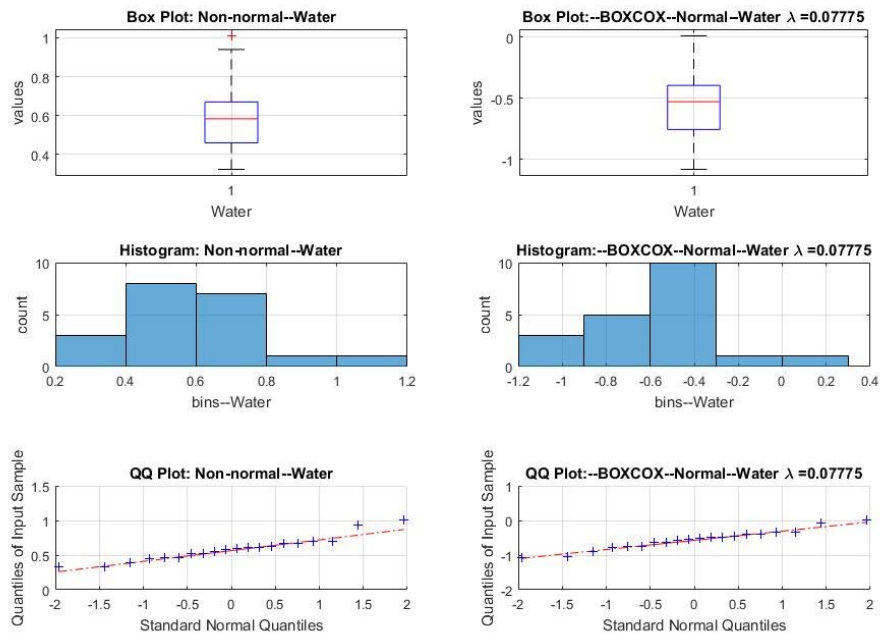


Figure 73 - Normality plots for a non-normal data set and the transformed (BoxCox) data set for the CLACs within the water testing parameter.

The non-normal and approximately normal (BoxCox transformation) box and whisker, histogram and QQ plots for the CLACs data sets within the water testing parameter before rectification is shown in Figure 73. The BoxCox transformation reduced the skewing seen in the histogram and box and whisker plots and the data points more closely follow the linear model in the QQ plot and thus made the data set more normal.

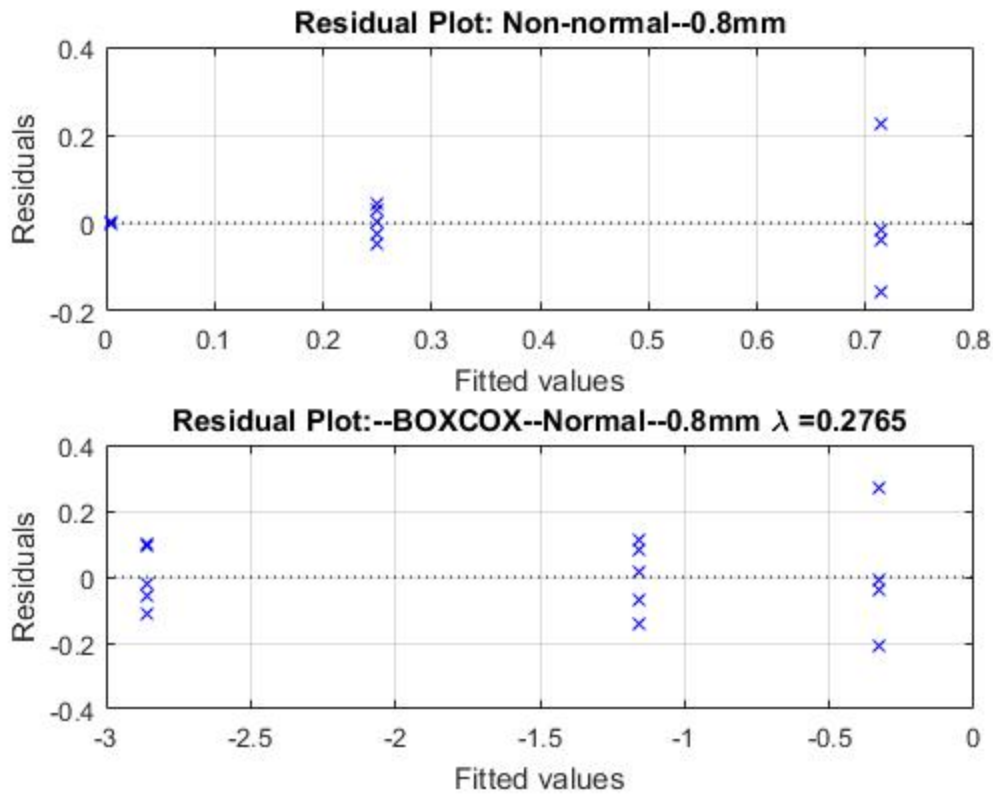


Figure 74 - Residual plot for non-normal data set and transformed (BoxCox) data set for media testing parameters within the 0.8mm CLACS

The non-normal and approximately normal (BoxCox transformation) residual plot for the CLACSs data sets within the water testing parameter before rectification is shown in Figure 74. The BoxCox transformation spread the residuals of the media testing parameter data sets more evenly about the zero line, making the data sets more normal. Now that the data sets are normal, a one-way ANOVA was run for each data set of CLACSs within a testing parameter and for all testing parameters within each individual CLACS. If the one-way ANOVA outputted significance, then a post-hoc Tukey-Kramer pairwise multi-comparison test was performed in MATLAB to determine significance between all comparisons.

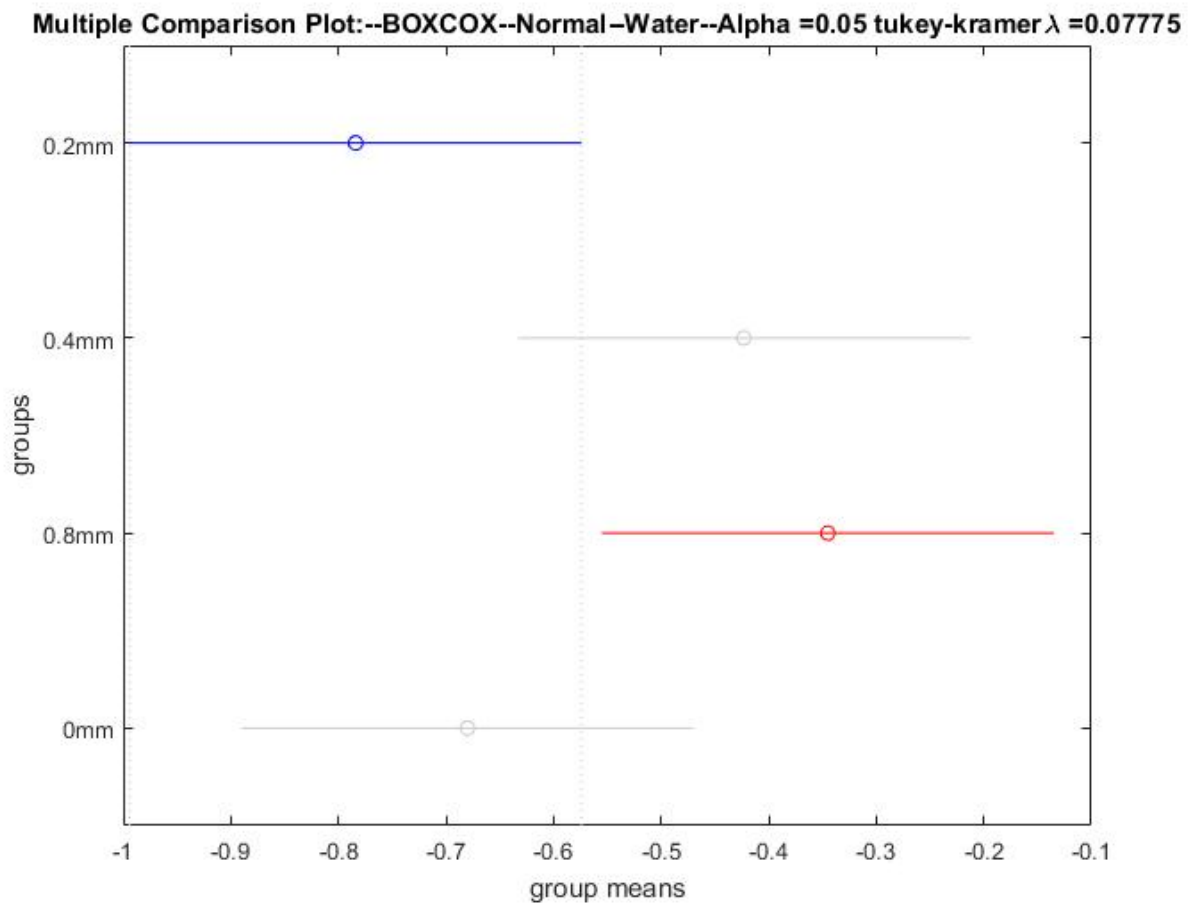


Figure 75 - Multiple Comparison Plot (Tukey-Kramer) comparing CLACS group means within the water testing parameter. The 0.2mm group mean is significantly different from the 0.8mm group mean ($p < 0.05$).

Figure 75 shows the result of running a Tukey-Kramer Multiple Comparison MATLAB function comparing the CLACSs group means within the water testing parameter. In addition to the Multiple comparison plots, MATLAB outputted arrays of information including p values of all compared groups, group means, group standard deviations, lower 95% confidence level limit, upper 95% confidence level limit, and differences between group means. These arrays were saved in the MATLAB workspace and were copied into an excel workbook. All significance tests (one-way ANOVA and Tukey-Kramer) were run with an alpha level of 0.05. This means that there is a 95% confidence level that groups means are significantly

different or they are not. Figure 76 shows how the data sets were put into MATLAB for normality and statistical analysis to be run.

	A	B	C	D
1	Specimen	Water	Tissue	TB
2	0mm	0.464	0.00608	0.0104
3	0mm	0.456	0.186	0.02
4	0mm	0.392	0.114	0.0021
5	0mm	0.592	0.282	0.0312
6	0mm	0.616	0.356	0.0392
7	0.2mm	0.576	0.083	0.00192
8	0.2mm	0.444	0.168	0.00212
9	0.2mm	0.628	0.077	0.00196
10	0.2mm	0.324	0.079	0.00204
11	0.2mm	0.332	0.089	0.00152
12	0.4mm	0.528	0.262	0.0044
13	0.4mm	0.528	0.0148	0.0054
14	0.4mm	1.01	0.26	0.022
15	0.4mm	0.616	0.34	0.0248
16	0.4mm	0.664	0.404	0.0196
17	0.8mm	0.94	0.2	0.0054
18	0.8mm	0.7	0.292	0.002
19	0.8mm	0.556	0.278	0.0027
20	0.8mm	0.676	0.224	0.0032
21	0.8mm	0.7	0.252	0.0055

Figure 76 – An example of a select portion of the before rectification data set used in the statistical analysis. Vectors of information were used in one-way ANOVA and Tukey-Kramer pair wise multicomparison tests to determine significance within that vector of information. The highlighted red column represents a vector of information in which statistical significance tests were run between CLACs (0mm, 0.2mm, 0.4mm, and 0.8mm) and a testing parameter (water). The highlighted blue square represents a vector of information in which statistical significance tests were run between testing parameters (water, tissue, tissue plus bone) within a CLACS (0mm).

The red column in Figure 76 represents data for each CLACS type within the water testing parameter.

The blue square was made into another column of data by taking the 5 data samples in the “Tissue” and “TB” column (tissue plus bone) and placing them under the first five data samples in the “Water” column. This column of information represents data for the media testing parameters within a CLACS type (0mm). The code used to perform normality and statistical analysis for this study can be seen in Appendix A.2.

Chapter 4. Conclusions and Future Work

By adding a compliant layer thickness between the PZT discs of the CLACS and by increasing that compliant layer thickness, generated electrical potential increased before rectification and thus power output increased after rectification. The effect of a compliant layer allows for more deformation to occur along the entire face and edges of the PZT discs during ultrasound loading and take advantage of the piezoelectric effect to improve power output. There were significant effects before and after rectification by varying media type and loading orientation, but little effect with varying media thickness (distance).

There were a couple of limitations in this study. It was not realistic to produce a large sample size of CLACS due to funding limitations and thus a small sample size ($n=5$ for each CLACS) was manufactured. This small sample size decreases the ability to detect an effect on average power output while varying testing parameters in the study (media type, media thickness, loading orientation, and load resistance) when there is one to be detected and therefore Type II error could have occurred in statistical analysis. Time to complete testing was also another limitation because another graduate student needed to use the CLACS and ultimately destroy them for a different study. In order for this work to get data, testing needed to be finished in a quick time frame so that it did not limit the other study being conducted in parallel to this one. Testing in a quick time frame rushed study design decisions such as electrical component selection and the method of placing all the CLACS consistently in the same spot above the ultrasound probe face during testing.

To compare the power output capabilities of this study to another for a spinal fusion application would be beneficial. The average total power output for the 0.8mm CLACS is 6.71 mW (@ 10M Ω load resistance value and all media types, media thicknesses, and loading orientations) and the average load power output for the 0.8mm CLACS is 0.00002203 μ W (@ 500K Ω load resistance value and all media

types, media thicknesses, and loading orientations). In Goetzinger et al., a spinal fusion composite was also investigated by using layers of PZT fibers and epoxy and at loading of 1,000 N and a frequency of 2 Hz (Uniaxial MTS), the maximum power achieved was up to approximately 1,300 μ W which is less than the average total power output for the 0.8mm CLACS (6.71 mW) but is much larger than the average load power output for the 0.8mm CLACS (0.00002203 μ W)². Similar power was produced by the CLACS (total power) using ultrasound as the loading source in this study compared to Goetzinger et al. for a spinal fusion application, but more studies could be conducted to enhance the energy harvesting capabilities of the CLACS in addition to the effect of compliant layers on power output across the load resistance (load power) that represents the lumped impedance of a DC electrical stimulation logic circuit used in spinal fusion applications.

Future work could build off this foundational study by further investigating the effect of compliant layers on power output of the CLACS with focused vs. unfocused ultrasound as sources of loading, different operating frequencies to match and mismatch the resonant frequency of PZT discs (5MHz), more varied loading orientations (angled), different input sound intensity levels on the ultrasound source, using a combination of radially and through-thickness poled PZT stacked layers in the CLACS, varying rectifying circuit components and design to reduce electrical energy reflection, and lastly implementing a DC electrical stimulation logic circuit after rectification to approach a more realistic application of DC electrical stimulation in bone healing for spinal fusion. Additionally, a theoretical study could be investigated using the foundational information provided in section 1.4 to model power output of a CLACS with ultrasound as the loading source and other parameters.

References

1. Kucharzyk DW. 1999. A Controlled Prospective Outcome Study of Implantable Electrical Stimulation With Spinal Instrumentation in a High-Risk Spinal Fusion Population: *Spine* 24(5):465–468.
2. Goetzinger NC, Tobaben EJ, Domann JP, et al. 2016. Composite piezoelectric spinal fusion implant: Effects of stacked generators. *J. Biomed. Mater. Res.* 104(1):158–164.
3. Wei X, Liu J. 2008. Power sources and electrical recharging strategies for implantable medical devices. *Frontiers of Energy and Power Engineering in China* 2(1):1–13.
4. Tobaben EJ, Goetzinger NC, Domann JP, et al. 2015. Stacked macro fiber piezoelectric composite generator for a spinal fusion implant. *Smart Mater. Struct.* 24(1):017002.
5. Friis, Elizabeth A, Galvis, Sarah N, Cadel, Eileen, Sis, Hadley L, Wong, Benjamin M, and Arnold, Paul M, "DC Stimulation for Spinal Fusion with a Piezoelectric Composite Material Interbody Implant: A Pilot Ovine Study," Society For Biomaterials, Charlotte, NC. Transactions of the 2015 Society For Biomaterials Meeting: (April 15, 2015 - April 17, 2015).
6. 2009. Spinal Disorders: Fundamentals of Diagnosis and Treatment. *American Journal of Neuroradiology* 30(3):e44–e44.
7. Kurtz SM, Edidin A. 2006. *Spine Technology Handbook*. Burlington, UNITED STATES: Elsevier Science. [cited 2017 Dec 22] Available from: <http://ebookcentral.proquest.com/lib/ku/detail.action?docID=270196>.
8. Toth JM, Seim HB, Schwaradt JD, et al. 2000. Direct Current Electrical Stimulation Increases the Fusion Rate of Spinal Fusion Cages: *Spine* 25(20):2580–2587.
9. Cook SD, Patron LP, Christakis PM, et al. 2004. Direct current stimulation of titanium interbody fusion devices in primates. *The Spine Journal* 4(3):300–311.
10. Gan JC, Glazer PA. 2006. Electrical stimulation therapies for spinal fusions: current concepts. *Eur Spine J* 15(9):1301–1311.
11. Platt SR, Farritor S, Haider H. 2005. On Low-Frequency Electric Power Generation With PZT Ceramics. *IEEE/ASME Transactions on Mechatronics* 10(2):240–252.
12. Denisov A, Yeatman E. 2010. Ultrasonic vs. Inductive Power Delivery for Miniature Biomedical Implants. In: 2010 International Conference on Body Sensor Networks. p 84–89.
13. [date unknown]. *ACDF_coronal_english.png* (3256×1394). [cited 2017 Dec 23] Available from: https://upload.wikimedia.org/wikipedia/commons/9/9a/ACDF_coronal_english.png.
14. [date unknown]. *Spinal-disc-protrusion-l5.jpg* (875×1024). [cited 2017 Dec 23] Available from: <https://upload.wikimedia.org/wikipedia/commons/e/e7/Spinal-disc-protrusion-l5.jpg>.

15. Zdeblick TA, Phillips FM. 2003. Interbody Cage Devices: Spine 28(supplement):S2–S7.
16. Fredericks DC, Smucker J, Petersen EB, et al. 2007. Effects of Direct Current Electrical Stimulation on Gene Expression of Osteopromotive Factors in a Posterolateral Spinal Fusion Model: Spine 32(2):174–181.
17. Bodamyali T, Kanczler J., Simon B, et al. 1999. Effect of Faradic Products on Direct Current-Stimulated Calvarial Organ Culture Calcium Levels. Biochemical and Biophysical Research Communications 264(3):657–661.
18. Bushinsky DA. 1996. Metabolic alkalosis decreases bone calcium efflux by suppressing osteoclasts and stimulating osteoblasts. American Journal of Physiology-Renal Physiology 271(1):F216–F222.
19. Cho M, Hunt TK, Hussain MZ. 2001. Hydrogen peroxide stimulates macrophage vascular endothelial growth factor release. American Journal of Physiology-Heart and Circulatory Physiology 280(5):H2357–H2363.
20. Ethier CR. 2007. Introductory biomechanics: from cells to organisms. Cambridge ; New York: Cambridge University Press.
21. Bassett CAL, Becker RO. 1962. Generation of Electric Potentials by Bone in Response to Mechanical Stress. Science 137(3535):1063–1064.
22. Bassett CAL, Pawluk RJ, Becker RO. 1964. Effects of Electric Currents on Bone In Vivo. Nature 204(4959):652–654.
23. Anton SR, Sodano HA. 2007. A review of power harvesting using piezoelectric materials (2003–2006). Smart Mater. Struct. 16(3):R1.
24. [date unknown]. 548px-Piezoelectric_effect.svg.png (548×397). [cited 2018 Jan 8] Available from: https://upload.wikimedia.org/wikipedia/commons/thumb/2/21/Piezoelectric_effect.svg/548px-Piezoelectric_effect.svg.png.
25. Vijaya MS. 2012. Piezoelectric Materials and Devices: Applications in Engineering and Medical Sciences. CRC Press [cited 2017 Dec 23] Available from: <https://www.crcpress.com/Piezoelectric-Materials-and-Devices-Applications-in-Engineering-and-Medical/Vijaya/p/book/9781439887868>.
26. Baker J, Roundy S, Wright P. [date unknown]. Alternative Geometries for Increasing Power Density in Vibration Energy Scavenging for Wireless Sensor Networks. In: 3rd International Energy Conversion Engineering Conference. American Institute of Aeronautics and Astronautics [cited 2017 Dec 23] Available from: <https://arc.aiaa.org/doi/abs/10.2514/6.2005-5617>.
27. Blackstock DT, Atchley AA. 2001. Fundamentals of Physical Acoustics. The Journal of the Acoustical Society of America 109(4):1274–1276.

28. Smith NB, Webb A. 2010. Introduction to Medical Imaging: Physics, Engineering and Clinical Applications. Cambridge University Press. 299 p.
29. Calderon C, Vilkomerson D, Mezrich R, et al. 1976. Differences in the attenuation of ultrasound by normal, benign, and malignant breast tissue. *J. Clin. Ultrasound* 4(4):249–254.
30. Acuson. (1991). Acuson 128XP Computed Sonography Systems Service Manual Service Manual: Service Manual for Acuson 128XP Computed Sonography System. Mountain View, CA: Author.
31. Lee SQ, Youm W, Hwang G. 2013. Biocompatible wireless power transferring based on ultrasonic resonance devices. *Proceedings of Meetings on Acoustics* 19(1):030030.
32. Cochran GVB, Kadaba MP, Palmieri VR. 1988. External ultrasound can generate microampere direct currents in vivo from implanted piezoelectric materials. *J. Orthop. Res.* 6(1):145–147.
33. Ozeri S, Shmilovitz D. 2010. Ultrasonic transcutaneous energy transfer for powering implanted devices. *Ultrasonics* 50(6):556–566.
34. Duck FA, Baker AC, Starritt HC. 1998. *Ultrasound in Medicine*. Bristol: CRC Press. [cited 2017 Nov 12] Available from:
<http://search.ebscohost.com/login.aspx?direct=true&db=nlebk&AN=27527&site=ehost-live>.
35. [date unknown]. *Medical ultrasonics 2.4.6*. [cited 2017 Nov 12] Available from:
http://www.kayelaby.npl.co.uk/general_physics/2_4/2_4_6.html.
36. White SM. 2005. Diagnostic Ultrasound: Physics and Equipment. *European Journal of Anaesthesiology* 22(9):734.
37. Larson PJ, Towe BC. 2011. Miniature ultrasonically powered wireless nerve cuff stimulator. *IEEE*. p 265–268 [cited 2017 Nov 13] Available from: <http://ieeexplore.ieee.org/document/5910538/>.
38. Arra S, Leskinen J, Heikkila J, Vanhala J. 2007. Ultrasonic Power and Data Link for Wireless Implantable Applications. *IEEE* [cited 2017 Nov 13] Available from:
<http://ieeexplore.ieee.org/document/4147127/>.
39. Song SH, Kim A, Ziaie B. 2015. Omnidirectional Ultrasonic Powering for Millimeter-Scale Implantable Devices. *IEEE Transactions on Biomedical Engineering* 62(11):2717–2723.
40. Songhvi NT, Hynynen K, Lizzi FL. 1996. New developments in therapeutic ultrasound. *IEEE Engineering in Medicine and Biology Magazine* 15(6):83–92.
41. Nyborg W. 2002. Safety of medical diagnostic ultrasound. *Seminars in Ultrasound, CT and MRI* 23(5):377–386.
42. Dalecki D. 2004. Mechanical Bioeffects of Ultrasound. *Annual Review of Biomedical Engineering* 6(1):229–248.

43. [date unknown]. 1N60P pdf, 1N60P description, 1N60P datasheets, 1N60P view ::: ALLDATASHEET ::: [cited 2017 Dec 7] Available from: http://pdf1.alldatasheet.com/datasheet-pdf/view/281737/SEMTECH_ELEC/1N60P.html.
44. [date unknown]. Say-AlternatingCurrentMachines.pdf. [cited 2017 Dec 13] Available from: <https://ia801403.us.archive.org/31/items/AlternatingCurrentMachines/Say-AlternatingCurrentMachines.pdf>.
45. [date unknown]. Box-Cox transformation - MATLAB boxcox. [cited 2017 Dec 16] Available from: <https://www.mathworks.com/help/finance/boxcox.html>.

Appendix A: MATLAB Code used for Analysis

This section of the Appendix provides the MATLAB code used to analyze Oscilloscope waveform data, statistical analysis, and after rectification filtering analysis.

Appendix A.1: MATLAB Code used to analyze Oscilloscope Waveform Data

This section of the Appendix contains the code used to analyze Oscilloscope waveform data for all Compliant Layer Adaptive Composite Stacks (CLACS) to calculate to calculate peak voltage for before rectification measurements and average DC power for after rectification measurements at every combination of media type, thickness of media, loading orientation direction, and load resistance. The code below is for the one of the 0.8mm CLACS (TS85). The code originally included an elementary method to find the impedance of the CLACS, but this idea was not validated and the additional 200 lines of code are not included in this paper.

MATLAB Code:

```
%%%%%%%%%%%%%%%%%%%%%%%%%%%%%%%%%%%%%%%%%%%%%%%%%%%%%%%%%%%%%%%%%%%%%%%%%
%%%%%%%%%%%%%%%%%%%%%%%%%%%%%%%%%%%%%%%%%%%%%%%%%%%%%%%%%%%%%%%%%%%%%%%%% Ultrasound Data Analysis Code %%%%%%%%%%
%%%%%%%%%%%%%%%%%%%%%%%%%%%%%%%%%%%%%%%%%%%%%%%%%%%%%%%%%%%%%%%%%%%%%%%%%
%Kyle Coates - Graduate Student (M.S.), Dr. Lisa Friis Spine Biomechanics
%Lab
%July 5 2017

%The purpose of this code is to characterize three things about the spinal
%fusion inserts being made in Dr. Friss's lab using Ultrasound as the
%source of mechanical testing. This code will calculate and characterize
%the inserts "lumped" internal impedance, electric potential being
%generated by the insert from the Ultrasonic waves (small pressure waves),
%and lastly the Power across a sweeping load resistance after the
%alternating current has been rectified (AC-DC). The electric potential
%being generated by the insert and Power across load resistances were all
%tested at different loading parameters from the Ultrasound probe/test
%setup. These parameters include different media types that were placed
%between the insert (receiver) and the Ultrasound probe (source), the
%distance of between the insert (receiver) and the Ultrasound probe
%(source), and lastly the orientation at which the PZT are aligned with the
%face of the Ultrasound probe. The three media that were tested in these
%experiments were water, tissue, and tissue + bone. The two distances that
%were tested for each media were approximately 20mm and 40mm. And lastly
```

%the two orientations that were tested were when the PZT discs are parallel
%and perpendicular to the flat surface of the Ultrasound probe.

%Function to initialize global variables used in all other functions and to
%setup foundation for all other functions.

```
function Ultrasound_Data_Analysis_xx_new()

    %clear/close all things
    clear
    close all
    clc
    %Declare global variables
    global specimen_name
    global file_path_temp
    global freq
    global c_water
    global c_tissue
    global c_bone
    global wavelength_water
    global wavelength_tissue
    global wavelength_bone
    global R_Oscilloscope
    global R_Load
    global num_distances
    global num_orientation
    global num_signals
    global num_resistances
    global num_samples
    global num_media
    global time_between_signal_groups
    global figure_count
    global ultrasound_hertz
    global output_headings
    global input_headings
    global R_Load_Insert_Impedance
    global num_resistances_insert_impedance
    global impedance_headings
    global insert_impedance_peak
    global insert_impedance_avg
    global Capacitor_Reactance
    global Capacitor_Capacitance
    global PI
    global fs;
    global fc;
    global n;
    %define global variables
    %The user must change these values/text if the testing was done
    %differently (different number of distances, different number of media,
    %different orientation, etc.).
    specimen_name = ('Specimen_xx'); %specimen name for output data
    file_path_temp = ('H:\Documents\KU_Career\Dr. Friis Research\Ultrasound
Data\specimen_xx'); %
    freq = 4E6; %4MHz medical imaging machine probe (1/s)
    c_water = 1500; %speed of sound in water (m/s)
    c_tissue = 1590; %speed of sound in tissue/muscle (m/s)
    c_bone = 4000; %speed of sound in bone (m/s)
```

```

wavelength_water = c_water/freq; %wavelength of acoustic wave through
%water media (m)
wavelength_tissue = c_tissue/freq; %wavelength of acoustic wave through
%tissue media (m)
wavelength_bone = c_bone/freq; %wavelength of acoustic wave through
%tissue media (m)
R_Oscilloscope = 1e6; %Resistance setting in oscilloscope for input
%channels (ohm)
R_Load = [100 1e3 5e3 10e3 40e3 100e3 500e3 1e6 5e6 10e6]; %Resistance
%sweep for Rvar (ohm)
num_distances = 2; %number of distances: ~20mm and 40mm of media
%material in between insert (reciever) and Ultrasound probe (source)
num_orientation = 2; %number of orientations: discs parallel and
%perpendicular to Ultrasound probe face
num_signals = 3; %Acoustic, reflection, and magnetic field induced
%electrical signals
num_resistances = length(R_Load); %number of resistances in resistance
%sweep
num_samples = 1; %number of samples taken at type of signal parameter
%set
num_media = 3; %number of media used in Ultrasonic testing: water
%(base), tissue, tissue and bone
time_between_signal_groups = 190e-6; %time between grouped electrical
%responses (sound, magfield, and reflection combined)
figure_count = 1; %initialize figure count
ultrasound_hertz = 27; % (1/s);
PI = 3.14159265358979323846;
Capacitor_Capacitance = 2.2e-6; %farads
Capacitor_Reactance = 1/(2*PI*freq*Capacitor_Capacitance);
%headings for input and output matrices of information
output_headings = {'DC_Load_Power (Watts)', 'DC_Total_Power (Watts)',
'Resistance (ohms)', 'Orientation Num', 'Distance Num', 'Media Num'};
input_headings = {'Vpeak Acoustic (V)', 'Vpeak MagField (V)', 'Vpeak
Reflection (V)', 'Vavg Acoustic (V)', 'Vavg MagField (V)', 'Vavg Refelction
(V)', 'Orientaion #', 'Distance #', 'Media #'};
%Call media_organization function to start looping through each media
%type that the insert was tested at to call other function to loop
%through different distances that the insert was tested at for both
%input and output sides of the testing circuit.
Ultrasound_data_input = media_organization_input();
Ultrasound_data_output = media_organization_output();
%Resistance sweep for insert impedance calculations
R_Load_Insert_Impedance = [1 2 3 5 10 50 100 500 1e3 5e3 10e3 100e3 500e3
1e6 5e6 10e6];
%number of resistances
num_resistances_insert_impedance = length(R_Load_Insert_Impedance);
%heading for insert impedance matrix of information
impedance_headings = {'Resistance (ohms)', 'Vpeak Acoustic (V)', 'Vavg
Acoustic (V)'};
%temporarily assign resistance value to insert_impedance for peak and
%avg
insert_impedance_peak = 1;
insert_impedance_avg = 1;
fs = 50E6; %sampling frequency
fc = 1E6; %cutoff frequency
n = 6; %butterworth filter order

```

```

%Call Ultrasound_insert_impedance function to start looping through
%insert impedance resistance sweep to calculate the inserts impedance
%based on average and peak voltage values in data.
Ultrasound_data_insert_impedance = Ultrasound_insert_impedance();
%save variables to workspace
save(['Ultrasound_Test_new_', specimen_name, '.mat']);
end

%%
%%%%%%%%%%%%%%%%%%%%%%%%%%%%%%%%%%%%%%%%%%%%%%%%%%%%%%%%%%%%%%%%%%%%%%%%
%%%%%%%%%%%%%%%%%%%%%%%%%%%%%%%%%%%%%%%%%%%%%%%%%%%%%%%%%%%%%%%%%%%%%%%% Input Analysis %%%%%%%%%%%%%%%%%%%%%%%%%%%%%%%%%%%%%%%%%%%%%%%%%%%%%%%%%%%%%%%%%%%%%%%%%
%%%%%%%%%%%%%%%%%%%%%%%%%%%%%%%%%%%%%%%%%%%%%%%%%%%%%%%%%%%%%%%%%%%%%%%%

%Function to loop through media types and call other function to loop
%through different distances.
function [media_data_input] = media_organization_input()

%Declare global variables
global file_path_temp
global num_distances
global num_orientation
global num_signals
global num_media
global input_headings
%Initialize arrays for space allocation
media_1_data = zeros(num_orientation*num_distances,(num_signals*2)+2);
media_2_data = zeros(num_orientation*num_distances,(num_signals*2)+2);
media_3_data = zeros(num_orientation*num_distances,(num_signals*2)+2);
%for loop to loop through each media type that the inserts were tested
%in/through
for i=1:num_media
    if i == 1
        %function call for data in which the insert is tested in media
        %1: water.
        file_path = [file_path_temp, '\water\'];
        media_1_data = distance_organization_input(file_path);
        temp_vector_0 = i*ones(num_orientation*num_distances,1);
    elseif i == 2
        %function call for data in which the insert is tested in media
        %2: tissue.
        file_path = [file_path_temp, '\tissue\'];
        media_2_data = distance_organization_input(file_path);
        temp_vector_1 = i*ones(num_orientation*num_distances,1);
    else
        %function call for data in which the insert is tested in media
        %3: tissue_bone (tissue + bone).
        file_path = [file_path_temp, '\tissue_bone\'];
        media_3_data = distance_organization_input(file_path);
        temp_vector_2 = i*ones(num_orientation*num_distances,1);
    end
end
%Return array of information that represents information for each
%orientation, distance, and media parameter
media_data_input = [media_1_data, temp_vector_0; media_2_data,
temp_vector_1; media_3_data, temp_vector_2];

```

```

media_data_input = [input_headings; num2cell(media_data_input)];
end

%Function to loop through distances and call other function to loop through
%orientation directions.
function [distance_data] = distance_organization_input(file_path)

%Declare global variables
global num_distances
global num_orientation
global num_signals
%Initialize arrays for space allocation
distance_1_data = zeros(num_orientation,(num_signals*2)+1);
distance_2_data = zeros(num_orientation,(num_signals*2)+1);
%for loop to loop through each distance that the inserts were tested at
for i=1:num_distances
    if i == 1
        %function call for data in which the insert is at distance
        %1: 20mm.
        distance_1_data = orientation_organization_input(i, file_path);
        temp_vector_0 = i*ones(num_orientation,1);
    else
        %function call for data in which the insert is at distance
        %2: 40mm.
        distance_2_data = orientation_organization_input(i, file_path);
        temp_vector_1 = i*ones(num_orientation,1);
    end
end
%Return array of information that represents information for each
%orientation and distance parameter
distance_data = [distance_1_data, temp_vector_0; distance_2_data,
temp_vector_1];
end

%Function to loop through orientation directions and call other function to
%loop through each signal type (acoustic, reflection, and magfield).
function [orientation_data] = orientation_organization_input(distance_num,
file_path)

%Declare global variables
global num_orientation
global num_signals
%Initialize arrays for space allocation
orientation_1_data = zeros(1,num_signals*2);
orientation_2_data = zeros(1,num_signals*2);
%for loop to loop through each orientation that the inserts were tested
%at
for i=1:num_orientation
    if i == 1
        %function call for data in which the insert is at orientaiton
        %1: discs are parallel to ultrasound probe face.
        orientation_1_data = input_organization(i, distance_num,
file_path);
        temp_vector_1 = i*ones(1,1);
    elseif i == 2

```

```

        %function call for data in which the insert is at orientaiton
        %2: discs are perpendicular to ultrasound probe face.
        orientation_2_data = input_organization(i, distance_num,
file_path);
        temp_vector_2 = i*ones(1,1);
    else
        %do nothing
    end
end
%Return array of information that represents information for each
%orientation parameter
orientation_data = [orientation_1_data, temp_vector_1;
orientation_2_data, temp_vector_2];
end

%Function to loop through each signal type and call other functions to loop
%through sample data.
function [input_data] = input_organization(orientation_num, distance_num,
file_path)

    %Declare global variables
    global num_signals
    %Prepare strings with numbers in them to concatenate with
    %file_location
    temp1 = sprintf('orientation_%i',orientation_num);
    temp2 = sprintf('distance_%i',distance_num);
    %For loop to loop through the Acoustic, reflection, and Magnetic Field
    %induced signals
    for k=1:num_signals
        if k == 1
            %If the signal is the acoustic signal
            try
                file_location =
[file_path,temp2,'\',temp1,'\input\acoustic\']; %raw data file location
                [V_acoustic_max, V_acoustic_avg] =
Ultrasound_test_input_analysis(file_location);
            catch
                %If the file or file location does not exist, an error will
                %not come up and instead the sample will be set to zero.
                V_acoustic_max = 0;
                V_acoustic_avg = 0;
            end
        elseif k == 2
            %If the signal is the reflection signal
            try
                file_location =
[file_path,temp2,'\',temp1,'\input\reflection\']; %raw data file location
                [V_reflection_max, V_reflection_avg] =
Ultrasound_test_input_analysis(file_location);
            catch
                %If the file or file location does not exist, an error will
                %not come up and instead the sample will be set to zero.
                V_reflection_max = 0;
                V_reflection_avg = 0;
            end
        else

```

```

        %If the signal is anything but the acoustic and reflection
signals
        %(magnetic field signal)
        try
            file_location =
[file_path,temp2, '\',temp1, '\input\magfield\']; %raw data file location
            [V_mag_field_max, V_mag_field_avg] =
Ultrasound_test_input_analysis(file_location);
        catch
            %If the file or file location does not exist, an error will
            %not come up and instead the sample will be set to zero.
            V_mag_field_max = 0;
            V_mag_field_avg = 0;
        end
    end
end
    %Return array of information
    input_data = [V_acoustic_max, V_acoustic_avg, V_reflection_max,
V_reflection_avg, V_mag_field_max, V_mag_field_avg];
end

```

```

%Function to calculate Amplitude Voltage and Average Voltage across a
%number of samples taken for the acoustic, reflection, and magfield
%signals.
function [V_max, V_avg] = Ultrasound_test_input_analysis(file_location)

```

```

    %Declare global variables
    global num_samples
    %Size arrays for number of samples taken for each type of signal
    %(acoustic, reflection, and magnetic field)
    Vavg = zeros(num_samples,1);
    Vamp = zeros(num_samples,1);
    %For loop to go through each specific wave data file to then average.
    for i=1:num_samples
        %Prepare string with looping csv files that the oscilloscope saves.
        file = sprintf('tek000%i.csv',i-1);
        %Make filename string.
        filename = [file_location file];
        %Read in data file.
        dat = csvread(filename,15,0);
        %Record TIME (seconds) and CH1 (voltage) data.
        TIME = dat(:,1);
        Vout = dat(:,2);
        %Calculate the size of the TIME array.
        size_TIME = size(TIME,1);
        %Calculate the time step for the TIME array.
        time_step = (TIME(size_TIME,1)-TIME(1,1))/size_TIME;
        %Make a new time array that will start at 0 time, and not some
        %negative time. The oscilloscope takes the centerline on the
        %display as zero time so anything to the left is negative time and
        %anything to the right is positive. The "time" array is just that
        %same time duration starting at 0 time.
        time = zeros(size_TIME,1);
        %Calculate absolute voltage for V_avg later on.
        Vout_abs = abs(Vout);
        %For loop to make time array based on time step starting at time =

```

```

%0.
for j=1:size_TIME
    time(j,1) = time_step*j;
end
%set a max and min to determine peak-to-peak response in another
%for loop.
max_temp = max(Vout);
min_temp = min(Vout);
%Initialize variable "sum" to do trapezoid rule for Vavg
sum = 0;
%For loop to compute Vavg and find max and min values in Vout array
for j=1:size_TIME
    if j == size_TIME
    else
        %Trapezoid rule formula
        sum = sum + (time(j+1,1)-
time(j,1))*((Vout_abs(j,1)+Vout_abs(j+1,1))/2);
        end
    end
    %Compute Vavg for particular sample
    Vavg(i) = sum/time(size_TIME,1);
    %Compute amplitude voltage of Vout array
    Vamp(i) = (max_temp - min_temp)/2;
end
%Initialize sum variables to average the number of samples taken at
%a signal type (acoustic, reflection, and magnetic field)
sum_Vavg = 0;
sum_Vmax = 0;
%for loop to add up all samples taken at a signal type
for i=1:num_samples
    sum_Vavg = sum_Vavg + Vavg(i);
    sum_Vmax = sum_Vmax + Vamp(i);
end
%divide sums to get average values across samples
V_avg = (sum_Vavg/num_samples);
V_max = (sum_Vmax/num_samples);
end

%%
%%%%%%%%%%%%%%%%%%%%%%%%%%%%%%%%%%%%%%%%%%%%%%%%%%%%%%%%%%%%%%%%%%%%%%%%%%%%%%
%%%%%%%%%%%%%%%%%%%%%%%%%%%%%%%%%%%%%%%%%%%%%%%%%%%%%%%%%%%%%%%%%%%%%%%%%%%%%% Output Analysis %%%%%%%%%%%%%%%%%%%%%%%%%%%%%%%%%%%%%%%%%%%%%%%%%%%%%%%%%%%%%%%%%%%%%%%%%%%%%%%
%%%%%%%%%%%%%%%%%%%%%%%%%%%%%%%%%%%%%%%%%%%%%%%%%%%%%%%%%%%%%%%%%%%%%%%%%%%%%%

%Function to loop through media types and call other function to loop
%through different distances.
function [media_data_output] = media_organization_output()

%Declare global variables
global file_path_temp
global num_distances
global num_orientation
global num_resistances
global num_media
global output_headings
%Initialize arrays for space allocation

```



```

media_1_data = zeros(num_resistances*num_orientation*num_distances,5);
media_2_data = zeros(num_resistances*num_orientation*num_distances,5);
media_3_data = zeros(num_resistances*num_orientation*num_distances,5);
%for loop to loop through each media type that the inserts were tested
%in/through
for i=1:num_media
    if i == 1
        %function call for data in which the insert is tested in media
        %1: water.
        file_path = [file_path_temp, '\water\'];
        media_1_data = distance_organization_output(file_path);
        temp_vector_0 =
i*ones(num_resistances*num_orientation*num_distances,1);
    elseif i == 2
        %function call for data in which the insert is tested in media
        %2: tissue.
        file_path = [file_path_temp, '\tissue\'];
        media_2_data = distance_organization_output(file_path);
        temp_vector_1 =
i*ones(num_resistances*num_orientation*num_distances,1);
    else
        %function call for data in which the insert is tested in media
        %3: tissue_bone (tissue + bone).
        file_path = [file_path_temp, '\tissue_bone\'];
        media_3_data = distance_organization_output(file_path);
        temp_vector_2 =
i*ones(num_resistances*num_orientation*num_distances,1);
    end
end
%Return array of information that represents information for each
%orientation, distance, and media parameter
media_data_output = [media_1_data, temp_vector_0; media_2_data,
temp_vector_1; media_3_data, temp_vector_2];
media_data_output = [output_headings; num2cell(media_data_output)];
end

%Function to loop through distances and call other function to loop through
%orientation directions.
function [distance_data] = distance_organization_output(file_path)

%Declare global variables
global num_distances
global num_orientation
global num_resistances
%Initialize arrays for space allocation
distance_1_data = zeros(num_resistances*num_orientation,4);
distance_2_data = zeros(num_resistances*num_orientation,4);
%for loop to loop through each distance that the inserts were tested at
for i=1:num_distances
    if i == 1
        %function call for data in which the insert is at distance
        %1: 20mm.
        distance_1_data = orientation_organization_output(i, file_path);
        temp_vector_0 = i*ones(num_resistances*num_orientation,1);
    else
        %function call for data in which the insert is at distance

```

```

        %2: 40mm.
        distance_2_data = orientation_organization_output(i, file_path);
        temp_vector_1 = i*ones(num_resistances*num_orientation,1);
    end
end
%Return array of information that represents information for each
%orientation and distance parameter
distance_data = [distance_1_data, temp_vector_0; distance_2_data,
temp_vector_1];
end

%Function to loop through orientation directions and call other function to
%loop through resistance sweep.
function [orientation_data] = orientation_organization_output(distance_num,
file_path)

%Declare global variables
global R_Load
global num_orientation
global num_resistances
%Initialize arrays for space allocation
orientation_1_data = zeros(num_resistances,2);
orientation_2_data = zeros(num_resistances,2);
%for loop to loop through each orientation that the inserts were tested
%at
for i=1:num_orientation
    if i == 1
        %function call for data in which the insert is at orientaiton
        %1: discs are parallel to ultrasound probe face.
        orientation_1_data = resistance_organization_output(i,
distance_num, file_path);
        temp_vector_1 = i*ones(num_resistances,1);
    elseif i == 2
        %function call for data in which the insert is at orientaiton
        %2: discs are perpendicular to ultrasound probe face.
        orientation_2_data = resistance_organization_output(i,
distance_num, file_path);
        temp_vector_2 = i*ones(num_resistances,1);
    else
        %do nothing
    end
end
%Return array of information that represents information for each
%orientation parameter
orientation_data = [orientation_1_data, transpose(R_Load), temp_vector_1;
orientation_2_data, transpose(R_Load), temp_vector_2];
end

%Function to loop through resistance sweep and call other functions to loop
%through sample data.
function [resistance_data] = resistance_organization_output(orientation_num,
distance_num, file_path)

%Declare global variables
global R_Load

```

```

global num_resistances
%Initialize arrays for space allocation
Resistance_Power = zeros(num_resistances,2);
%for loop to loop through each resistance in resistance sweep to call
%other functions that calculate local NRG and global NRG and power.
for i=1:num_resistances
    Resistance_Power(i,:) = resistance_analysis(i, orientation_num,
R_Load(i), distance_num, file_path);
end
%Return array of information that represents information for each
%resistance in resistance sweep
resistance_data = Resistance_Power;
end

%Function to loop through sample data files and then global data files to
%call other functions that calculate NRG output locally and then NRG and
%power output globally.
function [Resistance_Power] = resistance_analysis(resistance_num,
orientation_num, Rvar, distance_num, file_path)

    %Declare global variables

    %Prepare strings with numbers in them to concatenate with
    %file_location
    temp1 = sprintf('resistance_%i',resistance_num);
    temp2 = sprintf('orientation_%i',orientation_num);
    temp3 = sprintf('distance_%i',distance_num);
    %Try to call Ultrasound_test_output_analysis for the DC folder
    try
        file_location = [file_path,temp3,'\',temp2,'\output\DC\',temp1,'\'];
%raw data file location
        DC_Load_Power =
Ultrasound_test_output_analysis_DC_Load(file_location, Rvar);
    catch
        %If the file or file location does not exist, an error will
        %not come up and instead the sample will be set to zero.
        DC_Load_Power = 0;
    end
    %Try to call Ultrasound_test_output_analysis for the DC_bias folder
    try
        file_location = [file_path,temp3,'\',temp2,'\output\DC\',temp1,'\'];
%raw data file location
        DC_Power = Ultrasound_test_output_analysis_DC_Total(file_location,
Rvar);
    catch
        %If the file or file location does not exist, an error will
        %not come up and instead the sample NRGs will be set to
        %zero.
        DC_Power = 0;
    end
    %Return array of power information for DC_Bias and DC outputs
    Resistance_Power = [DC_Load_Power, DC_Power];
end

%Function to calculate DC power across load resistance on output (DC) side

```

```

%of circuit.
function DC_Power = Ultrasound_test_output_analysis_DC_Total(file_location,
Rvar)

%Declare global variables
global num_samples
global R_Oscilloscope
global Capacitor_Reactance
global fs;
global fc;
global n;
%Initialize arrays for space allocation
Vavg = zeros(num_samples,1);
Pavg = zeros(num_samples,1);
%For loop to go through each specific wave data file to then average.
for i=1:num_samples
    %Prepare string with looping csv files that the oscilloscope saves.
    file = sprintf('tek000%i.csv',i-1);
    %Make filename string.
    filename = [file_location file];
    %Read in data file.
    dat = csvread(filename,15,0);
    %Record TIME (seconds) and CH1 (voltage) data.
    TIME = dat(:,1);
    Vout = dat(:,2);
    %Calculate the size of the TIME array.
    size_TIME = size(TIME,1);
    %Calculate the time step for the TIME array.
    time_step = (TIME(size_TIME,1)-TIME(1,1))/size_TIME;
    %Make a new time array that will start at 0 time, and not some
    %negative time. The oscilloscope takes the centerline on the
    %display as zero time so anything to the left is negative time and
    %anything to the right is positive. The "time" array is just that
    %same time duration starting at 0 time.
    time = zeros(size_TIME,1);
    %Calculate absolute voltage for V_avg later on.
    %Vout_abs = abs(Vout);
    %For loop to make time array based on time step starting at time =
    %0 and make all data points that are negative in Vout equal to 0.
    for j=1:size_TIME
        time(j,1) = time_step*j;
        if Vout(j) < 0
            Vout(j) = 0;
        else
            end
    end
end
%Initialize variable "sum" to do trapezoid rule for Vavg
sum = 0;
%design butterworth filter that filters out high frequency signals
%in the DC responses
[b,a] = butter(n,fc/(fs/2),'low');
filtered_data = filter(b,a,Vout);
%filtered_data_abs = abs(filtered_data);
%For loop to compute Vavg and find max and min values in Vout array
for j=1:size_TIME
    if j == size_TIME

```

```

        else
            %Trapezoid rule formula
            sum = sum + (time(j+1,1)-
time(j,1))*((filtered_data(j,1)+filtered_data(j+1,1))/2);
        end
    end
    %Compute Vavg for particular sample
    Vavg(i) = sum/time(size_TIME,1);
    %Vavg(i) = mean(filtered_data);
    %Compute Equivalent Resistance of Circuit
    %Res_equivalent - Rload and Rosilloscope
    Res_equivalent = ((1/Rvar)+(1/R_Oscilloscope))^-1;
    Req_real =
(Res_equivalent*(Capacitor_Reactance^2))/((Res_equivalent^2)+(Capacitor_React
ance^2));
    Req_imaginary = -
((Res_equivalent^2)*Capacitor_Reactance)/((Res_equivalent^2)+(Capacitor_React
ance^2));
    Req = ((Req_real^2)+(Req_imaginary^2))^(1/2);
    %Req_angle = atan(Req_imaginary/Req_real);
    %Compute Pavg using V^2/Req
    Pavg(i) = (Vavg(i)^2)/(Req);
end
%Initialize sum variables to average the number of samples taken at
%a signal type (acoustic, reflection, and magnetic field)
sum_Pavg = 0;
%for loop to add up all samples taken at a signal type
for i=1:num_samples
    sum_Pavg = sum_Pavg + Pavg(i);
end
%divide sums to get average values
DC_Power = (sum_Pavg/num_samples);
end

%Function to calculate DC_Bias power across load resistance on output (DC)
%side of circuit.
function DC_Load_Power =
Ultrasound_test_output_analysis_DC_Load(file_location, Rvar)

%Declare global variables
%global ultrasound_hertz
global num_samples
global fs;
global fc;
global n;
%Initialize arrays for space allocation
Vavg = zeros(num_samples,1);
%Pavg_local = zeros(num_samples,1);
%NRG_avg_local = zeros(num_samples,1);
Pavg = zeros(num_samples,1);
%A_B = zeros(num_samples,1);
%For loop to go through each specific wave data file to then average.
for i=1:num_samples
    %Prepare string with looping csv files that the oscilloscope saves.
    file = sprintf('tek000%i.csv',i-1);
    %Make filename string.

```

```

filename = [file_location file];
%Read in data file.
dat = csvread(filename,15,0);
%Record TIME (seconds) and Vout (voltage) data.
TIME = dat(:,1);
Vout = dat(:,2);
%Calculate the size of the TIME array.
size_TIME = size(TIME,1);
%Calculate the time step for the TIME array.
time_step = (TIME(size_TIME,1)-TIME(1,1))/size_TIME;
%Make a new time array that will start at 0 time, and not some
%negative time. The oscilloscope takes the centerline on the
%display as zero time so anything to the left is negative time and
%anything to the right is positive. The "time" array is just that
%same time duration starting at 0 time.
time = zeros(size_TIME,1);
%Calculate absolute voltage for V_avg later on.
%Vout_abs = abs(Vout);
%For loop to make time array based on time step starting at time =
%0.
for j=1:size_TIME
    time(j,1) = time_step*j;
    %
    %
    %
    %
    if Vout(j) < 0
        Vout(j) = 0;
    else
        end
end
%Initialize variable "sum" to do trapezoid rule for Vavg
sum = 0;
%design butterworth filter that filters out high frequency signals
%in the DC responses
[b,a] = butter(n,fc/(fs/2),'low');
filtered_data = filter(b,a,Vout);
%filtered_data_abs = abs(filtered_data);
%For loop to compute Vavg and find max and min values in Vout array
for j=1:size_TIME
    if j == size_TIME
        else
            %Trapezoid rule formula
            sum = sum + (time(j+1,1)-
time(j,1))*((filtered_data(j,1)+filtered_data(j+1,1))/2);
            end
        end
    %Compute Vavg for particular sample
    Vavg(i) = sum/time(size_TIME,1);
    %Vavg(i) = mean(filtered_data);
    %Compute Pavg using V^2/Rvar
    %Pavg_local(i) = (Vavg(i)^2)/(Rvar);
    %A_B(i) = TIME(size_TIME,1)-TIME(1,1);
    %NRG_avg_local(i) = Pavg_local(i)*A_B(i);
    %Pavg(i) = NRG_avg_local(i)*ultrasound_hertz;
    %Compute Pavg using V^2/Rvar
    Pavg(i) = (Vavg(i)^2)/(Rvar);
end
%Initialize sum variables to average
sum_Pavg = 0;

```

```
%for loop to add up all samples taken at a signal type
for i=1:num_samples
    sum_Pavg = sum_Pavg + Pavg(i);
end
%divide sums to get average values
DC_Load_Power = (sum_Pavg/num_samples);
end
```

Appendix A.2: MATLAB Code used for Statistical Analysis

This section of the Appendix contains the code and statistical methods that were used to determine significance between CLACSs within each testing parameter and between testing parameters within each CLACS. A more detailed explanation of the methods used in the code is located in section 3.8.3.

MATLAB Code:

```
%%%%%%%%%%%%%%%%%%%%%%%%%%%%%%%%%%%%%%%%%%%%%%%%%%%%%%%%%%%%%%%%%%%%%%%%%%  
%%%%%%%%%%%%%%%%%%%%%%%%%%%%%%%%%%%%%%%%%%%%%%%%%%%%%%%%%%%%%%%%%%%%%%%%%% Ultrasound Data Statistical Analysis %%%%%%%%%%%%%%%%%%%%%%%%%%%%%%%%%%%%%%%%%%%%%%%%%%%%%%%%%%%%%%%%%%%%%%%%%%%  
%%%%%%%%%%%%%%%%%%%%%%%%%%%%%%%%%%%%%%%%%%%%%%%%%%%%%%%%%%%%%%%%%%%%%%%%%%  
%Kyle Coates - Graduate Student (M.S.), Dr. Lisa Friis Spine Biomechanics  
%Lab  
%December 12 2017
```

```
%The purpose of this code is to determine normality and then significance.  
%The data was checked for normality by plotting a box and whisker,  
%histogram, and residual plot. All checks for normality were done by the  
%user and it was determined by the user if the data was normal or not. The  
%check was not done numerically or by some other normality method. If the  
%data is not normal, then a transformation was performed on the data to  
%normalize it. Five different transformations were performed on a portion  
%of the data sets to determine which one across all the data would produce  
%the most normal data sets. These include a square-root, squared,  
%reciprocal, logarithm (base e), and BoxCox. All five transformations were  
%run for data sets before rectification and some data sets after  
%rectification for the 500 kilo-ohm and 10 mega-ohm data sets. The user  
%determined which of the five transformations made the data the most  
%normal. This was done for each of the data sets described previously and  
%the resulting transformation that made the data the most normal was  
%counted. At the end of running the transformations across the data sets,  
%the total count was observed. The BoxCox transformation made the data  
%sets the most normal. This transformation was then used for the rest of  
%the data set combinations to be compared. Now that the data sets are  
%normal, a one-way ANOVA was run for each vector of CLACS within a testing  
%parameter and for all testing parameters within each CLACS. If the one-  
%way ANOVA output significance, then a post-hoc Tukey-Kramer pair-wise  
%multi-comparison test was performed to determine significance. All  
%significance tests (one-way ANOVA and Tukey-Kramer) were run with an alpha  
%level of 0.05.
```

```
function Ultrasound_Data_Stats_Analysis_Kyle_Thesis_2017()  
%clear all variables in workspace, command window, and close all figures  
clear  
close all  
clc  
%sheet name to help identify sheet to look at  
sheet_name = 'Eff_LP_10MOhms_Orientation';  
transform_method = 'BOXCOX';
```



```

%file location
file_location = ('E:\Documents\KU_Career\Dr. Friis Research\Ultrasound
Data\Statistical Analysis\');
%file name
file = sprintf('Kyle_Stats_Data_new.xlsx');
%Make filename string.
filename = [file_location file];
%check if a folder exists in current directory with sheet_name
if exist(sheet_name, 'dir') == 7
    %if folder exists do nothing
else
    %if folder does not exist, make it
    mkdir(file_location, sheet_name);
end
%Read in excel data file
[dat, txt, raw] = xlsread(filename, sheet_name);
%input number of samples
num_samples = 5;
%gather size of data file array in sheet
[m, n] = size(raw);
%number of parameters
num_parameters = n-1;
%create categorical vector for specimen type
g = categorical(raw(2:end, 1));
%compute number of specimen type
num_spec_type = (m-1)/num_samples;
%prepare arrays to be filled later
Transdat = zeros(m-1, n-1);
lambda = zeros(1, n-1);
%transform specific parameter data for all specimen types using the
%specified transform method
if strcmp(transform_method, 'RECIPROCAL') == 1
    for i = 1:n-1
        Transdat(:, i) = dat(:, i).^(-1);
        lambda(1, i) = 10;
    end
elseif strcmp(transform_method, 'LOG') == 1
    for i = 1:n-1
        Transdat(:, i) = log(dat(:, i));
        lambda(1, i) = 10;
    end
elseif strcmp(transform_method, 'SQRT') == 1
    for i = 1:n-1
        Transdat(:, i) = dat(:, i).^(1/2);
        lambda(1, i) = 10;
    end
elseif strcmp(transform_method, 'SQ') == 1
    for i = 1:n-1
        Transdat(:, i) = dat(:, i).^2;
        lambda(1, i) = 10;
    end
else
    for i = 1:n-1
        [Transdat(:, i), lambda(1, i)] = boxcox(dat(:, i));
    end
end
end

```

```

%for parameter data, create plots to help determine normality and plot
%transformed data that has been made more normal than the original
%parameter data.
%For loop to loop through the different parameters
for i = 1:n-1
    %check if it is the first iteration to assign graph #s
    if i == 1
        %initialize graph #
        fig_count = 1;
    else
        %accumulate graph #
        fig_count = i*2-1;
    end
    %create temporary heading text for plots
    heading = txt(1,i+1);
    %create figure with tiled 3 x 2 plots
    figure(fig_count)
    %plot on subplot 1 - boxplot of parameter data
    subplot(3,2,1);
    boxplot(dat(:,i));
    grid; title(strcat('Box Plot: Non-normal--', heading));
    ylabel('values');
    xlabel(heading);
    %plot on subplot 2 - boxplot of transformed data
    subplot(3,2,2);
    boxplot(Transdat(:,i));
    grid; title(strcat('Box Plot:--', transform_method, '--Normal--', heading,
' \lambda = ', num2str(lambda(1,i))));
    ylabel('values');
    xlabel(heading);
    %plot on subplot 3 - histogram of parameter data
    subplot(3,2,3);
    histogram(dat(:,i));
    grid; title(strcat('Histogram: Non-normal--', heading));
    ylabel('count');
    xlabel(strcat('bins--',heading));
    %plot on subplot 4 - histogram of transformed data
    subplot(3,2,4);
    histogram(Transdat(:,i));
    grid; title(strcat('Histogram:--', transform_method, '--Normal--',
heading, ' \lambda = ', num2str(lambda(1,i))));
    ylabel('count');
    xlabel(strcat('bins--',heading));
    %plot on subplot 5 - QQ plot of parameter data
    subplot(3,2,5);
    qqplot(dat(:,i));
    grid; title(strcat('QQ Plot: Non-normal--', heading));
    %plot on subplot 6 - QQ plot of transformed data
    subplot(3,2,6);
    qqplot(Transdat(:,i));
    grid; title(strcat('QQ Plot:--', transform_method, '--Normal--', heading,
' \lambda = ', num2str(lambda(1,i))));
    %save figure to file location specified by the sheet_name
    %make temporary cell with two strings
    str_temp = [pwd strcat('\', sheet_name , '\Normality_Plots_', heading,
'_Param_', transform_method, '.fig')];

```

```

%concatenate cell elements to make one string and save figure
saveas(gcf,[str_temp{1} str_temp{2}]);
%create linear model fit for residual vs. fitted values plots
%parameter data model
mdl = fitlm(g,dat(:,i));
%transformed data model
Trans_mdl = fitlm(g,Transdat(:,i));
%create another figure tiled 2 x 1 to plot residuals vs. fitted values
%for parameter and transformed data
fig_count = fig_count + 1;
figure(fig_count)
%plot on subplot 1 - residual plot for parameter data
subplot(2,1,1);
plotResiduals(mdl, 'fitted');
grid; title(strcat('Residual Plot: Non-normal--', heading))
%plot on subplot 2 - residual plot for transformed data
subplot(2,1,2);
plotResiduals(Trans_mdl, 'fitted');
grid; title(strcat('Residual Plot:--', transform_method, '--Normal--',
heading, '\lambda = ', num2str(lambda(1,i))))
%save figure to file location specified by the sheet_name
%make temporary cell with two strings
str_temp = [pwd strcat('\', sheet_name , '\Residual_Plots_', heading,
'_Param_',transform_method, '.fig')];
%concatenate cell elements to make one string and save figure
saveas(gcf,[str_temp{1} str_temp{2}]);
close all
end
%accumulate figure count
fig_count = fig_count + 1;
%for specimen type data before transforming
%initialize arrays for storing specimen type info from dat
%q is the numerical values of dat stored conveniently for specimen type
q = zeros(num_samples*num_parameters,num_spec_type);
%g_q is the categorical array of dat stored conveniently for specimen type
g_q = categorical(zeros(num_samples*num_parameters,1));
heading_q = categorical(zeros(num_samples*num_parameters,num_spec_type));
%for loop to store dat and g data into convenient parameter type arrays
for i = 1:num_spec_type
    for k = 1:num_parameters
        for j = 1:num_samples
            if k == 1
                q(j,i) = dat(j+((i-1)*num_samples),k);
                heading_q(j,i) = g(j+((i-1)*num_samples),1);
            else
                q(j+((k-1)*num_samples),i) = dat(j+((i-1)*num_samples),k);
                heading_q(j+((k-1)*num_samples),i) = g(j+((i-
1)*num_samples),1);
            end
        end
    end
end
end
%for loop to store txt data into categorical parameter type array
for i = 1:num_parameters
    for j = 1:num_samples
        if i == 1

```

```

        g_q(j,1) = txt(1,i+1);
    else
        g_q(j+((i-1)*num_samples),1) = txt(1,i+1);
    end
end
end
%initialize arrays for storing transformed specimen type info from dat
%transformed data array
Transdat_q = zeros(num_samples*num_parameters,num_spec_type);
%lambda value array
lambda_q = zeros(1,num_spec_type);
%for loop to transform specimen type data using boxcox and show lambda
%values

%transform specific parameter data for all specimen types using the
%specified transform method
if strcmp(transform_method,'RECIPROCAL') == 1
    for i = 1:num_spec_type
        Transdat_q(:,i) = q(:,i).^(-1);
        lambda_q(1,i) = 10;
    end
elseif strcmp(transform_method,'LOG') == 1
    for i = 1:num_spec_type
        Transdat_q(:,i) = log(q(:,i));
        lambda_q(1,i) = 10;
    end
elseif strcmp(transform_method,'SQRT') == 1
    for i = 1:num_spec_type
        Transdat_q(:,i) = q(:,i).^(1/2);
        lambda_q(1,i) = 10;
    end
elseif strcmp(transform_method,'SQ') == 1
    for i = 1:num_spec_type
        Transdat_q(:,i) = q(:,i).^2;
        lambda_q(1,i) = 10;
    end
else
    for i = 1:num_spec_type
        [Transdat_q(:,i), lambda_q(1,i)] = boxcox(q(:,i));
    end
end
end
%for specimen type data, create plots to help determine normality and plot
%transformed data that has been made more normal than the original
%parameter data.
for i = 1:num_spec_type
    %create figure
    figure(fig_count)
    %plot on subplot 1 - boxplot of specimen type data
    subplot(3,2,1);
    boxplot(q(:,i));
    grid; title(strcat('Box Plot: Non-normal--', cellstr(heading_q(1,i))));
    ylabel('values');
    xlabel(cellstr(heading_q(1,i)));
    %plot on subplot 2 - boxplot of specimen type data
    subplot(3,2,2);

```

```

    boxplot(Transdat_q(:,i));
    grid; title(strcat('Box Plot:--', transform_method, '--Normal--',
cellstr(heading_q(1,i)), ' \lambda = ', num2str(lambda_q(1,i))));
    ylabel('values');
    xlabel(cellstr(heading_q(1,i)));
    %plot on subplot 3 - histogram of specimen type data
    subplot(3,2,3);
    histogram(q(:,i));
    grid; title(strcat('Histogram: Non-normal--', cellstr(heading_q(1,i))));
    ylabel('count');
    xlabel(strcat('bins--',cellstr(heading_q(1,i))));
    %plot on subplot 4 - histogram of specimen type data
    subplot(3,2,4);
    histogram(Transdat_q(:,i));
    grid; title(strcat('Histogram:--', transform_method, '--Normal--',
cellstr(heading_q(1,i)), ' \lambda = ', num2str(lambda_q(1,i))));
    ylabel('count');
    xlabel(strcat('bins--',cellstr(heading_q(1,i))));
    %plot on subplot 5 - QQ plot of specimen type data
    subplot(3,2,5);
    qqplot(q(:,i));
    grid; title(strcat('QQ Plot: Non-normal--', cellstr(heading_q(1,i))));
    %plot on subplot 6 - QQ plot of specimen type data
    subplot(3,2,6);
    qqplot(Transdat_q(:,i));
    grid; title(strcat('QQ Plot:--', transform_method, '--Normal--',
cellstr(heading_q(1,i)), ' \lambda = ', num2str(lambda_q(1,i))));
    %save figure to file location specified by the sheet_name
    %make temporary cell with two strings
    str_temp = [pwd strcat('\', sheet_name ,'\Normality_Plots_',
char(heading_q(1,i)), '_Param_',transform_method, '.fig')];
    %save
    saveas(gcf,str_temp);
    %create linear model fit for residual vs. fitted values plots
    %specimen type data model
    mdl_q = fitlm(g_q,q(:,i));
    Trans_mdl_q = fitlm(g_q,Transdat_q(:,i));
    %transformed data model
    fig_count = fig_count + 1;
    figure(fig_count)
    %create another figure tiled 2 x 1 to plot residuals vs. fitted values
    %for specimen type and transformed data
    %plot on subplot 1 - residual plot for specimen type data
    subplot(2,1,1);
    plotResiduals(mdl_q, 'fitted');
    grid; title(strcat('Residual Plot: Non-normal--',
cellstr(heading_q(1,i))));
    %plot on subplot 2 - residual plot for specimen type transformed data
    subplot(2,1,2);
    plotResiduals(Trans_mdl_q, 'fitted');
    grid; title(strcat('Residual Plot:--', transform_method, '--Normal--',
cellstr(heading_q(1,i)), ' \lambda = ', num2str(lambda_q(1,i))));
    %save figure to file location specified by the sheet_name
    %make temporary cell with two strings
    str_temp = [pwd strcat('\', sheet_name ,'\Residual_Plots_',
char(heading_q(1,i)), '_Param_',transform_method, '.fig')];

```

```

    %save
    saveas(gcf,str_temp);
    close all
    %accumulate figure count
    fig_count = fig_count + 1;
end
%%%%%%%%%%%%%%%%%%%%%%%%%%%%%%%%%%%%%%%%%%%%%%%%%%%%%%%%%%%%%%%%%%%%%%%%%%%%%%ANOVA%%%%%%%%%%%%%%%%%%%%%%%%%%%%%%%%%%%%%%%%%%%%%%%%%%%%%%%%%%%%%%%%%%%%%%%%%%%%%%
%comparison for specimen type within a parameter
%initialize an alpha level
alpha = 0.05;
%initialize structs for comparing specimen type within a parameter before
%being normalized all
p = struct;
t = struct;
stats = struct;
c = struct;
means = struct;
h = struct;
names = struct;
info = struct;
%initialize structs for comparing specimen type within a parameter after
%being normalized
Trans_p = struct;
Trans_t = struct;
Trans_stats = struct;
Trans_c = struct;
Trans_means = struct;
Trans_h = struct;
Trans_names = struct;
Trans_info = struct;
%for loop to loop through the different parameters to run a multiple
%comparison for specimen types within a parameter
for i = 1:num_parameters
    %before being normalized
    [p_temp,t_temp,stats_temp] = anoval(dat(:,i),g,'off');
    p(i).a = p_temp;
    t(i).a = t_temp;
    stats(i).a = stats_temp;
    figure(fig_count)
    [c_temp,means_temp,h_temp,names_temp] =
multcompare(stats(i).a,'Alpha',alpha,'CType','tukey-kramer');
    title(strcat('Multiple Comparison Plot: Non-normal--',
cellstr(txt(1,i+1)), '--Alpha = ', num2str(alpha), ' tukey-kramer'));
    ylabel('groups');
    xlabel('group means');
    %save figure to file location specified by the sheet_name
    %make temporary cell with two strings
    str_temp = [pwd strcat('\', sheet_name ,'\Multiple_Comparison_Plot_Non-
normal_', cellstr(txt(1,i+1)), '_Param_',transform_method,'.fig')];
    %concatenate cell elements to make one string and save figure
    saveas(gcf,[str_temp{1} str_temp{2}]);
    c(i).a = c_temp;
    means(i).a = means_temp;
    h(i).a = h_temp;
    names(i).a = names_temp;
    info(i).a = [names_temp num2cell(means_temp)];
end

```

```

    fig_count = fig_count + 1;
    %after being normailzed
    [p_temp,t_temp,stats_temp] = anoval(Transdat(:,i),g,'off');
    Trans_p(i).a = p_temp;
    Trans_t(i).a = t_temp;
    Trans_stats(i).a = stats_temp;
    figure(fig_count)
    [c_temp,means_temp,h_temp,names_temp] =
multcompare(Trans_stats(i).a, 'Alpha', alpha, 'CType', 'tukey-kramer');
    title(strcat('Multiple Comparison Plot:--', transform_method, '--Normal--
', cellstr(txt(1,i+1)), '--Alpha = ', num2str(alpha), ' tukey-kramer',
'\lambda = ', num2str(lambda(1,i))));
    ylabel('groups');
    xlabel('group means');
    %save figure to file location specified by the sheet_name
    %make temporary cell with two strings
    str_temp = [pwd strcat('\', sheet_name
, '\Multiple_Comparison_Plot_Normal_', cellstr(txt(1,i+1)),
'_Param_', transform_method, '.fig')];
    %concatenate cell elements to make one string and save figure
    saveas(gcf,[str_temp{1} str_temp{2}]);
    Trans_c(i).a = c_temp;
    Trans_means(i).a = means_temp;
    Trans_h(i).a = h_temp;
    Trans_names(i).a = names_temp;
    Trans_info(i).a = [names_temp num2cell(means_temp)];
    fig_count = fig_count + 1;
    close all
end
%comparison for parameter within a specimen type
%initialize an alpha level
alpha = 0.05;
%initialize structs for comparying specimen type within a parameter before
%being normalized
p_q = struct;
t_q = struct;
stats_q = struct;
c_q = struct;
means_q = struct;
h_q = struct;
names_q = struct;
info_q = struct;
%initialize structs for comparying specimen type within a parameter after
%being normalized
Trans_p_q = struct;
Trans_t_q = struct;
Trans_stats_q = struct;
Trans_c_q = struct;
Trans_means_q = struct;
Trans_h_q = struct;
Trans_names_q = struct;
Trans_info_q = struct;
%for loop to loop through the different parameters to run a multiple
%comparison for specimen types within a parameter
for i = 1:num_spec_type
    %before being normailzed

```

```

    [p_temp,t_temp,stats_temp] = anova1(q(:,i),g_q,'off');
    p_q(i).a = p_temp;
    t_q(i).a = t_temp;
    stats_q(i).a = stats_temp;
    figure(fig_count)
    [c_temp,means_temp,h_temp,names_temp] =
multcompare(stats_q(i).a,'Alpha',alpha,'CType','tukey-kramer');
    title(strcat('Multiple Comparison Plot: Non-normal--',
cellstr(heading_q(1,i)), '--Alpha = ', num2str(alpha), ' tukey-kramer'));
    ylabel('groups');
    xlabel('group means');
    %save figure to file location specified by the sheet_name
    %make temporary cell with two strings
    str_temp = [pwd strcat('\', sheet_name ,'\Multiple_Comparison_Plot_Non-
normal_', char(heading_q(1,i)), '_Param_',transform_method, '.fig')];
    %save
    saveas(gcf,str_temp);
    c_q(i).a = c_temp;
    means_q(i).a = means_temp;
    h_q(i).a = h_temp;
    names_q(i).a = names_temp;
    info_q(i).a = [names_temp num2cell(means_temp)];
    fig_count = fig_count + 1;
    %after being normailzed
    [p_temp,t_temp,stats_temp] = anova1(Transdat_q(:,i),g_q,'off');
    Trans_p_q(i).a = p_temp;
    Trans_t_q(i).a = t_temp;
    Trans_stats_q(i).a = stats_temp;
    figure(fig_count)
    [c_temp,means_temp,h_temp,names_temp] =
multcompare(Trans_stats_q(i).a,'Alpha',alpha,'CType','tukey-kramer');
    title(strcat('Multiple Comparison Plot:--', transform_method, '--Normal--
', cellstr(heading_q(1,i)), '--Alpha = ', num2str(alpha), ' tukey-kramer',
'\lambda = ', num2str(lambda_q(1,i))));
    ylabel('groups');
    xlabel('group means');
    %save figure to file location specified by the sheet_name
    %make temporary cell with two strings
    str_temp = [pwd strcat('\', sheet_name
, '\Multiple_Comparison_Plot_Normal_', char(heading_q(1,i)),
'_Param_',transform_method, '.fig')];
    %save
    saveas(gcf,str_temp);
    Trans_c_q(i).a = c_temp;
    Trans_means_q(i).a = means_temp;
    Trans_h_q(i).a = h_temp;
    Trans_names_q(i).a = names_temp;
    Trans_info_q(i).a = [names_temp num2cell(means_temp)];
    fig_count = fig_count + 1;
    close all
end

%temp_temp = 100000000;
temp_temp = 111111111;

if num_parameters == 2

```



```

    array_c = [c(1).a; ones(1,6)*temp_temp; c(2).a];
    array_info = [info(1).a; num2cell(ones(1,3)*temp_temp); info(2).a];
    array_c_q = [c_q(1).a; ones(1,6)*temp_temp; c_q(2).a;
ones(1,6)*temp_temp; c_q(3).a; ones(1,6)*temp_temp; c_q(4).a];
    array_info_q = [info_q(1).a; num2cell(ones(1,3)*temp_temp); info_q(2).a;
num2cell(ones(1,3)*temp_temp); info_q(3).a; num2cell(ones(1,3)*temp_temp);
info_q(4).a];

    arr_c = [array_c; ones(1,6)*temp_temp; array_c_q];
    arr_info = [array_info; num2cell(ones(1,3)*temp_temp); array_info_q];

    array_Trans_c = [Trans_c(1).a; ones(1,6)*temp_temp; Trans_c(2).a];
    array_Trans_info = [Trans_info(1).a; num2cell(ones(1,3)*temp_temp);
Trans_info(2).a];
    array_Trans_c_q = [Trans_c_q(1).a; ones(1,6)*temp_temp; Trans_c_q(2).a;
ones(1,6)*temp_temp; Trans_c_q(3).a; ones(1,6)*temp_temp; Trans_c_q(4).a];
    array_Trans_info_q = [Trans_info_q(1).a; num2cell(ones(1,3)*temp_temp);
Trans_info_q(2).a; num2cell(ones(1,3)*temp_temp); Trans_info_q(3).a;
num2cell(ones(1,3)*temp_temp); Trans_info_q(4).a];

    arr_Trans_c = [array_Trans_c; ones(1,6)*temp_temp; array_Trans_c_q];
    arr_Trans_info = [array_Trans_info; num2cell(ones(1,3)*temp_temp);
array_Trans_info_q];

elseif num_parameters == 3
    array_c = [c(1).a; ones(1,6)*temp_temp; c(2).a; ones(1,6)*temp_temp;
c(3).a];
    array_info = [info(1).a; num2cell(ones(1,3)*temp_temp); info(2).a;
num2cell(ones(1,3)*temp_temp); info(3).a];
    array_c_q = [c_q(1).a; ones(1,6)*temp_temp; c_q(2).a;
ones(1,6)*temp_temp; c_q(3).a; ones(1,6)*temp_temp; c_q(4).a];
    array_info_q = [info_q(1).a; num2cell(ones(1,3)*temp_temp); info_q(2).a;
num2cell(ones(1,3)*temp_temp); info_q(3).a; num2cell(ones(1,3)*temp_temp);
info_q(4).a];

    arr_c = [array_c; ones(1,6)*temp_temp; array_c_q];
    arr_info = [array_info; num2cell(ones(1,3)*temp_temp); array_info_q];

    array_Trans_c = [Trans_c(1).a; ones(1,6)*temp_temp; Trans_c(2).a;
ones(1,6)*temp_temp; Trans_c(3).a];
    array_Trans_info = [Trans_info(1).a; num2cell(ones(1,3)*temp_temp);
Trans_info(2).a; num2cell(ones(1,3)*temp_temp); Trans_info(3).a];
    array_Trans_c_q = [Trans_c_q(1).a; ones(1,6)*temp_temp; Trans_c_q(2).a;
ones(1,6)*temp_temp; Trans_c_q(3).a; ones(1,6)*temp_temp; Trans_c_q(4).a];
    array_Trans_info_q = [Trans_info_q(1).a; num2cell(ones(1,3)*temp_temp);
Trans_info_q(2).a; num2cell(ones(1,3)*temp_temp); Trans_info_q(3).a;
num2cell(ones(1,3)*temp_temp); Trans_info_q(4).a];

    arr_Trans_c = [array_Trans_c; ones(1,6)*temp_temp; array_Trans_c_q];
    arr_Trans_info = [array_Trans_info; num2cell(ones(1,3)*temp_temp);
array_Trans_info_q];

end

```

```
clc

save(strcat('Ultrasound_Stats_', transform_method, '.mat'));
end
```

Appendix A.3: MATLAB Code for after rectification filtering

This section of the Appendix contains the code and filtering method that were used to eliminate high frequency noise in after rectification voltage data. A more detailed explanation of the methods used in the code is located in section 3.8.1.

MATLAB Code:

```
%%%%%%%%%%%%%%%%%%%%%%%%%%%%%%%%%%%%%%%%%%%%%%%%%%%%%%%%%%%%%%%%%%%%%%%%%%
%%%%%%%%%%%%%%%%%%%%%%%%%%%%%%%%%%%%%%%%%%%%%%%%%%%%%%%%%%%%%%%%%%%%%%%%%% Ultrasound Data Filter Design Code %%%%%%%%%%%%%%%%%%%%%%%%%%%%%%%%%%%%%%%%%%%%%%%%%%%%%%%%%%%%%%%%%%%%%%%%%%%
%%%%%%%%%%%%%%%%%%%%%%%%%%%%%%%%%%%%%%%%%%%%%%%%%%%%%%%%%%%%%%%%%%%%%%%%%%
%Kyle Coates - Graduate Student (M.S.), Dr. Lisa Friis Spine Biomechanics
%Lab
%December 12 2017

%The purpose of this code is to determine design parameters for a
%butterworth filter by using a Fast Fourier Transform. Different orders
%and cutoff frequencies were explored and plotted to see the change in the
%FFT and the voltage data over time, filtered and un-filtered.

function DC_frequency_filter()
    %clear/close all things
    close all
    clear
    clc
    %Declare global variables
    global num_samples;
    global specimen_name
    global fs;
    global fc;
    global n;
    num_samples = 1;
    %Declare variables
    specimen_name = ('TS85');
    %file_location = ('C:\Users\k711c115\Desktop\Ultrasound
Testing\specimen_TS45\water\distance_1\orientation_1\output\DC\resistance_10\
');
    file_location = ('E:\Documents\KU_Career\Dr. Friis Research\Ultrasound
Data\specimen_TS85\water\distance_1\orientation_1\output\DC\resistance_10\');
    fs = 50E6; %sampling frequency
    fc = 1E6; %cutoff frequency
    n = 6; %butterworth filter order

    %Prepare string with looping csv files that the oscilloscope saves.
    file = sprintf('tek0000.csv');
    %Make filename string.
    filename = [file_location file];
    %Read in data file.
    dat = csvread(filename,15,0);
```

```

%Record TIME (seconds) and CH1 (voltage) data.
TIME = dat(:,1);
Vout = dat(:,2);
%Calculate the size of the TIME array.
size_TIME = size(TIME,1);
%Calculate the time step for the TIME array.
time_step = (TIME(size_TIME,1)-TIME(1,1))/size_TIME;
%Make a new time array that will start at 0 time, and not some
%negative time. The oscilloscope takes the centerline on the
%display as zero time so anything to the left is negative time and
%anything to the right is positive. The "time" array is just that
%same time duration starting at 0 time.
time = zeros(size_TIME,1);
%Calculate absolute voltage for V_avg later on.
Vout_abs = abs(Vout);
%For loop to make time array based on time step starting at time =
%0.
for j=1:size_TIME
    time(j,1) = time_step*j;
end

g = 100;

[b,a] = butter(n,fc/(fs/2),'low');
filtered_data = filter(b,a,Vout);
filtered_data_abs = abs(filtered_data);

Y = fft(Vout);
T = 1/fs;
L = size(Vout,1);
t = (0:L-1)*T;
P2 = abs(Y/L);
P1 = P2(1:L/2+1);
P1(2:end-1) = 2*P1(2:end-1);
f = fs*(0:(L/2))/L;

X = fft(filtered_data);
P4 = abs(X/L);
P3 = P4(1:L/2+1);
P3(2:end-1) = 2*P3(2:end-1);

figure(1)
plot(f(1,g:end),P1(g:end,1));
%plot(f,P1);
title('|Amplitude| vs. Frequency(Hz)')
xlabel('Frequency(Hz)')
ylabel('|Amplitude|')
hold on
plot(f(1,g:end),P3(g:end,1));
%plot(f,P3);
legend('Un-filtered FFT','Filtered FFT')
%legend('Un-filtered FFT')

figure(2)
plot(time(g:end,1),Vout(g:end,1));

```

```

%plot(time,Vout)
title('DC Voltage(V) vs. Time(s)')
xlabel('Time(s)')
ylabel('DC Voltage(V)')
hold on
plot(time(g:end,1),filtered_data(g:end,1));
%plot(time,filtered_data);
legend('Un-filtered Data','Filtered Data')

sum = 0;
sum_filt = 0;

%For loop to compute Vavg and find max and min values in Vout array
for j=1:size_TIME
    if j == size_TIME
    else
        %Trapezoid rule formula
        sum = sum + (time(j+1,1)-time(j,1))*((Vout(j,1)+Vout(j+1,1))/2);
        sum_filt = sum_filt + (time(j+1,1)-
time(j,1))*((filtered_data(j,1)+filtered_data(j+1,1))/2);
        end
    end
    %Compute Vavg for particular sample
    Vavg = sum/time(size_TIME,1);
    Vavg_filt = sum_filt/time(size_TIME,1);
%    Vavg = mean(Vout);
%    Vavg_filt = mean(filtered_data);
    percent_diff = ((Vavg_filt-Vavg)/(Vavg))*100;

    save(['Ultrasound_DC_Filter_data_', specimen_name, '.mat']);

end

```

Appendix B: Ultrasound Machine Startup Procedure

Due to a power up error complication in the Acuson 128XP/10 medical imaging machine, a new startup procedure had to be followed in order to operate the machine. The ultrasound machine was manufactured in 1993 and some of the electrical components were beginning to underperform. During preliminary testing, a startup error occurred during operation of the machine. A jumper wire was placed according to the service manual across two terminals on one of the circuit boards housed in the machine, to bypass the startup error logic and allow for operation to occur. After fixing this, the ultrasound probe could not be recognized by the ultrasound imaging machine and it is believed that there is also a battery with some memory attached to it that is associated with the encryption strings of the ultrasound probe. It is presumed that this battery no longer holds charge so every time the ultrasound imaging machine is turned off, the battery loses its memory or knowledge of the encryption strings. Every time the ultrasound machine was started up, this would happen, so now the user has to input the encryption strings every time the machine is turned on. The startup procedure steps and figures for input the encryption strings are shown below.

1. Plug in the Acuson Computed Sonography 128xp/10 Ultrasound Machine to a power strip or wall outlet.
2. Plug in the 4 MHz (or # MHz of your choice) Ultrasound Transducer into the Ultrasound Machine. To “lock” the transducer into the Ultrasound Machine rotate the ultrasound probe knob approximately 90 degrees clockwise.



Figure 77 - Plugging in V4 Ultrasound Probe

3. Turn on the Ultrasound Machine by flipping the power switch (a green light should be emitting if the machine is on).



Figure 78 - Location of power switch on Acuson 128XP/10 ultrasound medical imaging machine

4. Wait a few minutes for the Ultrasound Machine to start up. You should see this screen.



Figure 79 - Contents of Ultrasound Imaging Screen after waiting a few minutes for the machine to startup

5. Press any key to continue and wait approximately one minute. Then press the “Reset” button.

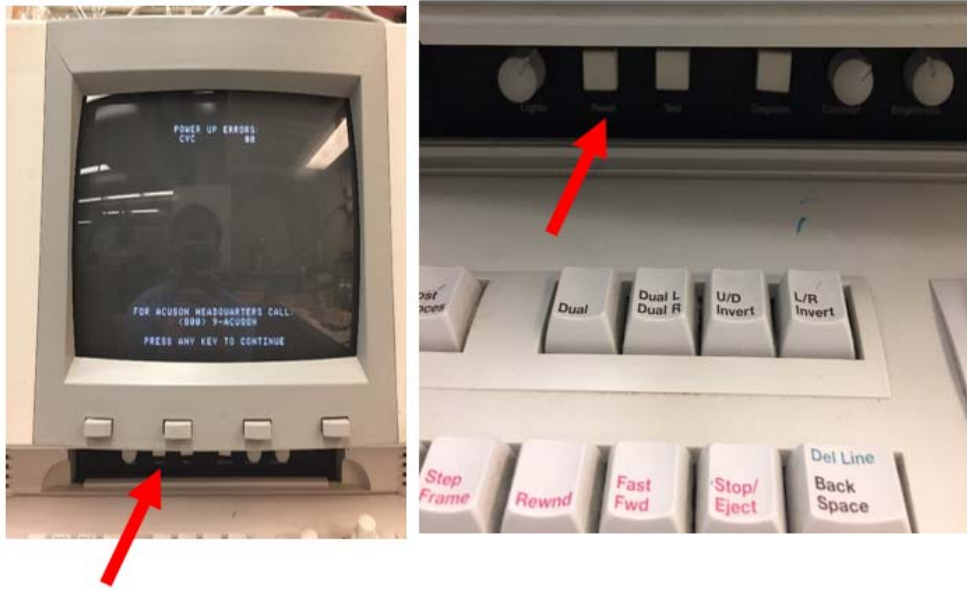


Figure 80 - Location of the "Reset" button

6. Wait for a few minutes until you see this screen again.



Figure 81 - Contents of Ultrasound Imaging Screen after waiting a few minutes again for the machine to startup

7. Press any key to continue and wait until you see this screen.



Figure 82 - Contents of ultrasound imaging screen after pressing any key to continue

8. Unplug the ultrasound transducer probe by “unlocking” it from the machine by rotating the knob back 90 degrees so that it is in a vertical position.



Figure 83 – Unlocking the V4 probe from the ultrasound imaging machine

9. Press the “Code”, “Shift”, “V” keys, and “Test” button all at the same time.

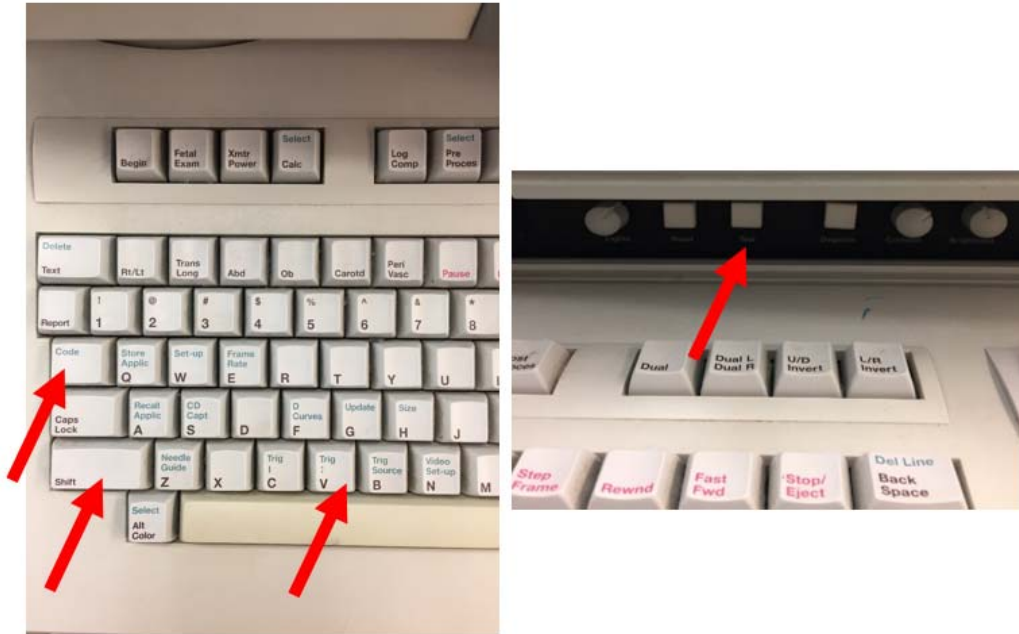


Figure 84 - Buttons pushed all at the same time to open General settings screen

10. You should then see this screen. Using the ultrasound ball (pictured to the right), scroll down to “Encryption Strings” and select “Encryption Strings” by pressing the left-most monitor button.

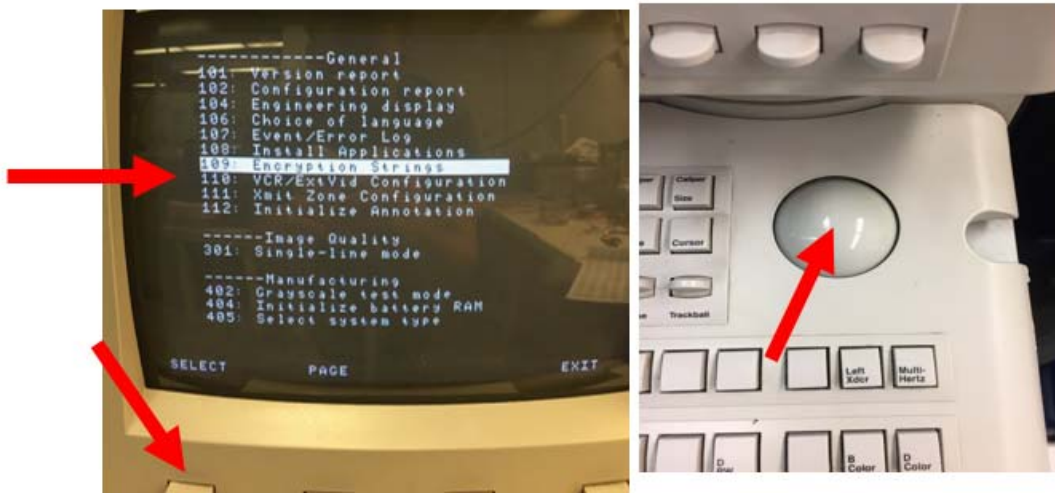


Figure 85 - General settings screen and roller ball on ultrasound imaging machine used to navigate through items on the screen

11. You should then see this screen.

13. After entering the Encryption Strings, your screen on the Ultrasound Machine should look like this.



Figure 88 - Filled out encryption strings

14. Save the newly input Encryption Strings by pressing on the monitor button below "Save" on the Ultrasound Machine Screen. There should be an indication on the screen that the new Encryption Strings were saved.

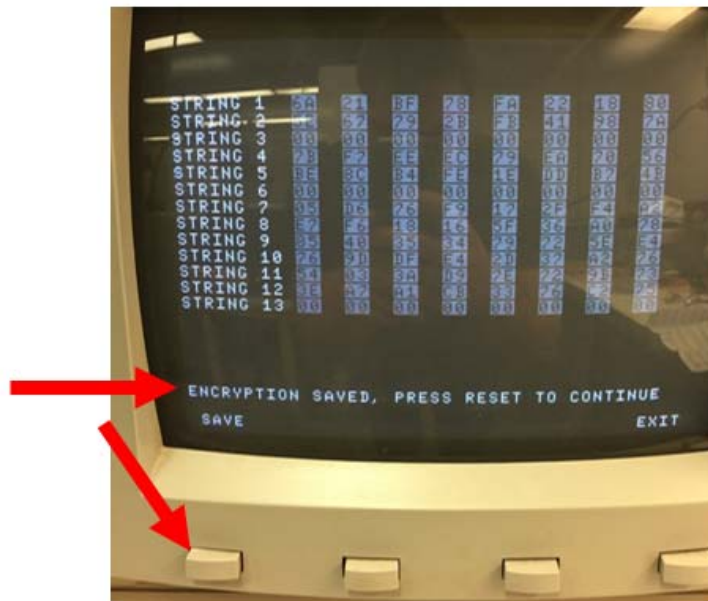


Figure 89 - Saving the encryption strings

15. Press the "Reset" button to reset the Ultrasound Machine with the new Encryption Strings.



Figure 90 - Reset the ultrasound medical imaging machine after entering and saving the encryption strings

16. Wait for a few minutes and then you should see a screen like this.



Figure 91 - Ultrasound imaging screen after resetting the machine after entering encryption strings

17. Now "lock" the Ultrasound Probe into the Ultrasound Machine by rotating the Ultrasound Probe knob approximately 90 degrees clockwise.

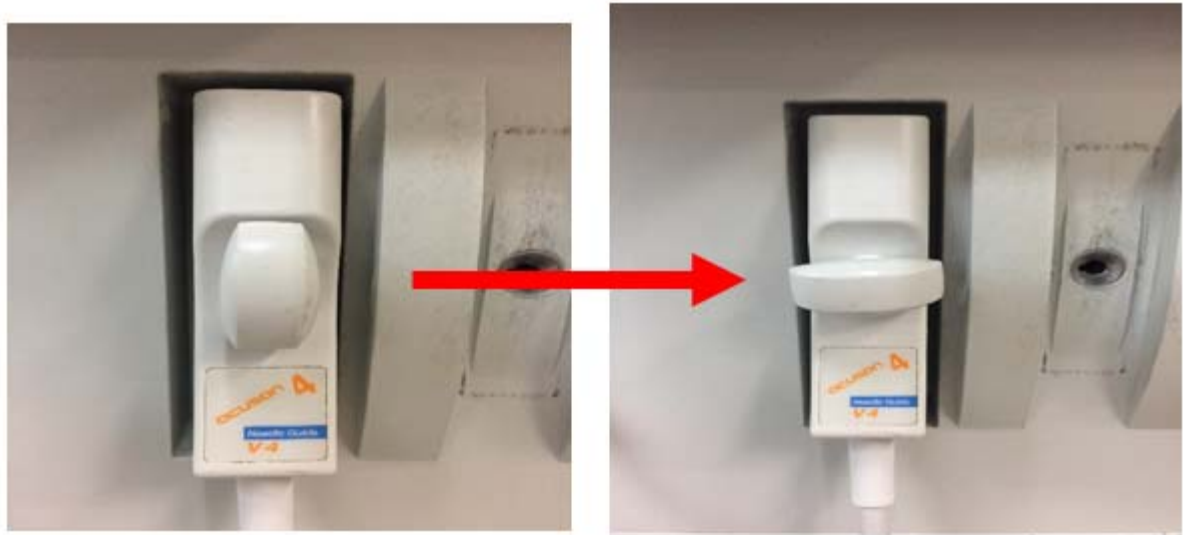


Figure 92 - Locking the V4 probe into the ultrasound imaging machine

18. If the screen indicates that the transducer has not been licensed, then rotate the Ultrasound Probe knob a little bit more in the clockwise direction.



Figure 93 - Ultrasound imaging screen if the probe is not fully connected to the machine

19. If done correctly, the Ultrasound Machine screen should indicate that the Ultrasound Transducer is initializing.

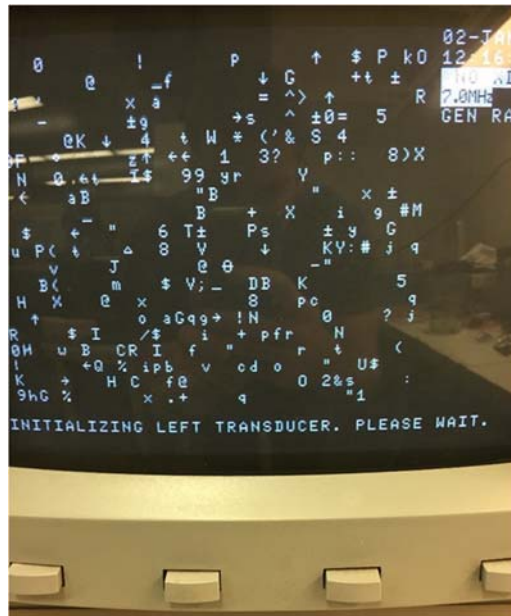


Figure 94 - Ultrasound imaging screen initializing if probe is connected to machine

20. Once the Ultrasound Machine is done initializing, the Ultrasound transducer the Ultrasound screen should indicate the appropriate MHz frequency of the probe that was chosen.

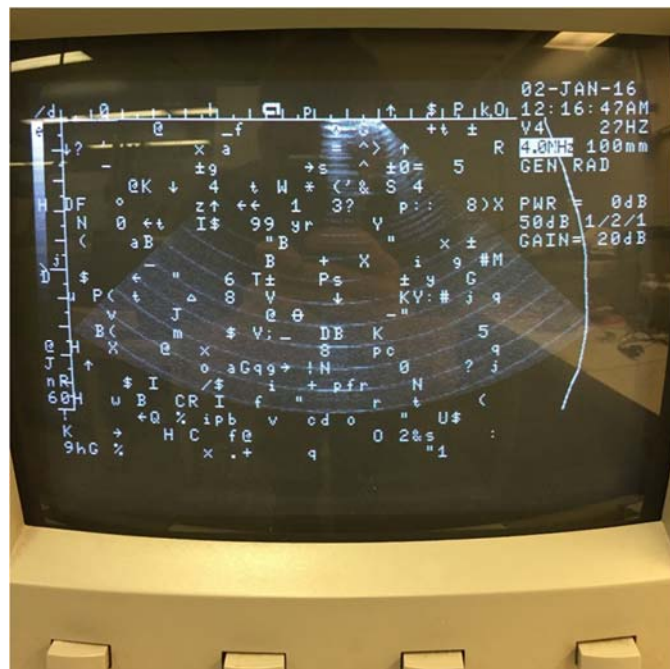


Figure 95 - Ultrasound imaging screen if probe is connected to machine after initializing is done

21. Now the Ultrasound Machine is producing sound waves out of the Ultrasound Probe. After testing, make sure to turn off the Ultrasound Machine by flipping off the power switch.



Figure 96 - Power off the ultrasound imaging machine

22. Unplug the Ultrasound Machine from the power strip/wall outlet to protect from electrical surges.